

Design of the field cage and charge response of the XENONnT dark matter experiment

vorgelegt von

Francesco Toschi

Dissertation

zur Erlangung des Doktorgrades
der Fakultät für Mathematik und Physik

**Albert-Ludwigs-Universität
Freiburg im Breisgau**



Freiburg, December 2022

Dekan der Fakultät

Prof. Dr. Michael Thoss

Betreuer der Arbeit

Prof. Dr. Marc Schumann

Zweitgutachterin

PD Dr. Andrea Knue

Prüfer

Prof. Dr. Stefan Dittmaier

Prof. Dr. Gregor Herten

Datum der mündlichen Prüfung

10.03.2023

*Alla mia famiglia,
per esserci sempre*

Abstract

A large number of cosmological and astrophysical observations suggest the existence of dark matter, which makes up more than 85 % of the matter in the Universe according to the current standard model of cosmology (Λ CDM). Weakly interacting massive particles (WIMPs) represent one of the most popular particle candidates for dark matter. Numerous experimental efforts have been focusing on their discovery either via direct production at colliders, indirect detection of their annihilation products or the direct detection of WIMP interactions with baryonic matter. The XENONnT direct detection experiment, located at the underground Laboratori Nazionali del Gran Sasso (LNGS), Italy, deploys a dual-phase time projection chamber (TPC) with a 5.9 t target of liquid xenon.

The central part of this work concentrates on the implementation of the field cage of the XENONnT TPC and its voltage divider. Their design heavily relied on finite element method (FEM) simulations of the electric field. The configuration was optimized by considering the homogeneity of the drift field in the active volume of the TPC and the fraction of target mass where liberated charges are drifted towards the detector walls and thus lost. Data from the first science run of XENONnT are used to validate the simulations. A discrepancy is observed, which is resolved by including a small sub- $\mu\text{C}/\text{m}^2$ charge accumulation on the sides of the active volume, estimated by matching the distribution of the reconstructed event positions. The top of the XENONnT field cage is independently biased by a power supply and not connected to the gate electrode via a resistor, as for the predecessor XENON1T. This allowed for the study of the impact of the field homogeneity on the detector response, proving the field-dependent nature of the electron lifetime, which quantifies the loss of free electrons to electronegative impurities. Lastly, a data-driven correction of the reconstructed position for the real electric field is presented, together with the study of its impact on the fiducial volume for the first results of XENONnT.

A system of capacitive sensors monitoring the position of the liquid xenon level has also been designed in the context of this work. The position of the liquid-gas interface is a crucial parameter for the simulation of the secondary signal in the gaseous phase. The simulation is done from first principles using the Garfield++ software, which returns the time distribution and intensity of the scintillation signal in gas. The good agreement with data allows also for the accurate modeling of the effects induced by extra “perpendicular” wires placed on the anode and gate wire electrodes. These additional wires were installed to avoid excessive deflection of the electrode wires predicted by a mechanical model developed in this work. Finally, variations in the thickness of the gas gap across the TPC surface are studied by comparing the data to the time profile from the Garfield++ simulations. Good agreement is found with the expected deformation of the wire electrodes.

Zusammenfassung

Zahlreiche kosmologische und astrophysikalische Beobachtungen deuten auf die Existenz dunkler Materie hin, die nach dem derzeitigen Standardmodell der Kosmologie (Λ CDM) mehr als 85 % der Materie im Universum ausmacht. Schwach wechselwirkende massive Teilchen (WIMPs) sind einer der populärsten Teilchenkandidaten für dunkle Materie. Zahlreiche experimentelle Bemühungen konzentrieren sich auf ihre Entdeckung, entweder durch die direkte Produktion an Collidern, den indirekten Nachweis durch ihre Annihilationsprodukte oder den direkten Nachweis von WIMP-Wechselwirkungen mit baryonischer Materie. Mittelpunkt dieser Arbeit ist das XENONnT-Experiment, das sich im Untergrundlabor Laboratori Nazionali del Gran Sasso (LNGS) in Italien befindet. XENONnT verwendet eine Zweiphasen-Zeitprojektionskammer (TPC) mit einem 5.9 t-Target aus flüssigem Xenon.

Der zentrale Teil dieser Arbeit befasst sich mit der Implementierung des Feldkäfigs der XENONnT TPC und seines Spannungsteilers. Sein Design basiert auf Finite Element Method (FEM)-Simulationen des elektrischen Feldes. Die Konfiguration wurde unter Berücksichtigung der Homogenität des Driftfelds im aktiven Volumen der TPC und des Anteils der Targetmasse, bei dem freigesetzte Ladungen zu den Detektorwänden driften und somit verloren gehen, optimiert. Messwerte der ersten wissenschaftlichen Datennahme von XENONnT werden zur Validierung der Simulationen verwendet. Dabei wird eine Diskrepanz beobachtet. Diese wird durch die Einbeziehung einer Sub- $\mu\text{C}/\text{m}^2$ -Ladungsakkumulation an den Wänden des aktiven Volumens gelöst. Die Ladungsakkumulation wird durch Anpassung der Verteilung der rekonstruierten Ereignispositionen geschätzt. Im Gegensatz zum Vorgängerexperiment XENON1T, ist der obere Teil des XENONnT Feldkäfigs unabhängig mit Spannung versorgt und nicht über einen Widerstand mit der Gate Elektrode verbunden. Dies ermöglichte die Untersuchung des Einflusses der Feldhomogenität auf die Detektorreaktionen und zeigte die Feldabhängigkeit der Elektronenlebensdauer, die den Verlust von freien Elektronen an elektronegative Verunreinigungen quantifiziert. Schließlich wird eine datengesteuerte Korrektur der rekonstruierten Ereignis-Position für das tatsächliche elektrische Feld vorgestellt, mitsamt ihrer Auswirkungen auf die Definition des Referenzvolumens für die ersten Ergebnisse von XENONnT.

Darüber inhaus wurde im Rahmen dieser Arbeit ein System kapazitiver Sensoren zur Überwachung des Flüssigkeitsstands von Xenon entwickelt. Die Position der Flüssigkeits-Gas-Grenzfläche ist ein entscheidender Parameter für die Simulation des Sekundärsignals in der Gasphase. Die Simulation erfolgt nach den ersten Prinzipien mit Hilfe der Software Garfield++, die die zeitliche Verteilung und Intensität des Szintillationssignals in Gas liefert. Die gute Übereinstimmung mit den Daten ermöglichte auch die genaue Modellierung der Ef-

fekte, die durch zusätzliche “senkrechte” Drähte an den Anoden- und Gate-Drahtelektroden hervorgerufen werden. Durch ein, in dieser Arbeit entwickelte, mechanische Modell, wurde eine übermäßige Ablenkung der Elektrodendrähte vorhergesagt. Um diese zu vermeiden, wurden diese zusätzlichen Drähte angebracht. Schließlich werden Schwankungen in der Dicke des Gasspalts entlang der TPC-Oberfläche untersucht, indem die Daten mit dem Zeitprofil aus den Garfield++-Simulationen verglichen werden. Es zeigt sich eine gute Übereinstimmung mit den Erwartungen, die sich aus dem Verformungsmodell der Drahtelektroden ergeben.

Contents

Introduction	1
1 The quest for dark matter	7
1.1 Dark matter evidence	7
1.2 Dark matter particle candidates	11
1.2.1 Alternatives to dark matter	13
1.3 The hunt for dark matter	13
1.3.1 Direct detection experiments	16
2 Liquid xenon for particle detection and the XENON dark matter project	23
2.1 Signal formation in liquid xenon	24
2.2 Dual-phase TPC detection principle	35
2.2.1 Background sources and mitigation	39
2.3 The XENON project	43
2.3.1 XENON10 and XENON100	43
2.3.2 XENON1T	45
2.4 XENONnT	49
3 Liquid level monitoring in the XENONnT TPC	55
3.1 Working principle of the capacitive level meter	56
3.2 Level meter design	58
3.2.1 Short level meters	58
3.2.2 Long level meters	60
3.2.3 Medium level meters	63
3.3 Read-out board	65
3.4 Level meters installation and calibration	67
3.4.1 Installation	67
3.4.2 Filling and calibration	69
3.5 Detector leveling	77

4 The XENONnT TPC field cage and field simulations	81
4.1 Field cage	82
4.2 Electric field simulations	94
4.2.1 COMSOL implementation	94
4.2.2 Systematic checks	97
4.2.3 Electron propagation using PyCOMes	102
4.3 Electric field optimization	103
4.3.1 Design optimal configuration	106
4.3.2 Bottom resistor performance	109
4.3.3 Design electric field	111
4.4 Mapping the transport properties of electrons	112
5 The electric field of XENONnT	117
5.1 Electric field in Science Run 0	118
5.2 Wall charge accumulation	121
5.2.1 Modeling and matching of the wall charge-up	124
5.2.2 Validation of the electric field map	126
5.3 Time dependence of the electric field	131
5.4 Impact of field cage tuning on TPC drift field	134
5.4.1 Charge-insensitive volume	135
5.4.2 Position distribution and wall charge-up	137
5.4.3 Electron lifetime evolution	140
5.5 Field distortion correction map	142
5.5.1 Working principle	143
5.5.2 The XENONnT field distortion correction map	145
5.6 Impact of the FDC on the fiducial volume	147
6 Simulating the S2 region	153
6.1 XENONnT electrodes	154
6.2 Wire sagging	157
6.2.1 Feedback effect	157
6.2.2 Measurements and validation	161
6.3 Perpendicular wires	163
6.3.1 Electric field simulations for the perpendicular wires	166
6.4 Electroluminescence simulation	172
6.4.1 Garfield++ framework	173

6.4.2	Single electron comparison	175
6.4.3	Perpendicular wires	178
6.5	Implementation in a full-chain waveform simulator	180
Summary and outlook		185
A Finite element method		191
B Sagging model		195
Bibliography		199

Introduction

In the last century an increasing amount of astrophysical evidence has supported the presence of a *dark matter* component in the Universe. The standard model of cosmology (Λ CDM) estimates that this dark component constitutes more than 85 % of the matter in the Universe, as determined from the observed anisotropies in the cosmic microwave background [1]. Among the many theories that have been proposed to explain the elusive nature of dark matter, the weakly interacting massive particle (WIMP) has gained particular popularity. A broad experimental effort is hunting for this particle, including collider searches at the LHC, indirect searches using satellites and ground-based observatories, and dedicated experiments for direct WIMP searches. Chapter 1 presents a summary of the dark matter enigma and the current state of the experimental searches for WIMPs.

Time projection chambers (TPCs) using liquefied noble gas as detection medium are an outstanding example of experiments for the direct search for WIMPs. A particle interaction in the liquid target produces a prompt scintillation signal (S1) and free ionization electrons. These electrons drift upwards towards the gas phase, where they are extracted to produce a secondary delayed signal (S2) proportional to the number of extracted electrons. The dual-signal response allows for three-dimensional position reconstruction and to distinguish whether the particle interacted with the nucleus or an electron of the target atom. The working principle of the dual-phase TPC is detailed in Chapter 2, along with an overview of the signal formation in liquefied noble gases, with a focus on the element xenon. Xenon is indeed a particularly suitable target for WIMP-nucleus interactions thanks to its good scintillation and ionization properties, its high atomic number, density, and the absence of natural radioisotopes. The current world-best limits for WIMP masses above $1 \text{ GeV}/c^2$ are mostly from xenon-based dual-phase TPCs [2]. Since its first stage, XENON10, commissioned in 2007 [3], the XENON dark matter project has deployed and further developed this technology and increased the size of the detector at each stage, setting world-leading limits on the WIMP-nucleon interaction cross section. The latest stage of the project is XENONnT, assembled and commissioned in 2020. It features an active target of 5.9 t, almost three orders of magnitudes larger than its “great-grandparent” XENON10.

Introduction

The first part of this work focuses on the design and implementation of two crucial components of the XENONnT TPC: the liquid xenon level meter system and the TPC field cage. The *level meter system* consists of a set of eight capacitive liquid level sensors, together covering the entire height of the TPC. The precise and continuous monitoring of the exact location of the xenon liquid-gas interface is important for the operation of XENONnT, both during filling of the detector and during nominal operations. Indeed, the position of the liquid xenon level between the anode and gate electrodes determines the intensity and time spread of the S2 signal produced in the gas gap below the anode. Chapter 3 describes the design of the level meter system and its read-out, as well as its installation and calibration. The successful operation of these sensors allowed for a precise leveling of the detector, reducing the tilt of the TPC to $\sim 0.02^\circ$. This ensured a uniform gas gap across the TPC, translating into a homogeneous proportional scintillation in the (x, y) plane.

A spatially uniform response of the TPC is crucial to maximize the sensitivity to WIMP-nucleon scattering. Since the charge and light production in liquid xenon directly depends on the strength of the electric drift field, a homogeneous field in the TPC target volume is as critical as a uniform gas gap. The homogeneity of the field is ensured by two nested arrays of field shaping copper electrodes (or rings) enclosing the liquid xenon target, forming the *field cage*. The arrays are connected via two redundant voltage dividers (or resistive chains) establishing a uniform field along the TPC. The top ring of the field cage is independently biased and this allows the electric field to be tuned once the detector is operational. The geometry of the field cage, together with the configuration of the resistive chain, were optimized to maximize the electric drift field, while minimizing the loss of electrons on the detector walls. This optimization is described in Chapter 4 and relies on the simulation of the electric field using the commercial software COMSOL Multiphysics[®] [4], which provides numerical finite element method (FEM) solvers.

The data from the first science run of XENONnT are used in Chapter 5 to study the electric drift field. The framework developed in Chapter 4 is used to compare the expected position distribution from simulations to the data from homogeneously distributed $^{83\text{m}}\text{Kr}$ calibration events. A good match is possible by including a charge distribution on the lateral reflectors of the TPC field cage. The required surface charge density is in the sub- $\mu\text{C}^2/\text{m}$ range. The obtained electric field map agrees with an independent estimation of the drift field using the ratio of the S1 signals from $^{83\text{m}}\text{Kr}$ events, and it solves the issue of the calibration source-dependence of the measured electron lifetime, as observed both by XENON1T [5] and XENONnT. The effect of the field homogeneity on the measurement

of the electron lifetime was also studied with dedicated data taking runs during which the field cage was tuned to different voltages. Eventually, a data-driven correction of the distortion due to the inhomogeneous drift field is presented, together with its impact on the estimation of the fiducial volume for the first results of XENONnT.

In Chapter 6 the work concludes with a study of the gaseous xenon region in which the S2 signal is produced. A model of the deformation of the wires of the anode and gate electrodes under the effect of electrostatic force is developed, including the feedback effect coming from the induced change of the electric field between the electrodes. The model agrees well with measurements carried out during a dedicated test of the gate electrode before the assembly of XENONnT. The deformation (or “sagging”) of the anode and gate wires due to their electrostatic attraction alters the gas gap and the electric field therein: this strongly affects the formation of S2 signal. The electroluminescence mechanism producing the S2 light is simulated using the Garfield++ software [6], using the FEM field simulation as an input. The agreement between these simulations and data is outstanding, especially considering that the Garfield++ output solely relies on first principles and the gas gap electric field simulation.

After a first test at liquid xenon temperatures, the wires of the XENONnT electrodes showed a loss in tension of more than 20 % on average. This resulted in excessive wire sagging at the design field configuration, leading to a larger risk of sparks and inactive detector regions for the production of S2 signals. A total of two (four) thicker wires were mounted perpendicularly to the grid wires of the gate (anode) electrodes in order to counteract the tension loss. The impact of these “perpendicular” wires on the formation of S2 and electron propagation is simulated and successfully compared to the observed data. Finally, the height of the gas gap is inferred from the shape of the S2 signal from extracted single electrons matched to the Garfield++ simulation. This map is then compared to the expectation from the model of the sagging of the wire electrodes, yielding a good agreement between the two independent expectations.

Personal contribution

The hunt for dark matter is ongoing since almost one hundred years and it has seen a large improvement, both on the experimental and theoretical sides. Chapters 1 and 2 represent a brief summary of this hunt and its state-of-art. The work presented in this thesis is the result of the efforts of many people from the XENON collaboration who developed and

Introduction

operated the XENONnT detector. Here I summarize my contributions to the present work. All data analyses are my original work unless otherwise stated in the following. The design of the field cage described in Chapter 4 and the studies on the electric field homogeneity of Chapter 5 are discussed in a paper currently under collaboration review and of which I am one of the corresponding authors.

Chapter 2 - Liquid xenon for particle detection and the XENON dark matter project

Some focus is given to the discussion of the gamma-spectroscopy facility GeMSE (Sec. 2.2.1) as I had an active role both in its operation and upgrade. I am an author of the paper reporting the latest background measurement and the facility upgrades [7].

Chapter 3 - Liquid level monitoring in the XENONnT TPC

Expanding on the previous work of C. W. Geis [8] at the University of Mainz I designed the long and medium level meters for the XENONnT TPC. The short level meters were machined according to the XENON1T design and afterwards tested. I cooperated with the electronic workshop of the University of Freiburg (in particular K. Mahboubi and V. Tyzhnevyi) for the development of a new read-out board, improving the design of XENON1T. This board design is currently used by other experimental setups of the Freiburg group like PANCAKE (DARWIN full-diameter demonstrator) and the gamma-spectroscopy facility GeMSE [7]. The installation of the level meters was performed by me and Dr. S. Lindemann. I performed the calibration of the level meters during the operations of filling and together with Prof. Dr. A. P. Colijn (Nikhef) I contributed to the successful leveling of the TPC.

Chapter 4 - The XENONnT TPC field cage and field simulations

I set up the entire COMSOL Multiphysics[®] simulation and the analysis framework for the optimization of the field configuration. This involved also the development of the custom-made package PyCOMes [9] to handle the COMSOL output files and track the drift of electrons in the liquid xenon target. The design of the field cage was led by Chicago and Freiburg universities. My main contribution to the design of the TPC was the implementation of the double-array field cage and its resistive chain, an effort lead by Dr. S. Lindemann. I also played an important role in different stages of the assembly of the XENONnT TPC, co-leading the installation of the field cage. Finally, I estimated the maps of the electron transport properties of Sec. 4.4 and implemented them in the full chain simulation framework of XENONnT [10].

Chapter 5 - The electric field of XENONnT

The data used for the analyses of this chapter are the final product of a large effort involving every member of the XENON collaboration. The cross-check studies for the field map derived from matching the $^{83\text{m}}\text{Kr}$ distribution were performed by Y. Ma (UCSD, data-driven field map from $^{83\text{m}}\text{Kr}$ S1s ratio) and Dr. M. Kobayashi (Columbia University, electron lifetime field correction). Dr. Kobayashi also developed the tool to estimate and correct the electron lifetime for a given field map which is used also for field cage tuning of Sec. 5.4. Finally, the data-driven correction of the position reconstruction due to the field distortion follows a similar study by Dr. J. Ye (Columbia University) for XENON1T, while the study of its impact on the fiducial volume is novel work.

Chapter 6 - Simulating the S2 region

The development and study of the electrodes was an effort shared among several groups. My original contribution was the development of the model describing the deformation of the grid wires under the electrostatic force, as presented in Sec. 6.2. The tests carried out at LNGS were performed mainly by Dr. F. Lombardi (Mainz University), Prof. Dr. C. Macolino (L'Aquila University) and Dr. P. Shagin (Mainz University). I developed the electroluminescence simulations using the Garfield++ framework, introducing for the first time in the XENON simulation framework a model for the production of the S2 signal solely based on first principles. This returned a good agreement with the observed waveforms of the single electrons. By comparing the shape of these signals with the simulations for different gas gap lengths, it is possible to define an (x, y) map of the gas gap profile. This study was performed by J. Long (Chicago University). The map is compared to the expectation from the sagging model, returning a good agreement.

Chapter 1

The quest for dark matter

The last century has seen an increasing number of astrophysical and cosmological observations requiring the presence of *dark matter* to be explained. Nowadays, the standard model of cosmology (Λ CDM) suggests that about 27% of the energy-matter content of the Universe consists of a non-relativistic (i.e., cold) dark component [1]. The overwhelming evidence motivates the large and diversified efforts towards the understanding and detection of dark matter, both in theoretical models and experimental searches.

The main evidences for the existence of dark matter are discussed in Sec. 1.1 and its particle candidates are presented in Sec. 1.2. Some theories have been proposed to explain the observations without including dark matter particles: they are discussed in Sec. 1.2.1. Finally, Sec. 1.3 presents an overview of the current experimental landscape of the search for dark matter. The main focus is the class of “direct” search experiments, relying on the direct interaction of a dark matter particle with the detector target.

1.1 | Dark matter evidence

In the most generic sense, dark matter is a component of the Universe whose existence is inferred from indirect measurements and not directly observed. This term was originally coined by the French mathematician and physicist Henri Poincaré [11, 12]. He used it to describe an hypothetical component of the Universe proposed by Lord Kelvin, capable of blocking light from the stars, thus explaining their observed inhomogeneous distribution [13]. Along similar lines, first models of the galactic mass distribution of this type of dark matter were developed by Oort [14] and Jeans [15] in the 1920s.

The first suggestion of the existence of dark matter in the modern sense dates back to 1933. Based on the measurements of the velocity of the galaxies in the Coma cluster by Hubble and Humason [16], Fritz Zwicky determined the gravitational mass of the cluster via the viral theorem [17,18]. The mass estimated by Zwicky was 500 times larger than the mass deduced from the luminosity of the system, a factor reduced to ~ 100 today when considering the Hubble constant from the Planck satellite $H_0 = (67.36 \pm 0.54)$ km/s/Mpc [1]. The existence of dark matter was neither discarded nor accepted by the scientific community until 1970, when the precise measurement of the rotation curve of the Andromeda spiral galaxy (M31) was published by Kent Ford and Vera Rubin [19]. The curve showed that the outer stars were characterized by a large and constant velocity, in disagreement with the expected behaviour from the observed mass distribution. Assuming the galaxy density to be confined in the central bulk of mass M_{bulk} and radius R_{bulk} , the rotation velocity goes as $v(r) \propto r^{-1/2}$ for $r > R_{\text{bulk}}$, with r being the radial distance from the center of the galaxy. The observations by Rubin and Ford can be explained by a density profile $\rho(r) \propto r^{-2}$, requiring the galaxy to be surrounded by a *halo* of dark matter. The rotation curves of two galaxies are shown in Fig. 1.1. They come from the SPARC database [20], based on the $3.6 \mu\text{m}$ photometry measurements of the Spitzer telescope [21]. The velocity distribution expected from the observable matter rapidly falls for large radii, requiring a

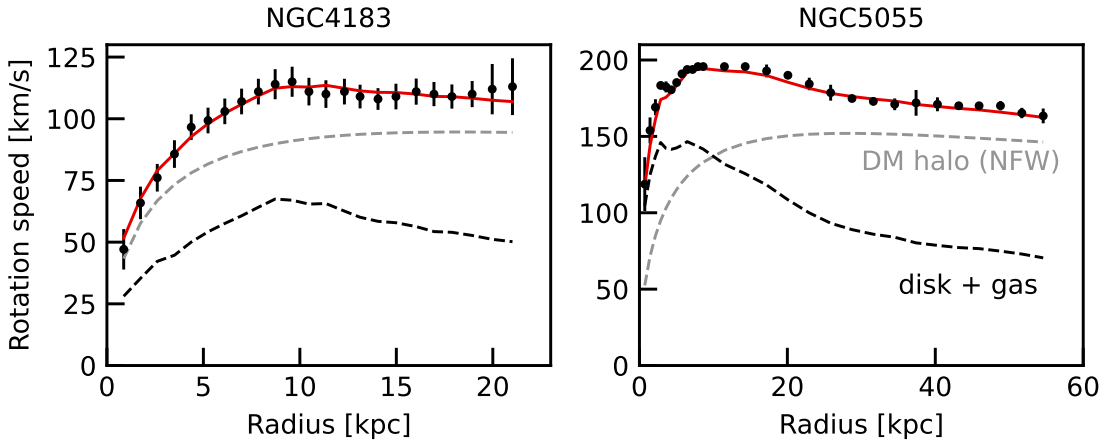


Figure 1.1 Rotation curves of two spiral galaxies from the SPARC database [20]. The data (black dots) come from $3.6 \mu\text{m}$ photometry measurements of the Spitzer telescope. The total fit (red line) is the sum of the baryonic component (disk + gas, dashed black) and the dark matter halo component (gray dashed). The Navarro-Frenk-White (NFW) density profile for the dark matter halo is assumed for the fit.

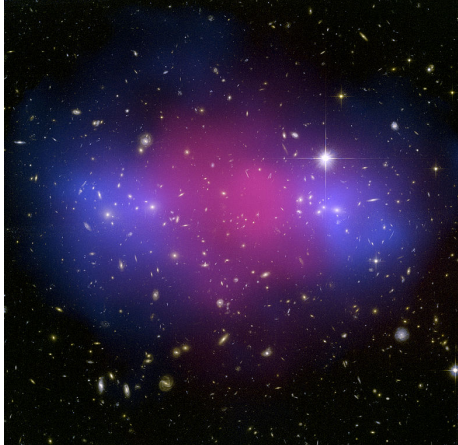


Figure 1.2 Galaxy cluster MACS J0025.4-1222 as observed by the NASA/ESA Hubble Space Telescope. The mass distribution from gravitational lensing is shown in blue. The density of the hot gas representing the majority of the cluster’s ordinary matter is shown in pink. This is derived from X-ray measurements using the Chandra observatory. Image courtesy of NASA.

dark matter halo contribution to match the measurements [22]. The halo is modeled using the Navarro-Frenk-White (NFW) density profile $\rho(r) \propto r^{-1} \cdot (1 + r/r_s)^{-2}$ [23], observed from N-body simulations of structure formation, with a free parameter known as the radius scale r_s . Other popular models to describe the dark matter halo include pseudo-isothermal density profiles [24, 25], hydrodynamical simulations of dwarf galaxies [26, 27] and N-body simulations including the baryonic gravitational feedback on dark matter [28].

Since the measurement of anomalous galactic rotation curves, the number of observations requiring a dark component has largely increased. Galaxy clusters have provided an additional piece of evidence of dark matter since Zwicky’s studies. The comparison of the X-ray emission profile of systems of massive colliding clusters with their gravitational profile shows a clear discrepancy in the distribution of radiation-emitting and gravitational mass. Examples of these systems are the so-called “Bullet cluster” (1E 0657-558, [29]) and MACS J0025.4-1222 [30]. The latter is shown in Fig. 1.2. The mass density as determined by the X-ray emission measured by the Chandra observatory [31] is shown in pink, while the mass density as determined from gravitational micro-lensing is shown in blue. The micro-lensing effect consists in the increase of luminosity of a light source due to the presence of a mass distribution sitting along the line of sight and acting as a gravitational convergent lens [32, 33]. The difference in the two distributions shows that the region with a larger concentration of baryonic mass (i.e., intergalactic gas) does not correspond to the region with larger mass density. This can be explained including a component interacting only gravitationally, like dark matter.

Evidence at the cosmological scale comes from the precise measurement of the cosmic microwave background (CMB), discovered in 1964 by Penzias and Wilson [34]. The CMB is the relic radiation from the early Universe, when free electrons and protons recombined

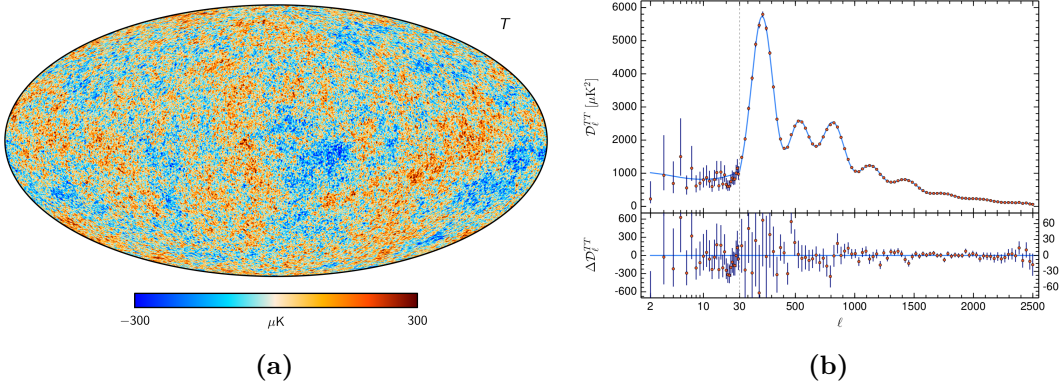


Figure 1.3 (a) *CMB map in galactic coordinates as measured by the Planck space observatory. The average and the $\ell = 1$ contributions are subtracted.* (b) *Power spectrum of the CMB as function of the multipole moment ℓ . The y-axis shows the values $D_\ell^{TT} = \ell(\ell + 1)C_\ell/2\pi$. Plot from [37].*

into neutral hydrogen atoms transparent to photons. In the standard model of cosmology the photons decoupled from matter 380 000 years after the Big Bang, when the Universe temperature dropped to 3000 K [35]. Today the CMB presents a black body spectrum with average temperature $T = (2.7255 \pm 0.0006)$ K, as given by combined results from COBE/FIRAS and WMAP [36]. Although highly isotropic, the CMB spectrum presents $\mathcal{O}(100 \mu\text{K})$ anisotropies. These can be measured thanks to the high resolution of the ESA space observatory Planck [1]. These anisotropies arose from density fluctuations in the early stages of the Universe that eventually led to the formation of the large structures we observe today. The Planck map of the CMB is shown in galactic coordinates in Fig. 1.3a. The most important information comes from the CMB decomposition into spherical harmonics $Y_{\ell,m}$:

$$\frac{T(\theta, \phi) - \langle T \rangle}{\langle T \rangle} = \sum_{\ell=0}^{+\infty} \sum_{m=-\ell}^{+\ell} a_{\ell,m} Y_{\ell,m}(\theta, \phi) \quad \Rightarrow \quad C_\ell = \frac{1}{2\ell+1} \sum_{m=-\ell}^{+\ell} a_{\ell,m}^2. \quad (1.1)$$

The power spectrum obtained from this decomposition is shown in Fig. 1.3b. Small ℓ values correspond to large angular scales, meaning that the first part of the spectrum carries information on the large scale of the Universe [38]. Large ℓ values present acoustic peaks associated to the oscillation of baryonic and dark matter in gravitational potential wells. By fitting these peaks in the Λ CDM framework, it is possible to infer the abundance of baryonic and dark matter, as well as dark energy. The excellent agreement of the fit with data is a validation of the cosmological standard model Λ CDM, where Λ indicates the *dark energy*.

component necessary to explain the present expansion rate of the Universe, and CDM is the cold (i.e., non-relativistic) dark matter component. A parameter $\Omega_{\text{DM}} h^2 = 0.1200 \pm 0.0012$ was inferred by Planck [1], representing 84 % of the total matter in the Universe. Ω_{DM} represents the dark matter contribution as a fraction of the critical energy density for a flat Universe, while h is the Hubble constant into units of 100 km/s/Mpc.

1.2 | Dark matter particle candidates

Despite the large evidence in support of the existence of dark matter, its nature is still unknown today. The baryonic nature of dark matter can be excluded by the CMB power spectrum leading to a baryonic content of $\Omega_b \sim 5\%$, and the measurement of the abundance of light elements that is in agreement with the predictions of Big Bang nucleosynthesis [39]. A dedicated search for Massive Compact Halo Objects (MACHOs) (e.g., brown dwarfs or black holes) using gravitational lensing was carried out by different collaborations, such as OGLE [40], MACHO [41] or EROS. The fraction of dark matter that can be explained by MACHOs was limited by the EROS collaboration to 8 % [42], further excluding a baryonic nature of dark matter.

Excluding the baryonic nature of dark matter, its presence requires the existence of massive, stable and neutral particles not interacting electromagnetically nor strongly, but only through gravitational and, possibly, weak interactions or via new interactions at the weak scale (or weaker). Natural candidates coming from the Standard Model (SM) are relic neutrinos forming the cosmic neutrino background ($C\nu B$) [43, 44], particles known to be massive due to their flavour oscillation [45, 46]. The neutrino nature of dark matter can be disproven by considering the impact of dark matter on the formation of the large scale structures of the Universe. These structures come from overdense regions of dark and baryonic matter, due to density fluctuations in the primordial Universe. In this simplified picture, the faster dark matter particles move, the more washed out the primordial structures are. Neutrino dark matter would be characterized by relativistic velocities at the decoupling time of baryonic matter and photons, hence it would be *hot*. This results in a top-down structure formation model, where the large structures form first to then cluster in smaller components [47]. The derived time scales are too long compared to current observations [48], therefore neutrinos were discarded as possible candidates. Numerical N-body simulations of the Universe formation show a good agreement with a bottom-up model [49], with small objects collapsing under their gravitational pull which

then cluster to form more massive objects. This model is explained only by non-relativistic *cold* dark matter.

In the rich landscape of hypothetical non-baryonic particles for cold dark matter, the weakly interacting massive particles (WIMPs) represent the most popular set of candidates. WIMPs, often labeled as χ , naturally arose in *supersymmetry* theories, which introduce a group of global transformations associating to each SM fermion (boson) a corresponding bosonic (fermionic) superpartner [50]. The new class of supersymmetric particles are expected to have masses of GeV/c^2 to hundreds of TeV/c^2 , with the lightest particle being the ideal candidate when assuming *R*-parity conservation [51]. More in general, WIMPs represent a class of dark matter candidates with mass in the range $10 \text{ GeV}/c^2$ to $10^3 \text{ TeV}/c^2$ which is characterized by a *freeze-out* production mechanism. This mechanism assumes an initial equilibrium of WIMPs with all other particles in the early stages of the Universe [52]. As the temperature decreased below the WIMP mass ($T < m_\chi$), the annihilation process of dark matter dominates over its production, leading to a density decrease following the Boltzmann factor $e^{-m_\chi/T}$. As the Universe expands, the annihilation process of the WIMP becomes less likely and the WIMP abundance “freezes out”, resulting in the current relic abundance. Approximating the freeze-out temperature to $T = m_\chi/20$, the relic abundance can be approximated by $\Omega_{\text{WIMP}} h^2 \approx 3 \cdot 10^{-27} \text{ cm}^3 \text{s}^{-1} / \langle \sigma_{\text{ann}} v \rangle$ [53]. Including the Planck results for the dark matter density [1], the obtained cross section values σ_{ann} agree well with weak interactions. This is known as *WIMP miracle* and it has been one of the main reasons behind the large experimental effort focused on WIMP searches [2]. As neither the mass nor the interaction strength of WIMPs with ordinary matter are known, it is important to scan a broad parameter range.

Another important dark matter candidate is the *axion*, originally proposed to explain the unbroken CP symmetry of QCD, known as the strong CP problem. The axion occur in the Peccei-Quinn theory [54, 55] as the pseudoscalar Nambu-Goldstone boson from a spontaneously broken U(1) symmetry, introduced to restore the CP symmetry in QCD. The mass of the axion is $m_a = 0.6 \text{ eV}/c^2 \frac{10^7 \text{ GeV}}{f_a}$, where f_a is the Peccei-Quinn energy scale. Typical axion masses are in the order of $\mu\text{eV}/c^2$ or few meV/c^2 . An extensive review of the status of the art of theory and experiments for axions is reported in [56].

A complete overview of the entire landscape of dark matter candidates is presented in [57], including the possibility that dark matter is constituted by more than a single type of particles. For the rest of the work the dark matter particle of reference is the WIMP.

1.2.1 | Alternatives to dark matter

The evidence for the existence of dark matter presented in Sec. 1.1 relies on the assumption that general relativity and its Newtonian approximation hold at the galactic and extra-galactic scales, where they have not been probed to a high precision. A family of theories was developed starting in the 1980s, proposing a different behaviour of the laws of gravity at large length scales. The first *modified gravity* theory was proposed in 1982 by Milgrom [58] to explain galactic rotation curves. His Modified Newtonian Dynamics (MOND) theory includes a parameter scale $\mu(a/a_0)$ in the second law of dynamics, such that $-\vec{\nabla}\Phi = m\mu(a/a_0)\vec{a}$, with the acceleration scale $a_0 \sim 10^{-8} \text{ cm/s}^2$. The parameter scale is defined such that $\mu \xrightarrow{a \gg a_0} 1$ and $\mu \xrightarrow{a \ll a_0} a/a_0$. By construction the MOND theory predicts flat galactic rotation curves [59] similar to the ones of Fig. 1.1, as for low acceleration values

$$\frac{a^2}{a_0} \approx \frac{G_N M(r)}{r^2} \Rightarrow a \approx \frac{\sqrt{G_N M(r)a_0}}{r} \Rightarrow v \approx (G_N M(r)a_0)^{1/4}.$$

A relativistic extension of Milgrom's theory was proposed by Bekenstein and it is known as Tensor-Vector-Scalar (TeVeS) theory [60].

An important breakthrough in the modified gravity theories came from the detection of the gravitational wave GW170817A by LIGO-Virgo [61]. This event was the first observation of a coalescence of a binary neutron star and the first gravitational wave with an observable electromagnetic counterpart. To date it represents the only signal of this type. The Fermi Gamma-ray Burst Monitor detected a short burst (1.74 ± 0.05) s after the wave detection [62], as shown in Fig. 1.4. The difference between the time propagation of the photons and gravitational waves set strong constraints on *Dark Matter Emulator* theories such as TeVeS. These theories emulate the presence of dark matter introducing a different space-time metric for ordinary matter and for gravitational waves, where the first is affected by a dark matter-like component. The different metrics lead to differences in the propagation time of photons and gravitational waves of up to 1000 days, in strong disagreement with the <2 s observation [63–66].

1.3 | The hunt for dark matter

The search for particle dark matter has been one of the most active fields of experimental physics in the last decades. The large number of dedicated experiments can be mainly divided into indirect and direct searches, the first looking for the products of the annihilation

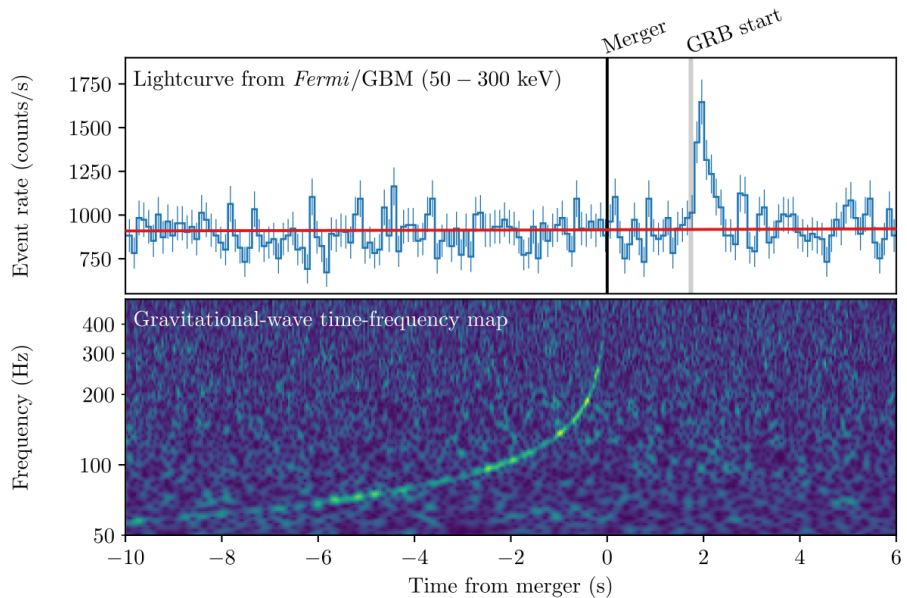


Figure 1.4 Gravitational wave from the coalescence of a binary neutron star (event GW170817A) as observed by LIGO-Virgo (bottom) and the electromagnetic gamma-ray burst observed by *Fermi*-GBM \sim 2 s later (top). Plot from [62].

of WIMPs and the second looking for its direct interaction with standard matter. These experiments rely on the presence of dark matter in the Universe to produce a signal. Differently, accelerator-based experiments use the interactions of SM particles to produce WIMPs and identify them as missing transverse momentum. Today the strongest constraints from colliders come from the multi-purpose detectors ATLAS and CMS at the LHC proton-proton collider [67]. Although these experiments cannot assess the dark matter relic nature of a newly discovered WIMP candidate, they represent the best tool to study its interaction with the Standard Model components. They also represent a complementary channel to direct and indirect searches, as they are sensitive to a large number of additional dark matter models.

The indirect search for dark matter focuses on the identification of anomalous fluxes of SM particles coming from the annihilation or decay of WIMPs, typically bound in heavy objects. Highly energetic (>1 GeV) neutrinos from WIMP annihilation inside the Sun represent an almost background-free signal. Assuming an equilibrium between WIMP capture within the Sun and their annihilation into neutrinos, the observed neutrino flux can be related to the cross section of the WIMP-proton interaction. Large scale neutrino observatories like IceCube, Super-Kamiokande and ANTARES have reported the best

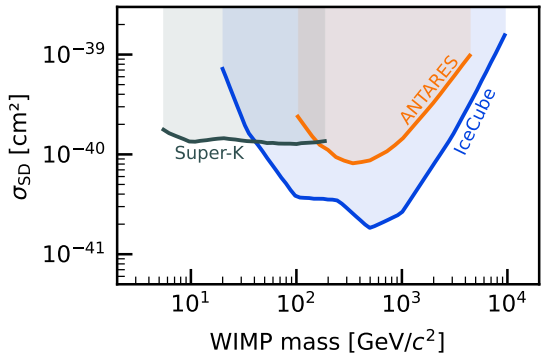


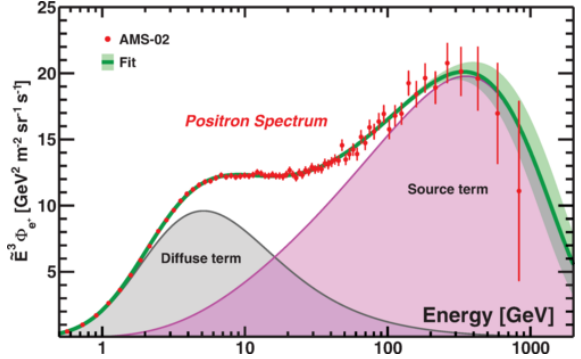
Figure 1.5 Limits on the spin dependent WIMP-proton cross section from the flux of high energetic solar neutrinos. Redrawn from [68].

limits for this type of interactions [68–70], as shown in Fig. 1.5. The limits reported in the plot are for spin dependent (SD) interaction cross section. This is due to the fact that the Sun is mainly composed of protons with spin $\frac{1}{2}$, making these measurements particularly sensitive to the impact of the spin in the WIMP-nucleon interaction.

The large dark matter density at the center of the Galaxy makes it the best candidate as a WIMP signal source. Together with the expected neutrino signature [71–73], strong constraints come from the search for an anomalous gamma-ray flux from the galactic center using satellite-based detectors or ground-based Čerenkov telescopes. The observation of an excess of energy E_γ could be the product from the decay of WIMPs with mass $m_\chi = E_\gamma$ into back-to-back gammas. This decay is possible thanks to the contribution of fermionic loops, as a direct coupling of the WIMP with the electromagnetic sector is forbidden. WIMP masses up to 1 TeV/ c^2 are strongly constrained by the Fermi - Large Area Telescope (LAT) [74], while larger masses are better probed by air Čerenkov telescopes such as HESS [75].

Important hints of the presence of WIMP annihilation in the Galaxy also come from the measurement of the primary cosmic ray composition. An excess of the positron flux in the energy range 0.5–500 GeV was first observed by the PAMELA detector [76]. These measurements were later confirmed and extended by the AMS-02 collaboration [77]. The measured positron spectrum is shown in Fig. 1.6. Its shape can be well described by a diffuse contribution coming from the cosmic rays’ propagation in the Galaxy and a “source” term for higher energies. The source term can be explained by the annihilation of leptophilic dark matter [78], however, a pulsar sufficiently close to the Milky Way can similarly explain the observed excess. A possible candidate for such pulsar was proposed in [79].

Figure 1.6 Positron spectrum measured by AMS-02 (red data points). The fit with the 68% C.L. interval is shown in green. The fit includes a primary cosmic ray diffuse term (gray) and a source term (pink). WIMP annihilation is a possible explanation of the nature of this source term. Plot from [77].



1.3.1 | Direct detection experiments

The strongest constraints on interactions of WIMPs with ordinary matter come from direct search experiments. These experiments aim for the detection of the interaction of dark matter particles with a massive target. The observed signal comes from the WIMP elastically scattering off a nucleus (nuclear recoil, NR) or an electron (electronic recoil, ER), which in turn deposits energy in the detector. Because of the smaller background, WIMP searches focus typically on the NR interactions with energy deposition in the order of tens of keV or less. Considering NR interactions, for a detector with a target of total mass M and atomic mass m_N the expected differential rate is [80]

$$\frac{dR}{dE_R} = \frac{\rho_0 M}{m_\chi m_N} \int_{v_{\min}}^{v_{\text{esc}}} v f(\vec{v}) \frac{d\sigma}{dE_R} d^3\vec{v}, \quad (1.2)$$

where the dark matter, with local density ρ_0 and mass m_χ , is characterized by a Maxwell-Boltzmann velocity distribution $f(\vec{v})$ with most probable speed $v_0 = 220$ km/s. The local dark matter density is usually taken as $\rho_0 = 0.3$ GeV/cm³, although also different values have been proposed in the last decades [81]. The differential cross section $\frac{d\sigma}{dE_R}$ is integrated within the kinematically accessible speed range between v_{\min} and v_{esc} . The upper limit is the Milky Way escape speed $v_{\text{esc}} = 544$ km/s [82], while the lower limit is the minimum WIMP speed to produce a recoil of energy E_R . Considering a head-on collision in non-relativistic conditions, the minimum speed is given by

$$v_{\min} = \sqrt{\frac{m_N E_R}{2\mu^2}}, \quad (1.3)$$

where μ is the reduced WIMP-nucleus mass.

For elastic WIMP-nucleus scattering, the average nuclear recoil energy is given by

$\langle E_R \rangle = \frac{\mu^2 v^2}{m_N} \langle 1 - \cos \theta \rangle = \frac{\mu^2 v^2}{m_N}$, where θ is the scattering angle. Assuming a WIMP with mass $m_\chi = 50 \text{ GeV}/c^2$ and velocity v_0 interacting with a xenon target ($m_N = 131.3 \cdot m_p$, with m_p the proton mass), the average recoil energy is around 5 keV. This corresponds to a de Broglie radius of around 8.5 fm, comparable to the radius of the xenon nucleus of ~ 6 fm. For this reason, WIMPs scatter elastically off the nucleus through a coherent process, instead of interacting with the single nucleons. The differential WIMP-nucleus cross section is expressed in its generic form as the combination of a spin dependent (SD) and independent (SI) component

$$\frac{d\sigma}{dE_R} = \frac{m_N}{2v^2\mu^2} \left(\sigma_{\text{SI}} F_{\text{SI}}^2(E_R) + \sigma_{\text{SD}} F_{\text{SD}}^2(E_R) \right). \quad (1.4)$$

The form factor $F(E_R)$ is different for spin dependent and independent interactions, but in both cases it represents the impact of the extended structure of the nucleus in the elastic scattering. The results from direct search experiments like XENONnT are typically presented in the SI scenario, where the form factor $F_{\text{SI}}^2(E_R)$ is the Fourier transformation of the nucleon density. Assuming a Woods-Saxon distribution, the form factor is approximated by an analytical function proposed by Helm [83]. The SI cross section for coherent elastic scattering of a WIMP off the nucleus can be written as

$$\sigma_{\text{SI}} = \sigma_n \frac{\mu^2}{f_n^2 \mu_n^2} [Z f_p + (A - Z) f_n]^2 \stackrel{(f_n=f_p)}{=} \frac{\mu^2}{\mu_n^2} A^2 \sigma_n \quad (1.5)$$

where μ_n is the WIMP-nucleon reduced mass and σ_n is the SI WIMP-nucleon cross section, which is the result typically reported to compare experiments using different targets. The coupling of the WIMPs to protons and neutrons is typically assumed to be identical ($f_n = f_p$). Because of the proportionality $\sigma_{\text{SI}} \propto A^2$, experiments with heavier target nuclei like xenon ($A \simeq 131$) have a larger SI scattering rate. The differential rate from Eq. (1.2) is shown in Fig. 1.7 for different targets and different WIMP masses. Although the rate is higher for larger nuclei, the form factor has a stronger impact in suppressing the rate for larger recoil energies. For lower WIMP masses the spectrum drops faster with the recoil energy E_R , especially for heavier targets, enhancing the importance of the energy detection threshold and affecting the discovery power of experiments using heavy nuclei. Light targets like small- A nuclei or electrons increase the maximal energy deposition, representing the best target candidates to search for sub-GeV WIMPs.

The energy deposited in the detector's target material can lead to three different types of signal: *heat* deposition, which results in the production of *phonons* in crystalline

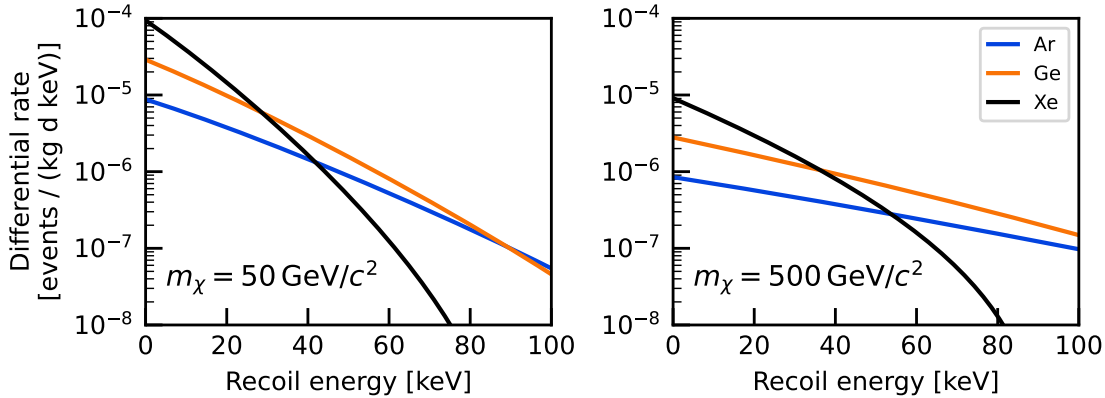


Figure 1.7 Differential interaction rates for SI WIMP-nucleus elastic scattering assuming $v_{\text{esc}} = 544 \text{ km/s}$, $v_0 = 220 \text{ km/s}$ and $\rho_0 = 0.3 \text{ GeV/cm}^3$. The assumed WIMP-nucleon cross section is 10^{-45} cm^2 , while WIMP masses of $50 \text{ GeV}/c^2$ (left) and $500 \text{ GeV}/c^2$ (right) are considered. Heavier nuclear targets lead to a larger rate as $\sigma_{\text{SI}} \propto A^2$, but the spectrum drops faster because of the form factor.

targets, and excitation of atoms with the emission of *photons* or atomic ionization liberating *electrons*. A schematic of the different types of signals and corresponding detector concepts is shown in Fig. 1.8. A detector using multiple signals improves the energy resolution and the discrimination power between nuclear and electronic recoils. This is especially important for experiments based on WIMP scattering off nuclei, as it allows a strong reduction of the ER background due to the different signal production between ERs and NRs, as detailed for liquid xenon in Chapter 2. Most experiments are designed to detect two signals, as any attempt to detect all of them has been unsuccessful to date.

Despite the large experimental efforts, no WIMP signal has been detected yet and only upper limits on the cross section of the WIMP-nucleon interaction have been set so far. The experiments setting the strongest limits for low mass WIMPs typically use phonon signals, as they allow for $\mathcal{O}(10 \text{ eV})$ detection thresholds. Phonons are detected as μK -scale temperature increases over a target temperature of $\mathcal{O}(10 \text{ mK})$. The target typically consist of solid crystals, although superfluid helium targets have been recently proposed [84, 85]. These microscopic temperature variations can be detected using transition-edge sensors (TES). They consist of a resistor kept at the threshold of superconductivity in order to enhance the thermal resistivity increase [86]. These detectors are known as *bolometers* and they are typically coupled to charge or light detectors in order to optimize the ER/NR discrimination. The CDMS experiment reached a discrimination power of 10^{-6} , i.e., only

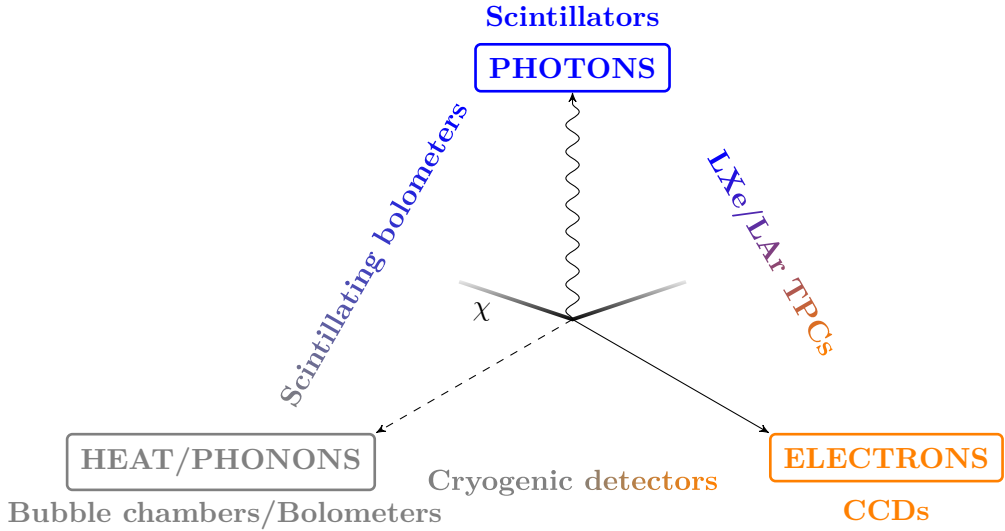


Figure 1.8 The energy deposition due to the scattering of a WIMP off a nucleus (or an electron) or background events can lead to the production of photons, electrons or heat (in the form of phonons in crystalline targets). Different detector technologies have been developed in the last decades to detect one or more of these signals.

one ER event out of one million is misidentified as NR [87, 88]. To date, the best limits on WIMP-nucleon scattering from an experiment deploying a bolometer come from the CRESST-III detector [89]. It uses a CaWO₄ crystal target operated at 15 mK and it is equipped with light sensors to detect the scintillation signal and TES for the phonon channel.

Since the phonon signal requires cryogenic temperatures, bolometers are restricted in size and this limits their exposure⁽¹⁾, hence their sensitivity. The detection of photons and electrons does not have the same cryogenic requirements, allowing for the development of experiments with $\mathcal{O}(1 \text{ t yr})$ exposure. The DAMA project is an example of direct search experiment based on scintillator. The current DAMA/LIBRA experiment is a highly radiopure NaI(Tl) target consisting of an array of 25 crystals for a total mass of about 243 kg [90]. Because of its inability to discriminate between ER and NR events, DAMA focuses on the detection of the *annual modulation* of the WIMP interaction rate. As the Earth revolves around the Sun, its revolution velocity is added to the Solar System's velocity effectively introducing a time dependence in the velocity distribution $f(\vec{v})$ of Eq. (1.2), modulating the flux of WIMPs crossing the detector. The maximum flux is expected in

⁽¹⁾The *exposure* of an experiment is defined as the product between its target mass and the data taking time.

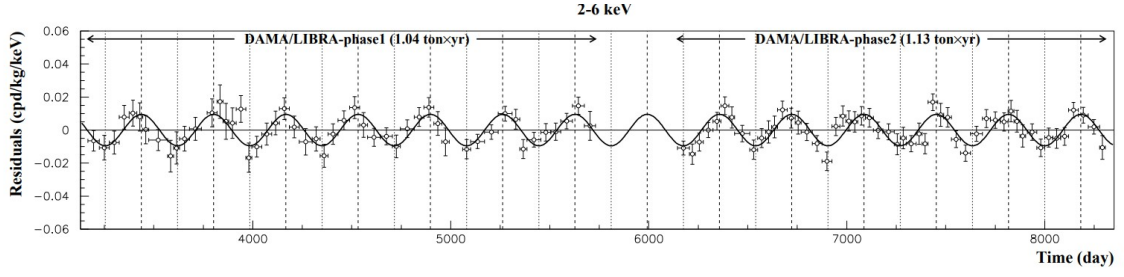


Figure 1.9 Residual event rate from the two phases of the DAMA/LIBRA experiment in the energy region 2–6 keV, after over 11 years of exposure. The superimposed curve is the expected annual modulation with amplitude coming from the fit. Plot from [91].

June, when the velocity of Earth and Solar System are parallel, and its minimum is in December. In the last 20 years the different stages of the DAMA project have observed a modulation of the rate, interpreted by the DAMA collaboration as the contribution of the “WIMP wind” over the background which is assumed to be constant. The combination of the DAMA results leads to evidence at 12.9σ C.L. (confidence level) [91] and the residual modulation amplitude during the two phases of DAMA/LIBRA are shown in Fig. 1.9. Although experiments like XENON100 [92], LUX [93] and XMASS [94] have excluded “vanilla” WIMP scattering cross section which could explain the DAMA results, “isospin-violating” WIMP models could explain the different observations [95]. However the COSINE-100 and ANAIS-112 detectors use the same NaI(Tl) technology and have recently reported results in strong tension with the DAMA observation [96, 97], but more data are needed to completely rule out the DAMA claim.

In the last years experiments detecting only the ionization signal have been proven to be competitive with cryogenic bolometers in constraining low mass WIMPs. This is possible thanks to the development of charge-coupled devices (CCDs) with low electronic noise and ultra radiopure materials [98]. CCDs are silicon detectors consisting of an array of coupled capacitors. Each capacitor is capable to store charge collected during an exposure time, after which they are read-out. These sensors have been largely used in digital imaging, with high-resistivity devices developed for astronomy especially suited for the WIMP search as they minimize the leakage currents. The DAMIC experiment at the SNOLAB underground laboratory uses a stack of 8 CCDs, each weighting 6 g and with a target sensitive to energy depositions as low as 1.1 eV. Results from an exposure of 11 kg d were published in 2020 [99].

Nowadays, the strongest limits on the WIMP-nucleon SI scattering cross section for

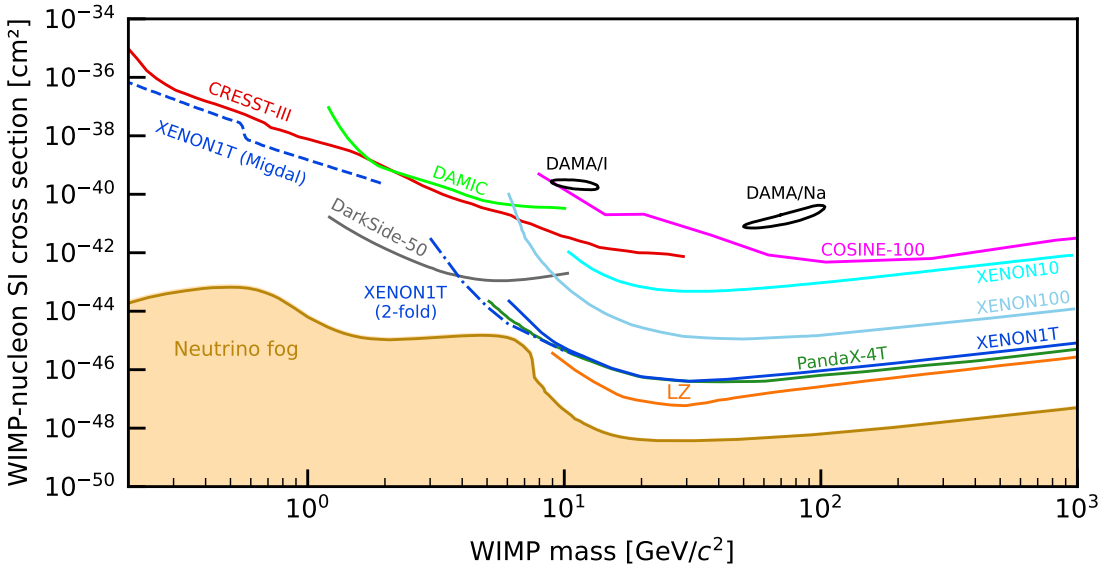


Figure 1.10 Current best exclusion limits at 90 % C.L. (confidence level) for SI WIMP-nucleon cross sections. The experiments are discussed in the text, with XENON10 and XENON100 briefly discussed in Chapter 2. The results from DAMA and COSINE-100 assume the standard isospin-conserving model, although their results are model independent. The DAMA contours are reported only for the phase 1 of DAMA/LIBRA and the results are interpreted in terms of scattering off iodine (I) and sodium (Na). From low to high masses, the reported results are: CRESST-III [89], XENON1T (Migdal) [100], DAMIC [99], DarkSide-50 [101], XENON1T (2-fold) [102], PandaX-4T [103], XENON1T [104], XENON100 [105], LZ [106], COSINE-100 [96], DAMA [107], XENON10 [108].

WIMP masses above $1 \text{ GeV}/c^2$ come from dual-phase time projection chambers (TPCs) using liquefied noble gases as a target, typically xenon or argon. An overview of the current WIMP-nucleon interaction “landscape” is shown in Fig. 1.10. Xenon-based TPCs like XENON1T [104], LZ [106] or PandaX-4T [109] set the strongest limit for the vast majority of WIMP masses above $1 \text{ GeV}/c^2$, with the argon-based DarkSide-50 experiment leading in the range $1.2\text{--}3.6 \text{ GeV}/c^2$ [101]. Thanks to the excellent ionization and scintillation properties of noble liquids, these detectors use both the light and charge signal to improve the energy resolution and the ER/NR discrimination power. Furthermore, the relatively simple technology allows for a “straightforward” scaling which led to multi-tonne xenon-based dual-phase TPCs within few decades after their initial development. Because of their relatively high energy threshold, these detectors perform better for large WIMP masses. Low masses can be probed by reducing the energy threshold for detection. This

is possible by reducing the requirement of PMT coincidence for the identification of a light signal, hence reducing the detection energy threshold: XENON1T set the best limit between $3.6 \text{ GeV}/c^2$ and $10 \text{ GeV}/c^2$ by reducing the coincidence requirement from 3- to 2-fold [102]. In addition, sub-GeV WIMPs were probed by xenon-based dual-phase TPCs by searching for the signal coming from the Migdal effect [110] using only the ionization signal, as the limit from XENON1T in Fig. 1.10 shows. The Migdal effect is the excitation or ionization coming from the delayed motion of the atomic electrons after a particle has elastically scattered off the nucleus. This effect is hypothetical and has never been observed for low energetic nuclear recoils, although there are ongoing experimental efforts to detect and study it [111]. Assuming the presence of this effect, XENON1T managed to set world-leading limits down to $85 \text{ MeV}/c^2$ [100]. A detailed discussion of the different experimental efforts in the direct search for dark matter is presented in [2] and [112]. The signal production in liquid xenon and the working principle of dual-phase TPCs are further discussed in Chapter 2, together with the details of the XENON project in its different stages.

Chapter 2

Liquid xenon for particle detection and the XENON dark matter project

The direct search for WIMP dark matter is currently led by dual-phase time projection chambers (TPCs) using liquefied noble gas as target. Thanks to the high scintillation and ionization yields, its strong self-shielding power and its radiopurity, TPCs using liquid xenon currently set the best exclusion limits for WIMP masses above $3.6 \text{ GeV}/c^2$ (see Fig. 1.10). The XENON project is one of the pioneers of this technology. The current phase of the XENON project is the XENONnT experiment, which deploys a 5.9 t active mass, almost three times larger than its predecessor XENON1T. XENONnT is expected to improve the sensitivity to spin-independent WIMP-nucleon scattering by an order of magnitude compared to XENON1T, up to $1.4 \times 10^{-48} \text{ cm}^2$ for $50 \text{ GeV}/c^2$ WIMPs [113]. This is possible thanks to its large target mass and low background rate, which was measured as $(16.1 \pm 1.3) \text{ events}/(\text{t yr keV})$ in the 1–30 keV range for electronic recoils, the lowest ever achieved in this type of detectors [114].

This chapter describes the signal production in the liquid xenon target and the working principle of the dual-phase TPC, with particular focus on the XENON project and the design of its later detector, XENONnT. The particle interaction and signal generation in liquid xenon is described in Sec. 2.1. Scintillation, ionization and electroluminescence processes are briefly described, as well as the propagation of free electrons in liquid xenon, with particular emphasis on the impact of the electric field. A more complete description of these processes can be found in [115, 116]. The working principle of the xenon-based dual-phase TPCs is explained in Sec. 2.2. In addition the main sources of backgrounds are presented, together with a brief description of the technologies deployed to measure the radiopurity of used materials. A brief overview of the past XENON phases is presented in

Sec. 2.3, together with the latest results from XENON1T. The XENONnT experiment and its subsystems are described in Sec. 2.4, with particular focus on the main improvements with respect to XENON1T. The first results from XENONnT are also presented.

2.1 | Signal formation in liquid xenon

Energy deposition

An interacting particle deposits energy in liquid xenon either via scattering off electrons (electron recoils, ER) or nuclei (nuclear recoils, NR): the first case is typical for beta and gamma radiation, the second for neutrons and WIMPs. Both for the electronic and nuclear recoil, the energy deposition per unit length is shared between excitational and elastic contributions:

$$\frac{dE}{dx} = \left(\frac{dE}{dx} \right)_{\text{exc}} + \left(\frac{dE}{dx} \right)_{\text{el}}. \quad (2.1)$$

The excitational channel includes atomic ionization and excitation, while the elastic contribution accounts for the energy released via elastic collisions with atomic nuclei, thus heat. As an ionizing particle of energy E_0 interacts with the liquid xenon, the excitational energy deposit is redistributed following the Platzman energy balance [117]:

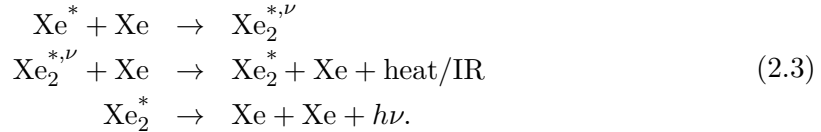
$$E_0 L = N_i \bar{E}_i + N_{\text{ex}} \bar{E}_{\text{ex}} + N_i \bar{\varepsilon}, \quad (2.2)$$

where L is the fraction of energy deposited in the excitational channel as in Eq. (2.1), N_i (N_{ex}) the number of ionized (excited) atoms at an average energy expenditure \bar{E}_i (\bar{E}_{ex}) and $\bar{\varepsilon}$ the average sub-excitational energy carried by the ionization electrons. As electrons have a negligible mass compared to the target nuclei, the elastic contribution is almost null and $L_{\text{ER}} \simeq 1$. This is different for nuclear recoils, for which nuclei have a velocity comparable to the one of its atomic electrons, resulting in a recoiling ion with an effective charge typically lower than unity [118]. These recoiling Xe ions have $L = 0.15 - 0.3$ for energies in the range 1–100 keV, as described by the Lindhard-Scharff-Schiøtt theory [119, 120]. The ratio N_{ex}/N_i reaches equilibrium about 10^{-12} s after the interaction, when all the particles set to motion by the energy deposition reach sub-excitational energies, before secondary processes start. This ratio is $N_{\text{ex}}/N_i = 0.06 - 0.20$ for electronic recoils and $0.9 - 1.1$ for nuclear recoils, independently of the energy deposition and electric field conditions [121, 122].

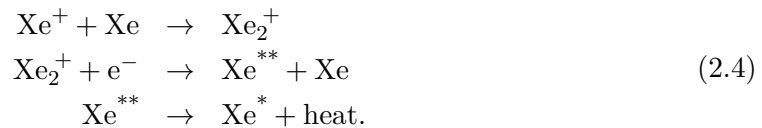
Scintillation and ionization

A schematic overview of the signal production for ERs and NRs is shown in Fig. 2.1. The signal detected by a dual-phase TPC consists of scintillation photons and liberated electrons, whereas the energy from elastic collisions $\left(\frac{dE}{dx}\right)_{\text{el}}$ or sub-excitational electrons $N_i \bar{\varepsilon}$ is dissipated into undetected heat.

While the observed electrons are the direct product of primary ionizations, the production of scintillation photons requires the formation of excited diatomic molecules, called *excimers*. The radiation from direct atomic de-excitation is resonantly absorbed by neighboring atoms and can be observed only at a gas pressure in the order of 100 mbar [123, 124]. For an excited xenon atom Xe^* , the scintillation photon $h\nu$ is produced as follows [116]:



The formation of excimers passes through excited vibrational states $\text{Xe}_2^{*,\nu}$ which need to decay into an electronically excited state with no vibrational excitation ($\nu = 0$). This energy is typically released through non-radiative channels (heat), although infrared radiation (IR) emission is possible [125]. The formed excimer Xe_2^* can be in a singlet ${}^1\Sigma_u^+$ or triplet ${}^3\Sigma_u^+$ state. The de-excitation from both states produces a vacuum-ultraviolet (VUV) photon with wavelength $\lambda = 175 \text{ nm}$ [126]. The singlet decay is fast with a time constant $\tau_s = (4.3 \pm 0.6) \text{ ns}$, while the triplet decay is slower with $\tau_t = (21 \pm 2) \text{ ns}$ [127]. The ratio between singlet and triplet components in the scintillation signal depends on the interaction type⁽¹⁾, with a higher singlet component for NR interactions [128]. Together with direct excitation, free excitons can also be formed through electron-ion *recombination*:



As discussed earlier, the ratio N_{ex}/N_i is rather small for ERs, while it is around unity for NRs. This means that in absence of an electric field suppressing electron-ion recombination by pulling them apart, the ER scintillation signal is dominated by the recombination

⁽¹⁾The singlet-to-triplet ratio is typically used in argon-based experiments to discriminate ER and NR. This is possible thanks to the argon decay times of $\tau_s = (6.8 \pm 1.0) \text{ ns}$ and $\tau_t = (1550 \pm 100) \text{ ns}$ [127].

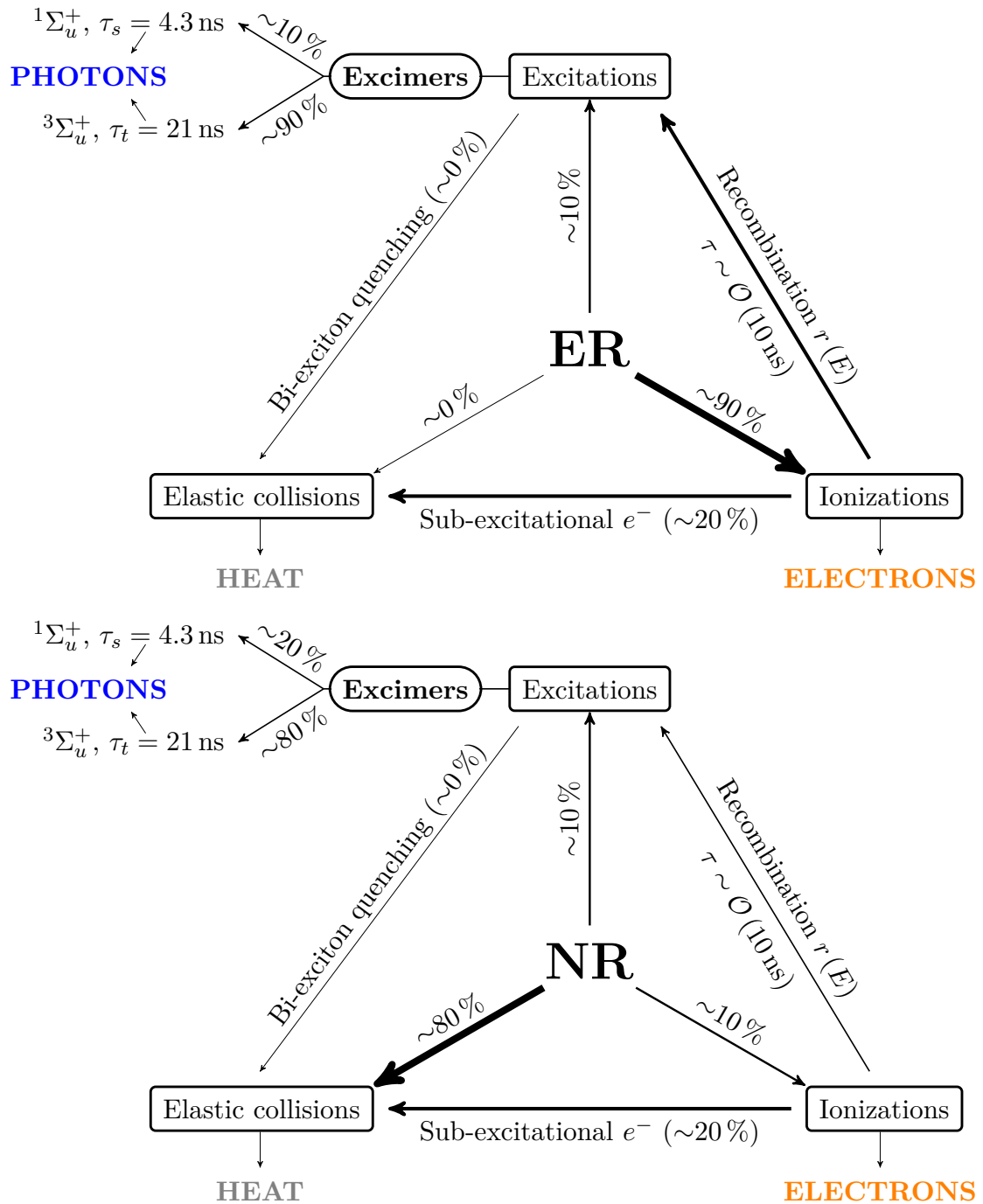


Figure 2.1 Schematic of the primary distribution of the energy deposited in liquid xenon by an electronic (top) and nuclear (bottom) recoil among the three possible channels: atomic excitation, ionization, and elastic collision (heat). The first two channels lead to the production of signals in the form of photons and electrons, respectively. Secondary processes can change the final distribution of the energy among the signals, as detailed in the text.

channel leading to a time constant of 45 ns [127]. This behaviour is not observed for alpha particles and NRs.

A liberated electron can recombine with an ion only after its thermalization. Assuming an average energy $\bar{\varepsilon} \simeq 5 \text{ eV}$ for sub-excitational electrons, the thermalization happens after about 6.5 ns [129]. During this time the electrons travel on average a distance of $4.5 \mu\text{m}$ [130], two orders of magnitude larger than the Onsager radius for liquid xenon, which is defined as the distance between positive ion and free electron at which thermal and Coulomb energy are equal. This excludes the hypothesis of *geminate* recombination in favor of a volume recombination theory [131]. Furthermore, the large thermalization length makes it possible for electrons to escape recombination also in case of no electric field, with disagreeing measurements of this escaping probability between 20 % and 70 %, both for ER and NR interactions [132].

Many models have been developed to describe the recombination process as a function of the stopping power dE/dx and the applied electric field. This is important to parameterize and simulate the detector response to particle interactions in the form of *charge yield* Q_y and *light yield* L_y , defined as the number of produced electrons or photons normalized to the energy of the incident particle. The Noble Element Simulation Technique (NEST) combines the Thomas-Imel box model [131] together with a series of heuristic models, matching free parameters to the available measurements [133]. This tool is widely used in the liquefied noble gas community as it is tuned to match the experimental data. NEST results for the charge and light yield as a function of the electric field for a 10 keV ER interaction and a 50 keV NR are shown in Fig. 2.2. As the electric field increases, the electrons have a larger escape probability, leading to an increase of the charge yield. This dependence is stronger for the ERs, for which recombination is the main contribution to the scintillation process.

Although the recombination process can convert primary ionization into excimers and eventually photons, the number of quanta observable in a dual-phase TPC is conserved. A reduction in the number of liberated electrons N_{el} is compensated by an equal increase in the number of scintillation photons N_{ph} , hence $N_{\text{ex}} + N_{\text{i}} = N_{\text{ph}} + N_{\text{el}}$. It is thus possible to write a balance equation similar to Eq. (2.1):

$$E_0 L = (N_{\text{ph}} + N_{\text{el}}) W, \quad (2.5)$$

where $N_{\text{ph}} = N_{\text{ex}} + r N_{\text{i}}$, with r being the field-dependent recombination probability, and W is the average energy needed to produce a quantum (photon or electron). W is measured

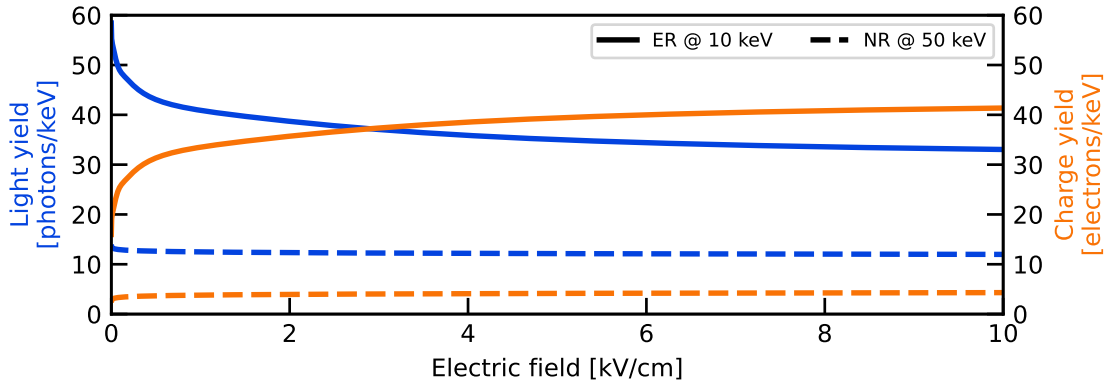
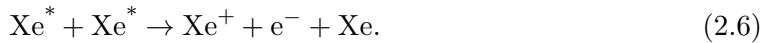


Figure 2.2 Light yield (blue) and charge yield (orange) in liquid xenon as a function of the applied electric field for an ER interaction depositing an energy of 10 keV (solid curve) and a NR interaction of 50 keV (dashed). Considering the $\sim 80\%$ fraction of energy lost in the heat channel for a NR, the energy deposited as observed signal of the NR interaction is about the same as of the ER. Values are obtained with NEST v2.3.6 [134].

to be $W = (13.7 \pm 0.2)$ eV for liquid xenon [135], however more recent results show a value around 11.5 eV [136, 137]. The only process able to affect the conservation of the number of observable quanta is the *bi-exciton quenching*, where two excited atoms interact producing an electron-ion pair and an atom in the ground state [138]:



This reduces the final product from two photons to a single electron (or photon in case of recombination). This process is particularly important for highly ionizing particles like alpha radiation or fission fragments, while for ER and NR interactions its contribution is negligible and Eq. (2.5) holds true.

Electron transport

Unlike in gas, the propagation of electrons in liquid xenon cannot be described as a sequence of independent and isolated elastic scatterings. This is due to the small distance between the atoms of about 0.3 nm, similar to the equilibrium distance for a bi-atomic xenon molecule, and much smaller than the thermal electron wavelength. Hence, in the liquid phase the electrons do not interact with single atoms, but they feel an “effective potential” from the combined effect of the atoms of the medium. Models based on this assumption

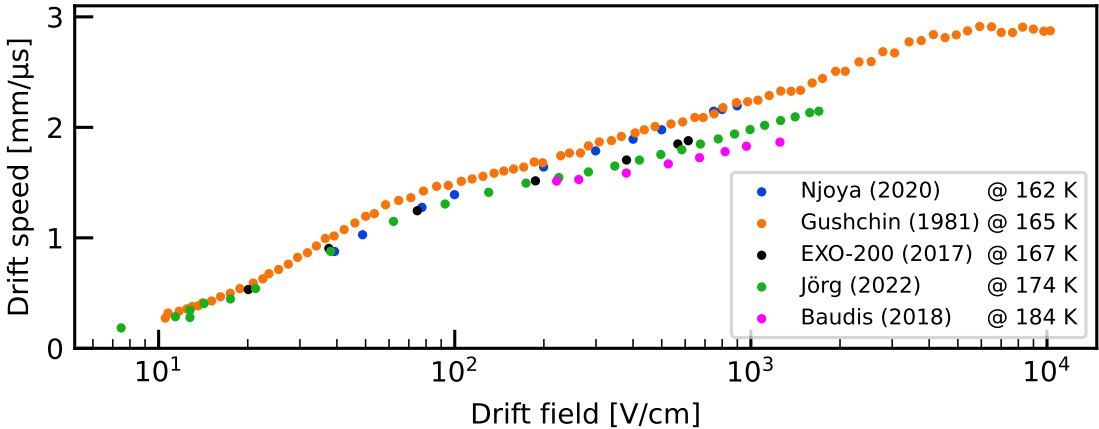


Figure 2.3 Electron drift speed in liquid xenon as a function of the applied electric field. A lower temperature of the liquid xenon results in a larger electron drift speed, possibly due to the higher density. Data points for different temperatures from Njoya [139], Gushchin [140], EXO-200 [141], Jörg [142] and Baudis [143].

can successfully explain the evolution of the drift speed v_d at low values of the applied field, as the kinetic energy of the electrons is not affected by the external field, resulting in a constant electron mobility μ_{el} , with $v_d = \mu_{\text{el}}E$. As the average kinetic energy of the electrons increases with the drift field, the mobility is not constant anymore and decreases with the applied field. This trend has been confirmed by numerous measurements of the drift speed carried out in the last decades. A selection of some experimental results is shown in Fig. 2.3. They show that the mobility is constant for low fields ($v_d \propto E$), but it decreases for fields larger than about 100 V/cm. The drift speed saturates for fields above several kV/cm. The theoretical models proposed over the years struggled to reproduce this drift velocity plateau [144, 145], predicting a decrease at large fields which can be corrected by including the contribution from inelastic cross section with Xe_2 diatomic molecules [146]. Good results have been achieved also considering *ab initio* elastic cross section calculations [147].

The compact atomic structure of liquid xenon is also responsible for a lower electron diffusion compared to its gaseous phase. This is of particular experimental importance for the precise reconstruction of the interaction positions in dual-phase TPCs, as explained in Sec. 2.2. The same theoretical framework used to describe the drift speed can be applied to estimate the diffusion coefficient, finding a good agreement with measurements for fields above 100 V/cm. For lower fields several theories predict a decrease of both the

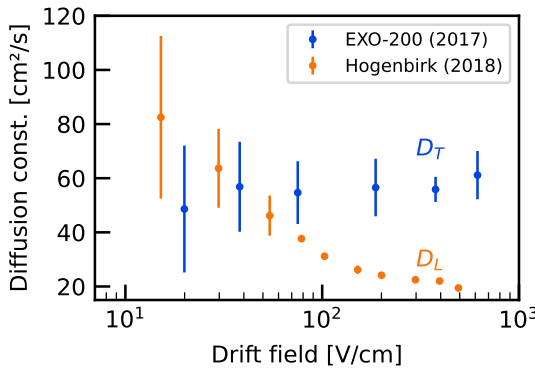


Figure 2.4 Transverse (D_T , blue) and longitudinal (D_L , orange) diffusion coefficient for electrons in liquid xenon. Data from Hogenbirk [132] and EXO-200 [141], respectively. These values are used in Sec. 4.4 to estimate the electron transport property maps.

longitudinal and transverse diffusion coefficients, in disagreement with the observations shown in Fig. 2.4.

Impurities in liquid xenon can capture drifting electrons, reducing the number of detected electrons and affecting the energy reconstructed with Eq. (2.5). The probability of an electron to attach to a molecule (or atom) depends on the energy difference between the initial neutral state and the final negative ion, known as *electron affinity*. A positive electron affinity means that the ground state of the negatively ionized molecule is more stable than the neutral state, making the process energetically favorable. In this case the molecule M is defined *electronegative* and represents a dangerous contamination for detectors like dual-phase TPCs. In liquid xenon, the attachment is a three-body process ($e^- + M + Xe \rightarrow M^- + Xe$), dominant over other possible channels important in the gaseous phase [148]. Because of the compact atomic structure, this process has more the characteristics of a N-body interaction, where the excess energy can be absorbed by more than a single Xe atom. The rate of electron loss $\frac{dN_{el}}{dt}$ due to attachment can be parameterized as

$$\frac{dN_{el}}{dt} = -k_s r_s n N_{el}, \quad (2.7)$$

where k_s is the rate constant depending on electric field and liquid density, and r_s is the concentration of impurities relative to the medium number density n , typically expressed in part per billion (ppb). $N_{el}(t)$ indicates the number of surviving electrons at a given time along the drift path, hence it coincides with N_{el} from Eq. (2.5) for $t = 0$, where $N_{el}(0) = N_{el}^0$. The solution of Eq. (2.7) returns a simple exponential decay function

$$N_{el}(t) = N_{el}^0 \cdot e^{-t/\tau_{e^-}}, \quad (2.8)$$

where the time constant $\tau_{e^-} = (k_s r_s n)^{-1}$ is usually called *electron lifetime* and it is used to

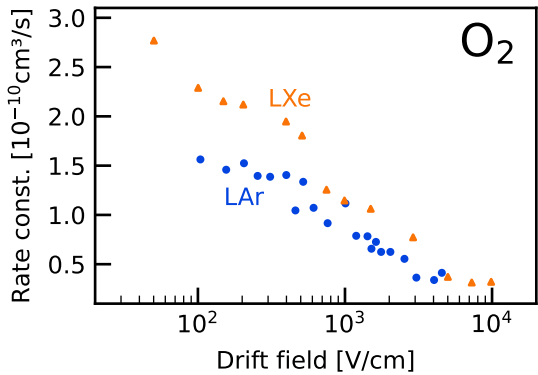


Figure 2.5 Rate constant for molecular oxygen O_2 in liquid argon (LAr, blue) and liquid xenon (LXe, orange). This quantity defines the electron attachment frequency as a function of the applied electric field. Data from [150].

characterize the detector's purity. Molecular oxygen O_2 is the most common electronegative impurity in liquefied noble gases, with an electron affinity of 0.45 eV [149] and an attachment rate constant k_s shown in Fig. 2.5 for liquid xenon and argon. The larger attachment rate constant for liquid xenon explains why its purification is more demanding than the purification of argon.

Scintillation in the gas phase: electroluminescence

A free electron in liquid xenon feels a potential barrier due to the polarization of the medium when it is sufficiently close to the interface with the gaseous phase. In addition, the electron has a potential energy from its interaction with the condensed phase: the difference with the energy it would have in vacuum is its binding energy V_0 . It was shown that V_0 is larger for heavier nuclei, meaning that more energy is required to extract electrons from liquid xenon into the gas phase than from liquid argon. Assuming the interface between liquid and gaseous xenon is at $z = 0$ and liquid xenon at $z < 0$, the potential that the electron feels can be written as a piece-wise function in the following way:

$$\phi(z) = \begin{cases} -A_{\text{LXe}}/z - eE_{\text{LXe}}z + V_0, & \text{for } z < 0 \\ -A_{\text{GXe}}/z - eE_{\text{GXe}}z, & \text{for } z > 0, \end{cases} \quad (2.9)$$

where the contribution $\propto 1/z$ comes from the polarization of the medium, estimated via the *image charge* method [151], and the contribution $\propto z$ is the effect of an external electric field. The shape of this potential is illustrated in Fig. 2.6 for xenon. The factors derived

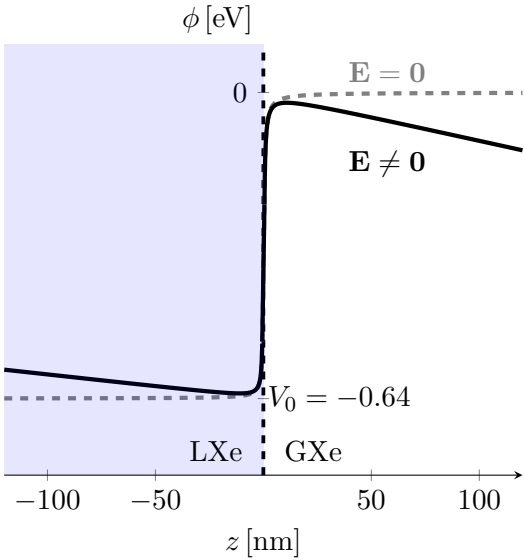


Figure 2.6 Potential barrier (solid line) at the liquid-gas interface in xenon with an electric field in liquid (extraction field) of 5 kV/cm perpendicular to the interface ($z = 0$). The dashed gray line shows the potential in absence of an external field.

with the image charge method are [116]

$$A_i = \frac{e^2}{16\pi\varepsilon_0\varepsilon_i} \delta_\varepsilon \quad \text{with} \quad \delta_\varepsilon = \frac{\varepsilon_{\text{LXe}} - \varepsilon_{\text{GXe}}}{\varepsilon_{\text{LXe}} + \varepsilon_{\text{GXe}}}, \quad (2.10)$$

where e is the elementary charge, ε_0 is the vacuum permittivity and ε_i is the dielectric constant of the considered medium i . The applied external electric field opposes the binding potential, such that the effective potential barrier ϕ_b is

$$\phi_b = |V_0| - 2 \left[\sqrt{eA_{\text{LXe}}E_{\text{LXe}}} + \sqrt{eA_{\text{GXe}}E_{\text{GXe}}} \right]. \quad (2.11)$$

For the configuration of Fig. 2.6, with an electric field $E_{\text{LXe}} = 5 \text{ kV/cm}$ in liquid xenon, the potential barrier is about 0.61 eV, with a decrease of only 0.03 eV. Comparing the potential barrier with the average thermal energy of the electrons in liquid xenon $k_B T \sim 0.014 \text{ eV}$, we can exclude a thermoelectric emission mechanism, contrary to what is observed in liquid argon [152]. On the other hand, the electrons gain energy from the field much faster in liquid xenon than argon, since their mean free path is six times larger [147]. The large energy gain explains the emission mechanism in terms of “hot” electrons, i.e., with a kinetic energy larger than the potential barrier ϕ_b . This is confirmed by the measurement of the electron extraction efficiency as a function of the electric field in liquid xenon, commonly known as *extraction field*, with a threshold lower than 2 kV/cm. This is shown in Fig. 2.7. Electrons with a kinetic energy below ϕ_b cannot be extracted and they are trapped in the potential minimum about 10 nm below the interface, where they thermalize and eventually

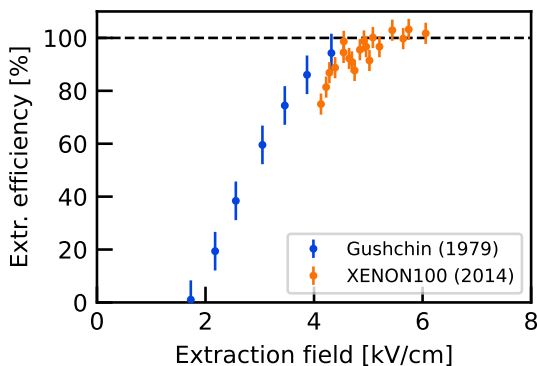


Figure 2.7 Efficiency of electron extraction from liquid to gas xenon as a function of the electric field in liquid xenon, known as extraction field. Data from Gushchin [153] and XENON100 [154].

attach to electronegative impurities.

Once the electrons are extracted into the gaseous phase, they feel the effect of a *multiplication field* approximately two times stronger than the extraction field. The energy that the electrons gain from the field leads to the production of a secondary light signal proportional to the number of extracted electrons via *electroluminescence*. Its microphysics mechanism is the same as the scintillation in liquid xenon, with the production of excimers in singlet and triplet states and the corresponding de-excitation with time constants $\tau_s = (5.88 \pm 5.50 \text{ ns})$ and $\tau_t = (100 \pm 8 \text{ ns})$ [155]. The different decay times compared to the liquid phase are due to the different number density, reducing the three-body collision probability. This electroluminescence mechanism leads to the emission of VUV photons with the same wavelength as those from primary scintillation ($\lambda = 175 \text{ nm}$). Together with the scintillation mechanism, photons can be produced via *neutral bremsstrahlung* with the interaction of the electrons with the dipole field of the neutral atoms [156]. This mechanism produces photons within a continuous spectrum and for fields far below the ordinary electroluminescence threshold. Once the field is above this threshold, the neutral bremsstrahlung contribution is two orders of magnitude smaller than the scintillation mechanism and it is typically neglected. Also atomic de-excitation between higher atomic levels can contribute to the electroluminescence emission [157], although these photons have a near-infrared wavelength ($\lambda > 800 \text{ nm}$ [158]). This mechanism becomes important at fields of around 10 kV/cm in gaseous xenon at a pressure of 2 bar, when the electrons gain enough energy to excite the atoms to highly excited states enabling reactions such as $e^- + \text{Xe} \rightarrow e^- + \text{Xe}^* (5p^56p^1) \rightarrow e^- + \text{Xe}^* (5p^56s^1) + h\nu$. As in the case of neutral bremsstrahlung, this contribution can be considered negligible at the practical level as its photon yield is about an order of magnitude lower than the scintillation electroluminescence mechanism and it is important only at higher fields.

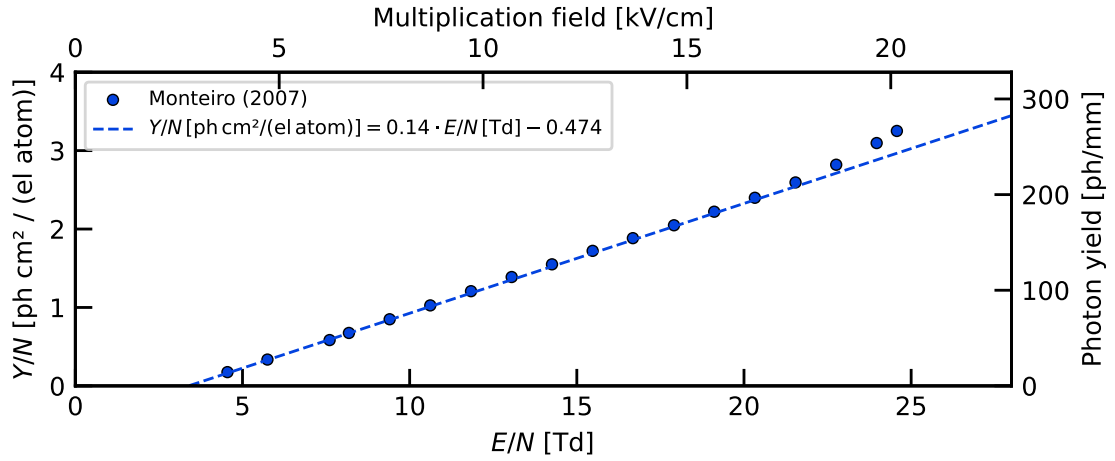


Figure 2.8 Electroluminescence light yield for a single extracted electron as a function of the reduced electric field in gas. On the left axis the reduced light yield is reported, while the absolute yield per unit length is given on the right axis for a pressure of 2 bar and a temperature of 177 K, similar to the XENONnT conditions. Data from [159].

The photon yield for the electroluminescence process in gaseous xenon has been measured by several experiments, showing an overall good agreement [159]. For reduced electric fields⁽²⁾ below 20 Td ($1 \text{ Td} = 10^{-17} \text{ V cm}^2/\text{atom}$) the photon yield shows a linear behaviour with the field, as Fig. 2.8 shows. The multiplication field in gaseous xenon at a temperature of 177 K and a pressure of 2 bar, similar to the XENONnT conditions, is shown along the reduced field, as well as the photon yield in units of photons per millimeter. The electroluminescence yield for reduced fields above 20 Td starts to diverge from the linear behaviour, which can be explained by the contribution of additional electrons produced by ionization. A proper implementation of the electroluminescence signal including the effect of secondary electrons is proposed in [160], where a good agreement between simulations and data is reached especially for heavy noble gases like xenon or krypton. This model is used in Chapter 6 to simulate the secondary proportional signal S2 in XENONnT, yielding an excellent agreement with data.

⁽²⁾The *reduced field* is defined as the electric field intensity divided by the number density of the medium.

2.2 | Dual-phase TPC detection principle

The technology of a dual-phase time projection chamber (TPC) relies on the two signals following the interaction of a particle with the liquefied noble gas target. Xenon is particularly suited for the dark matter search as it has a large mass number A , increasing the spin-independent WIMP-nucleus cross section ($\sigma_{\text{SI}} \propto A^2$) and a large density in its liquid phase, hence stopping power and self-shielding properties. Unlike argon, xenon has no long-lived isotopes that can effectively harm the WIMP search, but it features two isotopes (^{129}Xe and ^{131}Xe) with non-zero spins, rendering it sensitive to spin-dependent WIMP-nucleon interactions.

The basic principle of a dual-phase TPC is sketched in Fig. 2.9. A particle interacting with the xenon produces scintillation VUV photons and ionization electrons, as described in Sec. 2.1. The photons are emitted within $\mathcal{O}(10\text{ ns})$ and they are promptly detected by the top and bottom photomultiplier tube (PMT) arrays, forming the S1 signal. The detector is designed to optimize the light collection efficiency (LCE). This is done by maximizing the transparency of the electrodes placed between the target volume and the PMT arrays to establish the required electric field, and by placing reflective panels around the target volume. The used reflective material is polytetrafluoroethylene (PTFE), with a reflectivity $>98\%$ for a wavelength of 175 nm when diamond-polished [161].

The electrons liberated by the ionization process drift along the electric *drift field* established by the potential difference between the cathode electrode placed at the bottom of the target volume and the gate at the top. As described in Sec. 2.1, the drift field has an important impact on the recombination process, and ultimately on the relative intensity of the charge and light signals as shown in Fig. 2.2. The electrons drift towards the top of the TPC, where they are focused in the high field region between the gate and the anode electrodes, known as “S2 region”. The intense field of $\mathcal{O}(10\text{ kV/cm})$ extracts the electrons from the liquid phase into the gaseous xenon, where they produce a secondary electroluminescence signal proportional to the number of extracted electrons, known as S2 signal.

The localized PMT pattern of the S2 signal allows for the reconstruction of its (x, y) position. This position is assumed to be the same of the interaction, neglecting distortions introduced by the drift field which can be later corrected, as discussed in Sec. 5.5.1. In addition, the time difference between the S1 and S2 signals, the *drift time*, is proportional to the interaction depth z . This three-dimensional position reconstruction allows for the

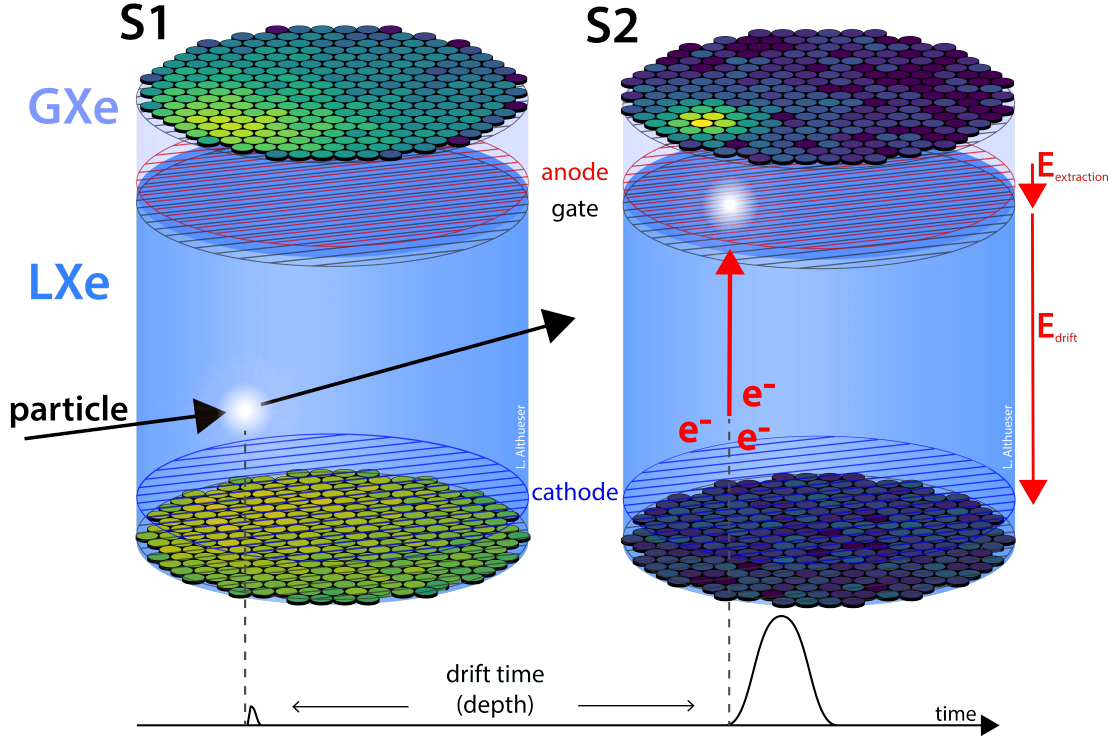


Figure 2.9 Working principle of a xenon-based dual-phase TPC. As a particle interacts in liquid xenon (LXe), it produces a prompt scintillation signal ($S1$) detected by top and bottom PMT arrays, and ionization electrons. The electrons follow the drift field E_{drift} towards the liquid-gas interface, where a stronger extraction field $E_{extraction}$ pulls them into the gaseous xenon (GXe). Here the electrons produce a secondary proportional scintillation signal ($S2$). From the top array detection pattern of the $S2$ signal it is possible to reconstruct the (x, y) position, while the z information is given by the time difference between $S1$ and $S2$.

fiducialization of the target volume. This is the selection of the events happening inside of an inner fiducial volume, where the background coming from materials-induced radiogenic activity is strongly suppressed thanks to the self-shielding power of liquid xenon. The position reconstruction is also important for the correction of detector effects affecting the size of the signals detected by the PMTs, corresponding to the area of the digitized waveform peaks, measured in photoelectrons (PE). An example of position-dependent effect is the electron lifetime, which introduces an exponential dependence of the $S2$ signal on the interaction depth, as shown by Eq. (2.8). Other corrections such as a three-dimensional LCE map for $S1$ s and an (x, y) $S2$ map ensure a uniform response throughout the entire detector. The $S2$ map accounts for changes in the length of the gas gap affecting the size of

2.2 Dual-phase TPC detection principle

the S2 signal and due to the deformation of the anode electrode's wires under electrostatic force, as discussed in Chapter 6.

The corrected signals are typically indicated as cS1 and cS2. As these quantities are proportional to the number of emitted photons and electrons, is it possible to rewrite the balance equation Eq. (2.5) as:

$$E = W \left(\frac{cS1}{g_1} + \frac{cS2}{g_2} \right). \quad (2.12)$$

The detector gains g_1 and g_2 represent the number of observed PEs per produced photon or electron, respectively. While g_1 includes only the LCE and the efficiency of the PMTs, the factor g_2 also encodes the extraction efficiency and the electroluminescence gain, i.e., the number of VUV photons per extracted electron into the gas phase. The resolution of the energy reconstructed using Eq. (2.12) decreases with the energy, going from $\sim 5\%$ at $\sim 10\text{ keV}$ down to $<1\%$ above 2 MeV [162]. The high energy resolution is due to the anti-correlation of the charge and light yield compensating the individual binomial fluctuations in the number of produced quanta.

Together with energy and position reconstruction, the two signals following an interaction in a dual-phase TPC allow for the discrimination of the interaction type. This is particularly important for the direct search of dark matter, as WIMPs are expected to scatter off nuclei producing NRs, while most of the background sources induce ERs. The discrimination is based on the fact that for the same size of the light signal S1, NR interactions have smaller S2 than ERs. As discussed in Sec. 2.1 and summarized in Fig. 2.1, ERs and NRs feature different distributions of the deposited energy into heat, excitation and ionization channels. An example of the (cS1, cS2) distributions of ER and NR interactions with uniformly distributed energies is shown in Fig. 2.10. The distributions of the two populations are typically referred to as ER and NR *bands*. The shape of the band for a given detector configuration can be experimentally determined using calibration sources such as ^{220}Rn [163] for the ER band and $^{241}\text{AmBe}$ or a neutron generator for the NR band [164, 165]. Once these bands are characterized, the ER background can be reduced by selecting only the events falling below the median of the NR band, shown as a dashed black line in Fig. 2.10. This decreases the acceptance for the WIMP NR signals to 50 %, but it typically reduces the background coming from ER interactions by more than 99 % [166]. The residual background, known as *ER leakage*, depends on the energy of the interaction and the electric drift field, as studied in [167] and shown in Fig. 2.10, where the separation of the two bands increases with cS1 and applied field. The latter dependence

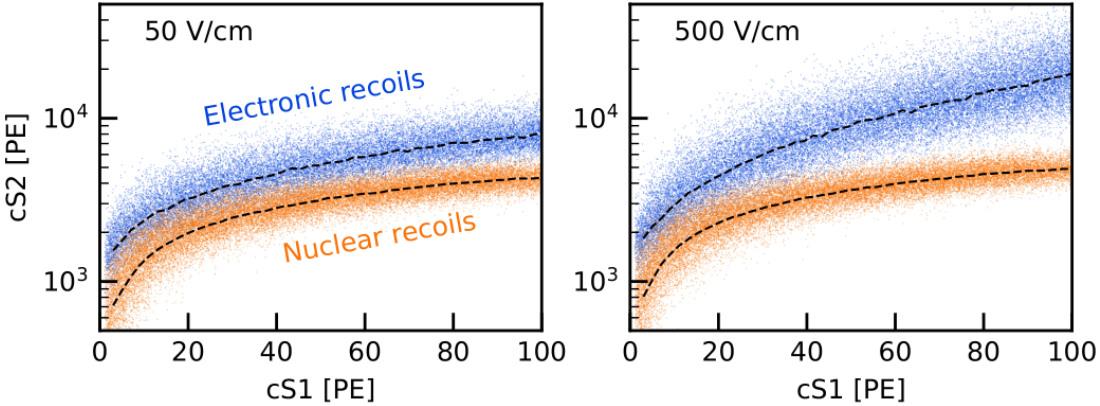


Figure 2.10 Simulation of the corrected S_1 and S_2 distribution for ER (blue) and NR (orange) interactions with a homogeneously distributed initial energy for two different drift fields (50 V/cm left, 500 V/cm right). The dashed lines indicate the median of the bands. An ER event is leaking into the NR band when it falls below the median of the NR band. Values obtained with NEST v2.3.6 [134].

is particularly important when considering the actual implementation of a detector, as it is practically impossible to perfectly correct the signals for the field dependence or to design a completely uniform drift field, as will be extensively discussed in Chapter 4. Any inhomogeneity of the field translates into a broadening of the bands, in particular the ER band, as nuclear recoils are less affected by changes in the electric field, as shown in Fig. 2.2.

The ER/NR discrimination cannot reduce the neutron-induced background, as neutrons interact with the nuclei of the active target producing NR signals. Although the type of the interaction of the neutrons is identical to the WIMPs', the former are more likely to scatter multiple times within the xenon active target before escaping it. The multiple scattering are tagged by resolving in time two or more S_2 peaks, possible only for interactions with different z positions. This is due to the $\mathcal{O}(10\text{ ns})$ time difference between subsequent interactions for a neutron which makes impossible to resolve multiple S_1 signals. By selecting only the single scatter it is possible to greatly reduce the neutron background, as it was the case for the XENON1T detector with a neutron background suppression of a factor ~ 5 [104].

2.2.1 | Background sources and mitigation

The reduction of the background is one of the greatest challenges for rare event search experiments. Excluding background events coming from the accidental pairing of uncorrelated S1 and S2 signals, the sources of background can be divided into three categories: cosmogenic, external and intrinsic. The following section represents a description of these background, with particular focus on the reduction techniques deployed by the XENONnT experiment. The gamma screening facility GeMSE is presented at the end of the section, as it was an important instrument in the selection of the materials for XENONnT and the XENON group at the University of Freiburg is responsible for its operations and maintenance.

The *cosmogenic* background originates from cosmic rays and mainly consists of muon-induced neutrons, and neutrinos inducing both ERs and NRs. Muons interact with matter and can produce neutrons, particularly dangerous as they scatter off nuclei mimicking the NR signal of WIMPs. Similarly, neutrinos can undergo coherent elastic neutrino-nucleus scattering (CEvNS) and induce NR signals, but they can also interact with the electrons of the target producing ERs. While neutrinos represent an irreducible background and CEvNS is the ultimate limiting background for dark matter detectors, the muon background can be reduced. This is possible by operating the detector underground, as the rock overburden can reduce the muon flux by several orders of magnitude. An additional reduction technique deployed by several experiments is the use of an active muon veto system [168, 169]. This typically consists of an instrumented water shield surrounding the TPC and detecting the Čerenkov light produced by a passing muon, used as a veto for the events detected in the active volume of the TPC.

The *external* background consists of events caused by the natural radioactivity of the materials of the detector and the surrounding environment. This radiation can be efficiently blocked by surrounding the active volume with a shield. An example for shielding is the water of a muon veto system, reducing the activity coming from the experimental hall by orders of magnitude. The liquid xenon itself provides self-shielding power thanks to its high density and large atomic number Z . The definition of an inner fiducial volume reduces the events coming from the materials of detector and the cryostat containing it. In addition, the selection of the materials used to build the detector and the cryostat is crucial to reduce their contribution to the total background. This is possible by conducting a *material radioassay* campaign in order to select materials with the lowest activities. For the XENONnT material selection campaign two independent screening techniques were

used: the inductively coupled plasma mass spectrometry (ICP-MS) and the gamma-ray spectroscopy using high purity germanium detectors (HPGe) [170], both described below. Other techniques like neutron activation analysis have been used by other experiments like LZ [171]. Radon emanation is another important selection criterion, as it affects the intrinsic background. The full material radioassay carried out for XENONnT is discussed in [172].

Detector materials can also contribute to the *intrinsic* background, consisting of radioactive sources distributed in the active liquid xenon target itself. In particular ^{222}Rn isotopes can be emitted from the materials' surface and homogeneously distribute in the liquid xenon due to their long half-life of 3.8 d. The radon daughter ^{214}Pb decays via β^- emission and represents one of the main sources of ER background at low energies for xenon-based dual-phase TPCs [173]. Unlike the other daughters of ^{222}Rn , the decay of ^{214}Pb is not followed by gamma or alpha radiation, rendering its identification and removal impossible in the analysis phase. This contribution can be reduced by performing radon emanation measurements as an additional material selection technique, as well as forcing the emission of adsorbed radium, decaying into radon, before the detector assembly by placing the components in vacuum. Because of the different atomic mass compared to xenon, the radon contamination can be removed via cryogenic distillation⁽³⁾ [175], with further details given in Sec. 2.4.

Cryogenic distillation is a powerful tool to also reduce another source of intrinsic background: ^{85}Kr . This krypton isotope has a half-life of 10.76 yr and decays via β^- emission with a Q-value of 687 keV. Natural krypton is present in commercial xenon gas with a fraction of $10^{-9} - 10^{-6}$ mol/mol, but the distillation of the xenon allows for the reduction of this concentration to 10^{-13} mol/mol [176]. Lastly, xenon itself has radioactive isotopes with very long half-lives ($> 10^{21}$ yr): the double beta decay ($2\nu\beta\beta$) of ^{136}Xe and the double electron capture ($2\nu\text{ECEC}$) of ^{124}Xe . The latter was observed first by the XENON1T experiment in 2019 [177]. The background contribution of these isotopes can be reduced only by isotopic depletion of the xenon. However, these isotopes are also fundamental to study the nature of neutrinos via the search for processes like the yet undetected neutrinoless double beta decay ($0\nu\beta\beta$) or neutrinoless double electron capture ($0\nu\text{ECEC}$) [178].

⁽³⁾The boiling temperature at atmospheric pressure is 165.1 K for xenon and 211.5 K for radon [174].

2.2 Dual-phase TPC detection principle

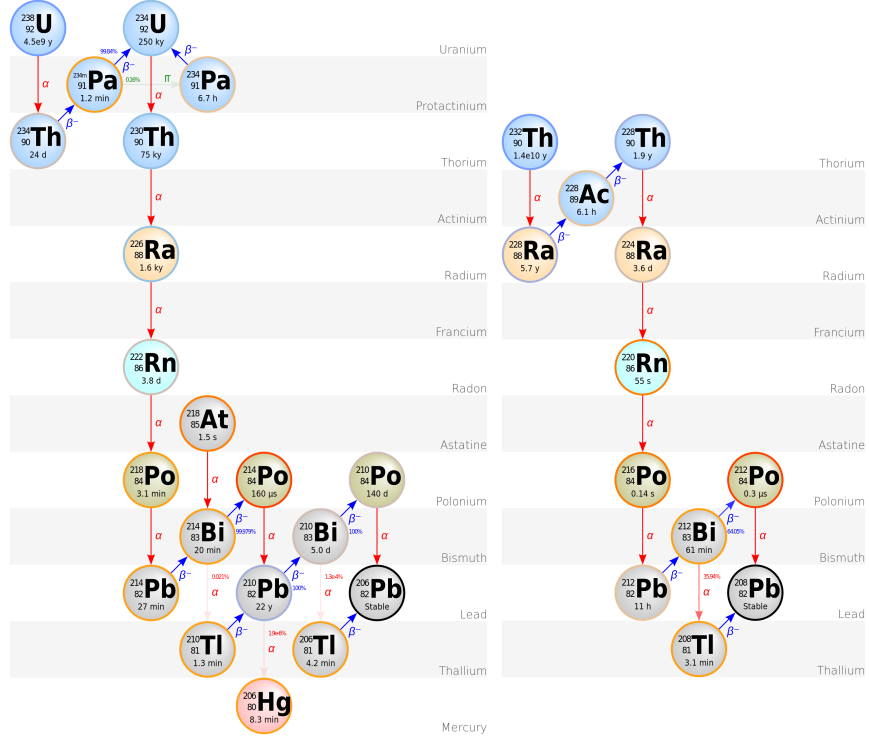


Figure 2.11 Decay chains of the primordial isotopes ^{238}U (left) and ^{232}Th (right). These chains represent the largest contribution both to ER and NR background for xenon-based dual-phase TPCs, as discussed in the text.

ICP-MS

ICP-MS is a destructive techniques which requires a few grams of sample to determine its isotopic composition. This is particularly useful for the determination of ^{238}U and ^{232}Th content, as their primordial decay chains shown in Fig. 2.11 are major sources of ER and NR background. The NR contribution comes from the spontaneous fission of isotopes along the decay chains and (α, n) reactions, where an α particle is captured by a nucleus followed by the emission of a neutron. This reaction is more common for low- Z nuclei since their Coulomb barrier is lower; for this reason materials characterized by low- Z elements like PTFE contribute more to the neutron-induced NR background. The ICP-MS measurements are a useful cross-check and complementary to the gamma-spectroscopy results.

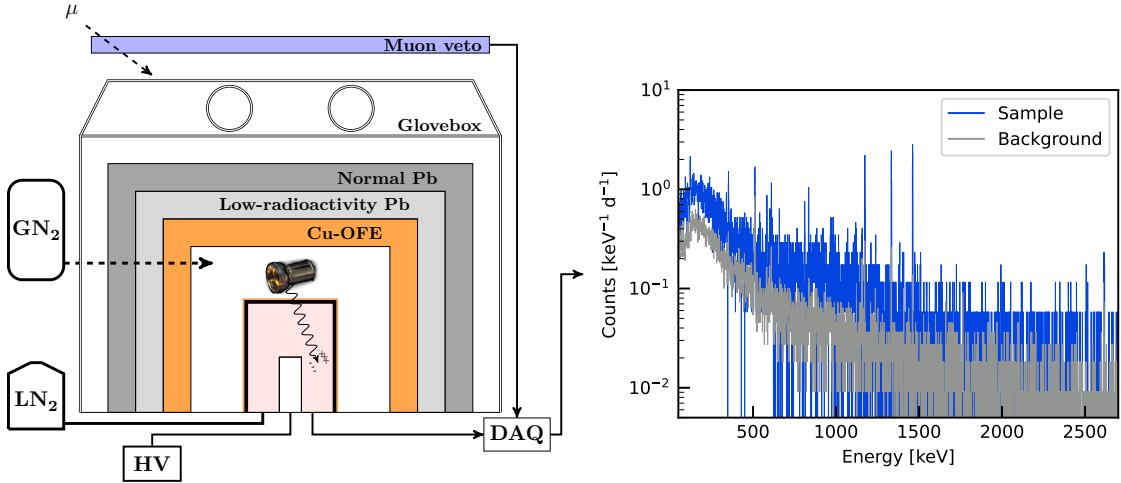


Figure 2.12 Sketch of the gamma-spectroscopy facility GeMSE located in the Vue des Alpes underground laboratory, Switzerland, under 620 mwe of rock overburden. The figure shown on the right is a comparison between the spectrum of the spectrometer background with no sample in the cavity (gray) and the spectrum of a batch of 10 Hamamatsu R11410-21 PMTs for XENONnT (blue).

The GeMSE gamma screening facility

The gamma screening facilities use commercially available low-background HPGe detectors sensitive to gamma radiation in the energy range from below 100 keV to 3 MeV. The GeMSE (Germanium Material and meteorite Screening Experiment) detector [179] is one of the most sensitive germanium spectrometers to date, despite the moderate rock overburden of only 620 mwe⁽⁴⁾. This should be compared to other detectors such as Gator [180] or GeMPI [181] located at Laboratori Nazionali del Gran Sasso (LNGS) in Italy, with a rock overburden of about 3600 mwe. The GeMSE facility is an interdisciplinary project located at the Vue des Alpes underground laboratory in Switzerland operated by the University of Freiburg in collaboration with the University of Bern. It played an important role in the material radioassay of XENONnT. The sketch of the detector is shown on the left of Fig. 2.12: a p-type HPGe coaxial crystal enclosed by a oxygen-free high thermal conductivity (OFHC) cryostat is located inside a cavity surrounded by a three-layer shielding. From inside to outside, the shield consists of oxygen-free copper (Cu-OFE, >99.99 % purity), low-activity lead with (7.2 ± 0.5) Bq/kg from ^{210}Pb and standard lead with a ten times higher ^{210}Pb activity. The cavity to place the samples is continuously purged with boil-off nitrogen gas:

⁽⁴⁾A quantity of 1 mwe (meter water equivalent) represents the attenuation power given by an overburden of one meter of water.

the induced overpressure reduces the concentration of ^{222}Rn , which otherwise would be too high and dominate the observed spectrum of low-activity samples. The cavity can be accessed using a top sliding door inside a glovebox enclosing the entire shielded detector. The facility features a muon veto consisting of two plastic scintillator panels optically coupled to three PMTs each. The signal produced by a muon crossing one of the panel is fed into a discriminator, whose signal vetoes the data acquisition (DAQ) system for 10 μs . This induces a total dead time of approximately 0.6 % with a total muon tagging efficiency of $(31 \pm 4)\%$ [7]. As a gamma-ray interacts with the depleted volume of the semiconductor detector, it produces electron-hole pairs proportional to the deposited photon energy. In order to collect the charge, a positive high voltage is applied to the n^+ region of the crystal while the grounded p^+ region is used for read-out. The thermal noise affecting the measurements is reduced by cooling the crystal down to 77 K via a cold finger thermally coupled to a liquid nitrogen dewar. The measured signals are processed by a 14-bit digital multichannel analyzer [182, 183]. An example of the resulting spectra is shown on the right of Fig. 2.12. By comparing the measured spectrum (blue histogram) to the background spectrum measured with an empty cavity (gray histogram), it is possible to determine the specific activity of the considered sample with a sensitivity as low as 50 $\mu\text{Bq}/\text{kg}$. This high sensitivity is possible thanks to the low background of (164 ± 2) counts/d, mainly dominated by cosmic muons [7].

2.3 | The XENON project

Despite technical challenges which are further discussed in Chapter 6, the dual-phase TPC technology is easily adaptable to any detector dimension. This relatively simple monolithic scalability is accountable for the success of the XENON dark matter project at LNGS in central Italy. This multi-stage project deploys xenon-based dual-phase TPCs of increasing size and reduced background, as shown in Fig. 2.13.

2.3.1 | XENON10 and XENON100

The pioneer of the project was XENON10, a cylindrical 20 cm \times 15 cm (diameter \times height) detector with an active target of about 15 kg [3]. The TPC was shielded by a 20 cm layer of high-density polyethylene (HDPE) against neutron background and by an additional 20 cm layer of lead against gamma and beta radiation. XENON10 was installed at LNGS and started commissioning in April 2006 with the goal to demonstrate the achievable energy

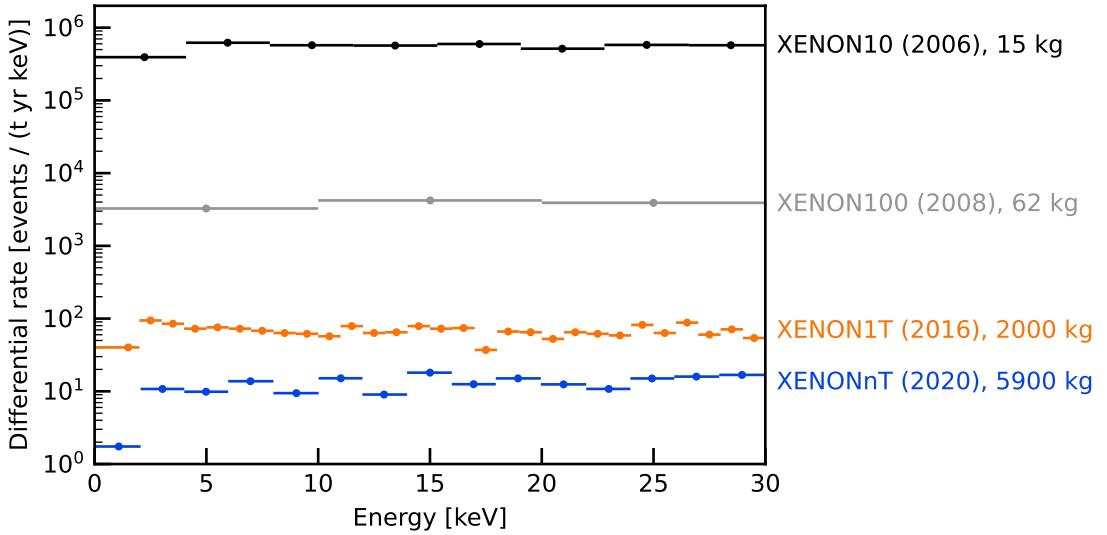


Figure 2.13 Comparison between the low energy spectra of the different phases of the XENON project, highlighting the total active mass. In less than 15 years the xenon-based dual-phase TPC technology increased its size of more than two orders of magnitude and lowered the background by almost a factor 10^5 . The data are from: XENON10 [3], XENON100 [105], XENON1T [173] and XENONnT [114].

threshold, background rejection power and operation stability in view of a larger following stage. Because of its prototype nature, many of its components were off-the-shelf and not screened to minimize the background: this explains the high rates of Fig. 2.13. After a blind analysis⁽⁵⁾, XENON10 set the best limits for SI and SD WIMP-nucleon interactions, demonstrating the great potential of the XENON project. The SI results of XENON10 are shown in Fig. 1.10.

After the successful operation of XENON10, the XENON project continued with the installation of the XENON100 dual-phase TPC in 2008. The new detector featured a target mass of 62 kg and reduced the background event rate of two orders by magnitude [184]. The reduction in background was mainly due to the proper material selection, the better self-shielding power of the larger active target and the improved passive shield. The inside of the shield was cladded with a 5 cm layer of OFHC copper, while an additional external H₂O/HDPE coat was added to further reduce the neutron background. In addition to the active 62 kg of active target contained in the 30.6 cm × 30.5 cm TPC, the 99 kg of liquid

⁽⁵⁾An analysis is *blind* when the signal region of interest is not accessible by the analysts before constructing the background and signal models in that region in order to avoid any bias.

xenon outside the TPC were instrumented, further enhancing the reduction of background radiation by tagging correlated signal between the TPC and this outer layer. The electric field of XENON100 was established by a set of hexagonal etched mesh electrodes and a field cage along both the outside and inside of the PTFE cylinder enclosing the active volume. The cathode voltage was limited to -16 kV for a final drift field of about 530 V/cm . XENON100 was operational from 2008 until 2016 and set the most stringent limits on SI and SD WIMP-nucleon scattering cross section with a final exposure of 48 kg yr [105]. The new WIMP limits improved the ones from XENON10 by more than two orders of magnitude, as shown in Fig. 1.10. This was possible thanks to an almost 50 times larger exposure and a reduction of the background by a factor 100.

2.3.2 | XENON1T

The XENON1T detector was commissioned in 2016. It was the first tonne-scale dual-phase TPC, with an active liquid xenon target of 2 t [169]. The detector was located in Hall B of the underground LNGS laboratory, where a $9.6\text{ m} \times 10.2\text{ m}$ water tank and an adjacent service building were built. A picture of the experimental setup is shown in Fig. 2.14, where the banner on the water tank shows a render of the detector therein.

The active volume of the TPC was 97 cm tall with a diameter of 96 cm . It was enclosed by 24 diamond-polished interlocking PTFE panels to reflect the VUV scintillation light. The volume was instrumented with a total of 248 PMTs shared between top array (127) and bottom array (121). Special 3" low-radioactivity PMTs (R11410-21) were developed by Hamamatsu in collaboration with the XENON collaboration. They reach high quantum efficiency ($\sim 34\%$) at the xenon scintillation wavelength of 175 nm [185]. The electric fields in the TPC were established by a set of five hexagonal etched mesh electrodes placed at the top and bottom of the target volume. The drift field defined by cathode and gate, which delimited the active volume, was “shaped” by a field cage consisting of 74 massive copper field shaping elements with a $5\text{ mm} \times 10\text{ mm}$ cross section and connected by two redundant voltage dividers. The cathode was initially set to a voltage of -12 kV during the first science run (SR0), but after a temporary interruption of the detector operations due to an earthquake in January 2018 this voltage had to be reduced to -8 kV for SR1. The cathode was negatively biased using a custom-made high voltage feedthrough (HVFT). It consisted of a conducting stainless steel rod inside an ultrahigh molecular weight polyethylene (UHMWPE) insulator, cryofitted into a 25.4 mm diameter stainless steel tube to make it vacuum-tight. A high extraction field at the liquid-gas interface was



Figure 2.14 View of the XENON1T experiment in Hall B of the LNGS underground laboratory. The 10 m-high water tank on the left acts as a passive shield and active Čerenkov muon veto. A render of its interior is shown on the banner fixed to the tank, from which the cryostat, the support structure and the umbilical pipe are clearly visible, together with the TPC. The service building with its glass facade on the right shows the different subsystems as sketched in Fig. 2.15.

ensured by the large potential difference between anode and gate, the first in the gaseous phase and set to 4.5 kV, while the second was grounded and positioned 5 mm below the anode in the liquid phase. The position of the liquid surface was measured by a set of four level meters and controlled by a diving bell which decoupled the pressure between its inside and the gas in the rest of the cryostat.

The XENON1T TPC was contained in a vacuum-insulated double-vessel cryostat made of 5 mm thick stainless steel, selected for its low radioactivity. The cryostat was suspended from a support structure via two sets of adjustment nuts, allowing for the correction of any tilt of the TPC, as discussed for the case of XENONnT in Sec. 3.5. A vacuum-insulated cryogenic “umbilical” pipe was used to route the cold xenon and the cables from the TPC towards the service building, where they were distributed among the different subsystems, as sketched in Fig. 2.15. The highly efficient vacuum insulation and additional superinsulation reduced the heat input to ~ 150 W, making it possible to reach temperatures of -96 °C using a “remote cooling” cryogenic system (CRY). This system

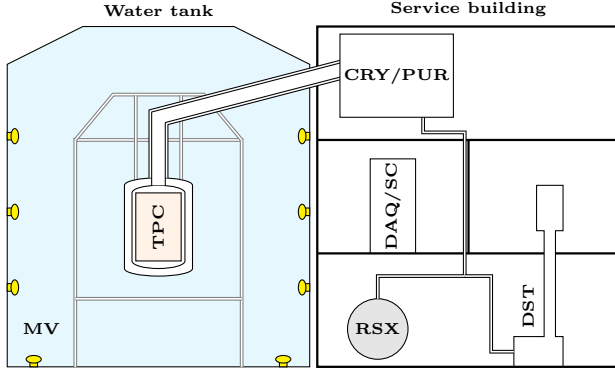


Figure 2.15 Schematic overview of the XENON1T subsystems located in the water tank and service building. The TPC was placed inside the water tank, instrumented as muon veto (MV). It was supported by a support structure and was connected to the cryogenic and purification systems (CRY/PUR) via an umbilical pipe. These systems were connected to a recuperation and storage system (RSX) and the krypton distillation column (DST). The second floor of the building hosted the electronics for the data acquisition (DAQ) and slow control (SC).

relied on two redundant pulse-tube refrigerators (PTRs [186]) providing up to 250 W of cooling power each. An additional backup liquid nitrogen system was implemented for safety reasons in case of sudden increase in the xenon pressure. The liquid xenon was extracted and directed towards the purification system through a heat exchanger, where the outgoing liquid was evaporated while cooling down the returning purified gas. The extracted gas was circulated through a couple of high-temperature rare gas purifiers, also known as “getters” (PUR): they remove electronegative impurities via chemical bounds with the zirconium cores [187]. The operation of the two redundant getters in parallel increased the electron lifetime to values $>600\text{ }\mu\text{s}$, comparable to the maximum drift time during SR0 and corresponding to a relative O_2 concentration $r_s < 10^{-9}\text{ mol/mol}$ (see Eq. (2.7)). A dedicated system for recuperation and storage, ReStoX (RSX), was developed to host up to 7.6 t of liquid or gaseous xenon, rated for pressures up to 73 bar thanks to its thick stainless steel wall and its spherical shape of 2.1 m diameter [169].

The cryogenic and purification system was also connected to the krypton distillation column (DST) [176]. The cryogenic distillation technique exploits the fact that the boiling temperature of krypton is about 60 °C lower than the one of xenon, leading to a higher concentration of gaseous krypton at liquid xenon temperature. By removing the gas at the top of the column, while recuperating the liquid at the bottom, it was possible to reach a

reduction factor up to 10^5 . The systems handling the xenon were hosted in the service building as shown in Fig. 2.15. The building also included a separate room to house the electronic modules for the DAQ and the slow control system (SC).

The cryostat containing the TPC was located at the center of a water tank instrumented with 84 PMTs (Hamamatsu R5912ASSY [188]) with a diameter of 20.4 cm [189]. The instrumented volume acted as a muon veto (MV), tagging the Čerenkov light produced by crossing muons or muon-induced showers. Thanks to the high light collection efficiency and the optimized sensitivity of the PMTs to the Čerenkov light wavelength of 300–600 nm, the tagging efficiency for crossing muons was 99.5 % [189]. This reduced the muon-induced neutron background to a negligible rate of <0.01 events/yr in a 1 t fiducial volume. The water also provided a very effective shield against the environmental radioactivity: while filling the tank, the DAQ observed a decrease in the TPC trigger rate of two orders of magnitude.

Summary of XENON1T science results

After first results using only 34.2 live days from SR0 [190], XENON1T published world-leading limits for SI WIMP-nucleon scattering in 2018 [104], improving upon the previous limits set by LUX [191] and PandaX-II [192]. This analysis used a live time of 278.8 days and a fiducial volume of (1.30 ± 0.01) t, being the first dark matter experiment reaching a total exposure of 1 t yr. The 90 % C.L. exclusion limit curve is shown in Fig. 1.10. Further studies focused on the reduction of the experimental threshold to improve the sensitivity to lighter WIMPs and to characterize the light and charge emission in liquid xenon at low recoil energies. This was achieved by using only the charge signal in a so-called “S2-only” analysis [193], also exploiting the hypothetical Migdal effect [100], already explained in Sec. 1.3.1. Another low-threshold analysis reduced the coincidence requirement for the S1 signals from 3 to 2 PMTs [102]. In this way smaller S1 signals corresponding to lower energy depositions are included in the analysis, lowering the energy detection threshold and boosting the sensitivity to lighter WIMP masses.

The improved detector shielding, the new distillation techniques and the accurate material selection resulted in a reduction of the XENON1T ER background by a factor 30 compared to XENON100 (see Fig. 2.13). This was the lowest background ever achieved by a dual-phase TPC detector and allowed for the first observation of the double electron capture of ^{124}Xe [177]. This decay was detected as a peak centered at 64.3 keV in the

reconstructed energy spectrum. This is the energy deposited by the cascade of X-rays and Auger electrons coming from the vacancies in a double K-shell capture. The significance of the signal was 4.4σ and the observed half-life was $T_{1/2} = (1.8 \pm 0.5(\text{stat}) \pm 0.1(\text{sys})) \times 10^{22}$ yr, the longest ever measured directly.

An excess above the expected ER background was observed close to the low energy threshold. The excess is clear in the spectrum of Fig. 2.13 for energies below 5 keV, where it is the most prominent in the 2–3 keV bins close to the rate drop due to the decreasing detection efficiency. Beyond SM solar axions could explain the excess with a global significance of 3.4σ , but also other theories like bosonic dark matter or a non-zero magnetic moment of the neutrino were suitable candidates with significances $\gtrsim 3\sigma$. The presence of tritium T (${}^3\text{H}$) was an alternative explanation of the excess: its β^- spectrum with Q-value of 18.6 keV describes the data at 3.2σ significance. Tritium is a long-lived isotope with a half-life of 12.3 yr [194] and it has a natural abundance of around 10^{-18} atoms per ${}^1\text{H}$, as measured in water. Assuming the same concentration for the water in xenon, an upper limit of 1×10^{-26} mol/mol ${}^3\text{H}/\text{Xe}$ was expected coming from tritiated water (HTO), insufficient to justify the $(6.2 \pm 2.0) \times 10^{-25}$ mol/mol required to explain the observed excess. Similar upper limits could not be set for the molecular hydrogen in its tritiated form (HT), since no measurements of the H_2 equilibrium emanation rate in XENON1T were available. To explain the excess by tritium, it would require a ~ 100 times higher concentration of molecular hydrogen than electronegative impurities like oxygen, *a priori* excluded by measurements of the electron lifetime and light yield. This does not include the potential contribution of other hydrogenated molecules such as organic compounds, although their removal via the zirconium getter is more efficient. A higher exposure and lower background are fundamental to confirm the presence of the excess and, in case, to discern its origin, further confirming the importance of an additional stage of the XENON project, XENONnT.

2.4 | XENONnT

The latest phase of the XENON project is the XENONnT experiment, currently taking data. The XENONnT detector was assembled and commissioned in 2020, following the disassembly of the XENON1T TPC in spring 2019 after more than three years of operation. The water tank and the service building were reused for its upgrade, together with the subsystems that were upgraded for the most part. The core of the XENONnT experiment

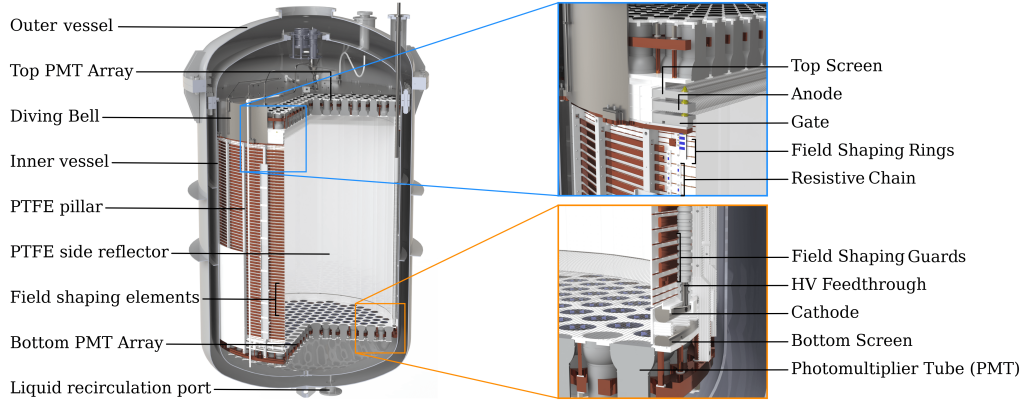


Figure 2.16 CAD rendering of the XENONnT cryostat and TPC. The top and bottom of the TPC are shown by the insets on the right, with particular emphasis on the arrangement of the electrode stacks.

is its dual-phase TPC with an active volume of 148 cm height and a diameter of 132.8 cm, enclosing a total target mass of 5.9 t. The design of the TPC is very similar to XENON1T and an overview is shown in Fig. 2.16. A total of 494 PMTs are installed in the TPC, with more than 150 light sensors being reused from XENON1T. The PMTs are shared between the top array containing 253 units and the bottom array with 241; the PMTs in both arrays are arranged in an hexagonal pattern to maximize the photocathode coverage. As in the previous detector stages, cathode, gate and anode electrodes define the drift and extraction fields, while two screen electrodes placed in front of the PMT arrays protect the light sensors from high fields. The cathode is biased by the same high voltage feedthrough used for XENON1T. Unlike XENON1T, the electrodes of XENONnT are made from individually fixed parallel wires. The drift field is shaped by a field cage consisting of two nested arrays of copper electrodes surrounding the active volume and set to a linear potential drop via two redundant voltage dividers. The field cage is discussed in Sec. 4.1, while the electrodes are discussed in details in Sec. 6.1.

The large volume of the TPC required the machining of a new inner cryostat and a vertical extension of the outer vessel. An additional umbilical pipe was installed in parallel to the existing one to host extra high voltage and signal cables due to the large number of PMTs. The additional umbilical pipe, together with the larger TPC and the new subsystems discussed in the following are shown in Fig. 2.17. The XENONnT inner vessel contains a total of 8.4 t of liquid xenon in addition to the $\mathcal{O}(100\text{ kg})$ xenon in the cryogenic and purification system. This quantity exceeds the 7.6 t capacity of ReStoX, requiring a second system for recovery and storage of xenon, called ReStoX-2 (RSX-2).

This consists of a $1.45\text{ m} \times 5.5\text{ m}$ cylinder rated for pressures up to 71.5 bar and capable to store xenon in gaseous, liquid and solid phase for a total capacity of 10 t.

The large amount of xenon requires a novel liquid purification system (LXePUR), working in parallel to the gas purification system inherited from XENON1T. Liquid xenon is extracted from a port at the bottom of the cryostat and circulated through a filter containing SAES St707 getter pills, an O₂-sorbent material selected for its low radon emanation rate [195, 196]. The system is equipped with two redundant cryogenic liquid pumps which can establish a volumetric flow up to 16 t/d. Thanks to this large purification flow, the electron lifetime during the first science run (SR0) of XENONnT reached values above 15 ms, as shown in Fig. 5.9. A purity monitor was installed along the LXePUR line to provide a measurement of the electron lifetime independent from TPC operation. The purity monitor design resembles the one described in [197] and measures the fraction of electrons lost after drifting the 20 cm separating its cathode and anode. This technique allows for reliable measurements of the electron lifetime up to 20 ms, with the main limiting factor being the short dimension of the monitor. The liquid xenon purification system is

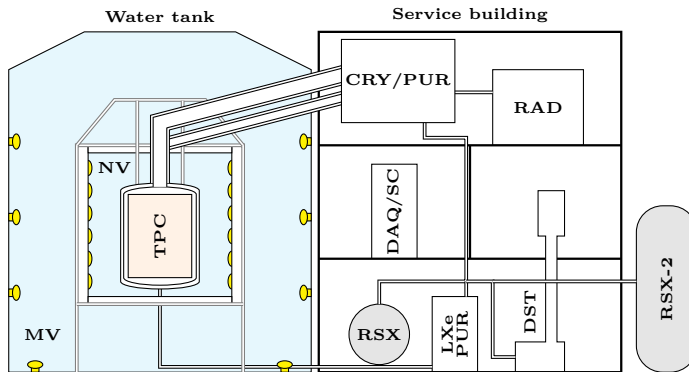


Figure 2.17 Schematic overview of the XENONnT subsystems located in the water tank and service building. Some of the subsystems are unchanged with respect to XENON1T, shown in Fig. 2.15. The larger TPC requires a second umbilical pipe to route additional signal and high voltage cables of the PMTs. The cryogenic system is connected to a liquid xenon purification system (LXePUR) located on the ground floor in front of ReStoX and to the radon distillation column (RAD). The larger amount of xenon also requires an additional recovery system (RSX-2), placed outside the service building. The new neutron veto (NV) detector surrounds the cryostat with reflective expanded PTFE and a total of 120 PMTs to detect the Čerenkov light produced by the gamma cascades following the neutron capture on hydrogen or gadolinium.

also connected to a new subsystem: the radon removal plant (RAD), described in [198]. It uses a radon distillation column, exploiting the same principle of the krypton column, although in this case the xenon is more volatile than the radon. The column is operated during normal data taking (“online” removal) and it aims at a reduction of the ^{222}Rn specific activity to less than $1\,\mu\text{Bq}/\text{kg}$ in liquid xenon. The first results of XENONnT reported a radon level of $1.7\,\mu\text{Bq}/\text{kg}$ during SR0 [114], but a further reduction of a factor two is expected for the next science runs.

Together with a reduction of the ER background thanks to the material selection campaign and the online radon removal system, also the neutron background is actively suppressed thanks to the implementation of the neutron veto (NV) detector. The detector surrounds the cryostat inside the water tank with an octagonal reflective structure made of expanded PTFE (ePTFE). The volume is instrumented with a total of 120 low-radioactivity 8" PMTs (Hamamatsu R5912-100-10 WA-D30 SEL Assy) and it is optically decoupled from the muon veto [199]. The neutron tagging relies on their capture inside the NV volume: for this reason the water in the tank is loaded with gadolinium sulphate octahydrate ($\text{Gd}_2(\text{SO}_4)_3 \cdot 8\,\text{H}_2\text{O}$), for a relative Gd mass concentration of 0.2 %. As a neutron interacts inside the TPC and escapes, it is thermalized by water and captured by gadolinium or, less likely, by hydrogen. The neutron capture is followed by the emission of a gamma-ray cascade with a total energy of 8 MeV for gadolinium and a single 2.2 MeV gamma for hydrogen. In both cases, the recoiling electrons from Compton scattering following the gamma emission allow for the production of Čerenkov light that can be detected by the neutron veto PMTs. The ePTFE reflectors surround the neutron veto volume and cover the outer cryostat, maximizing the light collection efficiency. The expected neutron tagging efficiency is 87 %, reducing the expected neutron background inside the fiducial volume from 0.321 events/(t yr) to 0.041 events/(t yr) [113].

First results from XENONnT

After a first science run from July to November 2021 acquiring a total livetime of 97.1 days, XENONnT released its first results in July 2022 [114]. These focused on the search for new physics in ER data with the main intention to confirm or disprove the excess observed by XENON1T [173]. The measured ER background of (16.1 ± 1.3) events/(t yr keV) in the 1–30 keV search region is the lowest ever achieved by a dual-phase TPC and a factor ~ 5 lower than XENON1T, as shown in Fig. 2.13. The ER spectrum below 140 keV is reported in Fig. 2.18: for the first time, the shape of the low energy spectrum is dominated by

two second-order weak processes, namely the $2\nu\beta\beta$ of ^{136}Xe and the $2\nu\text{ECEC}$ of ^{124}Xe . No excess in the low energy range is observed. When modeling the XENON1T excess

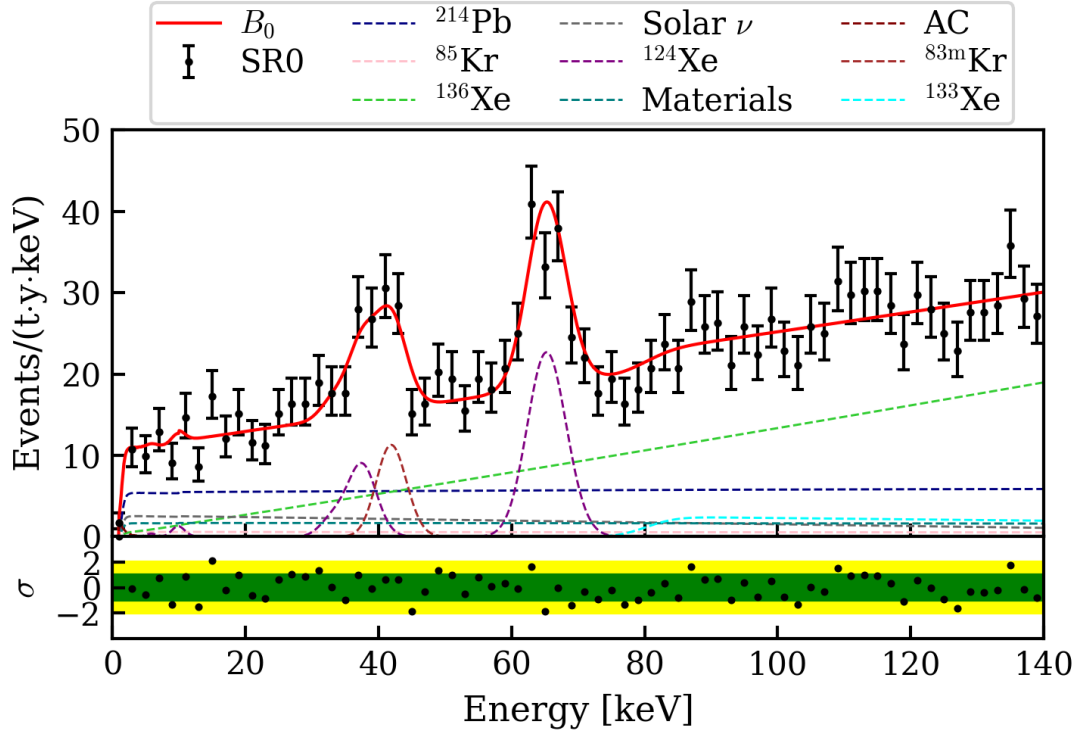


Figure 2.18 Low energy ER background of XENONnT in the first science run SR0 [114]. The result of the fit of the background model B_0 to the data (black data points) is the solid red line. Individual components of the background model are shown as dashed lines. The shape of the spectrum is dominated by two second-order weak processes: the $2\nu\beta\beta$ of ^{136}Xe and the $2\nu\text{ECEC}$ of ^{124}Xe . The excess at low energies observed by XENON1T [173] is excluded with a significance of $\sim 4\sigma$.

as a 2.3 keV monoenergetic peak, XENONnT excludes it with a statistical significance of $\sim 4\sigma$. These results exclude all beyond-SM explanations of the excess, favouring the tritium hypothesis. The lack of a tritium excess in XENONnT is explained as a result of the rigorous prevention measurements undertaken to minimize the contamination of HT and HTO in the detector. These measures included the outgassing of TPC and inner cryostat for three months before filling with gaseous xenon and the continuous purification of the xenon before filling the inner vessel.

Chapter 3

Liquid level monitoring in the XENONnT TPC

The position of the level of the liquid xenon is fundamental for the signal formation in a dual-phase TPC, as intensity and time profile of the proportional scintillation signal S2 depends on the drift path of the electrons in the gaseous gap. A precise measurement of the position of the liquid-gas interface allows the monitoring of the stability of S2 signals over the data taking. Furthermore, a large variation of the position of the interface could lead to operation instability and even sparks between anode and gate, resulting in a damage of the system. The monitoring of the liquid level is also important while filling the detector or recuperating xenon from it, as well as during cryogenic and purification operations, where the change in liquid level can be used to track the xenon content in the detector. The position of the liquid-gas interface is an important input parameter for the simulation of the S2 signal discussed in Chapter 6.

This chapter focuses on the capacitive level meter sensors developed in Freiburg starting in Fall 2018 and installed in XENONnT in March 2020, and the extensive test campaign to validate their design and read-out electronics. The working principle of the capacitive level meter is described in Sec. 3.1 and the actual implementation of the design of the level meters is discussed in Sec. 3.2. While the design of the “short level meters” for the fine level measurement between gate and anode was maintained from XENON1T, the larger dimension of the XENONnT TPC required the split of the previous “long level meter” in two: a long level meter extending along the field cage and a medium one along the diving bell. The read-out electronics is briefly described in Sec. 3.3: it is a straightforward upgrade of the board developed for XENON1T which was discussed extensively in [8]. The installation of the level meters and their calibration during and after filling the detector

are discussed in Sec. 3.4. The impact of the capillary effects and surface tension on the measurement is of particular interest. Indeed, a disagreement with the common assumption of a null contact angle between liquid xenon and metals is observed, favouring a $\sim 70^\circ$ angle both for short and medium level meter measurements. Lastly, the short level meters were used to measure the tilt angle of the detector. This information was used to correct the tilt of the XENONnT TPC using adjustment nuts supporting the outer cryostat, as detailed in Sec. 3.5. A final tilt angle as small as 0.02° was achieved after fine leveling.

3.1 | Working principle of the capacitive level meter

Among the different possible techniques to measure the liquid xenon level, the capacitive technique is characterized by a very simple and minimalistic sensor design. It simply requires two or more electrodes connected to cables for the read-out: neither moving nor electronic components are needed inside the detector. This not only reduces the risk of failure, but it also minimizes the amount of materials in contact with the xenon, reducing impurity and radioactive background sources. The measurement of the capacitance between the electrodes is realized by a dedicated read-out board placed outside of the detector as part of the slow control (SC) system, as further discussed in Sec. 3.3.

A typical capacitive level meter comprises two electrodes arranged in a geometry extending mainly along the dimension perpendicular to the liquid level, namely z . The main requirement for the sensor is that the electrodes' arrangement should be such that the electric field does not change along the z dimension. This ensures a linear response of the detector to changes of the liquid level, as by the definition of the capacitance [200]

$$C = \frac{Q}{\Delta V} = \frac{1}{\Delta V} \int_{\Omega} \nabla \cdot \vec{D}(x, y) d\omega = z \varepsilon_r \cdot \varepsilon_0 \underbrace{\frac{1}{\Delta V} \int_{\Sigma_{xy}} \nabla \cdot \vec{E}(x, y) dx dy}_K, \quad (3.1)$$

where K depends only on the cross-section geometry in the xy -plane of the capacitive sensor, $\varepsilon_0 = 8.85 \text{ pF/m}$ is the vacuum permittivity [201] and ε_r is the dielectric constant of the medium. Although any monotonic dependence $C(z)$ would serve the purpose, a linear proportionality $C \propto z$ simplifies the calibration and is therefore preferred.

When considering a level sensor in a xenon-based dual-phase TPC, this is partially filled with liquid xenon and gas, as depicted in Fig. 3.1. As the electrodes are the same in both phases of the xenon, this is equivalent to a system of two parallel capacitors: one of

3.1 Working principle of the capacitive level meter

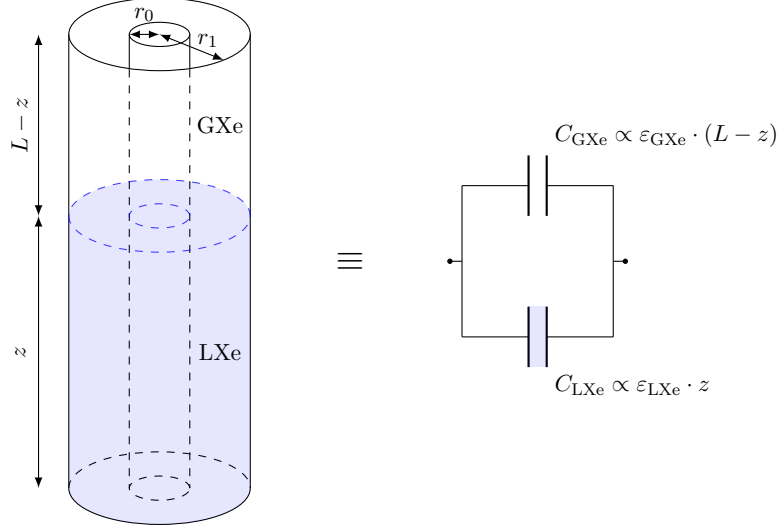


Figure 3.1 Sketch of a coaxial cylindrical capacitive level meter in liquid xenon. The total capacitance is equivalent to the parallel sum of the level meter fraction of length z filled with liquid xenon and the remaining $L - z$ filled with gas.

length z and filled with liquid xenon, and the other of length $L - z$ and filled with xenon gas, where L is the total length of the level meter. The total capacitance is equivalent to the sum of the individual capacitances:

$$C(z) = \underbrace{K\epsilon_{\text{LXe}}z}_{C_{\text{LXe}}} + \underbrace{K\epsilon_{\text{GXe}}(L-z)}_{C_{\text{GXe}}} = K\epsilon_{\text{GXe}}L + \underbrace{K(\epsilon_{\text{LXe}} - \epsilon_{\text{GXe}}) \cdot z}_{dC/dz}. \quad (3.2)$$

This corresponds to the capacitance C_{GXe} of the level meter in gas plus a conversion of the liquid level z into capacitance. The conversion factor dC/dz is proportional to the difference of the dielectric constants of the liquid and gaseous phases; with ϵ_{LXe} being in the range 1.85–1.96 [202–204] and $\epsilon_{\text{GXe}} \simeq 1$, xenon is a good medium for capacitive measurements when compared to similar media such as nitrogen or argon. The conversion factor dC/dz is a good figure of merit to understand the resolution of the sensor, independently of the read-out performance. Given a resolution of the capacitance measurement σ_C , the liquid level resolution is $\sigma_z = \sigma_C / (dC/dz) = \sigma_C [K(\epsilon_{\text{LXe}} - \epsilon_{\text{GXe}})]^{-1}$, indicating that a larger K and dielectric constant difference improve the precision of the level measurement. In case of a cylindrical coaxial geometry as the one shown in Fig. 3.1 the geometry factor is $K = 2\pi\epsilon_0 / \log(r_1/r_0)$, with inner and outer radius r_0 and r_1 , respectively. This means that closer electrodes improve the resolution, although they strongly reduce the measured capacitance.

3.2 | Level meter design

The level meter system of XENON1T [8] was composed by a total of six sensors: four short level meters (SLMs) and two long level meters (LLMs). As their names suggest, the former are short and small sensors installed on the copper plate supporting the gate electrode to monitor the liquid level position with high precision ($\sigma_z \simeq 30 \mu\text{m}$), once the detector is in its nominal conditions. The latter are sensors as long as the height of the TPC covering its full extension: they are less precise than the SLMs, but play an important role during filling and recuperation of the liquid xenon. The XENONnT system reuses the same design of four SLMs, but the longer TPC rendered the XENON1T LLMs obsolete. This required to design a new system of level sensors along with the SLMs. This system is composed by two redundant LLMs along the entire field cage and two additional medium level meters (MLMs) sitting along the diving bell.

3.2.1 | Short level meters

The short level meters (SLMs) consist of double-plate capacitors: a common electrode is sandwiched between two electrically coupled plates, acting as a single second electrode. This doubles the total capacitance of the sensor and its conversion factor dC/dz , improving its sensitivity. A 3D drawing of the SLM is shown in Fig. 3.2. The electrode plates are made of 0.5 mm-thick OFHC copper (> 99.99 % pure) with a 10 mm × 53 mm sensitive area. This is the area sensitive to the liquid level change. It is smaller than the actual electrode surface (10 mm × 61 mm) as its edges are inserted in PTFE holders. These keep the plates at a distance of 1 mm. The entire ensemble is encased by a copper enclosure of dimension 7 mm × 19.5 mm × 77 mm, grounded to minimize the electric field leakage inside the sensor as they are positioned at the liquid-gas interface where the fields can be as high as 16 kV/cm. While the bottom of the enclosure is open, holes on the top allow the liquid xenon to flow outside the sensor, avoiding the formation of gas pockets. The cable connection for the capacitance read-out is possible thanks to eyelet tabs at the edge of each copper plate which are sticking out from the bottom of the enclosure. This geometry leads to an expected gas-only capacitance $C_{\text{SLM}}(\text{GXe}) = 12.5 \text{ pF}$ and a liquid-only of $C_{\text{SLM}}(\text{LXe}) = 21.5 \text{ pF}$. Considering the total z extension of 10 mm, this yields an expected conversion factor $dC/dz = 0.901 \text{ pF/mm}$.

After the disassembly of XENON1T, the SLMs were stored in a clean environment. The copper enclosures and the screws were reused for XENONnT, while the copper electrode

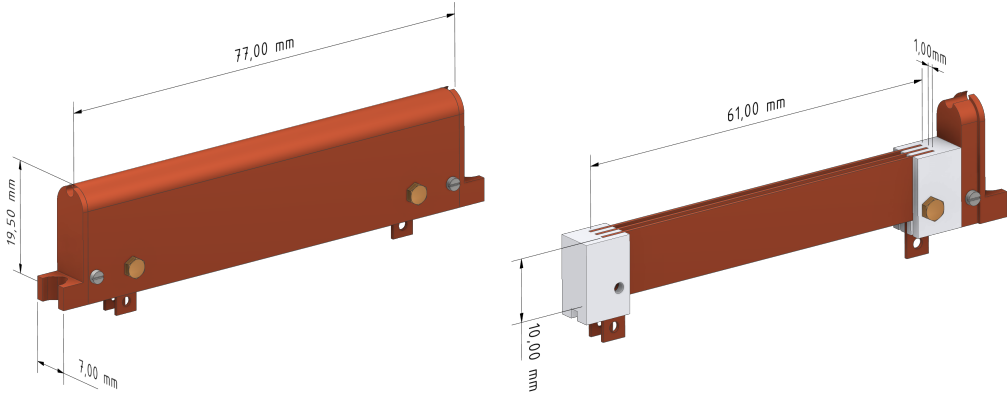


Figure 3.2 3D CAD drawing of the short level meters (SLMs) with (left) and without (right) the enclosure. The design developed for XENON1T [8] was used also for XENONnT.

plates and the insulating holders were re-machined following the original drawing. PTFE was used for the new holders instead of the original polyether ether ketone (PEEK), with a corresponding reduction in the expected capacitance as $\epsilon_{\text{PTFE}} < \epsilon_{\text{PEEK}}$. The machining was necessary because of the impossibility to remove the plates from the holders, likely due to the use of glue or cryo-fitting techniques. This resulted in a potential cleanliness problem as it was impossible to clean the different parts independently following standard procedures. These procedures involve the use of H_2SO_4 (1%) + H_2O_2 (3%) solution and citric acid for copper, while nitric acid is used for insulating material such as the PTFE of the holders [172]. A thorough and proper cleaning of these sensors is essential as they sit close to the liquid-gas interface and the active volume. In the same way their radiopurity is important. The components reused from the SLMs of XENON1T (copper enclosure and screws) were screened during the radioassay campaign [205]. The copper used to machine the new electrodes was not screened, but since copper is a particularly radiopure material, the main source of radioactive background is expected to be the holders. They were machined using the same raw material used for the holders of the medium and long level meters and their screening results are reported in Tab. 3.1. The screening results from the SLMs of XENON1T are reported in the same table for comparison. A reduction of 30 % for ^{60}Co and 5 % for ^{137}Cs is considered to account for the negligible cosmogenic activation while underground. The strong reduction of the specific activity is due to the radiopurer nature of the PTFE compared to PEEK, as evident from the results of the XENON1T [205] and XENONnT [172] screening campaigns.

3.2.2 | Long level meters

The two redundant long level meters (LLMs) developed for XENON1T are composed of coaxial cylindrical stainless steel (SS) electrodes extending from the bottom PMT array all the way above the diving bell. Referring to the sketch in Fig. 3.1, the sensor was characterized by $L = 1357\text{ mm}$, $r_0 = 1.5\text{ mm}$ and $r_1 = 2.7\text{ mm}$ [8]. A total of five 3 mm high PTFE spacers were placed along their extent. They were used as calibration points to estimate the conversion factor dC/dz . This is possible because the distance among them is known from design, while the capacitance in each calibration point can be directly measured. Indeed, at the height of these elements the liquid level inside the sensor does not change, resulting in a visible capacitance plateau. This allowed the calibration of the LLMs while filling the detector, as the amount of xenon available to XENON1T was not sufficient to completely submerge them.

Unlike the SLMs, the long level meters designed for XENON1T could not be used for the detector’s upgrade, as the sensor length of 1357 mm is not enough to cover the full extension of the XENONnT TPC. In addition, one of the two sensors (LLM1) stopped working during the filling operation of XENON1T. The failure was attributed to the electric connection of the read-out cable, which was based on a spring-loaded connection realized screwing a SS bolt inside a PTFE “cap” and sandwiching the cable between two nuts along the bolt. The hypothesis for the malfunction is that the thermal shrinkage of the PTFE cap disrupted the spring-loaded connection. This is supported by the fact that during the disassembly of XENON1T no damage to LLM1 was observed and the sensor properly worked at warm temperature. In order to avoid similar potential problems, the electric connection was changed in favor of a more stable and reliable design.

A possible solution for the XENONnT upgrade was to replicate the design of XENON1T by machining longer LLMs. This solution is the most straightforward, as it keeps the same configuration of four SLMs plus two LLMs without the need for any change in the read-out. These LLMs would need to have a total length of around 1860 mm , while at the same time the maximum capacitance should be below 300 pF , as the electronic read-out inherited from XENON1T loses linearity and reliability above this value. It is important to find a (r_0, r_1) combination compatible with the read-out system and with the XENONnT TPC design, as the gap between the diving bell and the inner cryostat is only 1.7 cm (see Fig. 2.16). The possible radius combinations are shown in Fig. 3.3, along with the corresponding conversion factor dC/dz , directly related to the measurement precision. Realizing the cross-section of the XENON1T LLM design is not possible, as it leads to a maximum

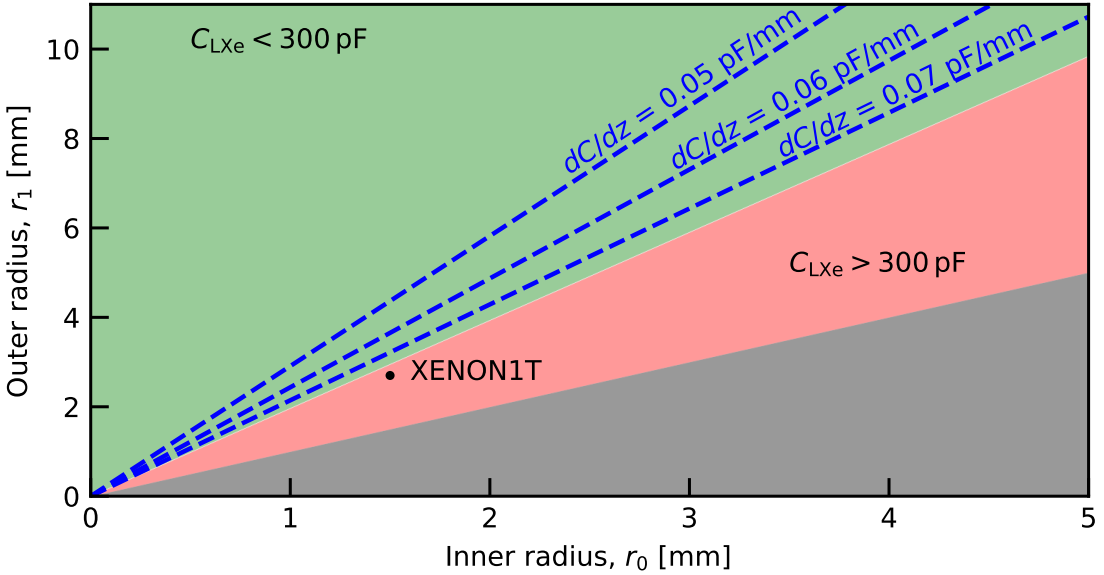


Figure 3.3 Allowed outer and inner radii for a single XENON1T-like long level meter with the length required for XENONnT ($L = 1860$ mm). The green area represents the configurations (r_0, r_1) with a liquid-only capacitance below 300 pF, hence compatible with the foreseen read-out electronics. The blue dashed lines represent conversion factors for different geometries. A cross-section similar to XENON1T is not possible as it would lead to capacitance values above the linearity range of the read-out board. The gray region represents the unphysical combination $r_0 > r_1$.

capacitance above 300 pF. Previous capacitance measurements in xenon suggest a relative resolution of $\sigma_{C,\text{rel}} = 0.2\%$, independently of the capacitance value [8]. Assuming this to be the case also for XENONnT, since the read-out system is basically unchanged, this means that the final resolution of the detector would be:

$$\sigma_z = \frac{\sigma_C}{dC/dz} = \frac{\sigma_{C,\text{rel}} \cdot C}{dC/dz} \stackrel{(3.2)}{=} \sigma_{C,\text{rel}} \cdot z + \sigma_{C,\text{rel}} \frac{\varepsilon_{\text{GXe}}}{\varepsilon_{\text{LXe}} - \varepsilon_{\text{GXe}}} L \quad (3.3)$$

ranging from $\sigma_z = 3.9$ mm in GXe to $\sigma_z = 7.6$ mm when the level meter is completely submerged. This poor resolution pushed for a different approach: splitting the LLMs into two sensors, the long level meters covering the TPC from the bottom PMT array to right below the bell, and the medium level meters (MLMs) covering only the height of the bell. In this way the worse resolution of the LLM is limited to the filling operation when a high precision is not required, while the MLMs can monitor the liquid level position during nominal operations with a better resolution.

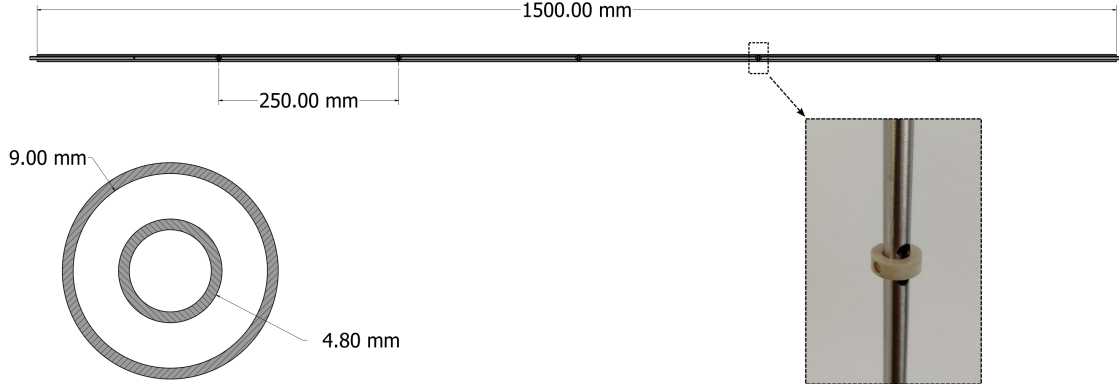


Figure 3.4 Dimension of the long level meters (LLMs). In the inlet a picture of the sensor without the external electrode shows the geometry of the PEEK spacer. The venting holes are punched in the inner pipe, with the liquid xenon flowing inside of it.

In their final design, the LLMs consist of coaxial cylindrical SS304 electrodes of length $L = 1500\text{ mm}$, with $r_0 = 2.4\text{ mm}$ and $r_1 = 4.5\text{ mm}$. This geometry corresponds to a capacitance range of about 130–240 pF and slightly improved resolution from $\sigma_z = 3.1\text{ mm}$ to $\sigma_z = 6.1\text{ mm}$. This resolution plays a role only during filling and recuperating operations, when a high precision is not needed. In nominal conditions these sensors are completely submerged and the liquid level outside the bell is measured by the MLMs, which feature a higher resolution. In the LLMs, a total of five 4 mm high PEEK spacers are placed 25 cm apart along the capacitor and are pin-joined to the inner electrode using PEEK pins. The liquid can flow through the inner electrode thanks to venting holes right above and below the spacers. Unlike XENON1T, these holes are punched along the inner electrode to prevent electric field leakage coming from the high field region on the outside of the LLM. This large field is due to the proximity ($\sim 4\text{ cm}$) of the grounded cryostat to the TPC field cage and the cathode frame, with design voltages as low as -30 kV . The spacer assembly and the LLM geometry are shown in Fig. 3.4.

An additional improvement with respect to XENON1T is the signal cable connection. The new design includes a threaded M3 SS stud spot-welded on the top of the inner and outer electrode. The open end of the read-out signal cable is soldered to a $\sim 1\text{ cm}^2$ copper plate with a punched hole: this is sandwiched between two nuts screwed to the stud. An example of these connections can be seen in Fig. 3.7c and 3.7d. Despite the intrinsic dirtiness of soldering, typically avoided for low-background detector, its small amount has a negligible impact on the cleanliness while assuring a reliable electric connection.

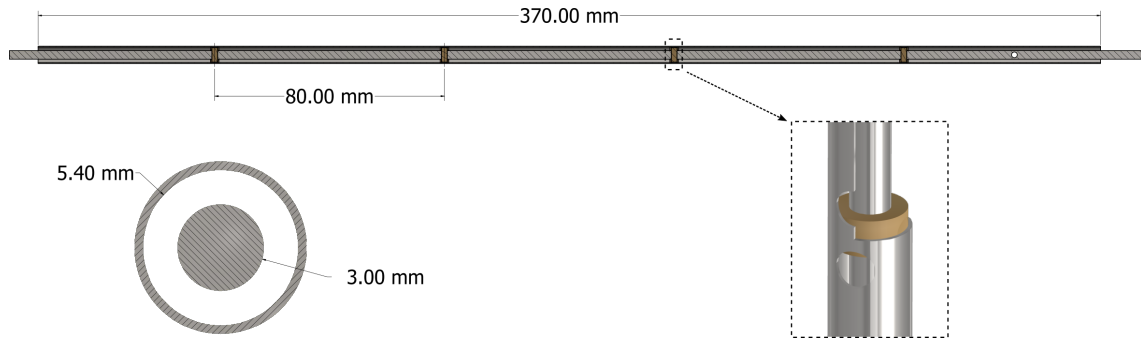


Figure 3.5 Dimension of the medium level meters (MLMs). In the inlet a sectional view of the PEEK spacer and the venting holes.

3.2.3 | Medium level meters

The novelty of the XENONnT level meter system is the introduction of medium level meters (MLMs), designed to measure the liquid level outside the bell. These are two redundant sensors consisting of coaxial cylindrical SS304 electrodes with $L = 370$ mm, $r_0 = 1.5$ mm and $r_1 = 2.7$ mm. Such geometry not only assures the sensor to fit within the small gap between diving bell and inner cryostat, but also yields an expected resolution from $\sigma_z = 0.78$ mm to $\sigma_z = 1.5$ mm. The capacitance range is expected to be around 35–65 pF. As the sensors are designed to cover up to 3.5 cm above the top of the diving bell, they are never completely submerged, hence it is necessary to provide them with calibrating spacers as the LLMs. These are four 3 mm PEEK spacers with a 7.5 cm gap fixed along the inner electrode in the same way of the long level meters, with the difference that the venting holes for the liquid flow are punched on the outer electrodes, as shown in Fig. 3.5.

Unlike the LLMs, the MLMs monitor the liquid level during normal operations. While this level has no correlation with the gas gap of the S2 region because of the decoupling effect of the diving bell, this quantity is related to the total amount of xenon in the detector and is thus particularly important for cryogenics and purification purposes. It is an important parameter to monitor the xenon mass exchange from the inner vessel to the outside. In this case the small gap between diving bell and the inner cryostat boosts the sensitivity to the mass variation, as a change of 1 kg translates into 4.4 mm for the liquid level. For reference, inside the bell the level would change of only 200 μ m.

The materials used for the medium and long level meters were screened, with the exception of the PEEK used for the spacers consisting of a total mass of less than 2 g.

The results are reported in Tab. 3.1 along with the activity of the SLMs of XENON1T corrected for the reduced cosmogenic activation. The electrode SS pipes were screened using the high-purity germanium (HPGe) well detector GeDSG [207]. These detectors maximize the geometrical acceptance as the crystal surrounds the sample, but they are limited to masses up to $\mathcal{O}(100\text{ g})$ because of the reduced dimension of the well. The PTFE used to machine the holders of MLMs and LLMs was screened using the coaxial HPGe detector GeMPI [206]. In this case it is the germanium crystal to be surrounded by the screened sample, reducing drastically the geometrical acceptance in favor of a larger cavity to host samples with masses up to $\mathcal{O}(100\text{ kg})$.

	XENON1T SLM	L/MLMs	L/M/SLMs
Material	Copper, PEEK	SS	PTFE
Mass	166.8 g	13.8 g	15.15 kg
Livetime	14 d	21.8 d	45.4 d
Detector	GeMPI [206]	GeDSG [207]	GeMPI [206]
Specific activity [mBq/kg]			
^{235}U	<0.6	<3	<0.049
^{238}U	<15	<280	<0.7
^{226}Ra	<1.1	<7.4	$(43 \pm 11) \times 10^{-3}$
^{228}Ra	<1.2	<10	<0.062
^{228}Th	<1.3	<16	<0.042
^{40}K	22 ± 8	<75	<0.42
^{60}Co	<0.56	7 ± 3	-
^{137}Cs	<0.61	<2.5	<0.01

Table 3.1 Activity measurements for the materials of the level meters. The top part of the table shows the material screened together with the mass used for the screening and the duration of the screening measurement (livetime). The detector used for the measurements is also reported. The bottom of the table contains the results of the specific activity for several radioisotopes, either reported as 68 % C.I. (confidence interval) or 90 % C.L. (confidence level) upper limit. The results for the XENON1T SLMs are taken from [8], including the reduced cosmogenic activation while underground.

3.3 | Read-out board

The read-out electronics board for the level meter system is a straightforward upgrade of the one developed for XENON1T and extensively discussed in [8]. It uses the Universal Transducer Interface (UTI) chip, capable of measuring capacitances in the range 0–300 pF [208]. This technology allows for the measurement of capacitance values as low as the SLMs' ones, despite the $\sim 10\text{ m}$ coaxial cables used for the read-out with a 105 pF/m [209] parasitic capacitance. This is possible thanks to the *four pole technique* [208], sketched in Fig. 3.6 alongside to the full read-out electronics scheme. Each level meter electrode is read-out via a coaxial cable: the core is connected to the electrode, while the shielding is grounded. One electrode is excited using a square wave signal with amplitude V_{in} , inducing on both electrodes a charge accumulation Q_x proportional to the total unknown capacitance C_x . As the voltage source is nearly ideal, i.e., the output impedance is almost zero, the

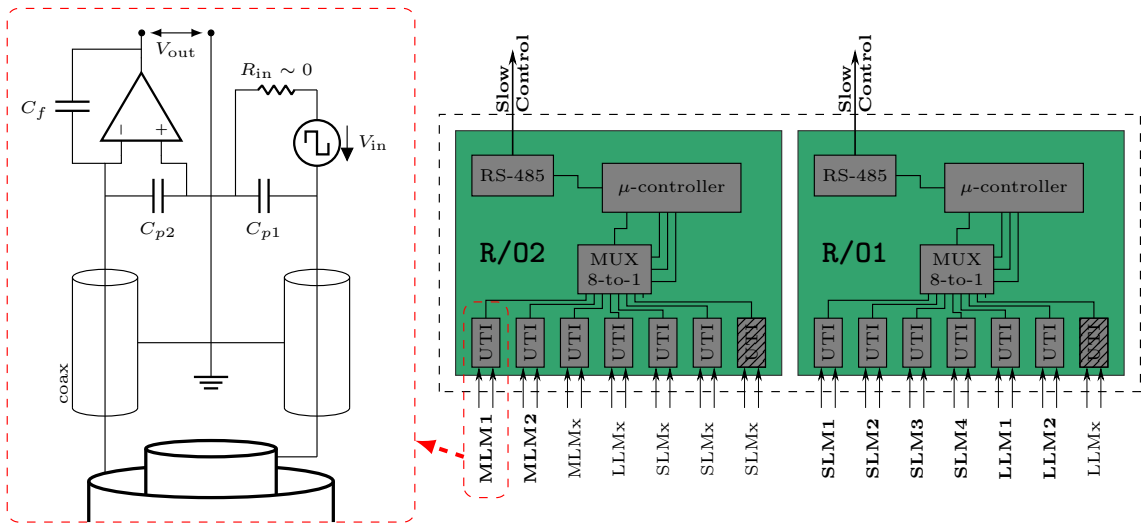


Figure 3.6 Summary sketch of the read-out board and the UTI circuit principle (red contoured inset). Two signal coaxial cables per level meter are fed to the board where a UTI chip uses a four pole technique to virtually short circuit the parasitic capacitances. The final read-out electronics consists of two similar boards, independently connected to the slow control system via serial communication. Each board periodically sweeps through all the UTI channels using a microcontroller and a 8-to-1 multiplexer, but only 8 out of 14 signals correspond to level meter measurements and they are labelled in bold. The hatched UTIs correspond to channels physically implemented, but skipped by the microcontroller: a change in its firmware can recover these channels.

parasitic capacitance C_{p1} of this cable is practically short-circuited and excluded from the measurement. The total charge Q_x induced on the other electrode is converted into a voltage via a charge amplifier. The electrode is connected to the inverting input ($-$) of the operational amplifier, while the non-inverting input ($+$) is connected to the same ground of the coaxial cable shield. Because of the huge amplification gain A_v , the voltage difference has to be almost zero, in order to have a finite output voltage $V_{\text{out}} = A_v(V_+ - V_-)$, with the inverting input becoming a “virtual ground” ($V_- \simeq V_+ = 0$). This means that also the parasitic capacitance C_{p2} has a negligible impact on the capacitance measurement. This leaves the charge Q_x to be completely accumulated on the charge amplifier feedback capacitor C_f , hence assuring a linear proportion between the unknown capacitance and the output voltage $V_{\text{in}} \cdot C_x = V_{\text{out}} \cdot C_f$.

A voltage-to-period converter translates the output voltage into a square wave signal with period $T_x = \kappa_0 \cdot V_{\text{out}} + \kappa_1 = a_0 \cdot C_x + a_1$, where the parameters are not known and depend on the individual UTI chip. This issue can be solved via the *three signal technique* [208]. Instead of measuring only the unknown capacitance, a total of three quantities are measured: the offset capacitance C_{off} including all the parasitic contributions of the UTI chip and board, a reference capacitance C_{ref} of known value and C_x . This returns three periods related to the corresponding capacitances via the same linear function; the unknown capacitance is then given by:

$$C_x = \frac{T_x - T_{\text{off}}}{T_{\text{ref}} - T_{\text{off}}} \cdot C_{\text{ref}}, \quad (3.4)$$

where the reference capacitance has to be known precisely and picked within the expected capacitance range measurement to maximize resolution and linearity. In the XENONnT case, the values of C_{ref} are 10 pF, 47 pF and 150 pF for SLMs, MLMs and LLMs.

The read-out board consists of a total of seven UTI chips, out of which only six are read out by the PIC16F877A microcontroller [210]. This sweeps through all the UTI chips thanks to a 8-to-1 multiplexer, collecting a total of four time measurements for each sensor: one for the reference capacitance, one for the level meter capacitance and two for the offset. Each period is converted to a 2 byte word. Including the acknowledgement byte between each sensor reading and an end-of-line byte, the final board output for a single measurement is a 55 byte long word. This is returned every time a command ‘X’ is issued to the microcontroller through the serial communication RS-485. As a single board is able to handle only six level meters, the final read-out electronics consists of two individual boards connected to the slow control (SC) system via independent serial ports, as shown in

Fig. 3.6. This allows for additional spare channels, featuring different reference capacitances based on the type of level meter they are designed for. These boards were designed and newly machined by the electronic workshop in Freiburg based on the XENON1T drawings developed in Mainz [8]. Among the changes done to the original design, one of the most important is the replacement of the cable connectors from mini MMCX to SMB embedded in the board front panel. This was done to prevent the connector to break because of the large force needed to plug and unplug the cables. The board is connected to the SC system SCADA, which asks every two seconds for a measurement from each board independently and translates the two 55 byte long words into six capacitance values following Eq. (3.4).

3.4 | Level meters installation and calibration

3.4.1 | Installation

The assembly of the XENONnT TPC started on February 24, 2020 and it was concluded with lifting and closing the inner vessel on March 14 of the same year. The majority of the operations were carried out in the clean room above ground in Hall di Montaggio at LNGS. Afterwards the detector was transported underground. The above ground clean room was a more suited environment for the detector assembly not only because of the larger dimensions, but also for logistical convenience. The four SLMs were installed on February 28. They were fixed in niches in the PTFE covers surrounding the gate and anode electrode frames in the top stack, as shown in Fig. 3.7a and 3.7b. These pictures were taken before inserting the TPC into the diving bell, as after this operation the sensors cannot be accessed anymore. The SLMs are fixed on 16.5 mm long PTFE spacers via PEEK M4 screws: the spacers align the active area of the sensors with the 8 mm gap between anode and gate. An additional thin PTFE layer was inserted in front of the SLMs before lifting the TPC inside the bell, in order to avoid electric contact with it. After lifting the TPC inside the top dome of the inner vessel, the connection with SLM3 was lost, probably due to the rupture of a soldered connection. As three working SLMs are compatible with the TPC operations no further action was taken in order to recover it.

The long and medium level meters were mounted underground. In the case of the MLMs, the additional height sticking above the top of the bell would have prevented the TPC to pass through the water tank door. The LLMs were mounted along opposite pillars using a PTFE holder placed in the bottom part of the TPC. Three additional PTFE pipe

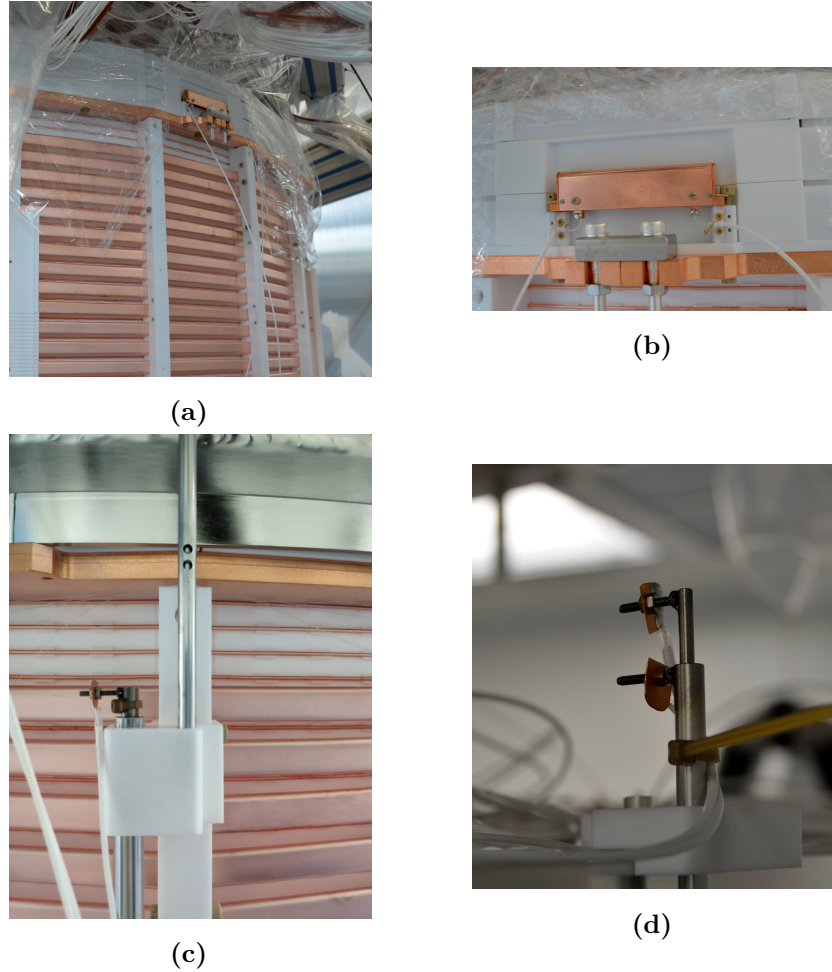


Figure 3.7 (a)-(b) The SLMs were installed inside niches of the PTFE electrode cover. The copper case is sitting on PTFE spacers used to optimize the z position of the sensor and as strain reliefs for the read-out cables. (c) Shared pipe guide between medium and long level meter, partially showing the z overlap of the two sensors. (d) Top of the MLM sticking above the top of the diving bell for more than 3 cm. It is also visible the improved electric connection using spot-welded studs and nuts sandwiching the connector. PEEK cable ties are used as strain relief for the connection cables.

guides were placed along the pillar. The long level meters can slide inside the guides while cooling down as the TPC thermally shrinks. These pipe guides are also used to fix PTFE insulators between the LLM electrodes and the field cage. These insulators avoid potential sparks in the high field region between the grounded LLM electrode and the field cage. The top pipe guide shown in Fig. 3.7c is also used by the MLMs, which is fixed on the top of the diving bell (Fig. 3.7d). Since the thermal shrinkage of PTFE was measured to be 1.4%

when cooled from room temperature to liquid xenon temperature, while for the stainless steel it is negligible, this results in a different z alignment of medium and long level meters at cold temperatures. The overlap in z between the sensors is 13.4 mm in warm gas, but it increases to around 32.5 mm at the liquid xenon temperature of about -96°C . PEEK cable ties are used as strain reliefs for the read-out cables, as shown in Fig. 3.7d.

3.4.2 | Filling and calibration

The cryostat was closed on March 14. Due to the COVID pandemic, the filling with liquid xenon started only at the end of August 2020. During this period the outer vessel was pumped to ultra-high insulation vacuum and the inner cryostat was filled with gaseous xenon. Starting mid-August its temperature was decreased with a cooling rate of $10^{\circ}\text{C}/\text{d}$ to avoid any thermal stress for the electrodes. The higher thermal mass of the electrode frames compared to the wires might lead to a large difference in shrinkage, resulting in mechanical damage. The filling procedure started in “GXe mode”, where the only source of liquid was the condensation of gaseous xenon around the cold-finger for a filling speed of around 12 kg/h. Once roughly 1550 kg of liquefied xenon were collected inside the cryostat, the operation switched to “LXe mode”, where liquid xenon was directly introduced from ReStoX, resulting in a doubled filling speed. The filling procedure was recorded by the LLMs and was characterized by days-long periods of stable level to allow for tests of the liquid xenon purification system (LXePUR), as shown in Fig. 3.8.

Calibrating the level meters means finding the linear relations between measured capacitance and the absolute position of the liquid level. Considering a level meter whose bottom is positioned at a distance h_{off} from the reference position, i.e., the top of the gate frame, the conversion is given by

$$z_{\text{LXe}}(C_{\text{LM}}) = \frac{C_{\text{LM}} - C_{\text{GXe}} - C_{\text{cap}}}{dC/dz} + h_{\text{off}}. \quad (3.5)$$

In this equation dC/dz is the conversion factor as in Eq. (3.2), C_{GXe} is the level meter capacitance when empty and C_{cap} is an offset capacitance due to the capillary rise of liquid xenon inside the level meter. The capillary effect introduces an offset between the liquid level outside and inside the level sensor due to surface tension effects. The capillary force is $F_{\text{cap}} = L \cos(\theta) \gamma_{\text{LXe}}$ where θ is the contact angle between liquid and solid interfaces, L is the interface edge length. The surface tension is $\gamma_{\text{LXe}} = 16.58 \text{ mN/m}$ [211]. This counterbalances the gravity acting on the liquid with a capillary rise h_{cap} , for a total weight

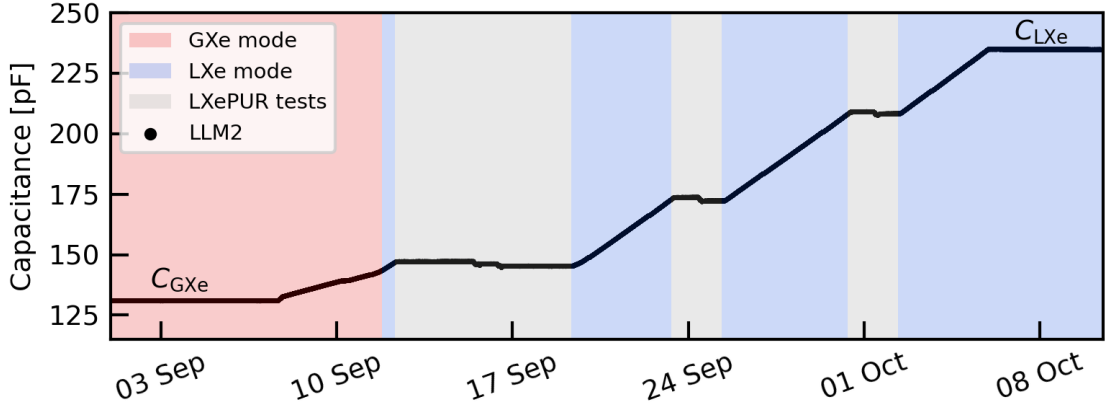


Figure 3.8 Liquid xenon filling operations as measured by LLM2. The cryostat was initially filled condensing gaseous xenon in the inner volume (GXe mode, red), then liquid was directly introduced from ReStoX increasing the filling rate (LXe mode, blue). The gray areas indicate periods of time when the filling was interrupted to perform liquid xenon purification (LXePUR) tests. The LLM was completely filled before the conclusion of the filling operations.

$F_g = Ah_{\text{cap}}g\rho_{\text{LXe}}$ where A is the cross-sectional area of the level meter and $g = 9.81 \text{ m/s}^2$. This results in a capillary rise height of

$$h_{\text{cap}} = \frac{L \cos(\theta) \gamma_{\text{LXe}}}{Ag\rho_{\text{LXe}}}, \quad (3.6)$$

where the contact angle for liquid xenon is typically unknown. From the results reported in [8], we expect a concave meniscus ($h_{\text{cap}} > 0$) when in contact with copper, hence $\cos(\theta) > 0$ and likely lower than unity. No conclusion was possible for stainless steel [8], as the long level meter resolution and geometry did not allow for any measurement of the capillary capacitance. Nevertheless, a similar behaviour for all metals is expected.

Calibration of the long level meters

The LLMs were calibrated while filling the inner vessel using the five PEEK spacers positioned along its length. During the first LXePUR test, LLM1 showed a slow increase in capacitance which was not observed by LLM2: this was attributed to some charge build-up due to the operation of one of the tested pumps. This change is clearly visible in Fig. 3.9, where the relative difference between LLM1 and LLM2 data points change between the

initial increase and the other measurements. This capacitance build-up was limited to a few days, after which the relative difference between LLM1 and LLM2 stabilized. For this reason the calibration between empty LLMs and first spacer was discarded. The conversion factor dC/dz between two spacers is evaluated as the ratio of the capacitance difference between two consecutive capacitance plateaus and the z distance between two consecutive spacers. The slow filling rate allowed for a high statistics per unit of time, reducing the statistical uncertainty to a negligible level. The uncertainty is thus driven by the mechanical tolerance of the LLM machining, assumed to be 1 mm over the 25 cm distance between spacers. The resulting conversion factors are summarized in Tab. 3.2 and they agree within the two level meters to a value of about 0.07 pF/mm. As it is not possible to use C_{GXe} for Eq. (3.5) because of the capacitance build-up, the capacitance measured at the first spacer is used instead together with its absolute position with respect to the gate electrodes, reported in the table.

Based on Fig. 3.1, the total length of the edge contact of the liquid with the electrodes is $L = 2\pi(r_0 + r_1)$ and the cross-sectional area is $A = \pi(r_1^2 - r_0^2)$. The capillary capacitance is then expected to be

$$C_{\text{cap}} = h_{\text{cap}} \cdot dC/dz_{\text{LLM}} = \frac{2 \cos(\theta) \gamma_{\text{LXe}}}{g \rho_{\text{LXe}} (r_0 + r_1)} \cdot dC/dz_{\text{LLM}} \simeq 0.043 \text{ pF}, \quad (3.7)$$

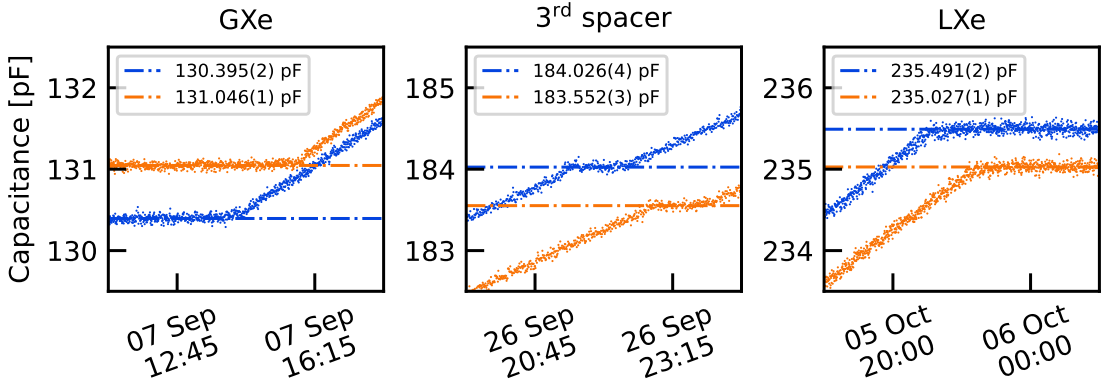


Figure 3.9 Subset of calibration points for the LLMs. A clear change in the relative difference between LLM1 (blue) and LLM2 (orange) can be observed between the empty levelmeters (GXe) and the 3rd spacer: this is attributed to a stray capacitance induced by the first LXePUR tests. No sudden capillary rise is evident as the liquid reaches the bottom of the level meters.

	$(dC/dz)_{LLM1}$ [pF/mm]	$(dC/dz)_{LLM2}$ [pF/mm]
1 - GXe	-	-
2 - 1	0.0690 ± 0.0003	0.0690 ± 0.0003
3 - 2	0.0677 ± 0.0003	0.0692 ± 0.0003
4 - 3	0.0687 ± 0.0003	0.0690 ± 0.0003
5 - 4	0.0679 ± 0.0003	0.0680 ± 0.0003
LXe - 5	0.0704 ± 0.0003	0.0702 ± 0.0003
Avg.	0.0690 ± 0.0001	0.0691 ± 0.0001
C_1 [pF]	149.569 ± 0.003	149.001 ± 0.001
h_{off} [mm]	-1313 ± 2	-1313 ± 2

Table 3.2 Calibration values for the LLMs between the different spacers (numbered from 1 to 5). The average of these values allows the conversion of the capacitance measurement into absolute liquid level position. The measurement between the completely empty sensor and the first spacer is discarded because of the stray capacitance induced during the first LXePUR test. For this reason C_{GXe} of Eq. (3.5) is replaced with C_1 and the offset h_{off} is the position of the first spacer with respect to the gate.

assuming a contact angle $\cos(\theta) = 1$ and $\rho_{LXe} = 2890 \text{ kg/m}^3$. This value is too small to be observed in real data due to the low resolution of the LLMs to fast variations of the liquid xenon level.

Calibration of the medium level meters

The MLMs are calibrated in the same way as the LLMs, with the difference that due to their position it was impossible to completely submerge them in liquid xenon. Additionally, when the liquid xenon reached the bottom of the diving bell, its overpressure decoupled the outer and inner liquid level, rendering the filling of the volume outside the bell less regular. For this reason only the first spacer is used to determine the conversion factor, as it is located 8 mm below the bottom of the bell: the MLMs response to the filling is shown in Fig. 3.10. The conversion factors for the two MLMs along with the other parameters for their calibrations are shown in Tab. 3.3.

The value of the capillary capacitance C_{cap} , measured thanks to the better resolution of the MLMs compared to the LLMs, is of particular interest as it is in disagreement with liquid nitrogen tests performed in Freiburg. These tests showed a good agreement between the expected capillary rise and the observed one assuming complete wetting, i.e., contact

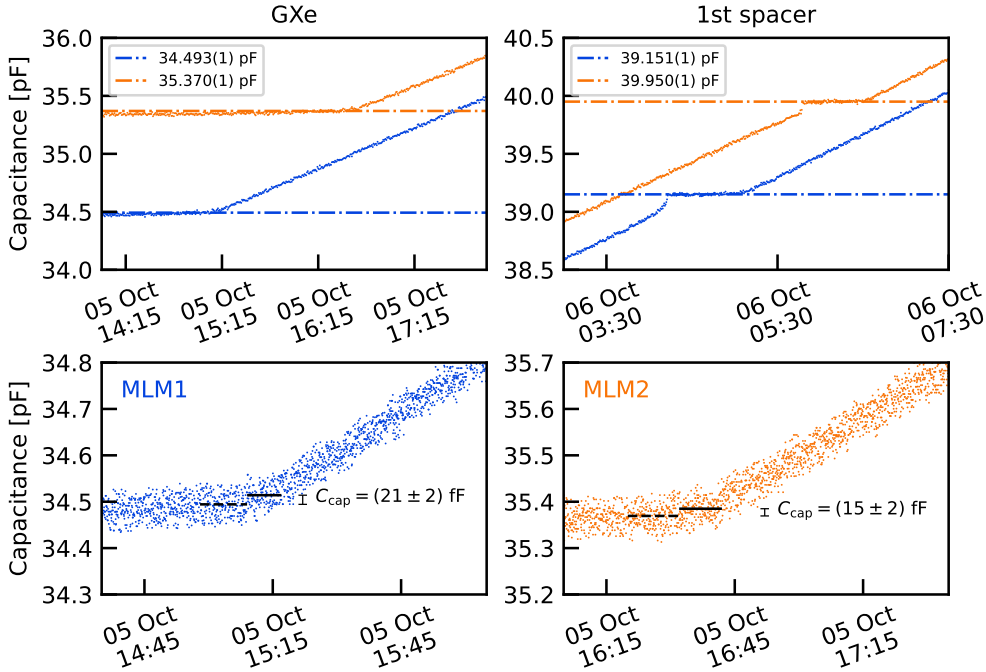


Figure 3.10 (top) Calibration points for the MLMs. Only the first spacer is used to determine the conversion factor dC/dz , as explained in the text. **(bottom)** Measurement of the capillary capacitance as the difference between the empty sensor measurement (dashed line) and the capillary increase (solid line). The obtained value is about 30 % than the expected one, suggesting a $\sim 70^\circ$ contact angle for the liquid xenon with stainless steel.

	MLM1	MLM2
dC/dz [pF/mm]	0.0761 ± 0.0012	0.0749 ± 0.0013
C_{GXe} [pF]	34.493 ± 0.002	35.370 ± 0.002
C_{cap} [fF]	21 ± 2	15 ± 2
h_{off} [mm]	-96 ± 1	-96 ± 1

Table 3.3 Calibration values for the MLMs.

angle $\theta = 0$. Following what done for the LLMs in Eq. (3.7), the expected capacitance increase for the MLMs is 85 fF, while the observed ones are (21 ± 2) fF for MLM1 and (15 ± 2) fF for MLM2, as measured in Fig. 3.10 (bottom). This suggests a contact angle $\theta \simeq 70^\circ$, in disagreement with the general accepted assumption that the liquid xenon completely wets metal surfaces such as stainless steel, even though no measured values could be found in literature. The possible effect due to a detector tilt angle φ with respect

to the liquid level enters in Eq. (3.7) as a factor $1/\cos(\varphi)$ [212]. From the angle $\varphi = 0.2^\circ$ determined in Sec. 3.5, this corresponds to a relative correction of the expected capacitance of 10^{-5} , clearly excluding detector tilt as source of this discrepancy.

The z overlap between MLMs and LLMs is expected to be 32.5 mm for each pair sharing a pipe guide, as shown in Fig. 3.7c. Using the conversion factors determined above, a good agreement between the liquid level measured by medium and long level meters is obtained and it is shown in Fig. 3.11. The total length of the overlap is measured to be (29 ± 2) mm, in agreement with the prediction. The uncertainties are driven by the tolerance in the positioning of the LLM (2 mm) and MLM (1 mm), as shown in the corresponding calibration tables.

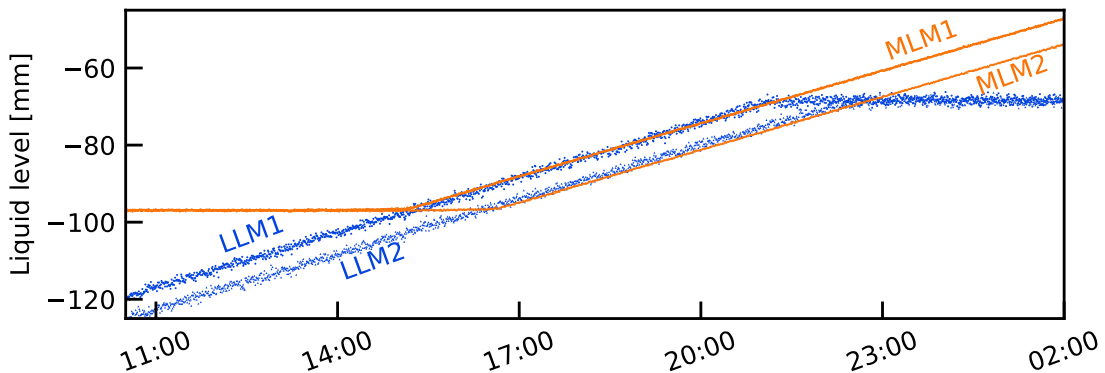


Figure 3.11 Overlap region of long and medium level meters after calibration, showing a good match between each pair. The difference between $L/\text{MLM}1$ and $L/\text{MLM}2$ is due to the shift tilt of the detector discussed in Sec. 3.5.

Calibration of short level meters

The small height of the SLMs does not require the use of spacers for calibrations, as it is possible to cover them completely with liquid xenon during filling within hours. Unlike long and medium level meters, the small distance between the electrodes of the SLMs leads to a large capillary rise. When plugged in Eq. (3.6), the cross-sectional area $A = 2dh$ and the edge interface length $L = 4(d + h)$ give

$$h_{\text{cap}} = \frac{2(d + h) \cos(\theta) \gamma_{\text{LXe}}}{dh g \rho_{\text{LXe}}} \stackrel{d \ll h}{\approx} \frac{2 \cos(\theta) \gamma_{\text{LXe}}}{dg \rho_{\text{LXe}}} = 1.3 \text{ mm}, \quad (3.8)$$

where $d = 1\text{ mm}$ is the distance between the copper plates, $h = 53\text{ mm}$ is the length of the active area (see Fig. 3.2) and the contact angle is assumed to be $\theta = 0$. This corresponds to an expected capillary capacitance of $C_{\text{cap}} = 1066\text{ fF}$. The calibration results are shown in Tab. 3.4 below.

	SLM1	SLM2	SLM4
dC/dz [pF/mm]	0.822 ± 0.008	0.806 ± 0.008	0.828 ± 0.008
C_{GXe} [pF]	12.967 ± 0.001	12.753 ± 0.001	13.031 ± 0.001
C_{cap} [pF]	0.354 ± 0.006	0.266 ± 0.006	0.348 ± 0.006
h_{off} [mm]	-0.7 ± 0.2	-0.7 ± 0.2	-0.7 ± 0.2

Table 3.4 Calibration values for the SLMs. The connection to SLM3 was lost while lifting the TPC in the top dome of the inner vessel. The nature of the different capillary capacitance of SLM2 with respect to the other sensors is still under investigation.

The capacitance evolution of SLM1 during filling is shown in Fig. 3.12, where the other short level meters are omitted as they behave in the same way. Despite the constant liquid xenon filling rate, the capacitance evolution is not entirely linear and it is possible to distinguish six different behaviours, explained in terms of temperature and surface tension effects. Initially the liquid level is rising below the SLM ([a]), therefore no change in capacitance is measured. As the liquid level touches the case of the sensor ([b]), the high thermal conductivity of the copper quickly brings the entire sensor to liquid xenon temperature. This leads to a small increase of the capacitance, possibly due to the combined effect of thermal shrinkage and an increase of the gaseous xenon dielectric constant. A total of 30 minutes passes between this small increase and the capillary rise. This agrees with the 2.5 mm distance of the SLM electrodes from the bottom of the case, when considering that the 10 mm electrode plates were covered by liquid in about two hours (from 11:30 to 13:30 in Fig. 3.12). The SLM capillary rise of [c] is on average $C_{\text{cap}} = (323 \pm 3)\text{ fF}$, again in disagreement with the expected 1066 fF. As it was the case for the MLM capillary rise, also in this case a contact angle $\theta \simeq 70^\circ$ better fits the observation. Tests performed in liquid nitrogen suggested a contact angle of $\sim 50^\circ$, but the coarse nature of these tests did not allow us to draw trustworthy conclusions. Assuming a 70° contact angle, the capillary rise is expected to be $h_{\text{cap}} = 0.44\text{ mm}$ with an additional concave meniscus of height $h_{\text{cap}}^{\text{m}} = 0.08\text{ mm}$, assuming a hemispherical surface of the meniscus. After the prompt rise due to the capillary action, the liquid level rises ([d]) following the filling rate of the detector. When the liquid level is $h_{\text{cap}}^{\text{m}} + h_{\text{cap}}$ or less below the top of the electrode plates, the surface tension of the liquid xenon will prevent it to overflow, almost stalling the

capacitance change ([e]). The small observed change can be attributed to a minimal tilting of the sensor and to the gradual flattening of the meniscus, which should translate in a capacitance increase of 23 fF, against an observed increase of ~ 150 fF. Considering the filling rate and the duration of this slow rise of about eight minutes, the liquid level is inferred to have increased of about 0.67 mm, in agreement with the expected capillary rise for the contact angle $\sim 70^\circ$ of about 0.52 mm. After the liquid xenon is completely covering the electrode plates of the sensor ([f]), the liquid-gas interface still has an impact on the electric field configuration inside the SLM, changing its capacitance until stable conditions.

During the filling of the SLMs, the three sensors showed a coherent common fluctuation with a period of approximately two minutes. This coherence is clear from Fig. 3.13, where a rolling average in two minute wide windows is subtracted from the measurement of the short level meters. The fluctuation is also evident in the right inset of Fig. 3.12, as it

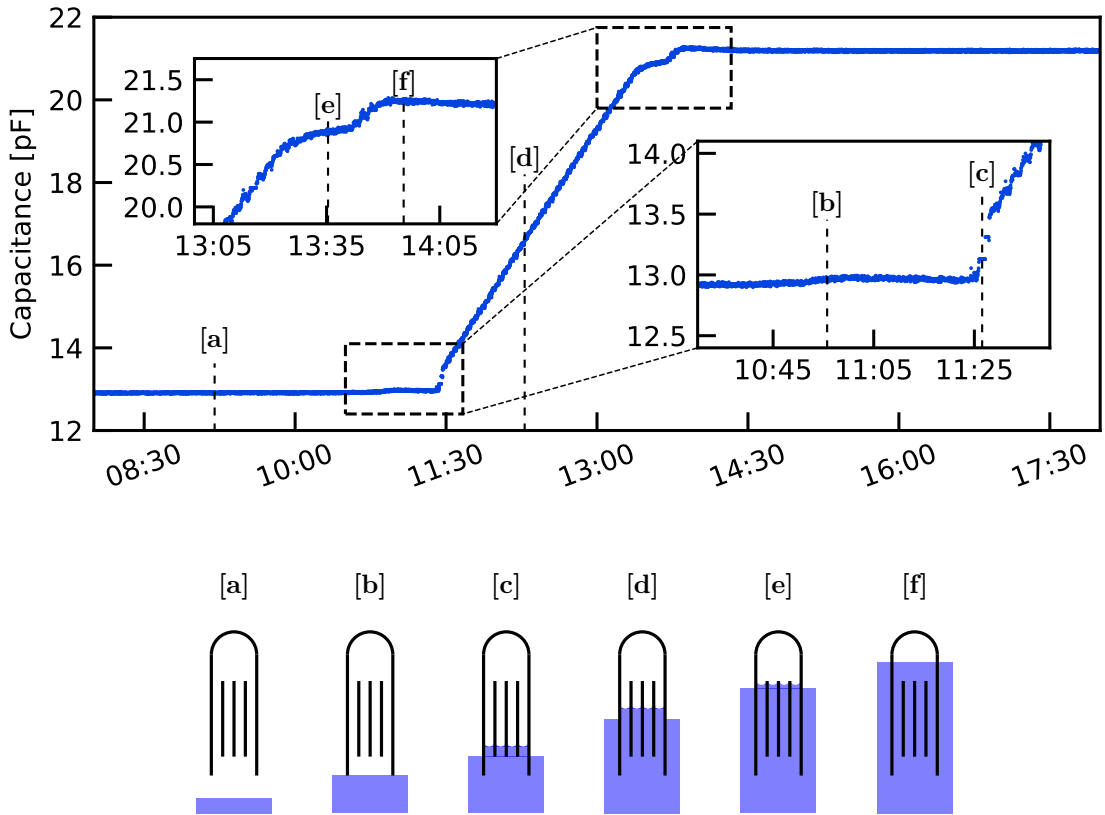


Figure 3.12 Capacitance evolution of SLM1 while filling (top) and proposed explanation for the observed features (bottom). The full description is given in the text.

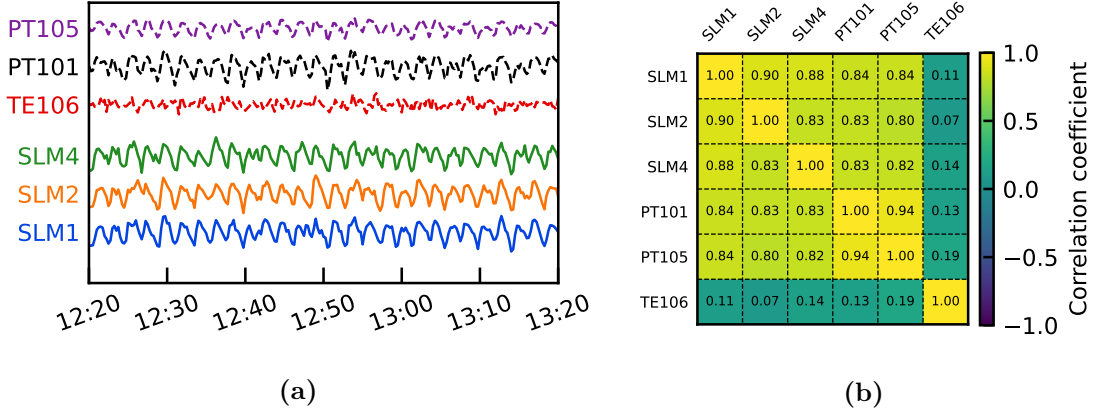


Figure 3.13 (a) SLMs readings and other SC parameters during filling. The SLM values are shown subtracting a two minutes wide rolling average from the measurements. The pressure inside (PT105) and outside (PT101) the diving bell are strongly correlated to the liquid level fluctuations. The temperature of the gaseous xenon inside the bell (TE106) does not show any fluctuation. This is shown also by the correlation matrix shown in (b)

affected the determination of the capillary rise. This can be correlated with other slow control parameters, such as the pressure of the gaseous xenon in the inner cryostat (PT101) and its pressure inside the diving bell (PT105). The relative fluctuations as well as the correlation matrix heat map is shown in Fig. 3.13. The liquid level fluctuation is driven by the change in pressure of the system, too fast for the gas to reach thermal equilibrium, hence not registered as a temperature variation (TE106).

3.5 | Detector leveling

The level meters are positioned in opposite locations of the TPC. This allows not only a local measurement of the liquid level, but also a global evaluation of the tilting of the detector. Since a minimum of three points is required to define the liquid xenon plane, a precise measurement of the tilt of the detector is possible using the short level meters. No additional information can be drawn from the medium level meters, as the liquid levels inside and outside the diving bell are decoupled. Considering a liquid-gas interface plane defined by the equation $p_0x + p_1y + p_2 = z$, the parameters p_i can be estimated by solving

the system of linear equations:

$$\begin{pmatrix} x_{\text{SLM1}} & y_{\text{SLM1}} & 1 \\ x_{\text{SLM2}} & y_{\text{SLM2}} & 1 \\ x_{\text{SLM4}} & y_{\text{SLM4}} & 1 \end{pmatrix} \begin{pmatrix} p_0 \\ p_1 \\ p_2 \end{pmatrix} = \begin{pmatrix} h_{\text{SLM1}} \\ h_{\text{SLM2}} \\ h_{\text{SLM4}} \end{pmatrix}. \quad (3.9)$$

From this solution, the normal vector to the liquid plane is

$$\hat{n} = (-p_0, -p_1, 1) / \sqrt{p_0^2 + p_1^2 + 1}, \quad (3.10)$$

where the position of the level meters and the coordinate system definition are shown in Fig. 3.14, with positive z direction pointing towards the top PMT array. From this vector, it is possible to obtain the tilting angle with respect to the z -axis, $\varphi = \arccos(\hat{n} \cdot \hat{z})$, and use this information to level the detector. The leveling is possible thanks to three fixing rods used to suspend the outer cryostat in the water tank. They are mounted using two different type of adjustment nuts: a coarser kind (2 mm/turn) and a finer one (1/6 mm/turn).

A clear tilt of the TPC and its improvement after leveling is observed in Fig. 3.15, showing the evolution of the SLMs during the two days when the detector was leveled. The

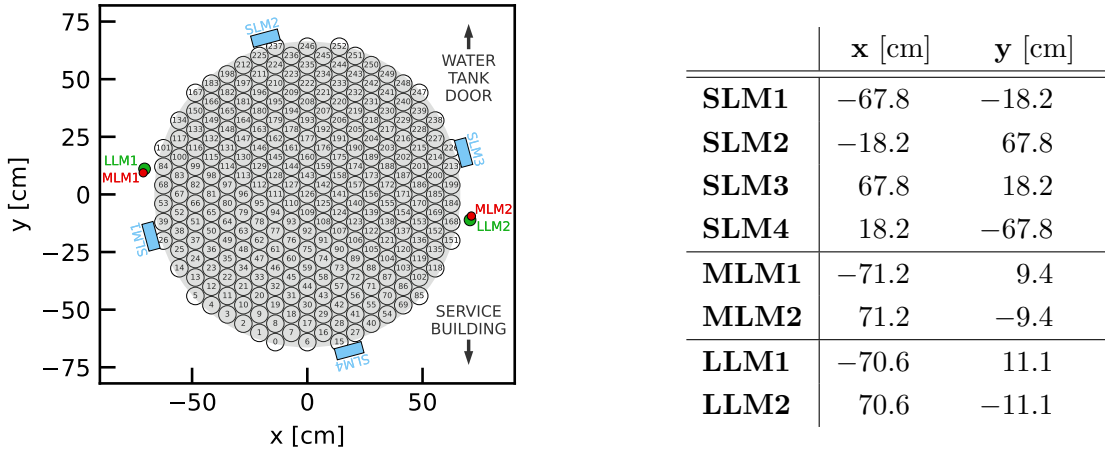


Figure 3.14 Positions of the XENONnT level meters with respect to the top PMT array (view from above). The coordinate system is defined by a positive ordinate towards the water tank door and a positive z directed towards the top array, following the right-hand rule. The gray area indicates the cross-section of the active liquid xenon target and each circle represents a PMT of the top array, with its corresponding channel number.

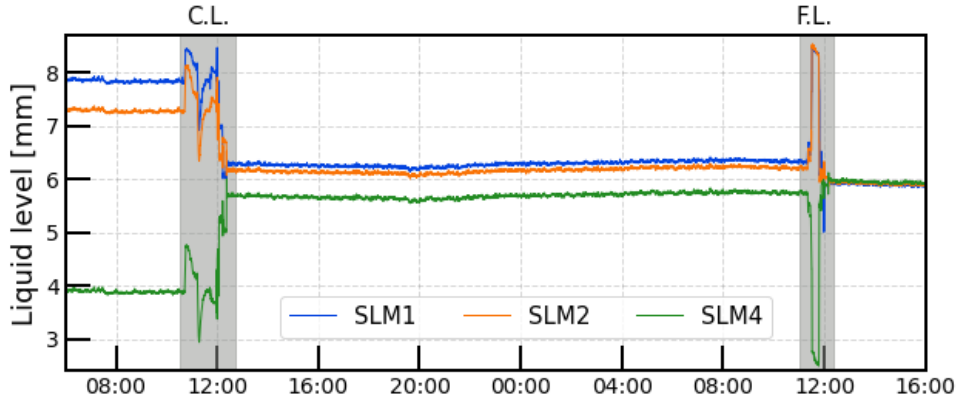


Figure 3.15 SLM readings during the detector leveling operations. A first coarse leveling (C.L.) reduced the maximum observed difference between the short level meters from 4 mm to below 1 mm. The following finer leveling (F.L.) reduced this difference to $>50 \mu\text{m}$, less than the sensor precision.

initially observed tilt was $\varphi_0 = (0.230 \pm 0.018)^\circ$. Such inclination is in good agreement with the position discrepancy observed by LLMs and MLMs: (5 ± 3) mm and (6.6 ± 1.6) mm, respectively, as shown in Fig. 3.11. The large errors come from the positioning and machining uncertainties of each level meter. When considering the initially measured liquid level plane defined by the SLMs, the expected difference is (5.63 ± 0.01) mm both for long and medium level meters, as their radial position is almost the same. A first rough leveling indicated in Fig. 3.15 as C.L. (coarse leveling) is done using the coarse adjustment nuts. After this first operation, the TPC tilting angle decreased to $\varphi_1 = (0.041 \pm 0.017)^\circ$. The finer leveling (F.L.) was completed the following day, reaching a final angle $\varphi_2 = (0.021 \pm 0.012)^\circ$. Under this final configuration the normal vector agrees with \hat{z} within its uncertainty and no further optimization is possible using the information coming only from the SLMs. An additional “ultra” fine leveling is possible using the proportional scintillation S2 signals coming from single electrons (SEs) extracted in the gaseous phase, as discussed in [8]. The total number of detected photoelectrons per electron (SE gain) and the spread of their time distribution (SE width) linearly depend on the gas gap size, allowing for the reconstruction of a residual tilt angle. The mapping of the SE gain and width in the (x, y) space did not return any compelling reason to execute an additional fine leveling, hence no further operation was carried out.

Chapter 4

The XENONnT TPC field cage and field simulations

The electric field in the TPC active region plays a key role in the generation of the light and charge signals, as it affects the recombination probability on which the signal yields depend. Since the discrimination between the WIMP-like nuclear recoils (NR) and the background electronic recoils (ER) relies on the S2/S1 ratio, large fluctuations of charge and light yield worsen the discrimination power. Similarly, a distortion of the electric field lines could push liberated charges onto the detector walls, leading to insensitivity to charge signal in a region of the TPC. Hence, the design of the field cage of the XENONnT detector is crucial for the sensitivity of the experiment to WIMP interactions. Its geometry and the voltage divider connecting its elements, known as *resistive chain*, were designed to maximize the homogeneity of the drift field inside the active volume. The optimization of these components was done by simulating the electric field using the finite element method (FEM) software COMSOL Multiphysics® [4].

The design of the XENONnT field cage is described in Sec. 4.1, while its implementation in COMSOL is detailed in Sec. 4.2. The FEM solver used by COMSOL is briefly introduced, together with the custom-developed module PyCOMes for particle tracking. The main sources of systematic uncertainties for the COMSOL simulations are quantified to about 1 % in the active volume, as described in Sec. 4.2.2. The optimization of the design drift field is presented in Sec. 4.3, where the optimal configuration of the resistive chain is identified. This is done by evaluating the field spread and the fraction of the volume where the electrons are lost by being pushed against the wall. This is repeated for different electrode voltage arrangements to test the resilience of the final configuration. In Sec. 4.4, the software PyCOMes is used to produce (r, z) maps of the active volume for the drift

speed and different diffusion coefficients, which are important inputs to the Monte Carlo framework of XENONnT.

4.1 | Field cage

The field cage is one of the main components of the XENONnT TPC, as it encloses and defines the active volume, while providing mechanical stability and field homogeneity. It can be divided into three main components with different purposes: the PTFE reflectors optically isolate the active volume, the field shaping electrodes give structural stability to the TPC and establish the field homogeneity, and the resistive chain sets the potential of each electrode of the field cage. The group of the University of Freiburg was the main responsible for the field cage design and production, as well as for the realization of the resistive chain. It also played an important role in the design of the PTFE reflectors.

Reflectors and pillars

The active region of the TPC is laterally encased by 48 PTFE reflective panels (or reflectors) mounted on 24 PTFE pillars, forming an irregular 48-sided polygon-based prism with an inscribed diameter of 132.8 cm, as shown in Fig. 2.16. These walls optically decouple the active volume from the outer uninstrumented liquid xenon “skin”. This avoids light leakage and the corresponding signal loss, but also prevents light leaking into the active volume from the outer skin. In this case the leaking photons induce low area “lone S1” signals which, if paired by chance with an equivalent “lone S2”, could mimic a fake low energy event. These events contribute to a background known as *accidental coincidence*, important for nuclear recoil searches such as WIMP or coherent elastic neutrino-nucleus scattering (CE ν NS) [102]. The panels’ side facing the active volume is diamond-polished to maximize the specular reflectivity of the vacuum ultraviolet (VUV) photons coming from xenon scintillation [161, 213]. The reflective panels are divided into two types and their arrangement is shown as sectional view in Fig. 4.1. A total of 24 narrower panels, the *blocking reflectors*, are slid along the pillars, thanks to a T-slot groove along their length. They are 4.8 cm wide and 1.5 m long, while their thickness varies from 6 mm at the center to about 1 mm at the edges. They are interleaved along the circumference of the active volume with other 24 panels, the *sliding reflectors*. These have the same height, but are 14.9 cm wide and 3 mm thick. The thickness of these panels was reduced with respect

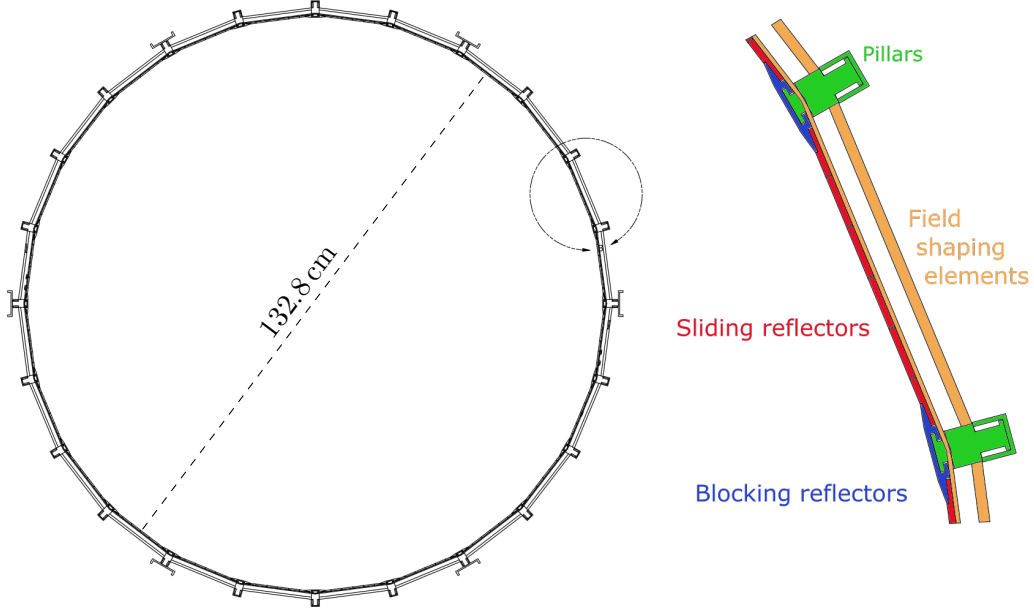


Figure 4.1 (left) Cross section of the XENONnT field cage. **(right)** Detail of a section of the field cage showing the two field shaping elements (orange), the pillars with covers (green) and the sliding (red) and blocking reflectors (blue).

to the 5 mm of XENON1T to minimize the material background, as PTFE is one of the main source of radiogenic neutrons [214]. The 3 mm thickness ensures <1% photon transmittance through the walls, minimizing the signal loss [215]. The different panels overlap a few millimeters along the full height of the TPC. This interlocking mechanism avoids any light leak while accounting for the 1.4% thermal shrinkage of PTFE. The 24 pillars supporting the reflectors are connected at the top to a copper frame known as “copper ring”, which is in turn connected to the diving bell, discussed in Sec. 2.4. The copper ring is visible in Fig. 2.16 right below the gate electrode. The bottom of the pillars is connected to another copper frame hosting the PMTs of the bottom array.

Both the sliding reflectors and the pillars are designed to accommodate the field shaping elements, as shown in Fig. 4.2. On the side facing the cryostat, the pillars show a comb structure with 64 grooves 15.25 mm wide and a 22 mm pitch (**III** in Fig. 4.2). The outer field shaping elements of the field cage are placed inside these grooves and they are

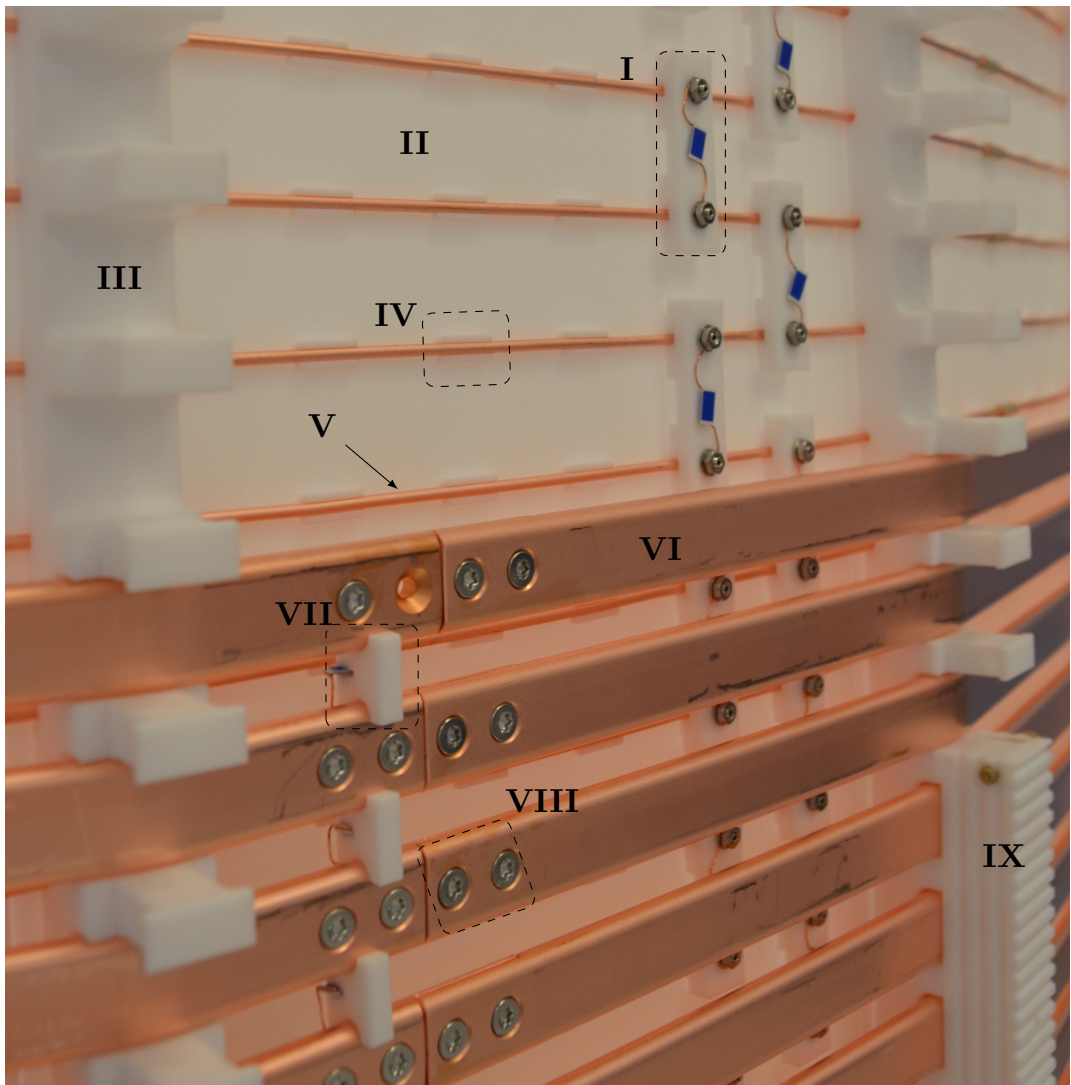


Figure 4.2 The XENONnT field cage viewed from the outside during assembly in the clean room. The different elements are: the field shaping rings (**V**) clipped in the notches (**IV**) on the panels (**II**), connected via the resistive chain (**I**). The guards (**VI**) and their resistive chain (**VII**) mounted next to the junction (**VIII**) are also visible. The pillars (**III**) are still open as this picture was taken during assembly, while during nominal operation covers (**IX**) are installed to fix the guards.

held in place by a cover fixed via a Torlon® bolted joint (**IX**). The pillar side facing the active volume is covered by the blocking reflectors and it features a total of 71 circular notches with radius 1.1 mm. Similarly, the sliding pillars (**II**) have extruded tabs featuring a dovetail groove (**IV**), positioned in rows of five and aligned to the 71 notches of the pillars. These are used to install the inner field shaping elements of the field cage, as described in the following.

Field cage

The field cage consists of two nested arrays of oxygen-free high thermal conductivity copper (OFHC, 99.99 % Cu) ring electrodes enclosing the PTFE panels along the entire length of the TPC. The double array nature of the field cage was motivated by the observation of a time-dependent radial distortion during the operation of XENON1T [5, 216]. The position distribution of the events coming from the homogeneously distributed source ^{83m}Kr presented a stronger inward push farther away from the pillars than closer, as shown in Fig. 4.3. This distortion was explained as an effect of a different charge accumulation on pillars and panels, the first in direct contact with the field shaping copper electrodes. The XENON1T field cage consisted of circular electrodes (“guards”) placed on notches along the pillars. These represented the only contact points between the copper and the PTFE of the icositetragonally⁽¹⁾ arranged walls. Where the copper touches the reflectors

⁽¹⁾An *icositetragon* is a 24-sided regular polygon.

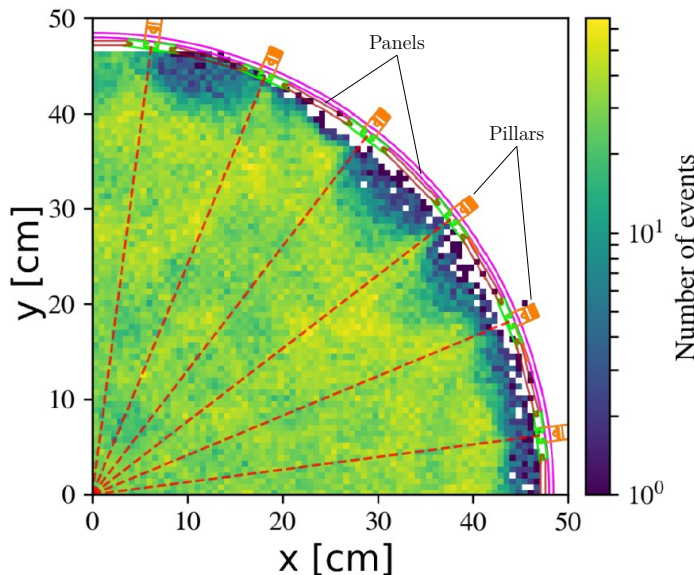


Figure 4.3 Event position distribution in the (x, y) space from a ^{83m}Kr calibration run of XENON1T. It shows a larger radial inward push around the panels than close to the pillars (radial position as red dashed line). Plot from [216].

the electrons were removed more efficiently as they could be collected by the metal, while no removal mechanism was available for the electrons collected on the PTFE far from it. Based on this observation, the XENONnT field cage was designed to maximize the direct contact between the copper and the PTFE reflectors. A straightforward solution was to replicate XENON1T design by machining icositetragonal rings. As metallic surfaces are equipotential surfaces, the large cross section of the XENON1T guards would have resulted into a deviation of the potential drop from its ideal linearity over z , especially close to the TPC walls. Reducing the size of the field shaping elements while increasing their number mimics a linear potential drop better and improves the field homogeneity. However, it is not mechanically reliable. For this reason a double array solution was chosen for XENONnT, combining the mechanical stability of more massive elements with the field homogeneity of smaller ones, while having an extended and well-defined contact between copper and PTFE.

The inner array consists of 71 “wires” with a 2 mm diameter (**V** in Fig. 4.2), machined from a single OFHC copper spool. They are usually referred to as *field shaping rings*, or simply “rings”. They are clipped inside the dovetail-shaped tabs of the sliding reflectors (**IV**): this ensures the contact between copper and reflectors. Tiny through-holes of 250 μm diameter were punched along the surface of the sliding panels in correspondence with these grooves, providing a direct line of sight between copper and liquid xenon active volume. Since the mobility of the electrons is larger along the PTFE surface than through its bulk, electrons reaching the PTFE walls can be collected faster by drifting them towards the copper rings moving through the charge-collecting holes. The rings are machined by first stretching the copper wire around an icositetragonal mock-up of 133.1 cm inner diameter. The wire is then cut to the right length and each end threaded with opposite handedness. During installation the ends are connected using PEEK fasteners, shown in Fig. 4.4a. The different handedness of the two edges allows adjusting the length of the ring during assembly by rotating the fastener. The material of the fastener was chosen to be PEEK after dedicated electrostatic field simulations using COMSOL Multiphysics[®] v5.4 [4]: the three-dimensional junction of the ring ends was simulated both for a plastic and copper fastener. The PEEK connection, electrostatically almost equivalent to a gap between the two edges, was favored as it induces less local field distortion. Assuming $z = 0$ to be the position of the electrode gate wires, the top ring is positioned at $z = -2.3$ cm and the bottom at $z = -148.6$ cm. The top four rings and the bottom three have a distance of 1.1 cm, while the rest of the array has a spacing of 2.2 cm. The denser distribution at the top and bottom of the field cage was driven by field simulations as it was shown to reduce

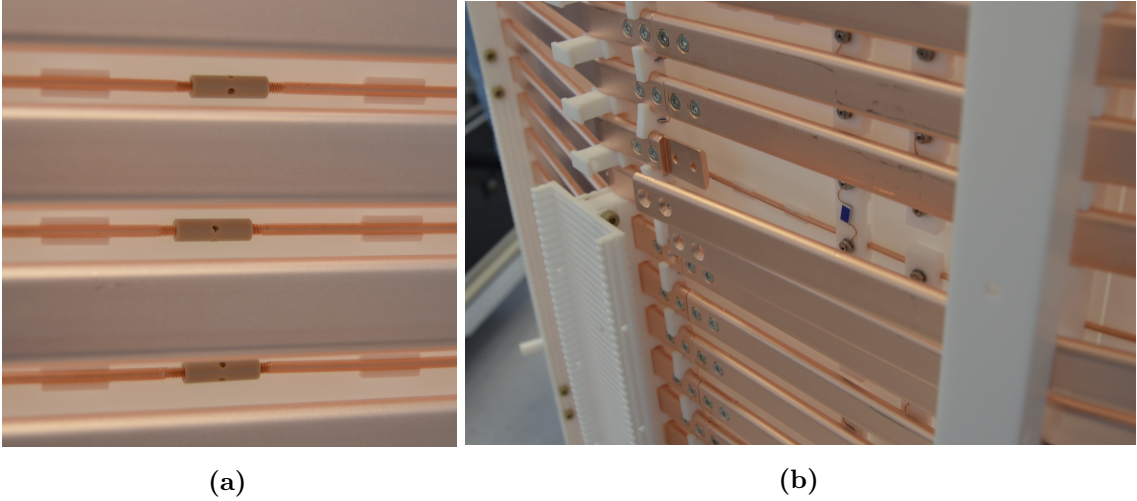


Figure 4.4 (a) PEEK fasteners to join the field shaping rings installed behind the field shaping guards. The small through-hole is used to rotate and fasten the connector. (b) Guards connection opened to access the rings’ voltage divider. The half field shaping guard bent outwards can be taken out entirely or simply moved, as in the picture.

the field leakage from the outside, improving the field homogeneity.

The outer field cage array consists of 64 massive copper beams with a cross section of $15\text{ mm} \times 5\text{ mm}$ and a 2.5 mm rounding radius (**VI** of Fig. 4.2). They are referred to as *field shaping guards*, or “guards”. They are shaped into an icositetragon with an inscribed diameter of 135.5 cm . This shape was favored over the circular one of XENON1T to keep the radial distance between the inner and the outer array of field shaping electrodes constant. Each guard consists of two halves connected by four countersunk M3 stainless steel (SS) bolts, two at each end (**VIII**). For each full guard, one half features two additional countersunk holes close to the junction. They are used to mount the voltage dividers. After TPC assembly, the guards’ halves hosting the resistive chains cannot be removed without disassembling the resistors. For this reason the resistive chains connecting the rings are placed behind the other halves which can be easily removed as shown in Fig. 4.4b. The guards are positioned between $z = -8\text{ cm}$ and $z = -145\text{ cm}$ in z and are staggered with respect to the inner rings. Their positioning along the TPC is mainly defined by the mechanical stability of the PTFE pillars as they support the guards. The radial position is constrained by the risk of discharges. Indeed, a large radius reduces the distance of the guards to the grounded inner cryostat and the cathode high voltage feedthrough (HVFT), increasing the local electric fields. The most critical region is between the guards and

grounded SS sleeve enclosing the top half of the HVFT, where the electric field is the highest. A three-dimensional electrostatic simulation was carried out for the region where the SS sleeve ends and the biased SS HVFT core insulated by ultra-high-molecular-weight polyethylene (UHMWPE) sticks out. The simulation is shown in Fig. 4.5a. The field was simulated for different values of the guards' radial position and a safety margin was included considering a HVFT biased to -40 kV , exceeding the design -30 kV . The simulation shows no dependence of the highest electric field on the radial distance between SS sleeve and guards, with the local maximum occurring around 110 kV/cm as in Fig. 4.5c. Since this value drops fast well below the safety limit of 50 kV/cm in the space between the guard and the HVFT, no risk of sparking is anticipated. The safety limit comes from the Paschen law,

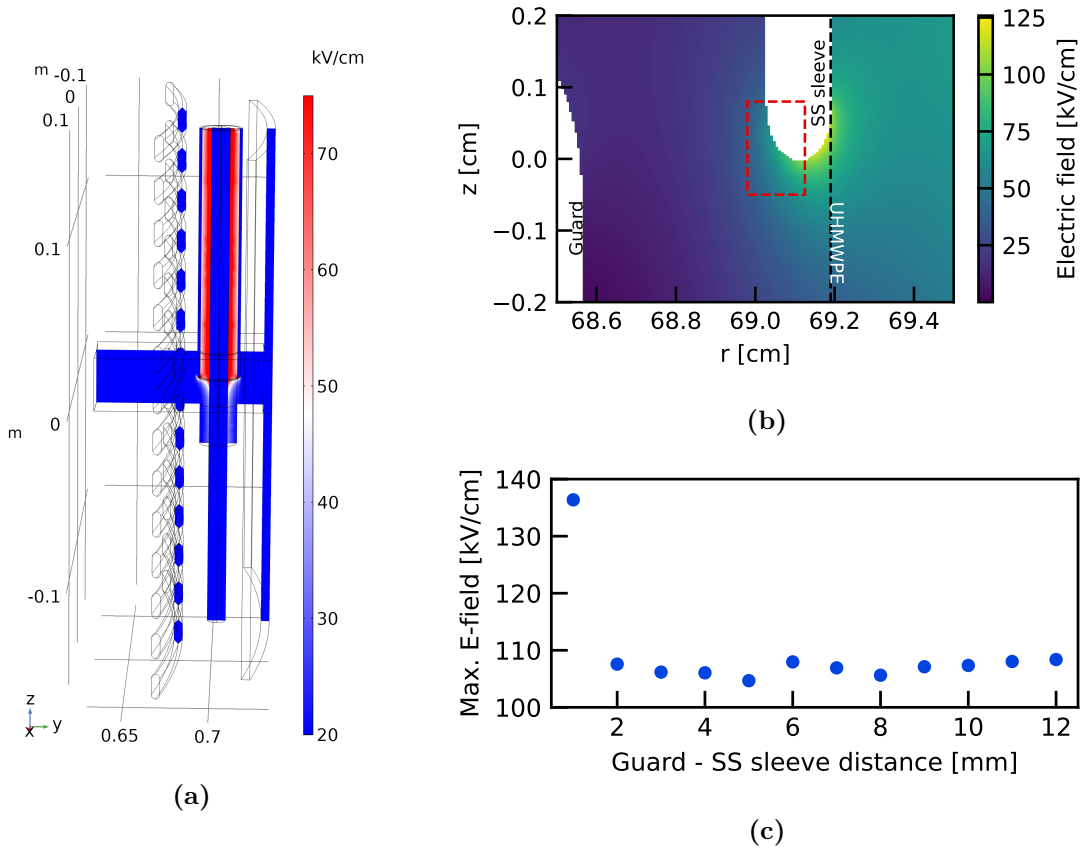


Figure 4.5 (a) Electric field simulation of the high voltage feedthrough (HVFT) between guard electrodes and cryostat from COMSOL Multiphysics. (b) Simulated field on the plane of minimum distance of the HVFT from the guards. The maximum electric field within the red rectangle as a function of the distance of the guard from the HVFT SS sleeve is shown in (c). This field is found to be independent of this distance.

conservatively assuming the medium to be gaseous xenon [217]. A final distance of 9 mm between the outer face of the guards and the HVFT SS sleeve was fixed. This translates into a distance between guards and rings of about 8.7 mm.

Resistive chain

The 2.2 cm vertical pitch of the field shaping electrodes was limited by the need of space to mount the resistive chain. This pitch translates into a narrow gap of 7 mm between the guards, as shown in Fig. 4.2. The resistive chain of the field cage consists of two redundant chains made entirely of $5\text{ G}\Omega$ SMD (Surface Mounted Device) resistors from OHMITE (HVF2512T5007FE [218]) with a 1% tolerance, currently out of production. These are the same resistors as used in XENON1T, hence reliably working in liquid xenon and extensively tested against failure. The high resistance minimizes the total current flowing through the field cage, reducing the heat input to $<3\text{ mW}$, to be compared to the total heat input of $\sim 280\text{ W}$. Where a different resistance along the chain is needed in order to ensure a linear potential drop, a proper combination of the $5\text{ G}\Omega$ resistors is used.

A sketch of the resistive chain is shown in Fig. 4.6, where different resistor colors indicate different resistance values. The chain connects the top ring of the field cage to the cathode. The top ring is independently biased in order to improve the field homogeneity within the active volume, while being flexible to react upon the voltage to face changes in the electrodes' configuration. This is further discussed in Sec. 4.3. The chain splits between inner and outer arrays where the guard array starts and reconnects where it ends, keeping each chain mechanically independent, but electrically coupled. This design is a trade-off between having independent resistive chains for rings and guards and implementing a single chain connecting the two arrays ("zig-zag" chain). The first design has a rather straightforward and practical implementation, but the failure of a single resistor in one of the two chains would lead to an overall offset between the two, strongly affecting the field. The "zig-zag" resistive chain design reduces the impact of a failing resistor as both arrays would be equally affected, but its mechanical implementation is particularly cumbersome. The chosen design is a good combination of the two possibilities, as it ensures a proper coupling of the two arrays while keeping the easy implementation.

The resistive chain is designed to establish a linear potential drop along the field cage as a function of z . This does not include the bottom resistance of the chain R_{bttm} (green in Fig. 4.6); its value is optimized during design to minimize the field leakage coming

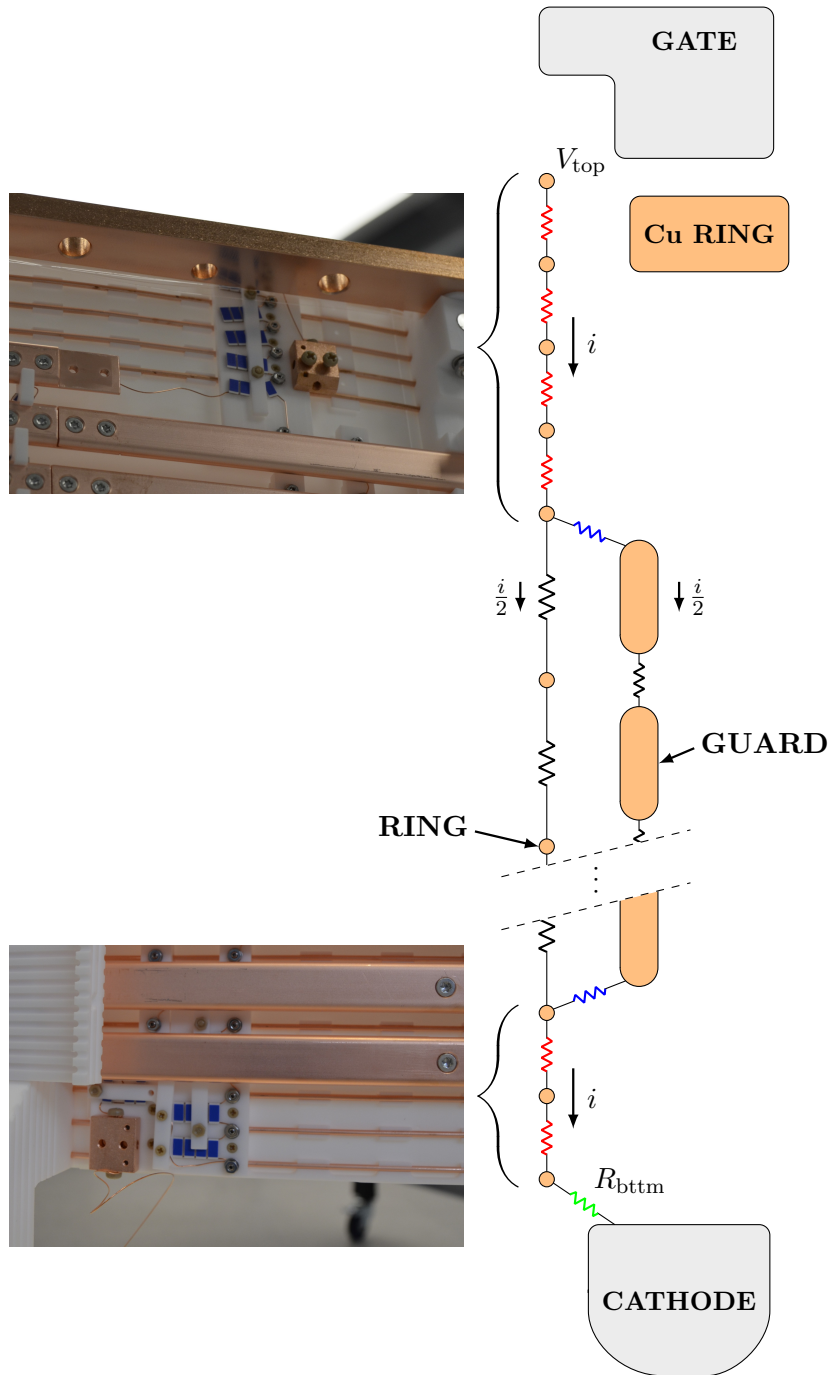


Figure 4.6 Sketch of the voltage divider (or resistive chain) along the field cage. The different color represents different resistance values: black is $5\text{ G}\Omega$, red is $1.25\text{ G}\Omega$ and blue is $2.5\text{ G}\Omega$. This ensures a uniform potential drop per unit length along the field cage, considering the different currents along the chain as indicated. The bottom resistor R_{bttm} (green) is discussed in Sec. 4.3, together with the independent bias voltage V_{top} . The photo insets show the resistive chain implementation at the top and bottom of the field cage.

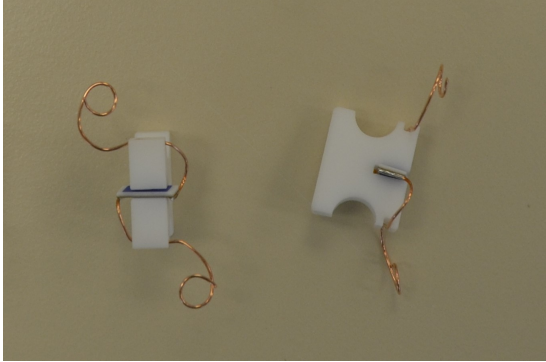


Figure 4.7 PTFE elements supporting the resistors of the guards' resistive chain. The wires are inserted in a small slot at the top and bottom of the PTFE, acting as a strain relief. The resistor's horizontal position has no relevant impact on the local electric field.

from below the cathode and to maximize the field homogeneity. The linear potential drop requires the voltage of a guard to be the average of the voltages of the two neighboring rings. In addition, the resistance between two guards or rings 2.2 cm apart (black) should be $5\text{ G}\Omega$. This minimizes the total number of resistors, beneficial both against failures and for material background reduction. The blue resistors in Fig. 4.6 are half the resistance of the black ones, as the current flowing through them is the same but the z distance is halved. Following a similar reasoning, the current flowing through the red resistors is twice the current floating through the black ones, but the distance is halved. Following Ohm's law, $\Delta V = Ri$, the red resistance is a fourth of the black one. The red and blue resistances are obtained as parallel connections of four and two $5\text{ G}\Omega$ resistors, respectively, as shown in the insets of Fig. 4.6. Considering the two redundant chains being in parallel, the total resistance of the field cage is $(87.25 \pm 0.05)\text{ G}\Omega$: this includes the $R_{\text{bttm}} = 7\text{ G}\Omega$, as fixed in Sec. 4.3, and the 1% tolerance from specifications.

The connections of the resistors between the guards (**VII** of Fig. 4.2) are based on the design of the resistive chain of XENON1T [169]. Two countersunk M3 threaded holes are drilled on each end of the fixed half of the guards, close to the junction. The copper wire connected to the resistor is then sandwiched between the guard and an M3 SS nut, fixed with a SS screw. This ensures a reliable electrical connection. The resistors are soldered to OFHC copper wires of 0.4 mm diameter and are kept in place by 7 mm \times 7 mm PTFE elements, shown in Fig. 4.7. These PTFE elements keep the resistors in the low field region between rings and guards, while providing a strain relief for the copper wire. A similar solution is not possible for the resistive chain of the field shaping rings due to their small diameter. Instead, the rings' resistive chain is realized using a spring loaded connection. The resistors are mounted on a PTFE basis, the *groove clamp*. This piece is flat on the side where the resistor sits and features two dovetail tabs on the other side, with a distance of 2.2 cm (**I**). An example of this assembly is shown in Fig. 4.8a. These features match

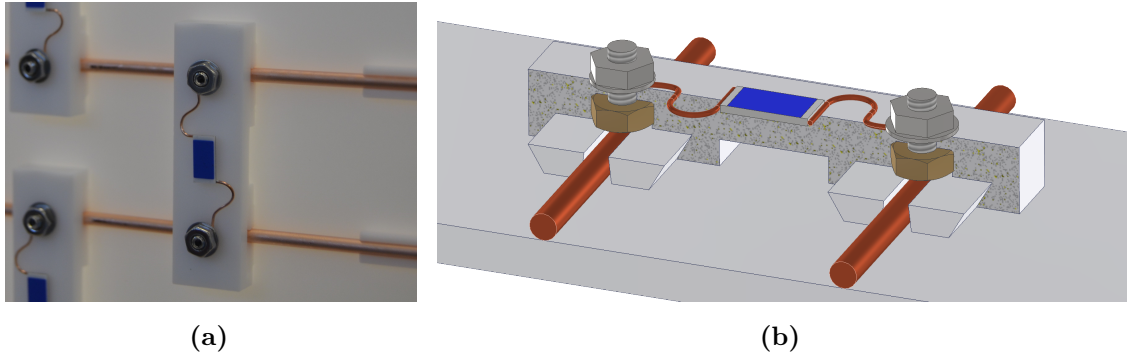


Figure 4.8 (a) *Groove clamp mounted along the field cage and connecting two TPC field shaping rings.* (b) *Section view of the spring-loaded clamping mechanism ensuring electrical connection between the resistor and the field shaping wires via the metallic screws, nuts and washers.*

dovetail tabs present on two special sliding TPC wall panels, designed to host the rings' resistive chain. After sliding the groove clamp on the corresponding dovetail along the panel, it is possible to tighten the set screws. This provides an electric connection using the reaction force of the sliding panel itself. The resistor is electrically connected to the set screws by the soldered copper wire sandwiched between a SS washer+nut system and the groove clamp itself. The set screw is held in place by a PEEK M1.7 nut embedded in a hole on the opposite side of the groove clamp. A cutout of the system is shown in Fig. 4.8b. This design was extensively stress tested in liquid nitrogen, proving a reliable and strong connection. A similar clamping was developed for the bottom and top field shaping rings; they are shown in the insets of Fig. 4.6. These pictures also show the $1\text{ cm} \times 1\text{ cm} \times 0.5\text{ cm}$ copper block used to connect the resistive chain to the HV supply providing V_{top} (top) or to the cathode (bottom).

Prior to assembly, a small mock-up of a part of the field cage was produced to test the mechanical and electrical connection of the resistive chain. It consists of the replica of a single sliding panel between two pillars, but only 18 cm high. It includes the features for the assembly of the rings' resistive chain, including the top and bottom TPC connections. It was also used as a platform to develop the assembly procedures. A picture of the fully assembled mock-up is shown in Fig. 4.9.

During the assembly of the resistive chain of the XENONnT TPC, the single connections were checked using an insulation multimeter able to measure up to $200\text{ G}\Omega$ with 10 % accuracy [219]. The resistance values were measured before and after the TPC was moved

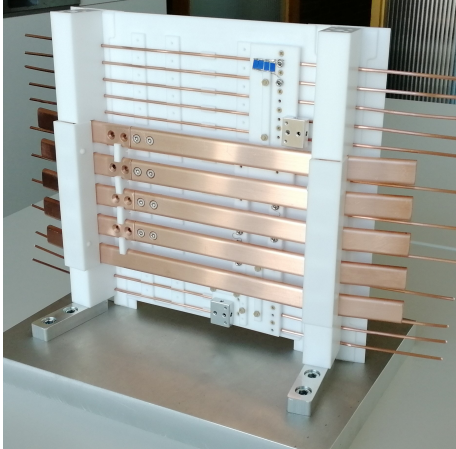


Figure 4.9 Mock-up of the field cage consisting of a 18 cm high sliding panel between two PTFE pillars. It was used to test the mechanical and electrical connection of the field cage, together with the assembly procedures.

underground. No connection was affected by the vibrations from the transportation, proving the reliability of the connection technique. After the cryostat was closed and the vessel evacuated, the resistance of the total field cage was still accessible as the top field shaping ring and the cathode are connected to the outside via the umbilical pipe. The measured value was found to be $(92 \pm 11) \text{ G}\Omega$, in agreement with the expected $(87.25 \pm 0.05) \text{ G}\Omega$. Although the accuracy of this measurement is not enough to identify the failure of single resistors, it can provide information on large scale effects.

All the materials used to machine and assemble the field cage and the resistive chains, as well as the PTFE used for the reflectors and pillars, were screened and selected by means of HPGe spectrometry. The specific activities are reported in Tab. 4.1. While the entire field cage represents less than 2.3 % of the ER background, the PTFE itself contributes to 27.5 % of the NR background [10].

	M_{tot}	^{238}U	^{235}U	^{226}Ra	$^{228}\text{Ra}(^{232}\text{Th})$	^{228}Th	^{40}K	^{60}Co	^{137}Cs
	[kg]	[mBq/kg]							
Guards Cu	170.4	0.03(1)	<0.02	<0.18	0.010(4)	0.18(5)	0.45(14)	0.03(1)	<0.05
Rings Cu	8.5	2.3	-	<0.1	<0.06	<0.04	0.55(2)	0.43(3)	<0.04
Pillars PTFE	50.1	0.26(9)	<0.05	0.04(1)	0.10(2)	<0.04	<0.42	-	<0.01
Panels PTFE	36.2	0.15(7)	<0.08	0.15(3)	0.05(3)	<0.09	4(1)	-	<0.07
	[piece]	[nBq/piece]							
Resistors	312	110(5)	2.3(5)	29(2)	13(2)	15(1)	60(10)	<1.1	<0.6

Table 4.1 Activity measurements for the field cage components from [172]. The largest mass contribution is from the guards, but the high intrinsic purity of copper makes them a minor background source. The resistors are “dirty” components, with a specific activity up to 3 Bq/kg for ^{238}U , but the very small mass renders their impact irrelevant.

4.2 | Electric field simulations

The simulation of the electric drift field is an important tool for the design of the XENONnT TPC, particularly for the development of electrodes and field cage. A two-dimensional axisymmetrical geometry of the TPC was implemented in COMSOL, a finite element method (FEM) software for the numerical solution of a large variety of physics problems. Local three-dimensional simulations were also employed during the design phase to estimate the risk of discharges in regions characterized by high fields. The electric field maps returned by the software are used to estimate the electron propagation within the liquid xenon and the homogeneity of the detector response in terms of light and charge yield. These results are compared to data and validated in Chapter 5. The propagation of electron is simulated using the custom-developed python library PyCOMes, developed to simulate the drift path of electrons within an electric field given as input from COMSOL, while optimizing the computing time.

4.2.1 | COMSOL implementation

The COMSOL Multiphysics[®] software solves a large range of physical problems using the finite element method (FEM) [4]. The FEM discretizes a complex problem in smaller *elements* and yields a precise solution at the points where those elements meet, called *nodes*. The discretization process is also known as *meshing*. The precise solutions are then interpolated and combined to return the numerical result of the initial problem in the entire space. A didactic two-dimensional example of FEM applied to an electrostatic problem is presented in Appendix A. This procedure can be easily extended to three dimensions and it can even include a time evolution. In the following, a two-dimensional axisymmetrical geometry is used: the mathematical framework is identical to the example of Appendix A, with the only difference in the definition of the gradient relationship in Eq. (A.5).

The electric field of XENONnT is simulated using the AC/DC module of COMSOL Multiphysics[®] v5.4 [4,220] on a 32 GB PC with Intel-i7 @ 4.2 GHz and Windows 10 operating system. The geometry of the TPC is implemented as a two-dimensional axisymmetrical (2D-ax) object. This is preferred over a three-dimensional (3D) geometry, as an equally fine-meshed 3D simulation would require $N^{3/2}$ elements, where the 2D-ax geometry requires only N . This means that a 2D-ax geometry meshed using 10^6 elements yields the same precision of a 3D mesh of 10^9 elements, requiring three orders of magnitude more computational power. A moderate use of the computing resources is particularly important during the

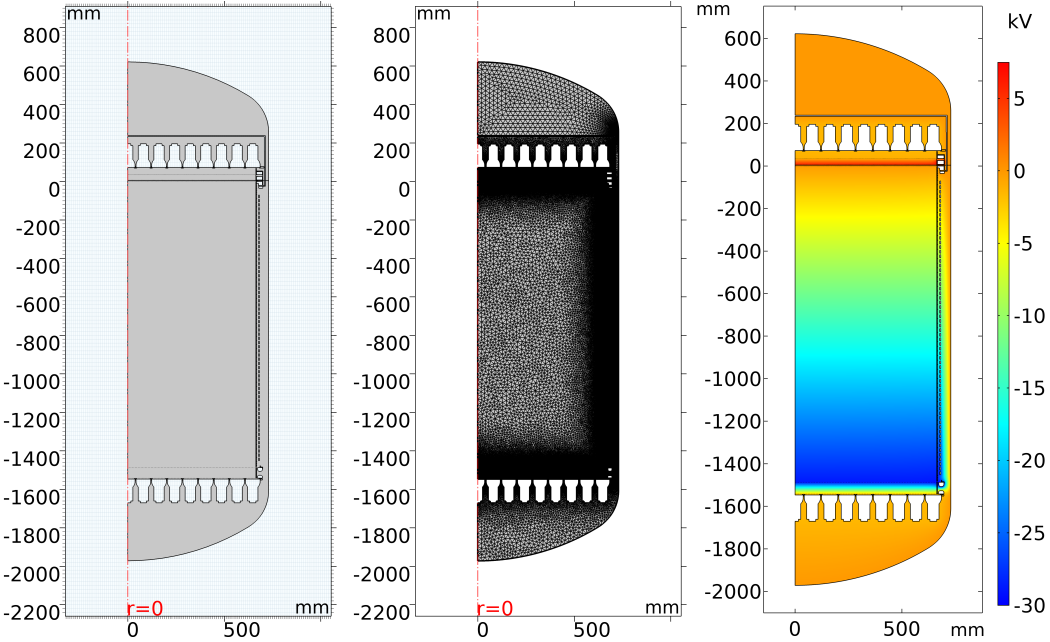


Figure 4.10 Implementation of the XENONnT TPC in COMSOL at different stages of the simulation: geometry (left), meshing (middle) and solution for the design configuration (right). The solution to the electrostatic problem is the distribution of the voltage within the area or volume simulated: the electric field can be retrieved by determining the voltage gradient.

design phase, when the number of simulations is large and results are needed at limited time scales. The implemented geometry reflects the TPC discussed in Sec. 2.4, including the effect of the thermal PTFE shrinkage [221]. The COMSOL geometry, as well as the meshing and the solution for the design configuration are shown in Fig. 4.10. The coordinate system is the one of the GEANT4 Monte Carlo (MC) geometry implementation [113], with $z = 0$ being the position of the bottom of the gate wire electrode. The 2D-ax implementation approximates the icositetragonal shape of the active volume to a cylinder of radius 66.4 cm. It also ignores elements that only cover a small azimuthal angle, like the PTFE pillars, the HVFT to the cathode, the resistive chains or the perpendicular wires, discussed in Chapter 6. These elements were individually studied with dedicated 3D simulations, as shown in Fig. 4.5a for the HVFT and in Fig. 6.10 for the perpendicular wires. The impact of the axisymmetry assumption is discussed in Sec. 4.2.2, together with other systematic effects affecting the electric field simulations.

The dimension of the TPC components spans several orders of magnitude, ranging

from the 216 μm diameter of the electrode wires up to the 1.5 m length of the reflector panels. The elements comprising the FEM mesh vary in the same way in order to properly reproduce the electric field behaviour inside the TPC. The mesh consists of triangular elements with linear dimensions ranging from $\sim 30 \mu\text{m}$ around the electrode wires up to 25 mm in the center of the liquid xenon target. An equilateral triangle is an ideal mesh element as its nodes are equidistant, leading to an optimal geometry for interpolation. A figure of merit for the quality of the mesh is the skewness of the elements [222], defined as

$$s = 1 - \max \left[\frac{\theta_{\max} - 60^\circ}{120^\circ}, \frac{60^\circ - \theta_{\min}}{60^\circ} \right]. \quad (4.1)$$

It represents the angular ratio for the maximum deviation from the ideal case of equilateral triangles, with θ_{\max} and θ_{\min} being the largest and smallest angles within the triangular element. The larger the skewness s , the closer to an equilateral triangle is the considered mesh element. An element is considered of good quality when its skewness $s > 0.5$. A low quality of the meshing elements does not necessarily mean low quality solution, but the solution could be unreliable in their proximity. The overall quality of the mesh implemented for the simulation of XENONnT is very high, with an average skewness of 0.83 and $< 0.2\%$ of the geometry elements having $s < 0.5$. These outliers have a completely negligible impact on the final electric field solution. The skewness distribution is shown in Fig. 4.11. The final mesh consists of about 4.8×10^6 elements and 2.4×10^6 nodes.

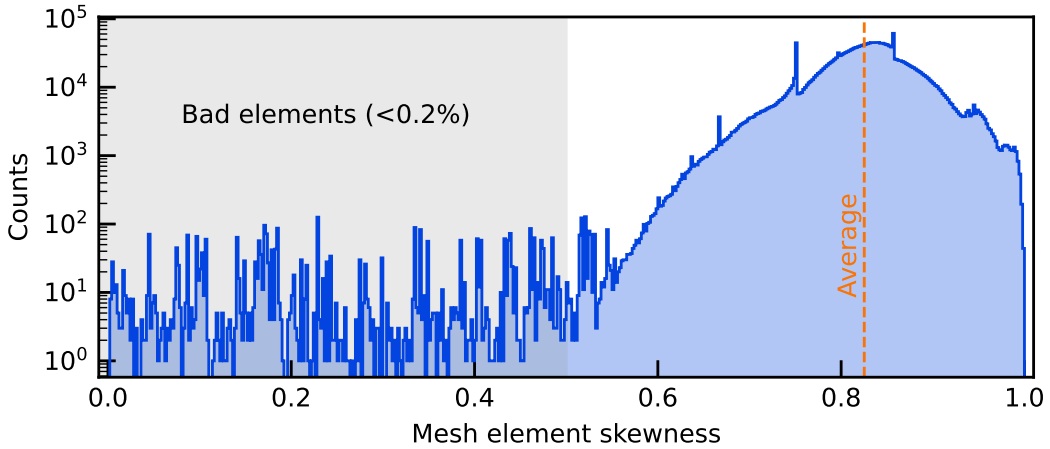


Figure 4.11 Distribution of the skewness describing the mesh quality for the XENONnT electric field FEM simulation. The skewness parameter s is defined in Eq. (4.1). Only $< 0.2\%$ of the elements are considered “bad” based on the conventional $s < 0.5$. Their impact on the final solution is completely negligible.

Along with the geometry implementation, the COMSOL electrostatic module requires the information about the materials included in the simulation. The metallic components are not meshed as they are implemented as empty surfaces, since the electric field inside them is known to be zero *a priori*. Hence, the only input needed is the dielectric constant of the xenon, both gaseous ($\epsilon_{\text{GXe}} = 1$) and liquid ($\epsilon_{\text{LXe}} = 1.96$ [223]), and of the PTFE ($\epsilon_{\text{PTFE}} = 2.1$ [224]). Once geometry and materials are specified, the boundary conditions are set. The inner SS cryostat containing the TPC acts as a grounded Faraday cage and defines the boundary condition for the environment. Other elements such as the diving bell or the copper support ring are also grounded, as they are in contact with the vessel itself. The potentials of the electrodes, PMTs and the field cage array are set following the desired configuration. The voltages of the field shaping electrodes are set calculating the voltage drop as coming from Ohm's law applied to the resistive chain sketched in Fig. 4.6.

The solution returned by COMSOL Multiphysics is a distribution of the electrostatic potential within the simulated area, as reported in the right panel of Fig. 4.10. The electrostatic field is retrieved by estimating the gradient of the potential $\vec{E} = -\vec{\nabla}V$. The results are presented in Sec. 4.3 in the context of the optimization of the electric drift field for the XENONnT TPC.

4.2.2 | Systematic checks

The electric field simulations of the TPC come from a FEM-based numerical solution using an idealized geometry and simplified assumptions. This can introduce biases in the simulation results with respect to the actual field inside the detector. The main contributions to the systematic effects are discussed in the following and their impacts are estimated.

Concentric TPC electrode grids

The 2D-ax geometry implements the TPC electrodes as concentric wires, implicitly assuming that this is equivalent to a grid of parallel wires. The impact of this approximation cannot be estimated by comparing 3D-geometries at the scale of XENONnT because of the limited computing resources. The 2D-ax simulation of the XENONnT TPC uses 4.5 GB of memory: an equivalent 3D simulation would require about 10 TB, assuming the memory requirement is linear with the number of elements. For this reason a small 10 cm \times 10 cm cylindrical "TPC" was simulated both in a 2D-ax and 3D geometry: this consists of two wire grid

electrodes at the top and bottom, and a field cage. The geometries are meshed in order to have a similar degree of accuracy, with the 3D simulation comprising 6×10^6 tetrahedral elements and the 2D-ax around 3×10^4 . The simulations are shown in Fig. 4.12, together with the distribution of the relative difference of the electric field at the same position. As expected, a clear difference can be observed along the symmetry axis close to the electrodes, where the inner most wire in the 2D-ax geometry corresponds to a torus of small major radius. The field far from this region is very similar between the two simulations, with a relative difference of 0.4 % inside an arbitrary large fiducial volume excluding the electrodes and the field cage region. This difference is approximately constant when reducing the extent of the fiducial volume, hence it is safe to assume that this value can be considered as a systematic uncertainty due to the axysymmetric approximation of the TPC electrodes also for larger geometries and it is considered negligible.

The output from the 2D-ax simulations is used also for the study of the production of the electroluminescence signal in Chapter 6. The simulation of the electroluminescence signal is carried out using single electrons extracted in the gaseous xenon. Because of the regular structure of the top stack, the S2 signal is simulated using only the field around a few anode and gate wires. The concentric nature of the electrode wires in the 2D-ax implementation is negligible as the selected wires are located at a fairly large radius of ~ 40 cm. While propagating from the interface to the anode wire, the diffusion of the electrons along the wire direction is far below 1 mm. Even assuming 1 mm, for a radius of 40 cm this corresponds to an angular extension of 0.4 mrad. At this scale, the circular shape of the electrode wires approximate the linear behaviour very well.

Meshing

The impact of the meshing of the 2D-ax geometry is considered by comparing the field solution to the one obtained with a coarser mesh. This coarser mesh is characterized by a linear element size ranging from $60\text{ }\mu\text{m}$ to 60 mm , with an average size being about twice the size of the finer elements of Fig. 4.10. When comparing the two simulations, it is possible to estimate a relative difference as done for the comparison between the 2D-ax and 3D geometries. The average difference of the field strength is 0.2 % within the entire simulation and <0.1 % inside a fiducial volume excluding the electrodes by 5 mm. Hence, we consider the meshing to be a negligible source of systematic uncertainty.

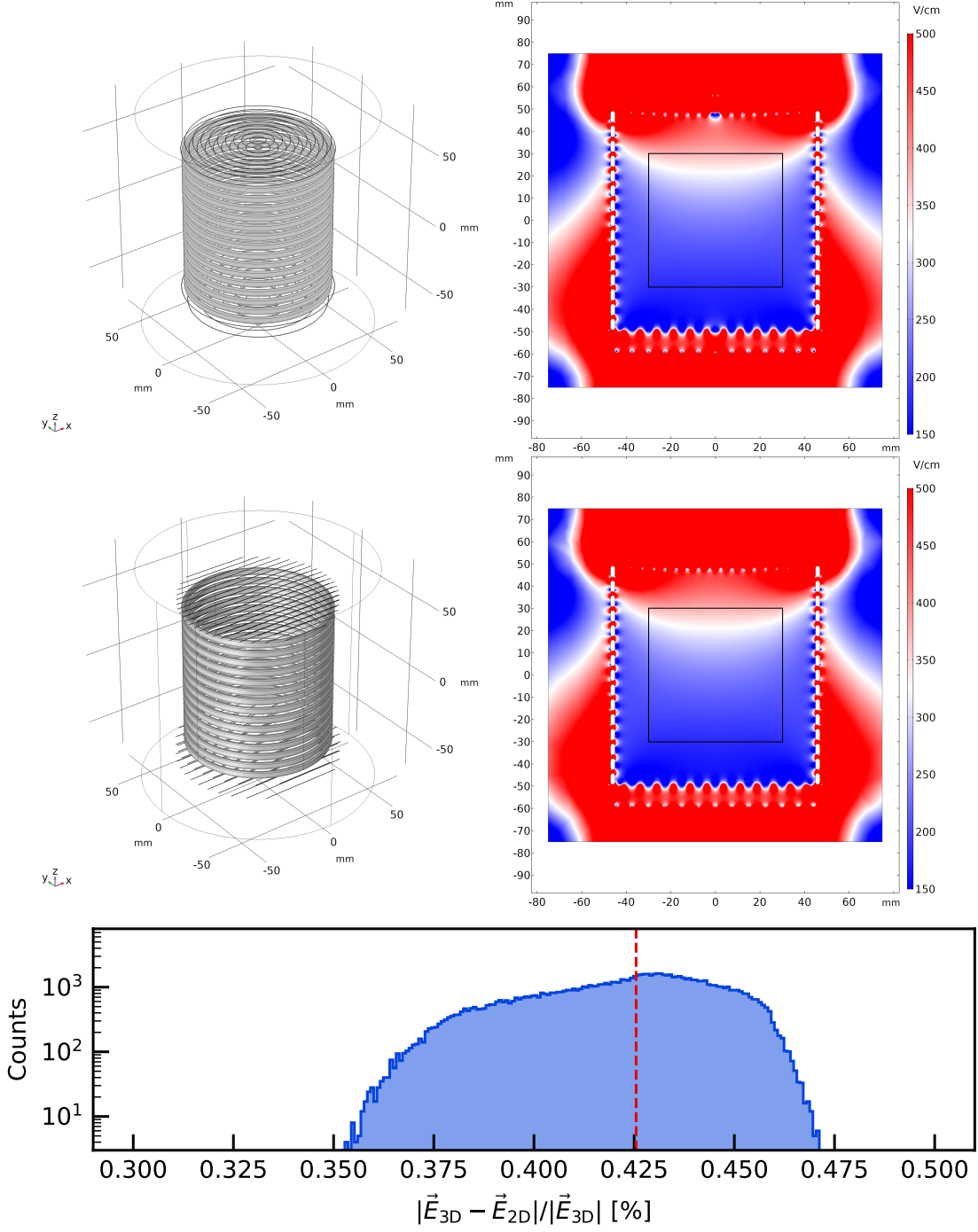


Figure 4.12 Field from a 2D-ax TPC toy simulation (top) compared to a full 3D simulation (middle). The relative field difference within a fiducial volume (black boxes) is shown in the bottom panel. The mean of the distribution is at 0.4%, which is considered negligible.

Polygonal field cage

Given the large radial dimension of the TPC, the difference between the inscribed and circumscribed circle radii is about 0.6 cm, less than 1 % of the radius. The final simulations consider the radius of the active volume to be the one of the inscribed radius, 66.4 cm. A study of the actual impact of the polygonal structure of the TPC would require the comparison of the 2D-ax simulation with the full three-dimensional. As this is not possible, the difference between the simulations with 66.4 cm and 67.0 cm active radius is considered. Also the frames of the top stack electrodes are increased in radius, as well as the position of the field shaping elements, as they share the icositetragonal shape. The cathode and bottom screen have a circular shape, therefore they are not affected by this change. The relative difference of the electric field is estimated within a fiducial volume of 66 cm radius and excluding 5 mm from the electrodes in z . In more than 98 % of the volume an impact <1 % is found. The difference is larger than 10 % only in the area within a 5 cm \times 5 cm square in the top corner of the (r, z) space, where the electric field is mostly influenced by the electrode frames.

Dielectric constant of liquid xenon

The value of the dielectric constant for liquid xenon was selected to be $\varepsilon_{\text{LXe}} = 1.96$ [223]. Two factors should be taken into consideration regarding this quantity: the values in literature do not all agree (e.g., $\varepsilon_{\text{LXe}} = 1.85$ was measured in [202]) and its temperature-dependence. This dependence can be estimated by measuring the change in capacitance of the long level meters (LLMs) in correspondence with temperature fluctuations. As detailed in Sec. 3.4, during normal operation the LLMs are completely submerged by liquid xenon. Hence, any variation of the capacitance is explained either in terms of read-out noise or change in the dielectric constant. The correlation is clear when plotting the LLM2 capacitance against the temperature of the liquid xenon in the middle of the detector (TE103). This is shown in the top panel of Fig. 4.13, where an average change of 0.31 pF/°C is found from the fit. This translates into a change of the dielectric constant of 0.13 %/°C, far below the difference found in literature. Hence, the larger impact comes from the literature disagreement. The difference of the field strength obtained with different dielectric constants and $\varepsilon_{\text{LXe}} = 1.96$ is shown in the bottom panel of Fig. 4.13. The average relative difference is plotted and the error bars represent the 5th and 95th percentiles of each distribution within a fiducial volume excluding 5 mm from the electrodes and from the

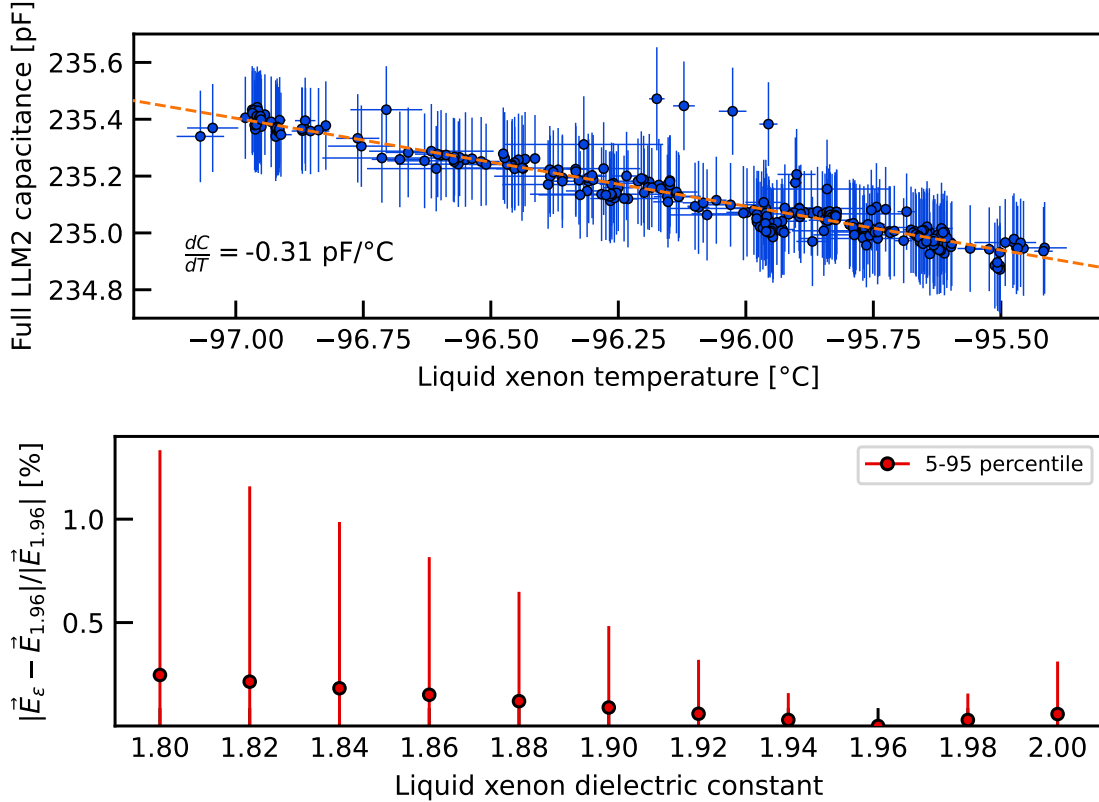


Figure 4.13 (top) Long level meter capacitance as a function of the liquid xenon temperature: as the sensor is always submerged, a change in the measured capacitance is attributed to the temperature-dependent change of the medium's dielectric constant. **(bottom)** Impact of a liquid xenon dielectric constant compared to 1.96, the value used in the COMSOL simulation. A difference well below 1 % is found when comparing to other values, e.g., 1.85 from [202].

walls. When considering the literature value of 1.85, the 95th percentile of the distribution of the difference of the field strength with respect to the simulation using $\epsilon_{\text{LXe}} = 1.96$ is below 1 %.

In conclusion, it was not possible to identify a strong source of systematic uncertainty in the electric field estimation, as all considered contributions have effects in the order of 1 % or below. For this reason, it is safe to assume an overall negligible systematic uncertainty of 1 % for the results obtained by the COMSOL simulations.

4.2.3 | Electron propagation using PyCOMes

As COMSOL returns the solution for the electric field within the simulated geometry, this information is handled separately by a custom-developed python library called PyCOMes [9]. This library was developed to import text files coming from COMSOL simulations with electric fields of any dimension and allows for an easy interpolation of the electric field at any position. Together with returning the value of the electric field, PyCOMes can return the electric field lines and simulate the propagation of the electrons within the electric field. The software was completely developed in python and it optimizes the computing time by relying on the just-in-time compiler *numba* [225] and a (bi)linear interpolation, proven to reduce the computing time when compared to other interpolators such as `RegularGridInterpolator` from *numpy* [226].

The text file input from COMSOL is handled by the PyCOMes class `Field`, which can recognize the dimensionality of the problem, the information included in the file (which field components and units) and the parameters in case of multi-parameter simulations. In this latter case, the class allows for an easy switch among the different field maps by selecting the desired parameters (e.g., the dielectric constant in the comparison of Fig. 4.13). By simply calling the instance of the class and passing a position within the simulated geometry, the value of the components of the field is determined via bilinear interpolation and returned. The field lines for a given electric field at a given position are computed by the class `FieldLines`, which follows the electric field with a selected step size. This is a first-order approximation of the trajectory of a charged particle and it is of particular importance to estimate the final position of the electrons produced in the liquid xenon bulk. The propagation of the electrons including drift speed and diffusion models from literature [132, 141] is implemented in the class `Propagate`. The electron trajectory is estimated by converting the step size length into a time step and using this information to calculate the corresponding longitudinal and transverse spread. This custom-software was developed as an alternative of the built-in particle propagator of COMSOL. The python implementation allows for the parallelization of this task into different jobs, particularly important when simulating the tracks of $\mathcal{O}(10^6)$ electrons. It also allows more flexibility as it is self-developed and can be easily customized, not possible for the commercial software COMSOL. The performance of the field line tracking as a function of the step size is shown in Fig. 4.14, where the typical step size for the field lines within the liquid xenon active volume is 0.25 mm. This step size corresponds to the computation of more than 20 electron paths within 1 s, assuming their starting position at the bottom of the TPC.

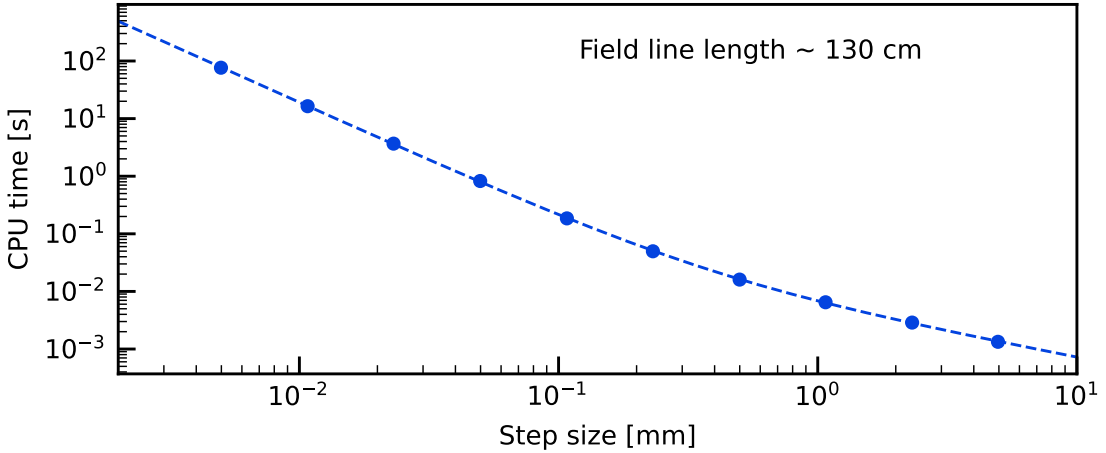


Figure 4.14 Time performance of the `Propagate` class of the PyCOMes module as a function of the trajectory step size. The typical step size used for the simulations is 0.25 mm. Assuming electrons produced almost at the bottom of the TPC ($z = -130$ cm), their trajectory to the liquid-gas interface is calculated in around 45 ms.

4.3 | Electric field optimization

The impact of the electric drift field on the signal is not limited only to the propagation of the electrons, but also affects the recombination probability within the target, as explained in Sec. 2.1. In case of a non-homogeneous field, identical interactions lead to different S1 and S2 signals at different positions within the active volume. The position-dependent response of the detector can be corrected thanks to the accurate position reconstruction and the use of calibration sources. Nevertheless, these corrections introduce additional uncertainties and can lead to an increase of the spread of the ER and NR bands, reducing the discrimination power, especially at low energies. Finally, the worsened discrimination power translates into a reduced WIMP sensitivity. The main source of inhomogeneity in the electric field are the electrodes. In order to optimize their optical transparency, the grid wires of the electrodes have a pitch of 5 mm or more. The large distance between the wires allows the electric field to leak through the electrodes. This affects the electric field uniformity especially where the intensity of the field on one side of the electrode is larger than the field on the other side, as it is the case for the active volume. The gate separates the drift field from the high extraction field at the top, while the cathode separates it from the strong reverse field at the bottom. An example of this effect is also observed in the simulation of the simplified TPC in Fig. 4.12.

An electric drift field larger than the 80 V/cm achieved by XENON1T during SR1 is preferred in order to improve the discrimination between single and multiple scatter interactions. A multiple scatter creates two or more electron clouds at the different locations of the interactions: each cloud produce a proportional scintillation S2 signals at different times, based on the interaction depths. The presence of more than one S2 signal in an event indicates multiple scattering. With a higher field, the longitudinal diffusion of the charge cloud is smaller and hence the separation of the S2 signals in the waveform improves. Tagging multiple scatter strongly reduces the neutron background, as neutrons are more likely to scatter more than once within the TPC in contrast to WIMPs. A higher drift speed also reduces the maximal drift time, hence decreasing the required time window to pair an S1 and S2 into an event. This limits the accidental coincidence background. Detailed studies on the improvement of the WIMP sensitivity as a function of the electric field are reported in [227], where a field $\gtrsim 200$ V/cm is found to be an optimal choice. Along with the drift field intensity, which relies on the performances of the electrodes, two other aspects should be considered: the homogeneity of the field and the presence of charge-insensitive volume. Unlike the intensity of the field, these aspects are directly influenced by the field cage. The charge-insensitive volume (CIV) is the region of the active volume from where electrons liberated by ionization cannot reach the liquid-gas interface due to the field lines ending up on the PTFE walls. The CIV effectively reduces the active volume as the S2 information is lost, while introducing a source of “lone-S1”, increasing the accidental coincidence background.

As explained in Sec. 4.1, the resistive chain features two degrees of freedom: the voltage V_{top} of the independently biased top ring and the resistance R_{bttm} between the field cage and the cathode. The optimization of the field mostly relies on these two tuning parameters, as a full optimization of the geometry of the field cage was limited by the compact design and low-radioactivity of the TPC. While the voltage of the top of the field cage can be changed and tuned during operation, the bottom resistance has to be fixed during design. An independent biasing of the bottom of the TPC would have required a second HVFT, which was impossible to implement in due time. Because of the flexibility of V_{top} , the optimization of the drift field focused on the selection of the best R_{bttm} . This was done simulating the electric field with different combinations of the parameters V_{top} and R_{bttm} , both for the design electrodes’ bias voltages and for other possible scenarios. The field maps were then compared and evaluated based on two independent *figures of merit*: the homogeneity of the drift field, quantified by the “field spread”, and the magnitude of the CIV. The best performing value for the bottom resistance R_{bttm} was implemented

in the final TPC design, also considering its performance under different electrodes' bias configurations.

Field spread

The field spread is defined as the ratio between the 5th-95th range percentile of the field strength distribution and the field average, both evaluated within the fiducial volume defined in the MC sensitivity paper [113]. This is a cylinder of ~ 61 cm radius with top and bottom boundaries ~ 14 cm from the electrodes, enclosing a total mass of around 4 t. An example of the simulated field distribution is shown in the bottom panel of Fig. 4.15.

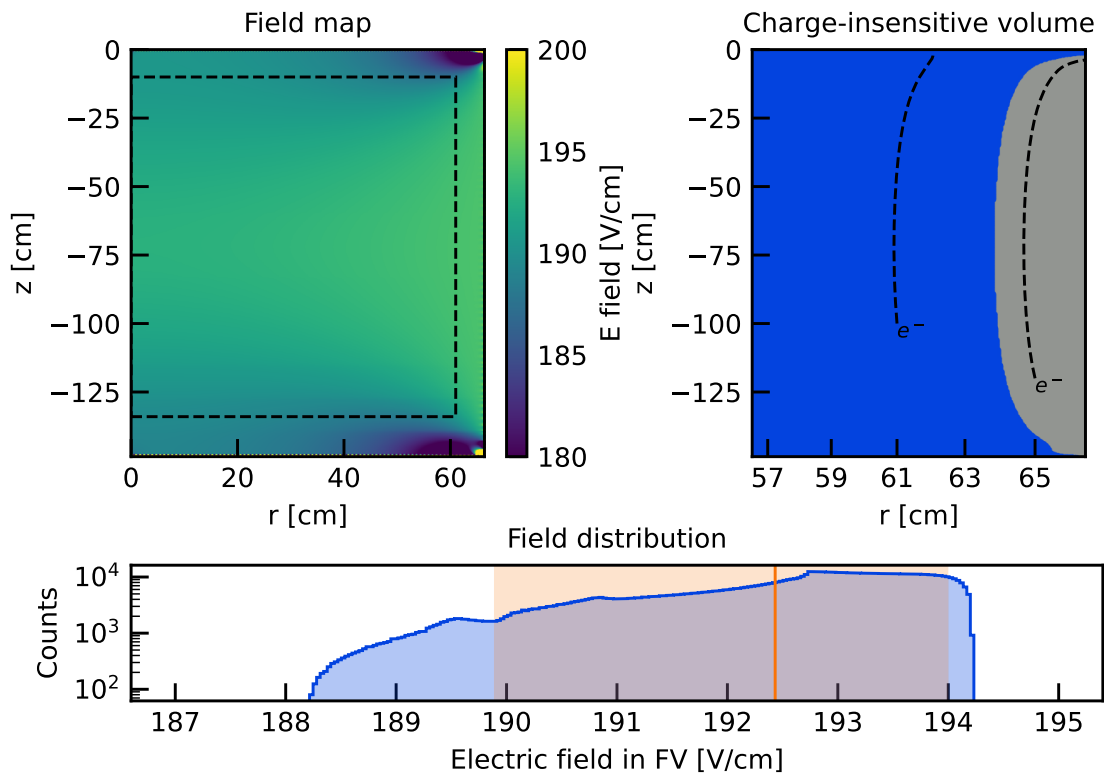


Figure 4.15 Figures of merit used to evaluate the electric field configurations. The field spread is the ratio between the 5th-95th range percentile and the average of the field distribution (bottom) within the volume indicated on the field map (top left). The CIV shown in gray (top right) is the volume where a produced electron ends up on the PTFE wall, as the field lines show. This example map is produced using the configuration discussed in Sec. 4.3.1 and $V_{\text{top}} = -0.55$ kV to highlight the CIV.

Charge-insensitive volume

For an electron liberated at a given interaction position, the probability to reach the gas phase depends on the liquid xenon purity and on the field line defining its drift path. The latter can be computed using the PyCOMes module and its final position determines whether the electron reaches the anode or is lost on the PTFE walls, tagging the interaction position as “charge-insensitive”. Since the field lines cannot cross each other and they have no azimuthal component, the CIV is uniquely defined by its edge along z . This means that the CIV estimation is reduced from the definition of a two-dimensional surface to the definition of a single boundary. This is done by first discretizing the active volume into a (N_r, N_z) grid. The “insensitivity” (whether the field line reaches the anode or not) of each position in the grid is estimated starting from the central bottom position at around $(0, -148)$ cm, and then moving radially outwards. As soon as the r -position is flagged as charge-insensitive, then all remaining positions with larger radii are also considered charge-insensitive. Then, the next z -position above is considered: if it is within the CIV, the estimation proceeds towards smaller radii, otherwise towards higher ones. This approach returns a good approximation of the CIV, although it does not consider the probabilistic nature for an electron to be observed due to its diffusion along the drift path. This contribution is considered negligible, as the diffusion can equally push the electrons inwards or outwards. An example of the CIV estimation and the electron’s path therein is shown in Fig. 4.15.

4.3.1 | Design optimal configuration

The design configuration of the electrodes’ voltages was chosen in order to have an electric drift field of around 200 V/cm and an electron extraction efficiency of 100 %, possible for extraction fields above 6 kV/cm [228]. This led to the following configuration:

	V [kV]
Top screen	−1.5
Anode	+6.5
Gate	−1.0
Cathode	−30.0
Bottom screen	−1.5
PMTs	−1.5

where the voltages of the PMTs are not set by the field requirement, however, the value is

an important boundary condition for the electric field. Once the voltages of the electrodes are set and the geometry is fixed, the electric field is then characterized only by the two degrees of freedom of the field cage: the top voltage V_{top} and the bottom resistance R_{bttm} . The field for different combinations of these parameters are simulated and spread and CIV of these fields are evaluated and compared. The considered combinations are V_{top} between -1.2 kV and -0.5 kV in 50 V steps and R_{bttm} between $5 \text{ G}\Omega$ and $10 \text{ G}\Omega$ in $0.5 \text{ G}\Omega$ steps. The results are shown in Fig. 4.16. For reference, applying the same framework to the XENON1T SR0 electric field returns a field spread of 7.3% and a CIV mass of 1.2 kg .

The field spread is a two-dimensional Gaussian distribution with the minimum of $<1\%$ spread centered at $V_{\text{top}} = -0.75 \text{ V}$ and $R_{\text{bttm}} = 8 \text{ G}\Omega$. A more positive voltage of the top field cage ring with respect to the gate leads to a better field homogeneity. This is due to the fact that the potential at the top of the TPC is the weighted average between the gate and anode voltage, due to the gate transparency. This “effective” potential is more positive than the gate voltage because of the effect of the anode. The possibility to match this effective potential is the reason why the top field shaping ring of the field cage is biased

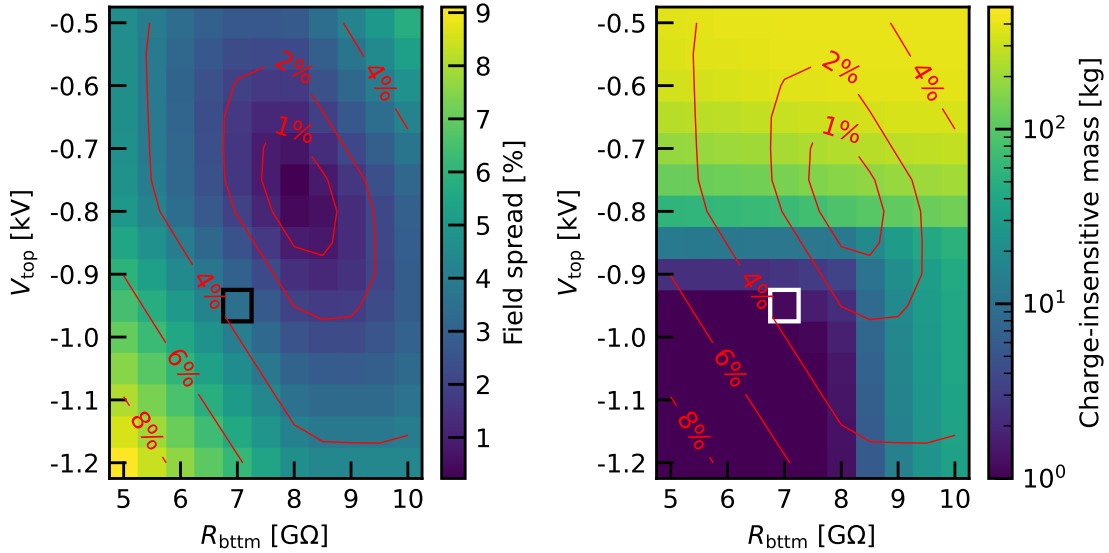


Figure 4.16 Field spread distribution (left) for different combinations of the top field cage voltage V_{top} and bottom resistance R_{bttm} for the design electrode configuration. The same contours for different values of spread are reported in the distribution of the charge-insensitive mass (right) in the same phase space. The highlighted bin indicates the optimal configuration and thus the XENONnT design configuration.

independently of the gate electrode. A resistive connection of the field cage with the gate would always result in a potential drop at the top field shaping ring. In the same way, the more positive voltage of the bottom screen leaks through the cathode electrode grid, changing the effective potential at the bottom of the detector. A more positive voltage at the bottom ring of the field cage is possible by increasing the resistance between field cage and cathode. For this reason the best scenario for the field homogeneity is reached at $8\text{ G}\Omega$, as simulations show. This corresponds to a voltage drop more than six times larger than expected for a linear drop.

When considering the best field homogeneity scenario, the corresponding CIV mass is around 320 kg , an unacceptable value as it corresponds to about 5 % of the active volume. As shown in the right panel of Fig. 4.16, this large electron loss is due to the combined effect of a too positive top voltage and a too large bottom resistance. Because of its more positive bias, the top field cage ring acts as anodic element with respect to the gate and attracts drifting electrons. While this can compensate the inward push, for too positive voltages the field cage can act as an actual anode. In this case the electrons produced at large radii are attracted by the top-most rings of the field cage and end up on the PTFE walls. This is shown in the top right panel of Fig. 4.15. The same principle applies to the bottom of the field cage. A large resistance establishes a large voltage difference between the cathode and the field cage, pushing electrons against the wall in the bottom TPC corner. This latter effect is small compared to the effect of the top ring voltage, as it involves only the bottom corner, while the electrons attracted by the top rings are produced close to the wall and along the entire TPC length.

As the field spread and the CIV are two independent figures of merit, it is not possible to combine them into a single quality factor. The best configuration is therefore picked with a certain degree of arbitrariness by ensuring a small charge-insensitive mass while minimizing the field spread. By looking at the CIV (right panel of Fig. 4.16), any $R_{\text{bttm}} \geq 7.5\text{ G}\Omega$ or $V_{\text{top}} \geq -0.9\text{ kV}$ are to be excluded to ensure a $\mathcal{O}(1\text{ kg})$ charge-insensitive mass. For this reason the design configuration of the field cage was decided to be $V_{\text{top}} = -0.95\text{ kV}$ and $R_{\text{bttm}} = 7\text{ G}\Omega$ for the bottom resistor. This returns a field spread of 3.5 % and a charge-insensitive mass of 1.2 kg , as detailed below in Sec. 4.3.3. While the voltage can be easily modified via the set-point of the HV supply module (CAEN A1580HDM [229]), the bottom resistance had to be implemented as a combination of the available $5\text{ G}\Omega$ SMD resistors. The desired resistance can be achieved connecting a resistor in series to three resistors in parallel, among which one is a series of two resistors as shown in Fig. 4.17.

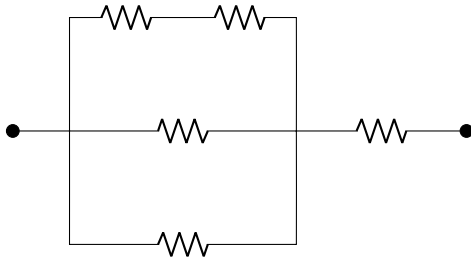


Figure 4.17 Arrangement of five $5\text{ G}\Omega$ resistors resulting in a $7\text{ G}\Omega$ resistance. This configuration was implemented using the SMD resistors and placed between the field cage and cathode.

4.3.2 | Bottom resistor performance

As already mentioned, the resistance R_{bttm} between the bottom field shaping ring and the cathode was set during the design phase. This means that in case of a change in the bias voltages of the electrodes, it is not possible to tune its value, what can be done for the field cage bias voltage V_{top} . For this reason the performance of $R_{\text{bttm}} = 7\text{ G}\Omega$ was tested under different field configurations. This was done by simulating different voltage arrangements for this bottom resistance and for different top field cage voltages, then evaluating the field spread and CIV as a function of V_{top} . The voltage V_{top} was kept as degree of freedom, since this can be tuned to optimize the electric field during operation. In case similar performances of the electric field can be reached by tuning the top voltage, the resistance value is considered acceptable.

In the history of xenon-based dual-phase TPCs, one of the main challenges has always been reaching the design cathode voltage [230]. For this reason, the resilience of the drift field given the chosen bottom resistor to a large range of cathode voltages is critical and it was extensively tested with simulations. The results are shown in Fig. 4.18 for cathode voltages between -40 kV and -10 kV . The simulated configurations show an acceptable level of field homogeneity and CIV, once V_{top} is properly tuned. The red dashed line in Fig. 4.18 shows the arbitrary threshold of 4% for the field spread: in the worst scenario of -10 kV , this spread can be reached with a CIV of $\sim 8\text{ kg}$. Inversely, considering a XENON1T-like field spread of about 7%, the charge-insensitive mass can be reduced to less than 2 kg. The worse behaviour at lower voltages of the cathode can be explained in terms of matching the effective potential at the top and bottom of the field cage. For a lower cathode voltage, the drift field is lower and therefore the impact of the anode on the effective potential on the top of the TPC is larger. This is corrected by increasing V_{top} to more positive voltages, which in turn increases the potential drop across the bottom resistance R_{bttm} . On the other hand, the reverse field leakage through the cathode is reduced and this would require a lower potential drop at the bottom of the TPC. Because

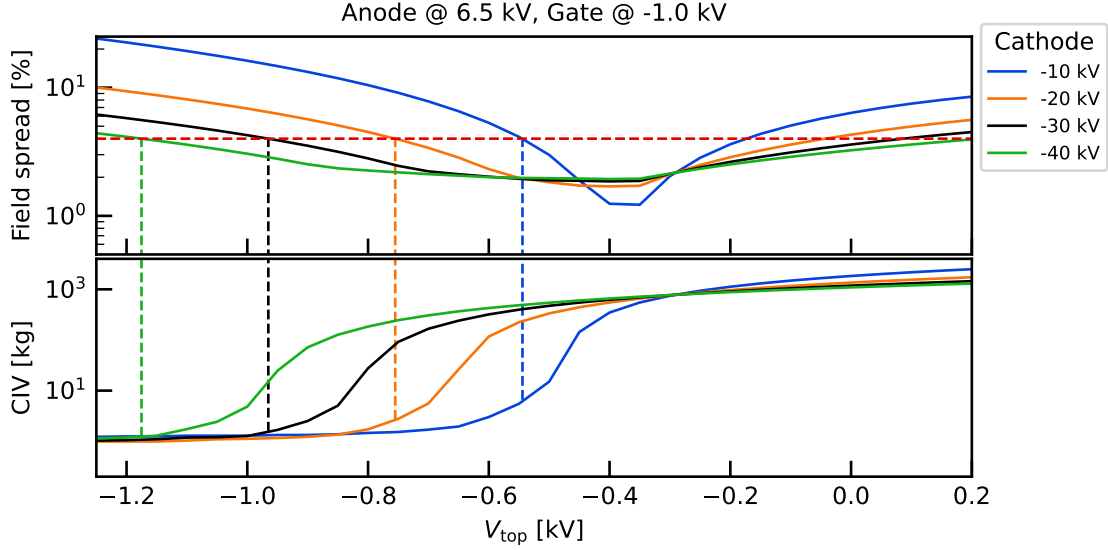


Figure 4.18 Field spread (top) and charge-insensitive mass (bottom) as a function of the top field cage voltage for different values of the cathode voltage, while keeping the other electrodes at the design bias voltages. As the cathode voltage changes, it is not possible to define a value of V_{top} for which field spread and CIV remain the same. For the same value of field spread (red dashed line at 4 %), the CIV increases as the cathode voltage decreases, as the horizontal lines show.

of this conflict the quality of the drift field worsens for lower cathode voltages. A similar behaviour is observed when the gate voltage is set to more negative voltages while keeping its voltage difference to the anode constant.

The impact of a different bias voltages applied to the top stack was also considered. Keeping the gate at the design voltage of -1 kV , the anode was varied between $+4.5 \text{ kV}$ and $+6.5 \text{ kV}$. The results in Fig. 4.19 show a shift of the field spread and CIV curves along V_{top} , with a change of around 100 V in V_{top} for an increase of 1 kV at the anode. This means that any change of the anode voltage alone can be easily corrected by tuning the top voltage of the field cage accordingly. A similar conclusion is observed when gate and anode voltages are changed coherently in order to keep the extraction field constant, while keeping the cathode at the same voltage. The effect of an increase of the anode/gate voltage can be counterbalanced by changing V_{top} . These results were considered satisfactory for the operations of XENONnT and the bottom resistor $R_{\text{bttm}} = 7 \text{ G}\Omega$ was implemented in the detector.

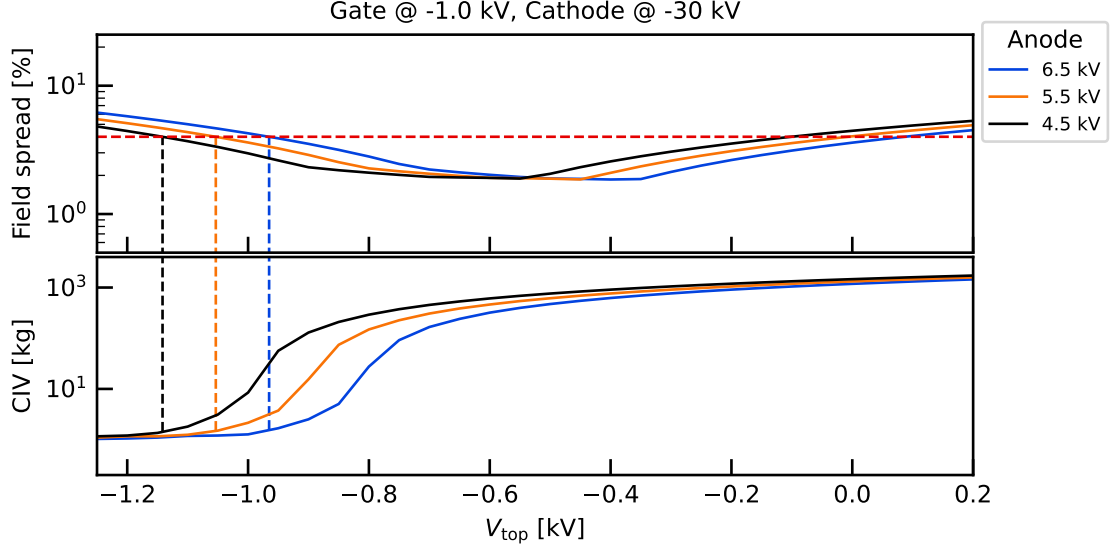


Figure 4.19 Field spread (top) and charge-insensitive mass (bottom) as a function of the top field cage voltage for different values of the anode voltage, while keeping the other electrodes at the design bias voltages. By tuning V_{top} , it is possible to reach identical performances as shown by the vertical lines, indicating the CIV achieved for a fixed field spread of 4 % (dashed red line).

4.3.3 | Design electric field

The design configuration of the TPC is characterized by the voltages reported in Sec. 4.3.1, $R_{\text{bttm}} = 7 \text{ G}\Omega$ and $V_{\text{top}} = -0.95 \text{ kV}$. The resulting electric field is shown in Fig. 4.20. It has a spread of 3.5 % in the selected fiducial volume, with an average value of 191.3 V/cm. This represents a factor two improvement compared to XENON1T, both in field intensity and homogeneity. This spread translates into a charge and light yield inhomogeneity of around 0.06 % for a nuclear recoil below 100 keV and <0.2 % for an electronic recoil below 100 keV, as calculated using [134]. The charge-insensitive mass for this configuration is 1.2 kg, representing 0.02 % of the entire active volume. Most of this insensitive volume is located at the top and bottom edges of the TPC, as these are the regions with the most inhomogeneous field. Because of diffusion, an electron liberated at a certain position in the active volume has a finite probability to reach the liquid-gas interface, thus producing a proportional scintillation signal S2. This means that a better characterization of the CIV should consider the charge-insensitive volume not as a volume with a well-defined boundary and a precise mass, but in terms of a probability map for an electron to reach

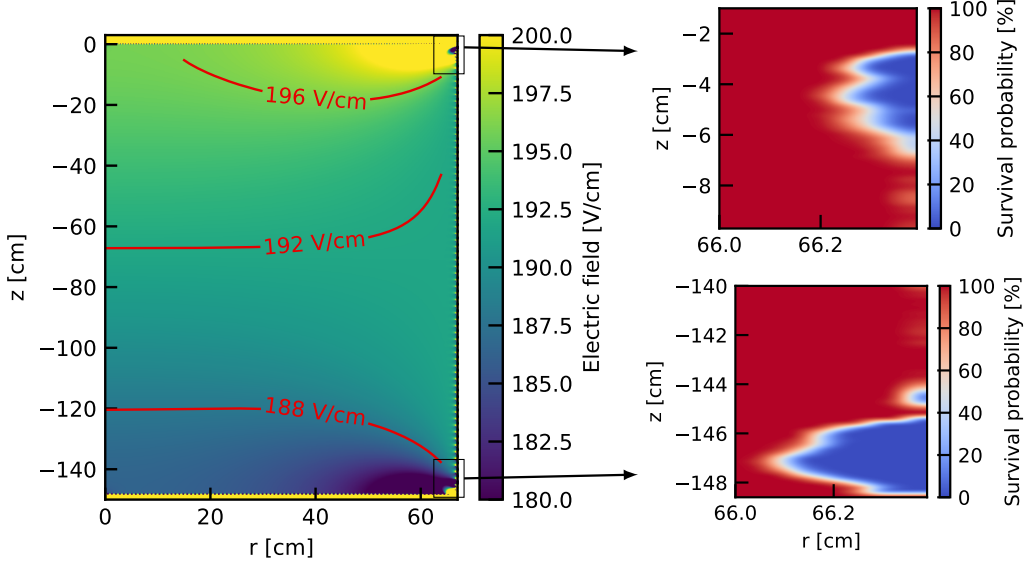


Figure 4.20 Final design electric field map (left) after optimization. The optimal field cage parameters are $R_{\text{bttm}} = 7 \text{ G}\Omega$ and $V_{\text{top}} = -0.95 \text{ kV}$. The electric field within the fiducial volume has a spread of 3.5 %. The zoomed-in plots on the right show the electron survival probability at the corners of the detector, where the value is different than 100 %.

the gas phase. This probability is known as *survival probability*. This quantity is estimated using the `Propagate` class of PyCOMes (see Sec. 4.2.3). A total of N (typically $N = 1000$) electrons are propagated within the electric drift field from a given initial position: the survival probability associated to that position is the fraction of electrons that reach the anode. This is repeated over many positions in the active volume, hence yielding a survival probability map as shown in the insets of Fig. 4.20. These are the only regions where the survival probability is below 100 %. The small extent of these regions suggests that the CIV has a negligible impact on the signal production and electron propagation.

4.4 | Mapping the transport properties of electrons

The proportional scintillation signal S2 has a two-fold dependence on the electric drift field. The charge yield, hence the signal size, depends on the electric field intensity at the interaction point, as a larger field quenches the recombination processes between electrons and ions. In addition, the liberated electrons follow the electric drift field which defines the properties of the electron cloud and the associated S2 signal. The understanding of these

properties is of extreme importance for the precise simulation of the S2 signal, as it is the case for the survival probability discussed above. A mapping of the surviving probability is necessary to properly reproduce the charge signal response of the TPC and to compare these results to the observed data. In a similar way, other properties such as the drift speed and the diffusion coefficients can be mapped and fed to the signal simulation framework.

As electrons propagate in the active volume, they feel different electric fields at different positions, leading to a varying drift speed and diffusion along their trajectory. This effect could be implemented in the simulation framework by propagating each electron of the ionization cloud independently. This procedure is extremely time-consuming as typical MC simulations produce millions of events, each including hundreds or thousands electrons. For this reason the simulation framework uses “path-weighted” maps for the electron transport properties, returning an average quantity for a given initial position. These transport property maps are produced in a very similar way to the survival probability map. The active volume is divided in a (300, 500) grid in the (r, z) space, and a total of 1000 electrons are propagated from each position. Initial and final position as well as timing information are stored for each electron, together with the initial and final position of the field line starting at the same point. An example of the simulation is shown in Fig. 4.21, where the electron trajectories are shown in the left panel and the final position distributions are shown on the right. In this way for each point i of the TPC grid it is possible to define the drift speed as the drifted z -distance over the average drift time:

$$v_d(\vec{x}_i) = \frac{\Delta z_i}{\langle t_{d,i} \rangle}, \quad (4.2)$$

with $\Delta z_i = z_{\text{fin},i} - z_{\text{in},i}$. Similarly, the different diffusion coefficients can be estimated by evaluating the spread in time for the longitudinal diffusion, and in (x, y) for the transverse diffusion. In particular the transverse diffusion is divided into radial and azimuthal. As the two-dimensional axysymmetric simulated map is limited to the (r, z) space, the electrons’ propagation is artificially extended to a three-dimensional space. This is possible by starting the propagation of each electron at the position $(r_0, 0, z_0)$ and for each new position along the trajectory the field is mapped by considering the radial position $r = \sqrt{x^2 + y^2}$. The radial diffusion is estimated considering the x spread in the simulation. The azimuthal diffusion similarly uses the y spread. The diffusion coefficients are estimated as:

$$D_{L,i} = \frac{(\sigma_{t_{d,i}} \cdot v_{d,i})^2}{2\langle t_{d,i} \rangle}, \quad D_{T,i}^{\text{rad.}} = \frac{\sigma_{x_{\text{fin},i}}^2}{2\langle t_{d,i} \rangle}, \quad D_{T,i}^{\text{azim.}} = \frac{\sigma_{y_{\text{fin},i}}^2}{2\langle t_{d,i} \rangle}, \quad (4.3)$$

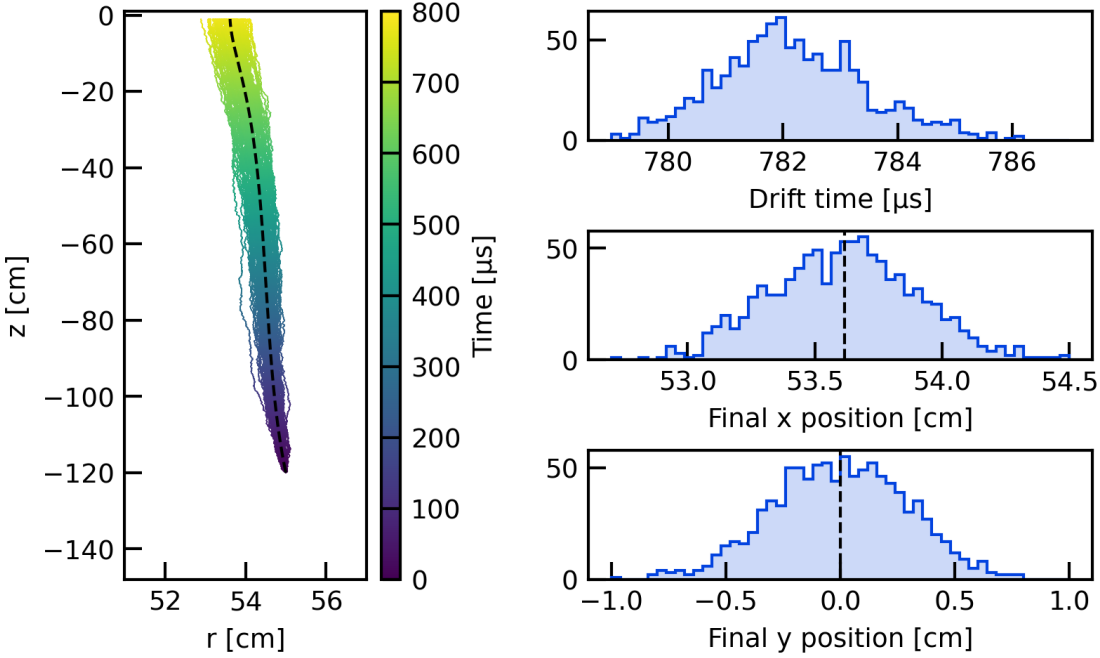


Figure 4.21 Simulated electron trajectories from the same initial position (55, −120) cm and distribution of the resulting drift times (top right), final x positions (middle right) and final y positions (bottom right). The x and y positions are returned by the PyCOMes propagation, with the electrons starting at $y = 0$. The black lines represent the end point of the electron trajectory with no diffusion.

where the spread of the final x and y position are the standard deviation of the distribution shown in Fig. 4.21. The results of these simulations are the electron transport properties maps shown in Fig. 4.22. The higher electric field at the top edge of the detector leads to a larger drift speed in the same region. The integration along the entire path averages out the effect of the lower field at the bottom of the TPC. The sudden increase in longitudinal diffusion close to the gate is likely an artifact due to the finite step size for the electron propagation, while the lower radial diffusion at the edges is caused by the field at the top edge of the detector. As the field lines reach this top corner, they are pushed inwards leading to a reduced spread along r (or x in the equivalent three-dimensional propagation).

The electron transport property maps are fed to the XENONnT full-chain simulation to estimate the properties of the S2 signal based on the true interaction position. The full-chain simulation is described in detail in [10]. It consists of a framework developed to reproduce the low level data (the waveforms) of XENONnT starting from the individual

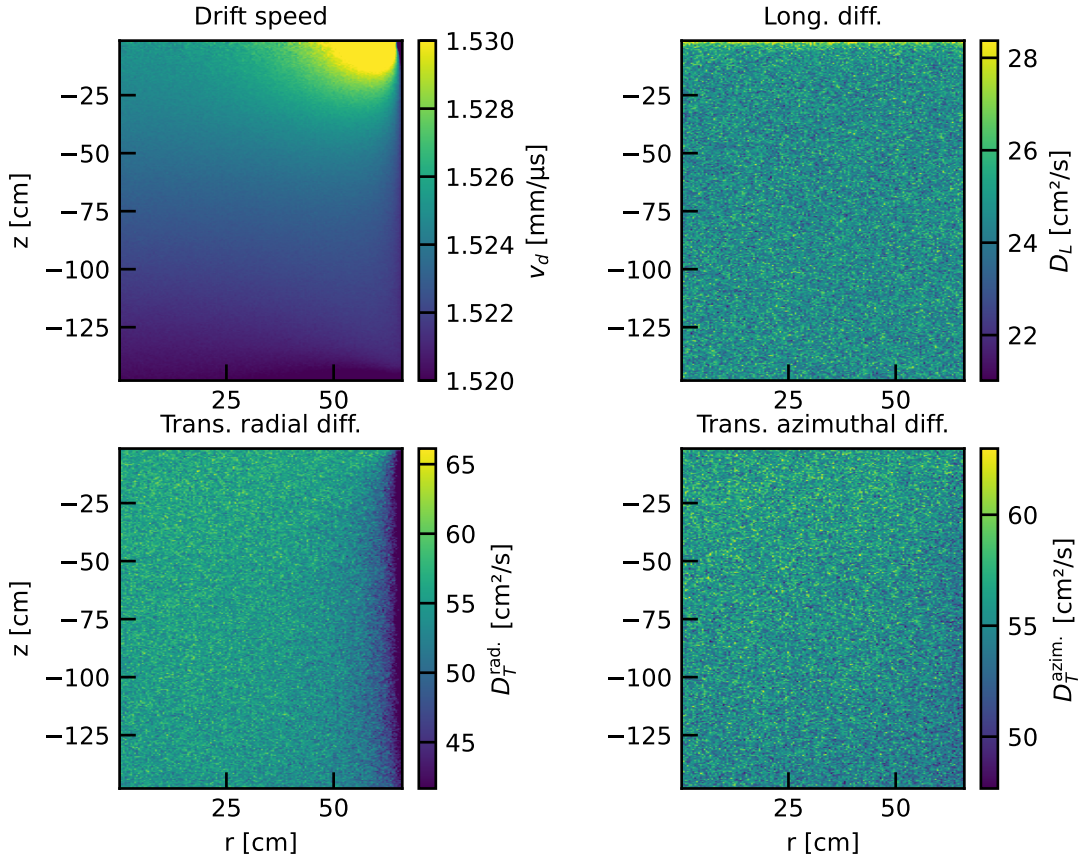


Figure 4.22 Electron transport properties maps obtained from the simulation using Py-COMes [9]. The maps are produced by simulating 1000 electrons from each point in a (300, 500) grid and using their final position and time information to calculate “path-weighted” drift speed and diffusion coefficients.

energy depositions inside the TPC. It is divided into three modules, each handling a different aspect of the simulation:

1. the geometry and optical properties of the detector are implemented in *GEANT4* [231], which returns precise information about interactions and energy deposition within the active volume;
2. the energy information is translated into light and charge quanta by the custom-developed framework *epix* [232], which uses the *NEST* software [133]. The electric field map is used at this stage to evaluate the charge and light yield at the interaction position, based on the local drift field strength;

3. the waveform simulator *WFSim* [233] processes the quanta information and returns the waveform in a DAQ-compatible format. Photon propagation information, detector and PMTs effects, as well as signal digitization are included in this step. The final output is then processed using the same software used for the actual data, *straxen* [234, 235].

The maps of Fig. 4.22 are included in the last step of the chain (WFSim), along with the survival probability map of Fig. 4.20 included as a binomial contribution to the total number of electrons producing S2. The addition of these maps in the simulation framework allows for a more realistic simulation of the S2 signals and the event reconstruction. The proper diffusion model improves the estimation of the multiple vs. single scattering resolution, especially important for the discrimination of neutron nuclear recoils. These maps can be produced for different electrodes bias voltages and can be used to compare the simulation with data in order to validate the knowledge about the electric drift field.

Chapter 5

The electric field of XENONnT

The first science run (SR0) of XENONnT started in July 2021 and finished in November of the same year. Due to a short-circuit of the cathode with the bottom screen, the electric drift field during the science run was limited to about 23 V/cm instead of the design field of 191 V/cm (see Sec. 4.3.3). The field simulation framework developed in Chapter 4 was thus applied to study the SR0 configuration. The position distribution returned by the simulation showed a clear discrepancy with the $^{83\text{m}}\text{Kr}$ calibration data. The mismatch was addressed and corrected by including a charge accumulation on the PTFE reflective walls in the simulation. Since a precise knowledge of the electric field inside the active volume is of great importance to correctly understand the detector response, the new field map was validated with two independent analyses presented in this chapter. A dedicated test of the impact of the field cage bias voltage was carried out after the end of SR0 and provides a further validation of the modeling of the electric field.

The XENONnT electric field configuration during SR0 is presented in Sec. 5.1. The mismatch of the reconstructed event distribution with the expectations from the electric field simulation and its correction including a charge accumulation on the PTFE reflectors is discussed in Sec. 5.2, proving that a small sub- $\mu\text{C}/\text{m}^2$ charge density is sufficient to resolve the discrepancy. The resulting new electric field map is then validated by independent analyses, solving the issue of source-dependent electron lifetime measurements already observed by XENON1T [5]. A time-dependence of the position distribution as observed in XENON1T is excluded for XENONnT in Sec. 5.3. A dedicated test to study the impact of the homogeneity of the electric field on the detector response was carried out after SR0. It consisted of a series of $^{83\text{m}}\text{Kr}$ calibration runs acquired with different bias voltages applied to the top field shaping ring of the field cage. The test and the results are presented in Sec. 5.4. The correction of the reconstructed event interaction position due to the

inhomogeneity of the drift field is discussed in Sec. 5.5. Finally, Sec. 5.6 discusses the impact of the field distortion correction on the fiducial volume used for the first results of SR0 [114].

5.1 | Electric field in Science Run 0

The electrodes' voltage configuration of the first science run of XENONnT was the following:

	SR0 voltage [kV]	Design voltage [kV]
Top screen	-0.9	-1.5
Anode	+4.9	+6.5
Gate	+0.3	-1.0
Top field cage	+0.65	-0.95
Cathode	-2.75	-30.0
Bottom screen	-2.75	-1.5
PMTs	-1.3	-1.5

During TPC commissioning, a short-circuit forced the cathode and bottom screen to be at the same voltage. The electrical connection between these electrodes was confirmed by measuring a resistance around 10Ω , consistent with the scenario of a single wire connecting the electrodes. This prevents the bottom stack (cathode and bottom screen) to reach values below -3 kV , the maximal rating of the high voltage connection of the screen electrode. In order to increase the drift field, the gate voltage was thus set to $+0.3\text{ kV}$ and the anode to $+4.9\text{ kV}$. This led to an extraction field in the liquid xenon of $(2.91 \pm 0.01)\text{ kV/cm}$, corresponding to an average extraction efficiency of $(53 \pm 4)\%$ for a liquid level of $(5.1 \pm 0.2)\text{ mm}$ above the gate [236]. The voltage of the top field shaping ring was selected following the same procedure as developed and detailed in Sec. 4.3. Because of the low voltage of the cathode, a larger charge-insensitive volume (CIV) is expected at the bottom corner of the TPC which cannot be reduced by tuning the voltage of the top ring of the field cage. From simulations, the expected charge-insensitive mass is around 104 kg and the field spread is 5.5 %, while the design configuration predicted a CIV of 1.2 kg and a field spread of 3.5 %, for an average value around 23 V/cm. The electric field from the COMSOL simulation is shown in Fig. 5.1a, while the CIV is plotted in terms of survival probability in Fig. 5.1b.

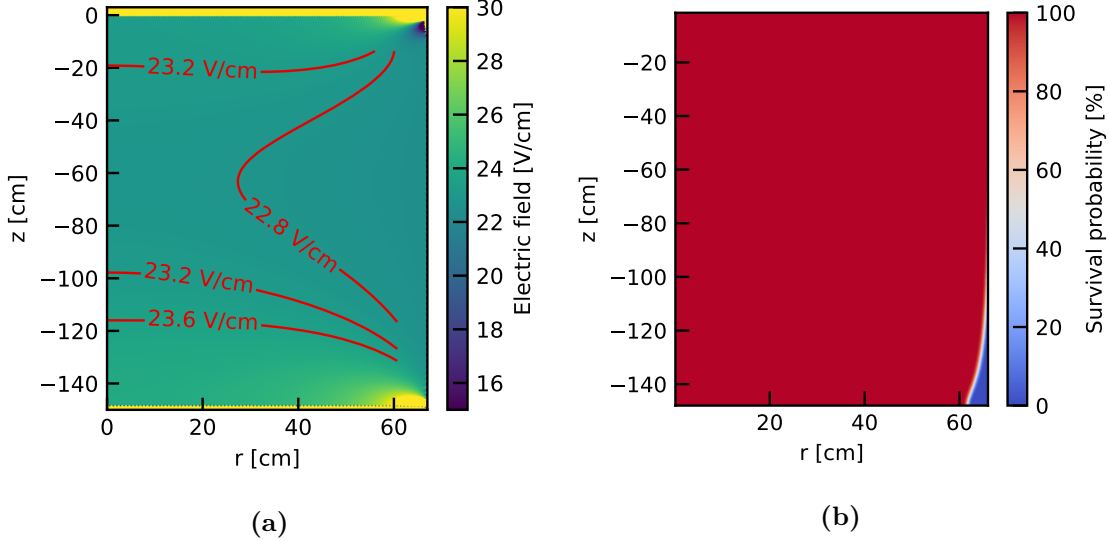


Figure 5.1 (a) Electric field map from COMSOL for the SR0 bias voltage configuration. (b) Survival probability map evaluated following the principle described in Sec. 4.3.3. The charge-insensitive mass of 104 kg is concentrated in the bottom corner of the active volume.

Important data-driven information about the detector’s spatial response and the electric drift field comes from the $^{83\text{m}}\text{Kr}$ calibration. This source is a volatile daughter of ^{83}Rb which is periodically injected into the TPC through the gas purification loop, where it mixes homogeneously with the liquid xenon [5, 237]. The $^{83\text{m}}\text{Kr}$ isotope has a lifetime of 1.83 h and is characterized by a two-step transition emitting electrons with 32.2 keV and 9.4 keV, with an intervening lifetime of 154 ns [238]. Because of this short lifetime, comparable to the typical widths of S1 and S2 peaks, the majority of the $^{83\text{m}}\text{Kr}$ events are reconstructed as a single S1 and S2, adding up to a single 41.6 keV “event”. These events are selected with a box cut in the (S1, S2) space, while the events where two individual S1s can be identified are selected using their time separation and the ratio between their signal areas. As the $^{83\text{m}}\text{Kr}$ is expected to mix homogeneously with the liquid xenon, the selected population is assumed to be uniformly distributed within the detector, representing a useful way to map the properties of the electric field in the active volume. As discussed in Sec. 2.1, the charge and light yields carry important information about the intensity of the electric field. In particular, the ratio between the two light S1 signals from $^{83\text{m}}\text{Kr}$ events can be used to estimate a data-driven field map, as done in Sec. 5.2.2. Similarly, the observed position distribution carries information about the field lines that the ionization electrons follow towards the S2 region. The \$(r, z)\$ distribution is shown in Fig. 5.2, together with the \$(x, y)\$ distribution for two \$z\$ slices. The measured \$(r, z)\$ distribution is characterized

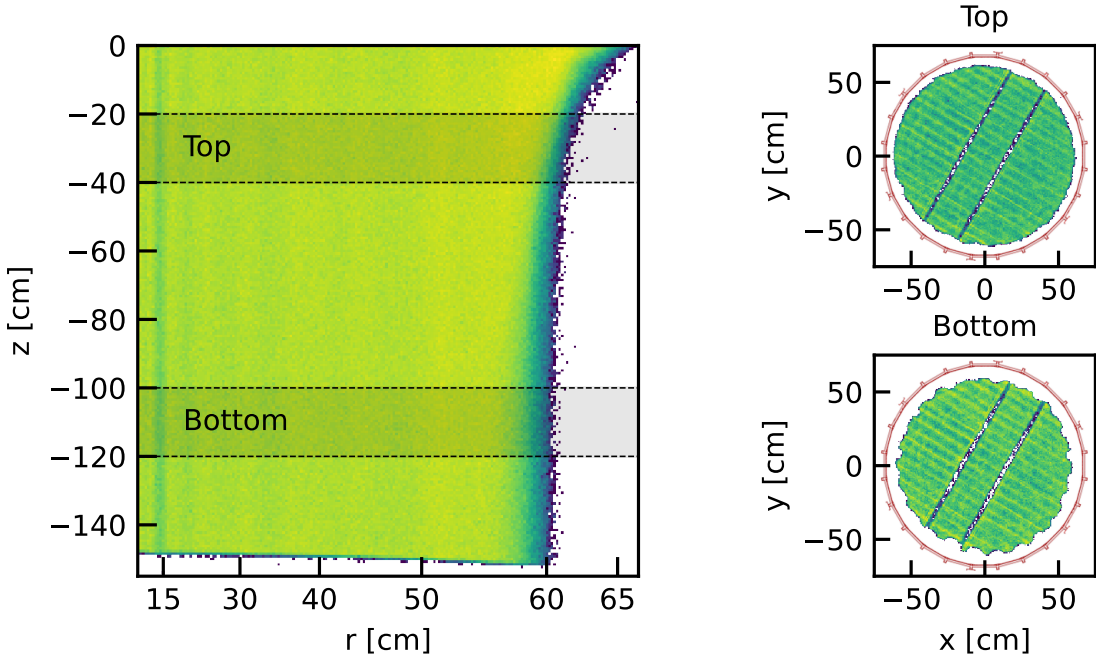


Figure 5.2 Reconstructed position distribution for measured ^{83m}Kr events acquired during one of the biweekly calibrations. The left panel shows the (r, z) distribution with a clear inward push, up to 6 cm with respect to the TPC radius of 66.4 cm. The right panels show two z slices of the (x, y) distribution. The blue structures correspond to the perpendicular wires of the gate, an artifact discussed in Sec. 6.3. The irregular borders of these distributions remind of the “bite” structure observed in XENON1T [5] and they are further discussed in the text. The color scale is logarithmic.

by an inward push increasing with the drift length. This feature was already observed by XENON1T [5] and is caused by a positive radial component of the field which pushes the electrons towards the center of the TPC. This distortion is corrected during analysis as detailed in Sec. 5.5, but it allows also for a direct comparison of the simulations to the data.

The (x, y) distribution shows two regions of lower event number density across the entire TPC. These are located at the positions of the perpendicular wires installed at the gate. The origin of these structures is explained and modeled in Sec. 6.3.1. In addition, a similar “bite” structure as the one observed in XENON1T and shown in Fig. 4.3 is observed also for XENONnT. Unlike XENON1T, the inward push is stronger close to the PTFE pillars, as becomes clear by comparing the distribution shape to the cross section view of

the field cage shown in red in the right panels of Fig. 5.2. Assuming the explanation of XENON1T for the angle-dependent wall charge-up as source of this structure, this suggests that the design choices for the field cage have the desired effect. Indeed, a more efficient charge removal is expected at the panels because of the lower thickness of the PTFE wall and the presence of the charge collecting holes (see Sec. 4.1). This difference in the charge removal efficiency translates into a larger charge accumulation at the pillars with respect to the PTFE panels, resulting in this “inverted” bite structure as compared to XENON1T.

5.2 | Wall charge accumulation

The framework presented in Sec. 4.2 can be used to compare the distortion of ^{83m}Kr data to the expectation based on the COMSOL electric field map. For a given field map, the position distribution of the krypton source as reconstructed in the detector is simulated by propagating electron tracks using the PyCOMes module [9]. A homogeneous distribution of starting positions within the active volume is sampled and used to propagate individual electrons. Their final radial positions and drift times define the expected position distribution. The bias coming from simulating the final position using individual electrons instead of an electron cloud is negligible once the distribution of several thousand events is considered. To quantify the difference of the spatial distribution between simulation and data, the 90th percentile of the r -coordinate for different z bins is extracted and referred to as *radial distribution*. The uncertainty in each bin is estimated by considering the 16th and 84th percentile of the cumulative binomial distribution of probability $p = 0.9$, corresponding to the 90th percentile. The radial distribution is shown in Fig. 5.3 for data (orange) and simulation (blue). The choice of the 90th percentile is not entirely arbitrary. Lower percentiles carry less information about the radial distortion, while the 100th percentile is strongly affected by outliers due to the position reconstruction resolution. The impact of considering the 90th percentile is later considered as part of systematic uncertainty.

The comparison of Fig. 5.3 shows a clear mismatch between simulation and data, with a difference as large as 6 cm at the bottom of the TPC. The possibility of a faulty resistor was initially considered to explain the strong discrepancy. Both the case of a short-circuited and a broken resistor along different positions of the field cage were simulated. In the first case the faulty resistor is modeled as a null resistance, while in the second case as a doubled resistance because of the redundant nature of the chain. The results are shown in

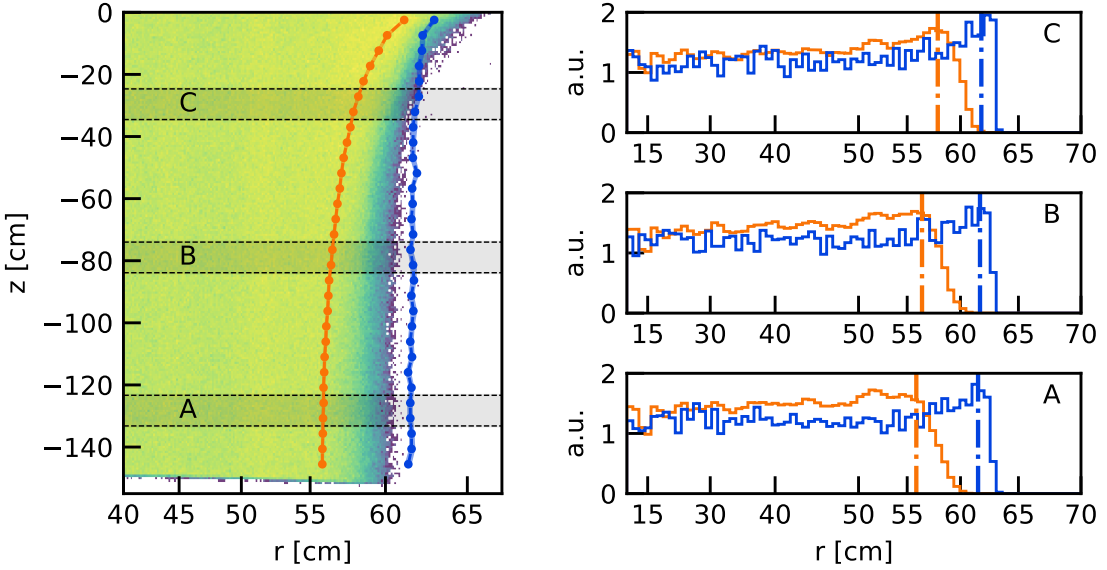


Figure 5.3 Comparison between the 90th percentile radial distribution of ^{83m}Kr data (orange) and the SR0 field simulation (blue) in the (r, z) space (left). The two-dimensional histogram represents all data and its color scale is logarithmic. The distributions of the radial positions in different z slices are plotted on the right, together with the 90th percentile of the distributions (dash-dotted lines).

Fig. 5.4 for a faulty connection at the bottom of the field cage, where the strongest impact is in the case of short-circuit. The induced modification in the field is limited to a very localized area and has a negligible impact on the position distribution. Given the reliability of the deployed resistors and their connection method, the possibility of more than one faulty connection is not considered. Furthermore, the measured value of the field cage total resistance is $(92 \pm 11)\text{ G}\Omega$, in agreement with the expected value $(87.25 \pm 0.05)\text{ G}\Omega$, excluding a large-scale failure of the voltage divider. Thus, a broken resistive chain cannot explain the observed discrepancy.

Therefore, the mismatch between the observed position distribution and the simulation is attributed to a charge accumulation on the PTFE panels. This follows previous works by the LUX collaboration [239] and XENON1T [216, 240], resulting in a good match of simulations and ^{83m}Kr data. In LUX the charge accumulation was observed after a “conditioning” operation of the electrodes, with excessively large UV light emission from the metallic grids ionizing the PTFE, characterized by a larger mobility for holes than electrons hence leading to an accumulation of negative charges [241]. The nature of the TPC walls’

charge accumulation of XENON1T was not completely understood, especially its evolution during the lifetime of the experiment as suggested by the variation over the different science runs of the position distributions [5, 216]. Unlike XENON1T, no time-dependence of the position distribution of ^{83m}Kr events was observed in XENONnT even after six months of operation, hinting towards a more effective charge removal from the TPC walls. This is further discussed in Sec. 5.3. An estimate for the charge accumulation on the PTFE walls is presented below, together with the validation of the new field map using different probes of the electric field.

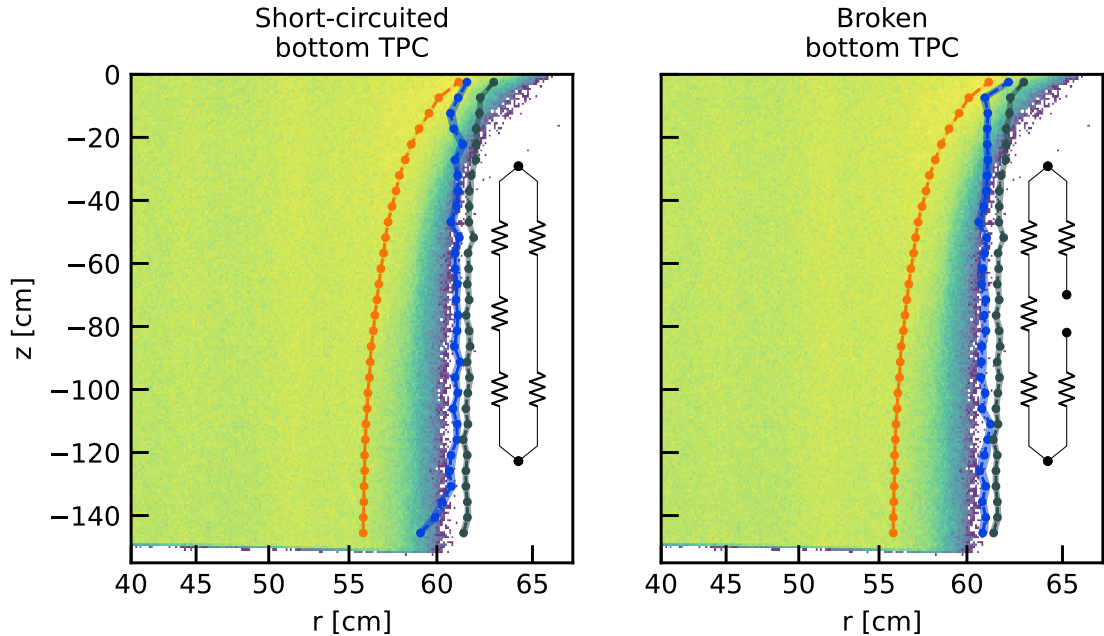


Figure 5.4 Comparison between the 90th percentile radial distribution of ^{83m}Kr data (orange) and simulations with two different resistor failure scenarios located at the bottom of the TPC (blue). The radial distribution without resistive chain rupture is shown in dark gray. The “short-circuited” configuration refers to a null resistance, while the “broken” one refers to a missing connection, simulated as infinite resistance. A sketch of the resistor failure scenario is shown for each configuration. None of the configurations can resolve the mismatch with data. The two-dimensional histogram represents the measured data and its color scale is logarithmic.

5.2.1 | Modeling and matching of the wall charge-up

Because of the lack of a theoretical framework, the charge distribution on the PTFE walls cannot be estimated from first principles, but instead has to be retrieved in a data-driven way. Previous studies by LUX [239] and XENON1T [240] modeled the surface charge density using a piece-wise function both in z and azimuthal angle. Their results showed that the best-matching charge distributions could be well approximated by linear functions. Hence, for XENONnT we consider the surface charge density to follow a linear charge distribution in z :

$$\sigma_w(z) = \lambda \cdot \frac{|z|}{h_{\text{TPC}}} + \sigma_{\text{top}}, \quad (5.1)$$

where $h_{\text{TPC}} = 148.6$ cm is the height of the TPC, σ_{top} the surface charge density at the top of the panels and λ is the difference between top and bottom charge density of the panels, i.e., $\sigma_{\text{bottom}} = \sigma_{\text{top}} + \lambda$. The simulated field maps and position distributions are then evaluated for different combinations of the parameters σ_{top} and λ . This is analogous to what was done and shown in Fig. 5.3 for the SR0 configuration, which corresponds to the configuration $\sigma_{\text{top}} = 0$ and $\lambda = 0$. The *superposition principle* is exploited to minimize the amount of FEM simulations required. This reduces the total amount of simulations to nine “unitary” maps where voltage or charge is non-zero only for a single element. A map for each electrode set to 1 kV was produced, as well as one for the PMT arrays (top and bottom equally biased) and one for the top-most field shaping ring and the entire field cage. Two additional maps were produced corresponding to the case of $\sigma_{\text{top}} = 1 \mu\text{C}/\text{m}^2$ and $\lambda = 1 \mu\text{C}/\text{m}^2$. The field map corresponding to the desired voltage configuration is obtained by summing the individual maps weighted for the corresponding voltage or charge density value.

The optimal values λ and σ_{top} are found by comparing the expected radial distribution along z for different charge distributions with the observed $^{83\text{m}}\text{Kr}$ data. Maps were simulated for parameters in the range $\sigma_{\text{top}} \in [-2, 1.5] \mu\text{C}/\text{m}^2$ and $\lambda \in [-1, 1.5] \mu\text{C}/\text{m}^2$, both with steps of $0.1 \mu\text{C}/\text{m}^2$. For each set of parameters the chi-square χ^2 is estimated as:

$$\chi^2 = \sum_{z_i} \frac{(r_{90p}^{z_i}(\text{data}) - r_{90p}^{z_i}(\text{sim}))^2}{\sigma_{z_i}^2}, \quad (5.2)$$

where $\sigma_{z_i}^2$ is the squared sum of data and simulation uncertainties, and $r_{90p}^{z_i}$ is the 90th percentile of the r -distribution in a given z_i slice. A total of 30 bins in z is considered. The distribution of χ^2 in the $(\sigma_{\text{top}}, \lambda)$ parameter space is shown in Fig. 5.5 left. The right plot

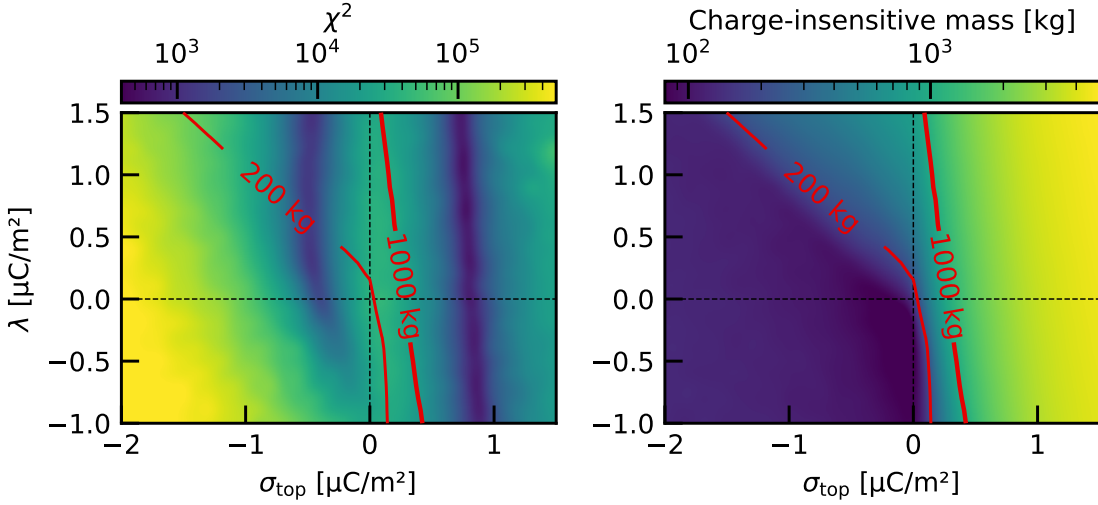


Figure 5.5 Distribution of the χ^2 (left) and charge-insensitive mass (right) for different parameters of the linear surface charge density on the PTFE walls (see text for details). The χ^2 minima for positive σ_{top} can be rejected as they lead to a charge loss of more than half of the TPC's active volume. The contours indicate the configuration with a charge insensitive mass of 200 kg and 1000 kg.

shows the charge-insensitive mass corresponding to each simulated configuration. The χ^2 distribution presents two minimum regions, one characterized by a positive charge at the top of the detector and the other one being negative. Although the χ^2 values are lower for $\sigma_{\text{top}} > 0$, indicating a better agreement between simulation and data, the positive sign of the charge accumulation is suspicious as the high electronegativity of the fluorine in the PTFE polymer makes it more likely to accumulate negative charge. In addition, the right plot of Fig. 5.5 shows that this minimum is characterized by a charge-insensitive mass >3000 kg, corresponding to $>50\%$ of the active volume. This roughly suggests a charge-insensitive liquid xenon skin of 20 cm thickness. This is enough for the TPC to be insensitive to most of the radiogenic gammas from the materials, but this background is observed in XENONnT with a distribution in agreement with the Monte Carlo (MC) simulations. For this reason, this minimum region is not considered as a possible solution. Including the boundary $\sigma_{\text{top}} < 0$, the best match is achieved at $\sigma_{\text{top}} = -0.5 \mu\text{C}/\text{m}^2$ and $\lambda = 0.4 \mu\text{C}/\text{m}^2$.

The statistical uncertainty of the surface charge density is estimated via *bootstrap* technique [242]. The simulated position distribution for each parameter combination is resampled and the configuration of minimum χ^2 is evaluated comparing it to the measured

^{83m}Kr position distribution. This is repeated 1000 times, obtaining a distribution for the best-matching σ_{top} and λ , hence an estimation of the statistical uncertainty of these parameters. The systematic uncertainties are evaluated by changing the binning in z from 15 to 30 with steps of 5, and by considering different percentiles, varying from 80th to 98th. While the σ_{top} parameter shows a large stability, this is not the case for λ . As electrons drift along the TPC, they feel an integrated effect of the surface charge density: the path of an electron produced at the bottom of the TPC is equally affected by the top and bottom charge distribution, while an electron produced at the top feels only the effect of the charge distribution in the upper part of the TPC walls. This means that the observed position distribution carries more information about the surface charge density of the upper section of the TPC than of the lower section. This difference could explain the larger uncertainty on the λ parameter than on σ_{top} , as the former encodes the surface charge distribution at the bottom of the TPC. The final parameters for the linear charge model of the reflectors are:

$$\begin{aligned}\sigma_{\text{top}} &= (-0.50 \pm 0.05_{\text{(sys)}} \pm 0.02_{\text{(stat)}}) \mu\text{C}/\text{m}^2, \\ \lambda &= (0.40 \pm 0.15_{\text{(sys)}}^{+0.20}_{-0.10_{\text{(stat)}}}) \mu\text{C}/\text{m}^2.\end{aligned}$$

The resulting radial event distribution is shown in the left plot of Fig. 5.6. The corresponding electric field map is shown in the middle plot, as well as its associated survival probability map on the right. Including the surface charge distribution on the TPC wall, the average electric field within the FV is 22.6 V/cm with a spread of 13.2 % as derived from simulation, while the CIV corresponds to a mass of 112 kg. For comparison, if the top-most field shaping ring had not been independently biased but simply short-circuited with the gate (as the optimization of the field design suggested), the field spread under these conditions would have been 46 %, more than three times larger, and the charge-insensitive mass would be 91 kg.

5.2.2 | Validation of the electric field map

The new field map obtained by matching the position distribution is solely based on the impact of the drift field on the propagation of electrons. However, the field affects also charge and light yields, as detailed in Sec. 2.1. This means that the amplitude of the S1 and S2 peaks carries information about the electric field of the position inside the TPC where scintillation photons and free electrons were generated. Two different method exploiting the yields' dependence on the field are used to validate the new field map of Fig. 5.6. In the

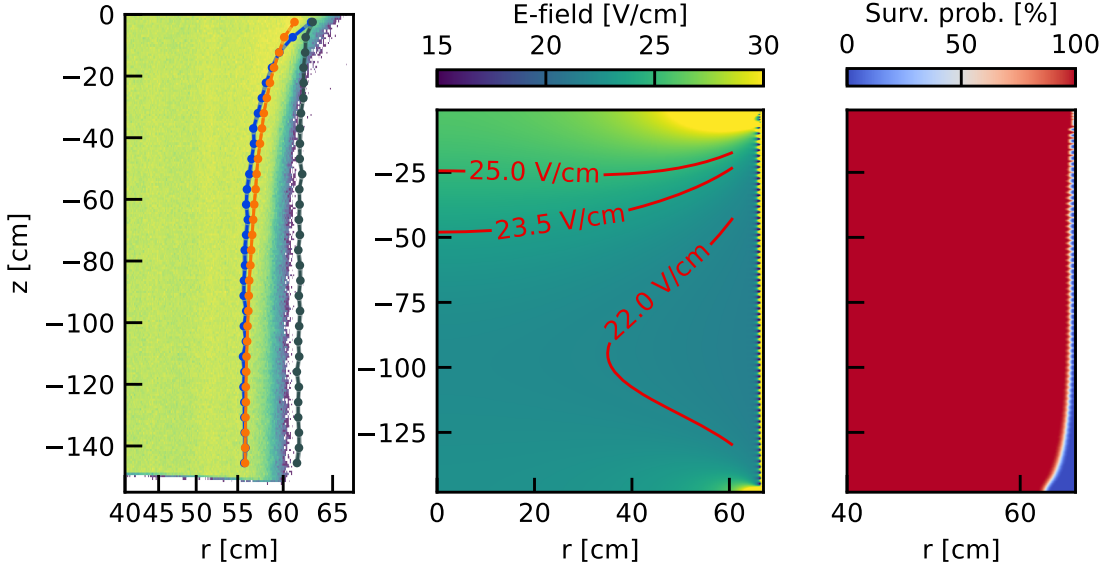


Figure 5.6 (left) Measured 90th percentile radial distribution of the ^{83m}Kr data (orange) with the simulated one with charge PTFE walls (blue) and without (dark green). The two-dimensional histogram shows the event distribution and its color scale is logarithmic. **(middle)** Electric field map with the best-matching charge distribution. **(right)** Survival probability map using the field map shown in the middle.

first case a data-driven map is obtained by studying the ratio between the two S1 signals of the ^{83m}Kr events. The two maps agree within uncertainties. In the second case, the new field map is used to correct the S2 amplitude accounting for the charge yield dependence in the electric field. The inclusion of this correction leads to the match of the electron lifetimes obtained with different calibration sources which are otherwise in disagreement with the established knowledge that the lifetime solely depends on the xenon purity.

S1 ratio of ^{83m}Kr events

A fraction of the ^{83m}Kr events observed in XENONnT is characterized by two distinct S1 peaks, S1_a from the 32.2 keV transition and S1_b from the 9.4 keV one. The light yield of the different energy depositions have different dependence on the electric field. Hence, the ratio between the signal sizes returns useful information on the field intensity at the interaction position as long as the motion of the ^{83m}Kr isotope is negligible. A 32.2 keV electron emitted from the atom at rest leads to a recoil of the krypton atom of about 10 mm/s:

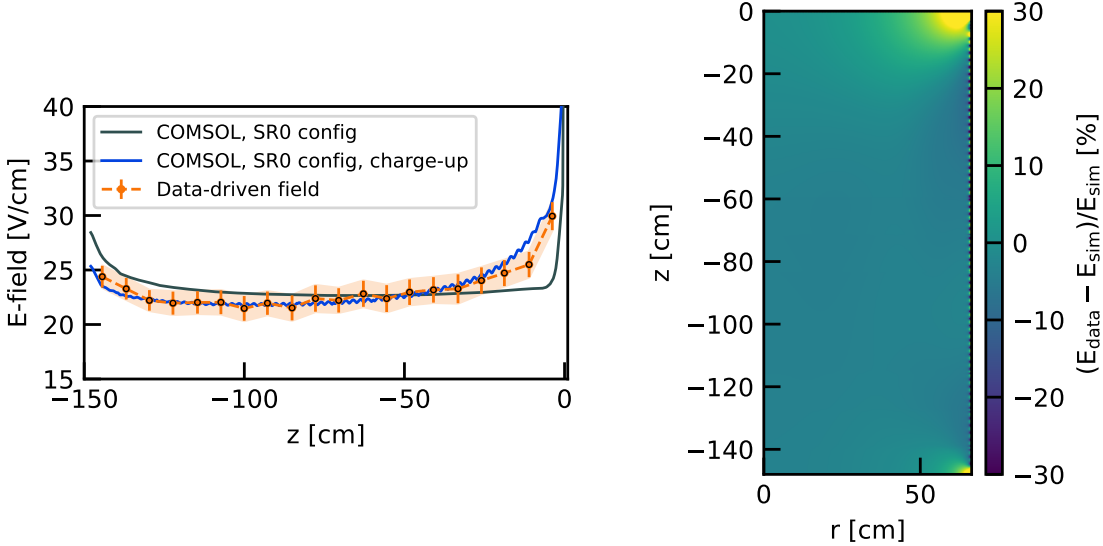


Figure 5.7 Results from the data-driven electric field computation using the ratio of the two ^{83m}Kr scintillation signals S_1 . In the left panel, the projection along z for $r < 66\text{ cm}$ (orange line) is compared to the COMSOL results with (gray) and without (blue) charge-up of the walls. The better agreement when including the charge-up at the reflectors is evident. The relative difference between the data-driven field map and the simulation is shown in the (r, z) space (right panel). The data-driven and simulated electric fields differ of only $(3 \pm 2)\%$ within the fiducial volume used for the first results of SR0 (see Sec. 5.6).

including also the XENON1T convection speed of 3 mm/s [243], the expected displacement for a krypton isotope in $1\text{ }\mu\text{s}$ is less than 15 nm . This is far below the mm-scale position resolution of the XENONnT TPC, thus the energy depositions can be assumed to be at the same position. The S_{1b}/S_{1a} ratio as a function of the field is modeled using dedicated low field measurements by the MPIK Heidelberg group [142]. Because of the space-charge effect from the 32.2 keV interaction, the S_{1b}/S_{1a} ratio depends on the time separation between the two S_1 s [244]. As the ^{83m}Kr events in XENONnT and in the Heidelberg measurements are selected using different S_1 time differences, this introduces a bias in the model. This is solved by normalizing the S_1 s ratio model for the value measured in an inner TPC “control region” with a highly homogeneous field estimated with COMSOL. The data-driven field is presented in the left panel of Fig. 5.7 as projection for different z bins and $r < 66\text{ cm}$. The result is compared to the same projection from the simulated SR0 field map, with and without charge-up at the walls. The data shows a much better agreement with the new field map, especially in the top part of the detector ($z > -50\text{ cm}$).

The relative difference between the two maps is shown in the right panel of Fig. 5.7. A difference $<10\%$ is one of the main requirements for the definition of the fiducial volume for the SR0 analyses, as discussed in Sec. 5.6. The final difference between the observed electric field and the simulation in the fiducial volume has an average of $(3 \pm 2)\%$, showing slightly smaller values for the data-driven map than the simulation.

Electron lifetime

The electron lifetime introduced in Sec. 2.1 describes the loss of ionization electrons to electronegative impurities in the liquid xenon as they drift towards the liquid-gas interface. This quantity is estimated by fitting the median of the S2 signal with an exponential function of the drift time:

$$S2(t) = S2(0) e^{-t/\tau_{e^-}}, \quad (5.3)$$

with τ_{e^-} being the electron lifetime and $S2(0)$ the signal amplitude at zero drift time, hence not affected by electron losses. An example of the exponential fit is shown in Fig. 5.8 for a ^{83m}Kr calibration. This measurement assumes that the original signal size $S2(0)$ for

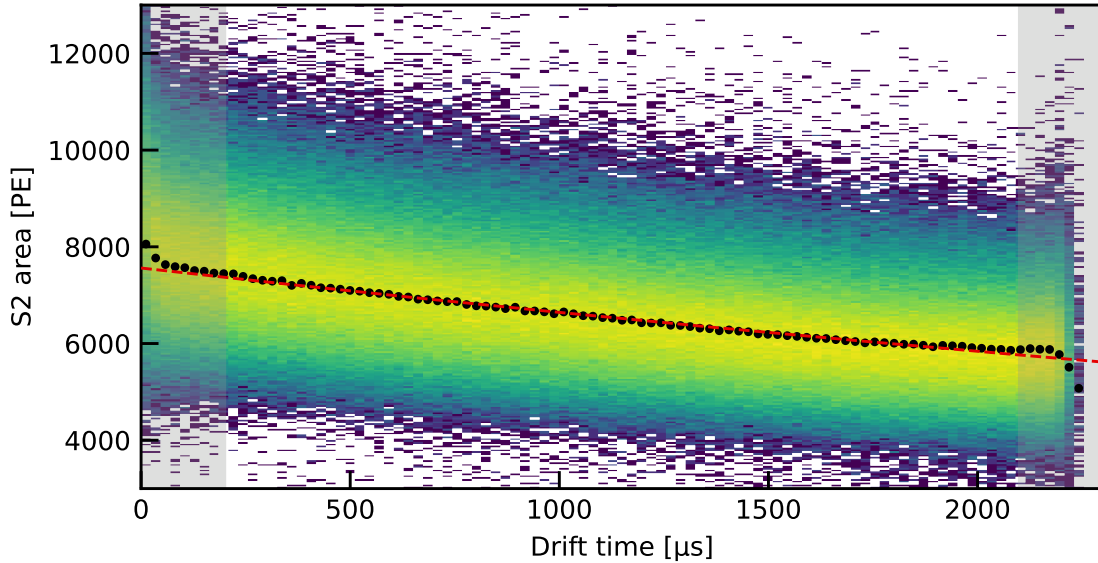


Figure 5.8 Example of an exponential fit of Eq. (5.3) to the median of the S2 area as a function of the drift time to derive the electron lifetime estimation. The color scale is logarithmic. The gray regions are excluded from the fit to avoid the impact of the more inhomogeneous field at the top and bottom of the TPC.

the calibration event is the same throughout the entire detector. Since the charge yield depends on the electric field at the interaction site, this assumption does not hold in case of a non-homogeneous field. This means that the electron lifetime derived from the fit is an effective parameter $\tau_{e^-}^{\text{eff}}$ that includes drift field effects. Thus, the proper fit to estimate the physical electron lifetime needs to be rewritten as:

$$S2(t) = S2(0) e^{-t/\tau_{e^-}^{\text{eff}}} = S2(0) Q_y(t) e^{-t/\tau_{e^-}}, \quad (5.4)$$

where $Q_y(t)$ includes the impact of the electric field on the charge yield as a function of the interaction depth z in the TPC. The effect $Q_y(t)$ of the electric field on the charge yield depends on the type of interaction and the total energy deposition, hence this term can explain the 10 % difference in electron lifetimes derived from $^{83\text{m}}\text{Kr}$ and ^{222}Rn sources in XENON1T [5].

XENONnT also derived different electron lifetime values from different sources, when using the definition of Eq. (5.3). The electron lifetime evolution during SR0 is shown in the top panel of Fig. 5.9 as coming from three different sources: $^{83\text{m}}\text{Kr}$, the 5.9 MeV α decay of ^{222}Rn , and the 2.8 keV peak from ^{37}Ar K-shell electron capture. Because of its long lifetime, the ^{37}Ar calibration was carried out only at the end of SR0. These values disagree amongst each other and also with the independent measurement of the purity monitor (PM) detailed in Sec. 2.4, shown as a gray shaded area. Following Eq. (5.4), the effect of the charge yield coming from the non-homogeneous field can be decoupled from the electron lifetime. This is done by scaling the observed S2 size with the charge yield term $Q_y(t)$. The value of this scaling parameter depends on the event position, the considered field map and the calibration source. The results from [142] are used for $^{83\text{m}}\text{Kr}$ and ^{222}Rn , while an extrapolation of the results of [245] are used for ^{37}Ar . The middle and bottom panels of Fig. 5.9 show the electron lifetime as a result of this S2 correction using the field map without and with the charge-up of the walls. The correction based on the new map shows an agreement among all sources and the PM within the uncertainties for almost the entire SR0. These results can be used as a validation of the new electric field map only once the field-dependent nature of the electron lifetime measurement is confirmed. This was tested during a special set of runs after SR0 which are discussed in Sec. 5.4, proving that the matching of the measured electron lifetimes during SR0 using the new field map is not simply due to a statistical fluke.

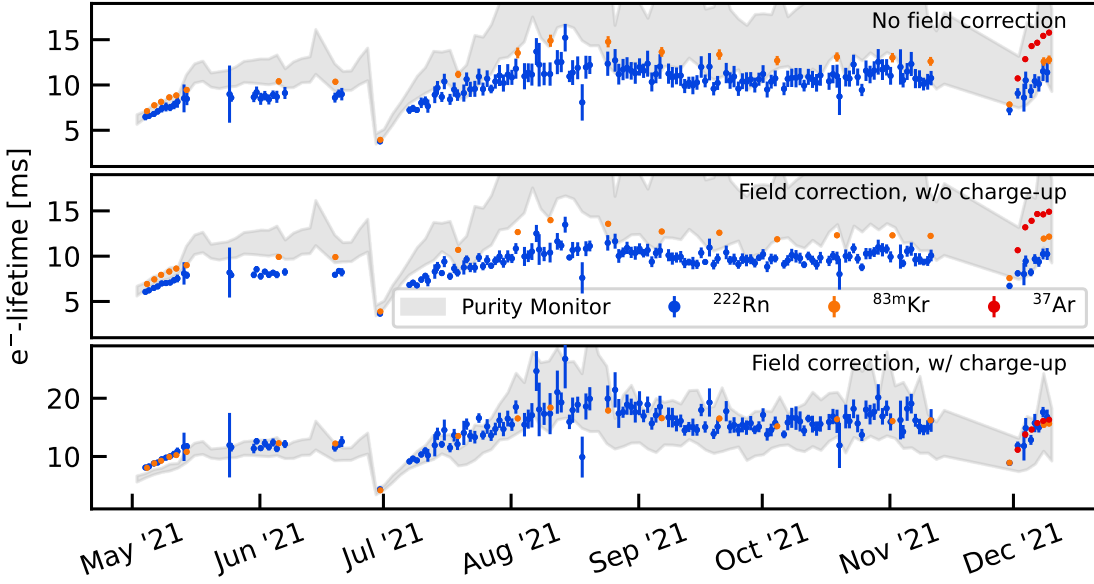


Figure 5.9 Electron lifetime evolution during SR0 as derived from three different calibration sources (^{222}Rn , $^{83\text{m}}\text{Kr}$ and ^{37}Ar) and the independent measurements of the purity monitor. For each panel, a different field correction is applied: (top) no correction, (middle) field-corrected using the field map of Fig. 5.1a, (bottom) field-corrected using the map with wall charge-up of Fig. 5.6. Using the latter map, the measurements from the different sources agree with each other and with the purity monitor values.

5.3 | Time dependence of the electric field

The radial event distribution observed in XENON1T presented a stronger inward push at the end of the second science run (SR1) than at its start [216]. In the time span of about a year (from February, 2017 to January, 2018) the reconstructed 95th percentile of the $^{83\text{m}}\text{Kr}$ population at the bottom of the TPC was pushed inwards by 3.9 cm. This time-dependence was explained in terms of an increasing charge accumulation on the PTFE walls over the entire data taking period, leading to a non-stationary electric field. Looking at XENONnT data, the radial distribution comparison shown in Fig. 5.10 between a $^{83\text{m}}\text{Kr}$ calibration from May and November 2021 does not indicate any time evolution. The difference of the distributions with respect to the average over SR0 is shown in the right panel of Fig. 5.10, with effects in the order of few millimeters or less.

A XENON1T-like time dependence of the electric field would be observed in data as an increasing inward push of the position reconstruction. This translates in a decreasing

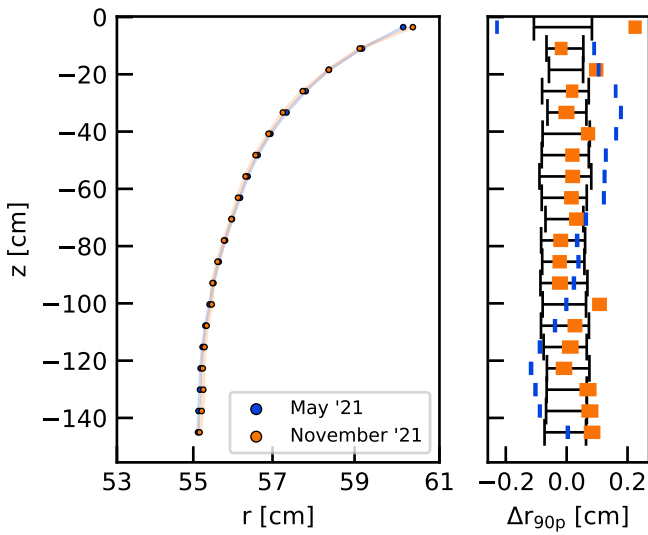


Figure 5.10 Comparison of the radial distribution of $^{83\text{m}}\text{Kr}$ calibrations from May (blue) and November (orange) 2021. The residual plot shows the difference compared to the average of the entire SR0 calibration data set. In black the 68 % C.L. of the SR0 average.

position of the 90th percentile of the radial distribution of the $^{83\text{m}}\text{Kr}$ population over time along the entire detector. The possibility of a time evolution of the position distribution of the $^{83\text{m}}\text{Kr}$ events is tested over a time span of seven months, using a total of 15 krypton calibration campaigns. Similarly to what done in Fig. 5.3 for the calibration distribution (orange), the radial distribution is evaluated for each SR0 $^{83\text{m}}\text{Kr}$ calibration. For each 90th percentile radius $r_{90\text{p}}$ along the TPC, the 68 % C.L. interval is estimated by considering the 16th and 84th percentile of the cumulative binomial distribution with probability 90 %. These values return the indices corresponding to the lower and upper limit of $r_{90\text{p}}$ in the given z bin. In the case of a constant electric field, the difference between the average $\langle r_{90\text{p}} \rangle_{\text{SR0}}$ and $r_{90\text{p}}$ for a given calibration is solely due to its normally distributed statistical nature. The value $r_{90\text{p}}$ for each z slice has the same probability of being larger or smaller than the average $\langle r_{90\text{p}} \rangle_{\text{SR0}}$ for the same slice. In the case of a radial distribution of calibration data $r_{90\text{p}}$ which is consistently larger (smaller) than the SR0 average along the entire TPC, this would hint towards an accumulation of negative (positive) charge. Hence, the hypothesis of a time-independent charge-up of the TPC walls can be tested by considering the p -value of the binomial distribution for the difference $\Delta r_{90\text{p}}^i = r_{90\text{p}}^i - \langle r_{90\text{p}} \rangle_{\text{SR0}}$, where the i^{th} $^{83\text{m}}\text{Kr}$ calibration is compared to the SR0 average. This is done using a total of 20 slices in z , but similar results are obtained when changing the binning. Given a $^{83\text{m}}\text{Kr}$ data set i and fixing the bin size along z , the double-tailed p -value for the observed number of non-positive $\Delta r_{90\text{p}}^i$ is estimated for a binomial distribution with 50 % probability. The double-tailed p -value is chosen as it is sensitive both to positive and negative differences, corresponding to outwards and inwards pushes. An example of

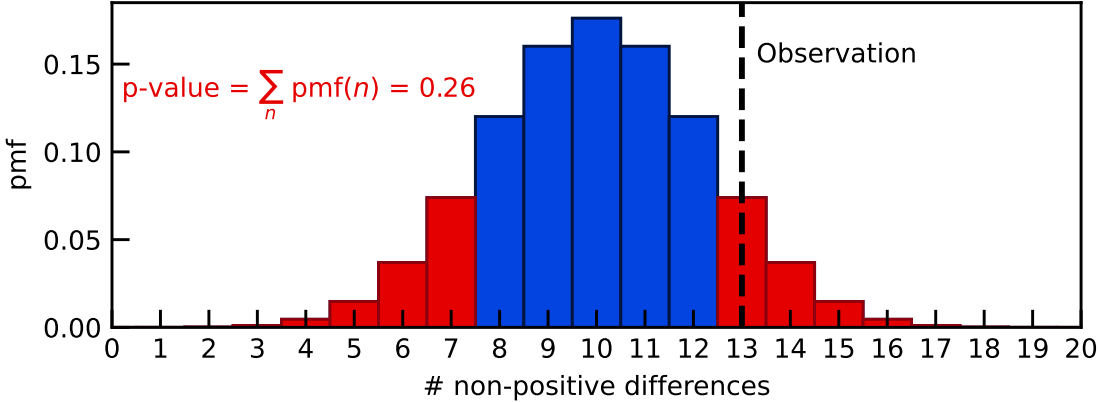


Figure 5.11 Example of a double-tailed binomial p -value calculation for a radial distribution of 20 bins in z and an observation of 13 non-positive differences (i.e., compatible to an inwards field push). The p -value is given by the sum of the individual probabilities (pmf, probability mass function) for an equally or less probable observation (red bars, opposite to the blue bars indicating more probable observations).

a binomial distribution for 20 z bins with 13 non-positive $\Delta r_{90\text{p}}^i$ differences is shown in Fig. 5.11, resulting in a p -value of 0.26. The large p -value makes it not possible to exclude the hypothesis of time-independence. The results for different calibration sets are shown in Fig. 5.12. The uncertainties are the 16th and 84th percentile of the p -value distribution, as obtained via MC toys. The hypothesis of a time-independent charge-up cannot be rejected with p -value $< 5\%$ for most of the calibrations and no clear trend is observed in the time distribution of the p -values. The absence of a clear change in the position distribution over a period of seven months excludes a XENON1T-like charge accumulation. The exclusion of such accumulations supports the design choices for XENONnT taken to reduce the charge accumulation on the PTFE walls, such as the field cage touching the reflectors and the “charge-collecting” holes along the sliding reflectors (see Sec. 4.1).

A few data sets in Fig. 5.12 present a p -value lower than 1%: two calibrations from June and one from December. A XENON1T-like accumulation process is excluded as explanation, as it can hardly explain a change in the position distribution for only a limited period of time. During SR0, spatially localized increases of the detected single electron rate (*hot spots*) forced a temporary ramp-down of the anode, typically ramped up again within 24 hours. Each ramping cycle of the anode voltage resulted in a “relaxation” period of ~ 3 days. During this period, the electroluminescence gain of a single electron extracted from the liquid xenon (SE gain) showed an exponential decrease of up to 10%, eventually

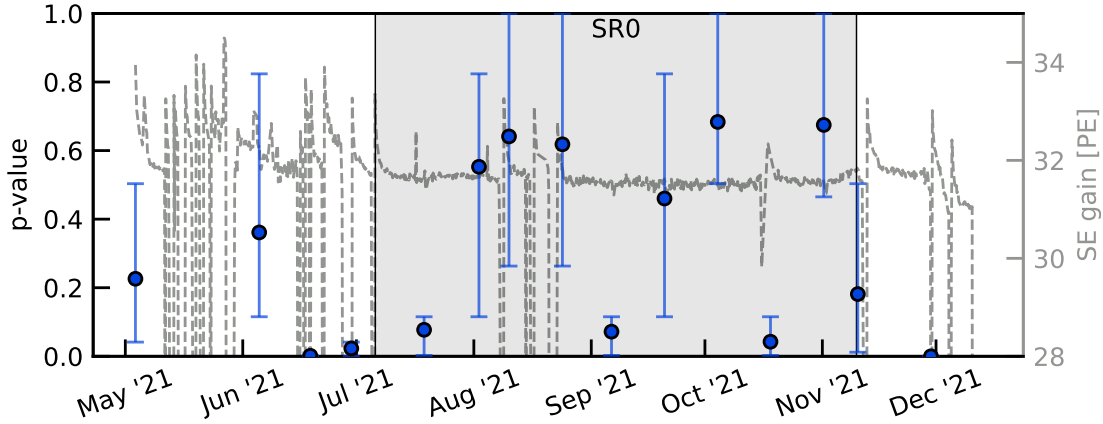


Figure 5.12 Time evolution of the double-tailed binomial p -value of the SR0 $^{83\text{m}}\text{Kr}$ calibrations using 20 bins in z . The SE gain (dashed gray line) is overlaid to highlight the correspondence between its changes and low p -values. The calibration data sets with p -value $<1\%$ happen within three days from an anode voltage cycle.

stabilizing around the nominal operation value. The SE gain is plotted as a dashed gray line in Fig. 5.12, where these relaxation periods are evident as “spiky” features. In addition, after each anode ramping cycle the electron extraction efficiency is smaller, as observed by comparing the $^{83\text{m}}\text{Kr}$ size to the SE gain. This follows a similarly increasing exponential trend as the SE gain, until it is stabilizing around the nominal value within around 3 days. A possible explanation for this relaxation period is a change in the width of the gas gap, possibly due to the charge-up of the liquid-gas interface. This hypothesis is further supported by the evolution of the time spread of the SE signal, which is narrower after the anode cycle and increasing following the same trend of the SE gain. Fig. 5.12 shows that the calibration sets with the lowest p -values happened within three days from the anode ramping cycle, unlike the other calibrations. This means that the conditions of the detector were not the same, explaining the differences in the observed event position distribution.

5.4 | Impact of field cage tuning on TPC drift field

After the end of SR0 a set of dedicated $^{83\text{m}}\text{Kr}$ runs was acquired to study the impact of the electric field homogeneity on the electrons’ propagation in the liquid xenon target. This test was realized by varying the voltage of the top field shaping ring V_{top} while otherwise keeping the SR0 electrodes’ voltages. The tuning of the field cage has a negligible impact

on the average strength of the electric field, but affects *de facto* only the field homogeneity and the direction of the field lines. As XENONnT’s independent bias voltage for the top of the field cage is an innovation for multi-tonne liquid xenon TPCs, this work represents the first study of this kind.

The entire test took about one day and it consisted of three 3 h-long runs with V_{top} set to +300 V, +500 V and +750 V, and two 2 h-long runs at +900 V and +1000 V. The later runs were shorter as a large CIV is expected for this high values of V_{top} . Although the charge accumulation on the PTFE panels due to the CIV is expected to be in the order of few negligible pC/d, it was decided to reduce the run time, which was, however, still sufficient given the high $^{83\text{m}}\text{Kr}$ rate. Several calibration runs were taken at SR0 configuration ($V_{\text{top}} = 650$ V) before and after the test. These were used not only as additional data point for the study, but also to estimate time-dependent effects, e.g., from wall charge up.

5.4.1 | Charge-insensitive volume

As discussed in Sec. 4.3, a large voltage difference between gate electrode and the field shaping ring of the field cage with $V_{\text{top}} > V_{\text{gate}}$ leads to an increase of the charge-insensitive volume (CIV). The evolution of the CIV as a function of V_{top} can be directly measured during the field cage test by observing the evolution of the $^{83\text{m}}\text{Kr}$ event rate. The krypton source rate does not depend on the electric field, as its injection in the liquid xenon depends solely on the gas handling system. For this reason, an increase of the CIV will manifest as a loss of S2 signals, thus a decrease of the detected $^{83\text{m}}\text{Kr}$ S2 rate and an unaffected S1 rate. This results in an overall decrease of $^{83\text{m}}\text{Kr}$ event rate, as the processing algorithm cannot pair an S1 and S2 peak.

Due to the different field configurations during the test, a loose box cut in (S1, S2) was preferred over the specialized $^{83\text{m}}\text{Kr}$ selection cuts used in SR0. The use of looser cuts on the uncorrected signals avoids the introduction of biases coming from the population selection, at the price of a less pure data set. Individual S1 and S2 peaks were selected within the range of the box cut for the $^{83\text{m}}\text{Kr}$ selection. In this case no matching between peaks is required, while the selected area ranges are the same as the event selection: [150, 800] PE for S1 and [2500, 17 500] PE for S2. During the krypton calibration campaign the ^{83}Rb source is left open, hence the $^{83\text{m}}\text{Kr}$ activity is in secular equilibrium with the 86.2 d half-life of its isotope parent [238]. The decay is estimated from the krypton rate

evolution before and after the test, as shown in Fig. 5.13. A linear function is fitted to the data, returning an event rate decrease of $(1.01 \pm 0.12)\%$ in one day, in agreement with the expected 0.8% from the ^{83}Rb lifetime. An identical decrease is observed for the ^{83m}Kr S1 peaks: this excludes an increasing CIV as source of this rate reduction, as this would affect only S2 signals leaving the S1 rate unaffected.

The rate for different values of V_{top} is plotted in Fig. 5.14. The rates are corrected for the source decay discussed above. No change in S1 rate is observed, while a clear drop of the S2 and event rates is observed for $V_{\text{top}} > 750$ V. This is an indication of an increase of the CIV with a trend resembling the results shown in Fig. 4.16. The expected rates from field simulations are compared to the measurements. The rate is calculated by estimating the CIV for each configuration and normalizing the simulated rates to match the data at $V_{\text{top}} = 300$ V. A disagreement between data and simulation for larger top field cage voltages is clear in Fig. 5.14. This is likely due to the simplified modeling of the charge distribution in the simulation and the dependence of the CIV on the field lines. Indeed, the direction of the field lines is overall more sensitive to the distribution of the surface charge density on the reflector than the intensity of the electric field is.

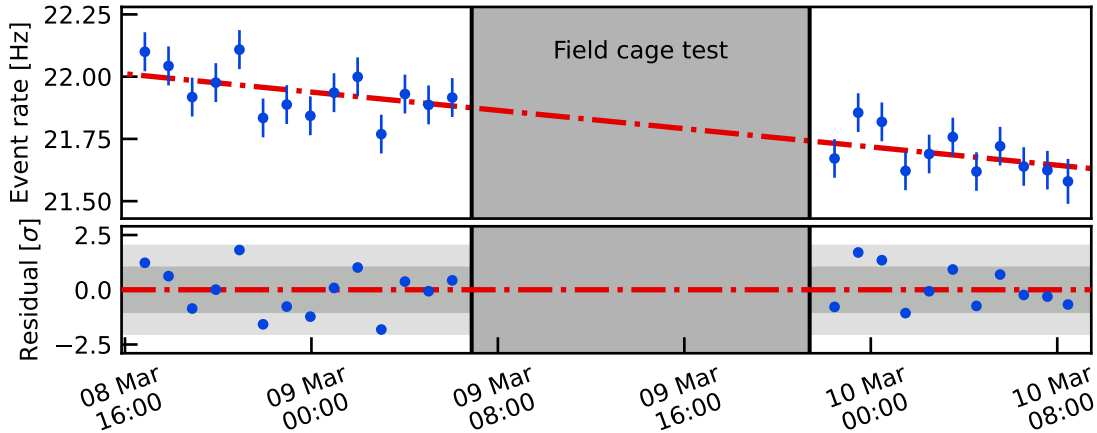


Figure 5.13 ^{83m}Kr event rate acquired at the SR0 voltage configuration before and after the field cage test. The observed rate decrease agrees with the lifetime of the parent isotope ^{83}Rb . The red dash-dotted lines show the exponential fit to the data.

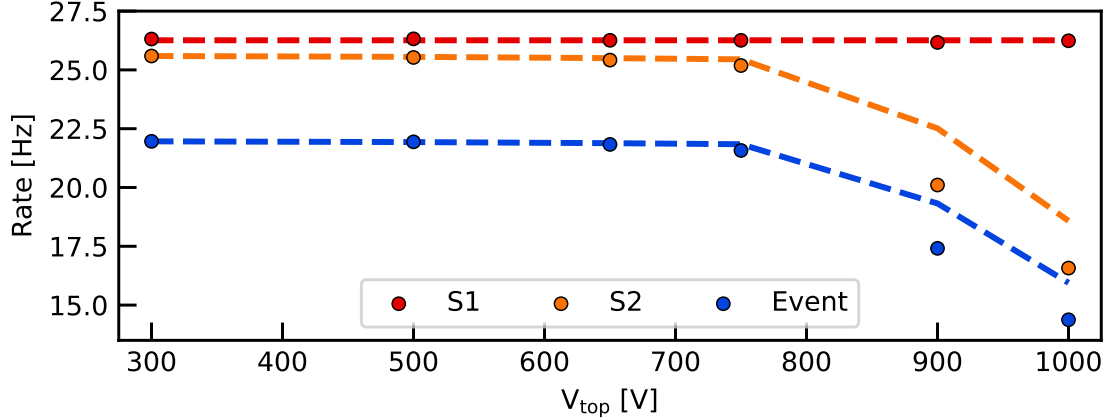


Figure 5.14 Rate as a function of the voltage of the top field shaping ring for ^{83m}Kr events and S1 and S2 peaks within the same ^{83m}Kr selection ranges. The effect of the charge-insensitive mass is evident for $V_{\text{top}} > 750$ V, as S2 and event rates decrease while the S1 rate stays constant. The observed data points are compared to the corresponding simulations normalized to match at 300 V (dashed lines).

5.4.2 | Position distribution and wall charge-up

The variation of the field cage bias voltage V_{top} has a major impact on the field lines and the path of the electrons in the drift region. This becomes clear when looking at the position distribution of ^{83m}Kr events as the field cage is tuned to different voltages. The distributions are shown in Fig. 5.15. A stronger inward push characterizes lower values of V_{top} , while almost no distortion is observed for higher values. For low voltages, the “effective” potential coming from the field leakage through the gate grid electrode is such that the electrons feel a repulsive force from the field cage. As V_{top} increases, the top field shaping ring of the field cage acts more as an anodic element, attracting electrons and thus counteracting the inward push. This is observed for voltages up to 750 V: the position distribution becomes more uniform the higher the voltage applied. However, no improvement is observed for even higher voltages. This behaviour can be explained in terms of charge-insensitive volume, as suggested by the correlation of this change with the rate evolution of Fig. 5.14. The electrons drifting close to the TPC walls feel a stronger attraction towards the field shaping electrodes than towards the anode as they reach the top of the TPC. This leads to a relatively thin charge-insensitive liquid xenon layer surrounding the active volume, equivalent to the gray volume of Fig. 4.15. Independently of the size of this insensitive layer, the electrons liberated right outside it are focused at

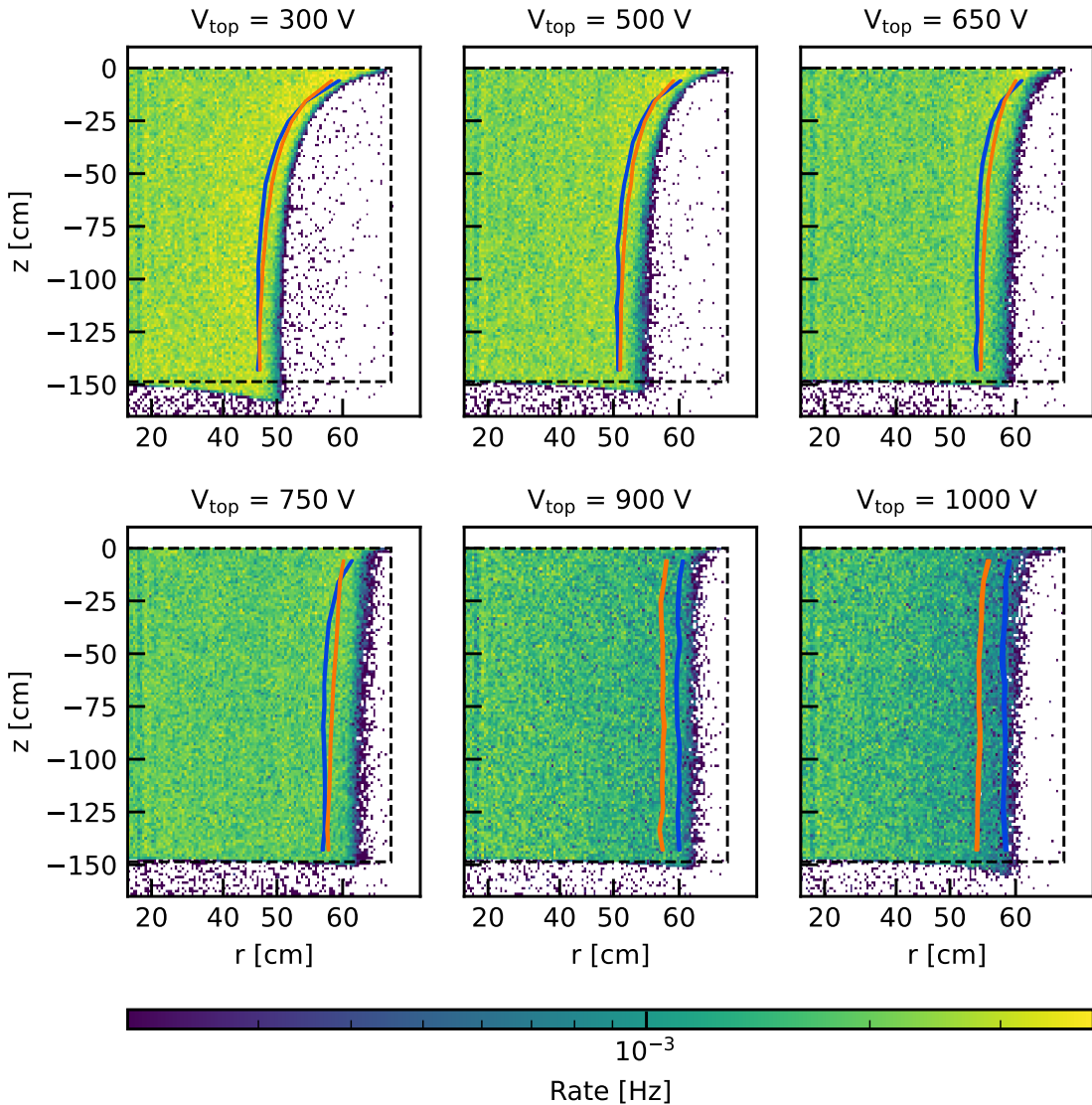


Figure 5.15 (r, z) position distribution of the ^{83m}Kr events for different field cage tuning voltages V_{top} . The orange line represents the 90th percentile radial distribution from data, in good agreement with the simulated distribution (blue line) for voltages up to 750 V, using the charge-up model from Sec. 5.2.

the same radial position of ~ 60 cm at the liquid-gas interface. This results in an almost constant reconstructed radial distribution, together with a fast increase of the CIV. Since the rate decreases while the observed position distribution is unchanged, a lower event density characterizes voltages above 750 V.

The 90th percentile radial distribution along z is plotted in orange for each distribution in Fig. 5.15. This observable is compared to the corresponding expected distribution (blue) coming from the simulations with the same V_{top} and the charge accumulation estimated in Sec. 5.2. A good agreement is observed for voltages up to 750 V. Above this voltage the radial distribution from simulations is up to 7 cm larger than data. As for the CIV estimation, the 90th percentile depends on the direction of the field lines and it is more sensitive to a mismodeling of the surface charge distribution. The framework of Sec. 5.2 was applied to each test run to estimate the parameters σ_{top} and λ , and the results are shown in Fig. 5.16. Systematic and statistical errors are estimated in the same way. The parameters agree among them for voltages below 750 V, showing a slight disagreement with

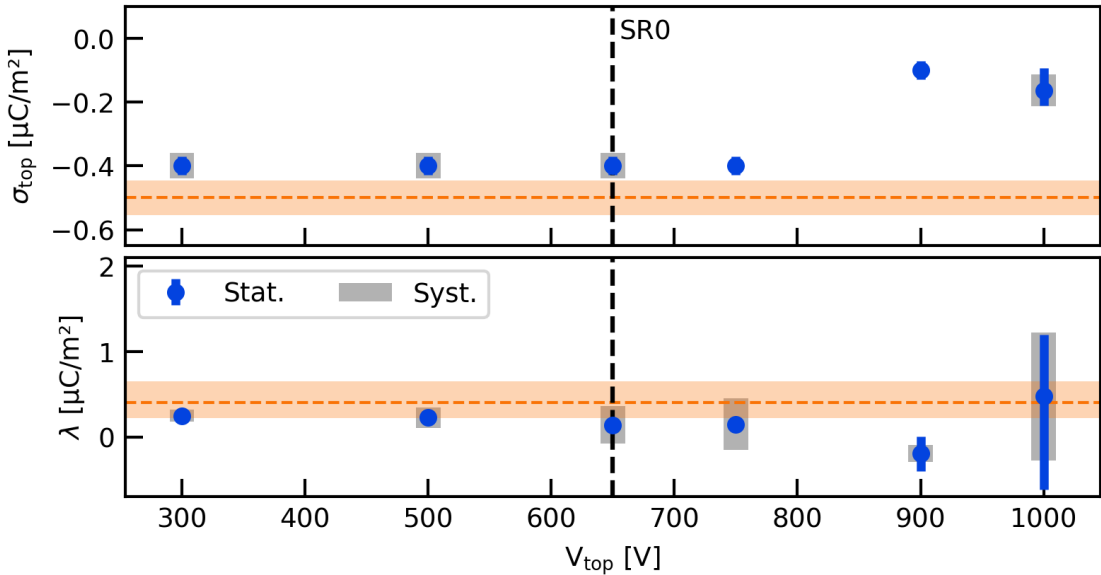


Figure 5.16 Results from matching the observed radial event distributions (see Fig. 5.15) for different field cage tuning voltages V_{top} to simulations including a linear charge-up of the PTFE reflectors, as done in Sec. 5.2. For $V_{\text{top}} \leq 750$ V the results agree with the SR0 results shown as orange dashed lines with their uncertainties. The value shown for $V_{\text{top}} = 650$ V (SR0 value) considers only the calibration data from the test and not all the SR0 ^{83m}Kr calibration campaigns and it uses an updated processing software.

the results obtained in Sec. 5.2, reported as orange lines with uncertainty in Fig. 5.16. This small shift can be explained by the fact that the version of the software used to process the data, *straxen* [234], are not the same. The results for voltages $V_{\text{top}} \geq 900$ V deviate from the rest of the runs and present very large uncertainties at 1000 V. This might be due to the loss of information coming from the position distribution as the CIV increases, as discussed above. The results shows no change in the charge distribution on the panel, excluding the migration of charges as the electric field configuration is changed.

5.4.3 | Electron lifetime evolution

The observed discrepancy of the electron lifetime measurements using different sources was already discussed in Sec. 5.2.2. The mismatch could be fixed by correcting the S2 signals for their relative charge yield based on the field intensity at the interaction position, as derived from the simulated drift field map. This successful correction suggests that the electron lifetime is an effective parameter which includes the impact of the field inhomogeneity. This hypothesis can be further tested by studying the evolution of the electron lifetime for different voltages of the top field shaping ring. The electron lifetime for each voltage configuration was measured using events within the inner 40 cm radius. This excludes any edge effect coming from the strong field deformation. The median of the S2 area in different drift time slices is fitted with an exponential decay, as following Eq. (5.3). This returns the same “effective” electron lifetime as reported in the top panel of Fig. 5.9. An example of this fit for $V_{\text{top}} = 300$ V is shown in Fig. 5.17 (top). The distribution departs from the exponential decay at the top of the TPC. This is in agreement with the expected electric field map, characterized by a larger field at the top of the detector, hence leading to a larger charge yield. Considering the ^{83m}Kr charge yield model from [142], it is possible to correct the S2 signal of each event based on the reconstructed position and the V_{top} value. The resulting corrected S2 ($S2'$) area as a function of the drift time is shown in Fig. 5.17 (bottom). This distribution is well described by an exponential function, even at the top of the TPC. Drift times close to 0 and above 2200 μs are characterized by a steep jump in the $cS2$ values. The reconstructed positions of these events lie in the TPC region characterized by a higher field intensity, such as around the gate or cathode wires. This is the result of the comparison of the field map calculated based on an idealized geometry with the reconstructed position of the interactions, characterized by a finite resolution.

After applying the proper field correction to each data set, the electron lifetime is estimated for different field cage bias voltages. The results are shown in Fig. 5.18 in blue,

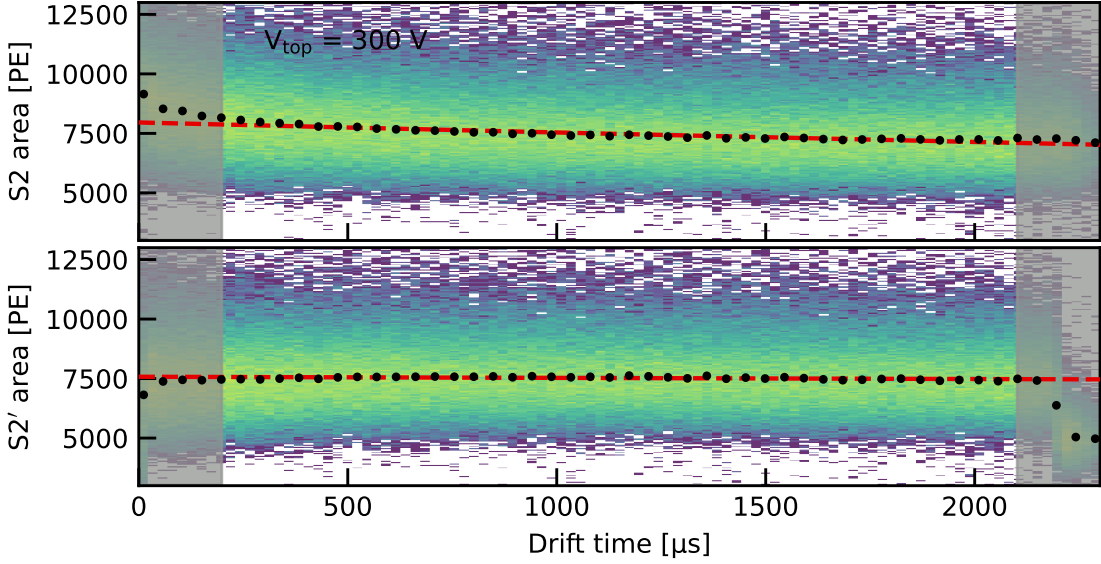


Figure 5.17 Size of the ^{83m}Kr S2 signal as a function of the interaction drift time for $V_{\text{top}} = 300 \text{ V}$, both uncorrected (top) and corrected (bottom) for the charge yield at the interaction position. The median for different z bins (black dots) are fitted with an exponential function excluding the shaded regions. The result (red dashed line) returns the electron lifetime. The color scale is logarithmic.

along with the orange data points representing the electron lifetime naively measured using the uncorrected S2 size. The correlation between the uncorrected electron lifetime and the voltage of the top field shaping ring is striking: the lifetime increases of about an order of magnitude when ramping from 300 V to 1000 V. This evolution can be intuitively explained by the fact that a lower V_{top} implies a higher electric field at the top of the TPC. A higher field strength boosts the electron-ion separation which lowers the recombination probability and increases the charge yield. A larger charge yield at the top of the detector with respect to its bottom mimics the effect of electronegative impurities, reducing the inferred electron lifetime. As this difference decreases with V_{top} , the effective lifetime increases and gets larger than the actual value in case the field at the top is lower than at the bottom. Any time dependent effect is excluded by estimating the lifetime before and after the test at SR0 voltage configuration. When applying the field corrections, all lifetimes agree within uncertainties with the average (37.9 ± 0.6) ms.

These results prove that the electron lifetime calculated using the observed S2 area returns an effective value which includes an effect due to the inhomogeneities of the charge

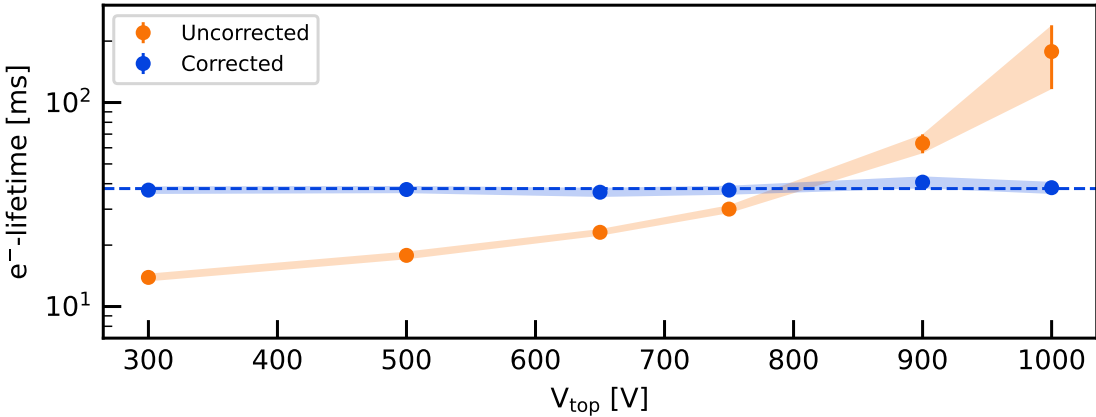


Figure 5.18 Electron lifetime derived from a fit to the data for different voltages V_{top} of the top field cage shaping ring. The lifetime derived ignoring field effects (orange) shows a strong dependence on the field cage tuning voltage. Once these effects are included using the proper field map, all electron lifetime measurements (blue) agree within uncertainties, with the average shown as dashed blue line. The shaded areas indicate the uncertainties.

yield. Using this effective lifetime to correct the S2 area is inaccurate, as this would assume the charge yield dependence of the calibration source used to obtain the electron lifetime, e.g., $^{83\text{m}}\text{Kr}$, even when this is different like in the case of NR interactions due to WIMP scattering.

5.5 | Field distortion correction map

The inhomogeneity of the electric drift field leads to a distortion of the path of the liberated electrons due to the non-zero radial component of the drift field. For this reason, the *reconstructed* position of the S2 signal produced by these electrons differs from the *true* interaction position. The distortion of the position reconstruction of the events was used in Sec. 5.2 to estimate the charge distribution on the PTFE walls, as it carries information on the field itself as observed during the field cage tuning test in Sec. 5.4.2. The true position of the interaction is obtained using a *field distortion correction* (FDC). A simulation-driven approach was followed by XENON100, where the distortion was estimated from a COMSOL-based field simulation [184]. Nevertheless, the two-dimensional nature of the FEM simulation fails to account for angular effects. The approach used by XENON1T [5] was data-driven and based on a previous study by LUX [237]. It is a three-dimensional

FDC based on the assumption that the $^{83\text{m}}\text{Kr}$ source is uniformly distributed inside the detector. The basic principle is described in the following, together with its application to XENONnT data and its performance.

5.5.1 | Working principle

The three-dimensional field distortion correction is based on two assumptions: the radial spatial homogeneity of the $^{83\text{m}}\text{Kr}$ source and that the electric field is only radially distorted. Since the electric field lines cannot cross each other, the assumption that the distortion of the field has no azimuthal component space leads to a conserved radial ordering for events with the same initial z . This means that for two interactions happening at the same depth, and with true radial position $r_2^{\text{true}} > r_1^{\text{true}}$, the reconstructed radii maintain the relation $r_2^{\text{rec}} > r_1^{\text{rec}}$. In terms of distribution, this corresponds to the conservation of the percentile p under the field distortion transformation ($p^{\text{true}} = p^{\text{rec}}$). This invariance is useful when considering the (assumed) uniform distribution of $^{83\text{m}}\text{Kr}$ in r^2 , for which the percentile is linearly proportional to the squared radius $r^2/p = \text{const}$. As the $^{83\text{m}}\text{Kr}$ events are uniformly distributed within the TPC, hence $r^2 \sim \mathcal{U}(0, r_{\text{wall}}^{\text{true}})$ with $r_{\text{wall}}^{\text{true}} = 66.4\text{ cm}$, it is possible to correlate the true percentile p_1 to the true radius r_1 . As the percentile is invariant under field distortion, it is then possible to correlate a reconstructed radius at a given percentile to its true radius, as $p^{\text{true}} = p^{\text{rec}}$. For a reconstructed radius of $^{83\text{m}}\text{Kr}$ events r^{rec} with radial percentile p , the true correlated position r^{true} is then

$$r^{\text{true}} = r_{\text{wall}}^{\text{true}} \sqrt{\frac{p}{p_{\text{wall}}}}. \quad (5.5)$$

The true wall radius $r_{\text{wall}}^{\text{true}}$ should correspond to the 100th percentile as no physical interaction from outside the active volume can be observed. Nevertheless the position reconstruction has a finite resolution which should be considered as it cannot be decoupled from the reconstructed position: this leads to an observed radius of the wall with $p_{\text{wall}} < 100\%$. A toy MC with a radial position resolution of $\sigma_r = 0.6\text{ cm}$ (as estimated by data) returns a percentile for the wall position of $p_{\text{wall}} = 99.2\%$. Similarly, it is possible to consider a set of equally spaced percentiles p_i from 0 to p_{wall} and the corresponding difference between true and reconstructed radius $\Delta r_i = r_{\text{wall}}^{\text{true}} \sqrt{p_i/p_{\text{wall}}} - r_i^{\text{rec}}$.

The principle described above accounts for a generic radial distribution within the detector, yielding to a set of Δr_i (r_i^{rec}). These values are interpolated and used to correct the reconstructed radius, returning the true interaction position. The procedure described

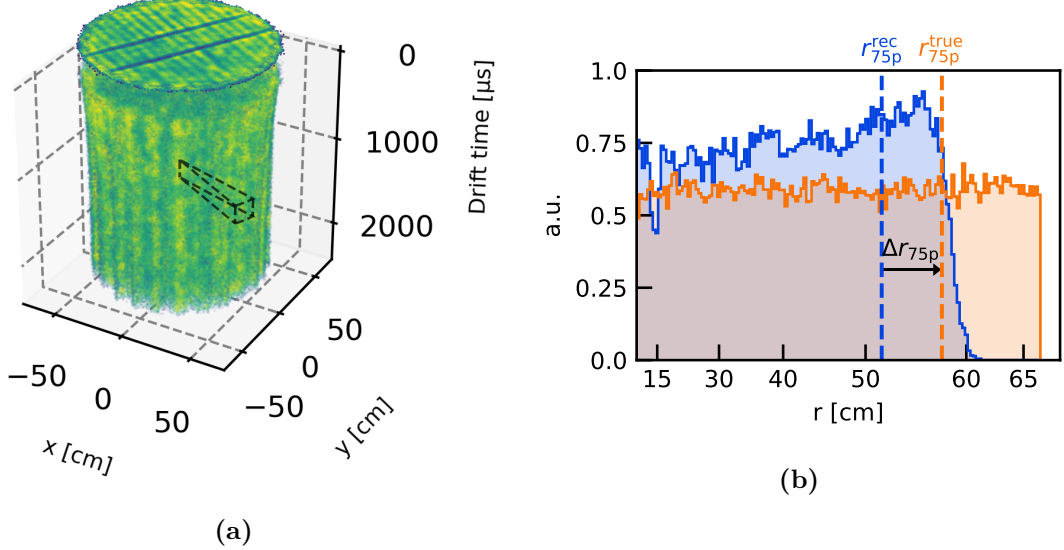


Figure 5.19 (a) Three-dimensional spatial distribution of measured $^{83\text{m}}\text{Kr}$ events. The field distortion correction (FDC) map is produced dividing the detector in t and θ slices. The color scale is logarithmic. (b) Radial distribution within the selected TPC slice for the observed $^{83\text{m}}\text{Kr}$ events (blue) and the equivalent uniform true distribution (orange). The difference between the expected true radial position for the 75th percentile and the observed radius at the same percentile is defined as $\Delta r_{75\text{p}}$. This value is estimated for other several percentiles and in different slices, resulting in a three-dimensional FDC map.

above applies to a given radial distribution where all events are affected by the same field distortion. When considering the case of the XENONnT TPC, the reconstructed position distribution of $^{83\text{m}}\text{Kr}$ events of Fig. 5.2 shows that the radial distribution is different for different (z, θ) slices of the TPC, as the presence of the bite structure clearly indicates. For this reason the procedure described above is applied to individual slices in drift time t - and θ -coordinate, returning a three-dimensional FDC map $\Delta r_i(r_i^{\text{rec}}, \theta_i, t_i)$, as sketched in Fig. 5.19. As the binning of the map is fine enough, this correction can also account for the “bite” structure observed in Fig. 5.2. The evident features crossing the TPC shown in the projected distribution of Fig. 5.19a break the radial-only field distortion requirement. These are attributed to the perpendicular wires installed on the gate and they are successfully modeled in Sec. 6.3.1. Thanks to the fine binning in θ and the large number of reference percentiles p_i , these features can be partially corrected under the assumption of a radial nature. For slices perpendicular to these features, this assumption is correct, while it is an approximation elsewhere.

5.5.2 | The XENONnT field distortion correction map

The FDC map for XENONnT combines all $^{83\text{m}}\text{Kr}$ calibration data sets acquired during the entire SR0. This is possible as a time-dependence of the field is excluded in Sec. 5.3. Given the large data set of more than 20 million events, the detector is divided into 180 azimuthal slices and 80 slices in $[200, 2150]$ μs of drift time and 15 in $[0, 200]$ μs . The finer binning at low drift times is used to better correct the feature at the top edge, clear in the (r, z) distribution of Fig. 5.2. In contrast to XENON1T, the FDC map is produced in the (r, θ, t) space, with t being the drift time replacing the z position. This was preferred to decouple the FDC map from the measurement of the drift speed and other factors that could affect the definition of z . For each slice the reconstructed radii for a total of 101 percentiles are estimated, corresponding to equally spaced true radii as from Eq. (5.5). This leads to a final three-dimensional FDC map with a total of $180 \times 95 \times 101$ entries, corresponding to about 1.7×10^6 values. A map is produced for each of the three machine learning algorithms used for position reconstruction in XENONnT: a multilayer perceptron (MLP), a convolutional neural network (CNN) and a graph constrained network (GCN) [246]. Since the FDC map is defined, after converting drift time to z , on the $(r_{\text{rec}}, z, \theta)$ grid with no regular spacing as r_{rec} depends on the radial distribution at the given slice, fast multidimensional numerical interpolation as the one implemented in the `scipy.interpolate.RegularGridInterpolator` class [247] cannot be used. A standard interpolation algorithm for irregularly spaced data is the *weighted nearest neighbors* (WNN) [248], where the N closest values from a given position are weighted by the inverse of their distance from it. For the FDC map interpolation $N = 6$ was adopted. The map is used to correct only the radial position, unlike for XENON1T where also the z position was corrected using the Pythagorean theorem and assuming the electron path to be a straight line. This correction was discarded as it proved to poorly correct the distortion of the cathode at larger radii, while introducing a strong artifact around the top edge of the detector.

The “performance” of the FDC map on $^{83\text{m}}\text{Kr}$ data is shown in Fig. 5.20 for the MLP position reconstruction algorithm. The expected (by construction) behaviour of the field distortion correction on the position distribution of the $^{83\text{m}}\text{Kr}$ events is that the final position distribution should be homogeneously distributed within the active volume of the TPC. The top panels represents the (r, z) distribution, clearly showing the correction of the inward push while maintaining the z distortion close to the cathode at the bottom of the TPC, as no z correction is applied. The (x, y) distribution in the middle panels

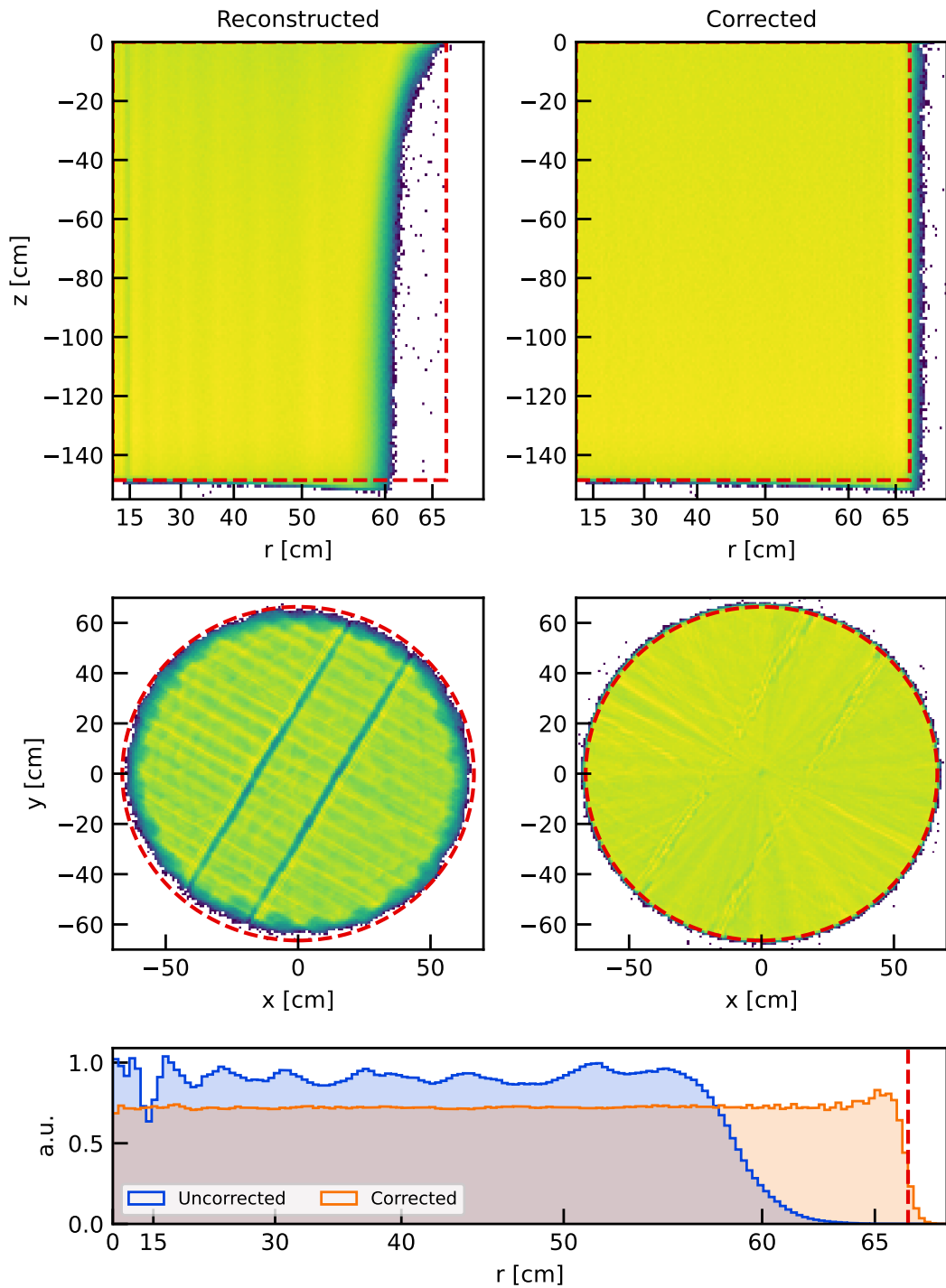


Figure 5.20 ^{83m}Kr event distribution before (left) and after (right) the application of the field distortion correction. The known TPC boundaries are included as red dashed lines. The radial distribution after the correction (bottom, orange histogram) shows a uniform behaviour except at the edges, as discussed in the text. The color scales are logarithmic.

shows an overall improvement of the spatial uniformity. The FDC map strongly reduces features from the perpendicular wires, but it is unable to remove them completely as it is not a radial-only distortion. An additional feature is clear from the distribution in the left middle plot: a higher density of events is reconstructed along stripes parallel to the grid electrode wires, with a spacing consistent with the PMT diameter. The most plausible explanation for this artifact is the combination of the focusing effect of the gate on electrons and the shadowing of the electroluminescence photons by the anode wires. This feature is not radial and therefore cannot be properly accounted for by the FDC map, leading to residual artifacts along the direction of the electrode wires after the correction. Finally, the radial distribution is plotted in the bottom panel. The corrected distribution (orange) presents an almost uniform behaviour, except for a bump at higher radii. This is due to a combination of the interpolation technique and the increasing correction at larger radii. In case of an event with radius r_0 close to the TPC wall, the WNN algorithm is more likely to select events with smaller radii and estimate the correction as a weighted average of the corresponding Δr_i . As the field distortion increases with the radius, this means that the correction computed for r_0 is smaller than it needs to be, pushing events to lower corrected radii. Together with the (x, y) and (r, z) distributions, the radial distribution shows that the FDC map correctly reproduces the homogeneous behaviour of the position distribution of the $^{83\text{m}}\text{Kr}$ events, hence proving the proper behaviour of this correction.

5.6 | Impact of the FDC on the fiducial volume

The data-driven field distortion correction (FDC) described above implicitly assumes that every interaction happening inside the active volume is reconstructed. This is included in the assumption of the radial homogeneity of the $^{83\text{m}}\text{Kr}$ source, essential to correlate the reconstructed radii to the corresponding true ones via the percentile conservation. The presence of a charge-insensitive volume is in contrast with this requirement, as interactions happening inside of the CIV cannot be properly reconstructed since they don't show the associated ionization signal. As discussed in Sec. 5.2.1 and shown in Fig. 5.6, a total charge-insensitive mass of around 112 kg (out of 5.9 t of the active target) is expected for the XENONnT SR0 electric field configuration, once the charge accumulation on the PTFE panels is taken into consideration. The CIV boundary acts as an “effective” TPC wall, hence a proper FDC map should consider a position-dependent $r_{\text{wall}}^{\text{true}} = r_{\text{CIV}}^{\text{true}}(\theta, z)$ when estimating the true radii using Eq. (5.5). However, since electrons diffuse in liquid xenon, the CIV is not defined by a precise boundary and it should be treated as a deformation of

the radial $^{83\text{m}}\text{Kr}$ distribution. This requires a good knowledge of the shape of the CIV, hence relying on the electric field simulations or on data-driven measurements. Data-driven techniques based on the α background originating in the ^{222}Rn decay chain are described in [249]. These results were used to validate the shape of the charge-insensitive volume predicted by the simulations, returning an overall agreement in the magnitude of the effect and its shape, but they did not yield the required level of precision to be used for the FDC maps production.

For the XENONnT SR0 analysis, the FDC map was calculated assuming no charge-insensitive mass, leading to a corrected $^{83\text{m}}\text{Kr}$ distribution as shown in Fig. 5.20. This corresponds to ignoring that $r_{\text{CIV}}^{\text{true}} < r_{\text{wall}}^{\text{true}}$ in the region of the detector where the CIV volume is non-zero. This assumption leads to an overcorrection of the inward push, stretching the corrected positions to radii larger than the true ones. As the target fiducialization uses the corrected position, this stretch results in an overestimation of the fiducial mass. For this reason, the impact of the CIV is accounted for in the final analysis by a scaling factor of the fiducial mass. This effect is estimated using the simulated field map derived in Sec. 5.2 and the procedure is described in the following. At first a simulation-based FDC map is calculated. A total of 10^7 initial positions \vec{x}_0 are uniformly sampled in the active volume of the TPC. Interpolating the survival probability map plotted in Fig. 5.6, the events with an expected charge loss below 66 % are considered to be reconstructed. This comes from the selection of $^{83\text{m}}\text{Kr}$ events: the average S2 signal size of $^{83\text{m}}\text{Kr}$ events is 7500 PE, but the selection criterion requires $\text{S2} > 2500 \text{ PE}$. This means that on average if more than 66 % of the ionization electrons are lost, the $^{83\text{m}}\text{Kr}$ interaction does not pass the selection cuts. The reconstructed position of the surviving events is estimated using field distortion maps which are produced in the same way as the drift speed and diffusion maps of Sec. 4.4. These distortion maps return the drift time ($t \propto z$) and radius at the liquid-gas interface for a given initial position. The simulated reconstructed position is then obtained by applying the Gaussian reconstruction resolution as estimated for the $^{83\text{m}}\text{Kr}$ S2s, around 0.6 cm close to the edges and 0.3 cm in the inner volume. Once the simulated $^{83\text{m}}\text{Kr}$ distribution is available, the FDC map is calculated following the procedure of Sec. 5.5. This correction map is then used to determine the corrected distribution of a $^{83\text{m}}\text{Kr}$ population simulated in the same way as the one used to derive the FDC map itself. Producing a different population avoids any potential bias that might come from using the map on the data set used to calculate it. An example of the steps to produce the simulated distribution is shown in Fig. 5.21.

Once a simulated $^{83\text{m}}\text{Kr}$ distribution is available, estimating the impact of the FDC map

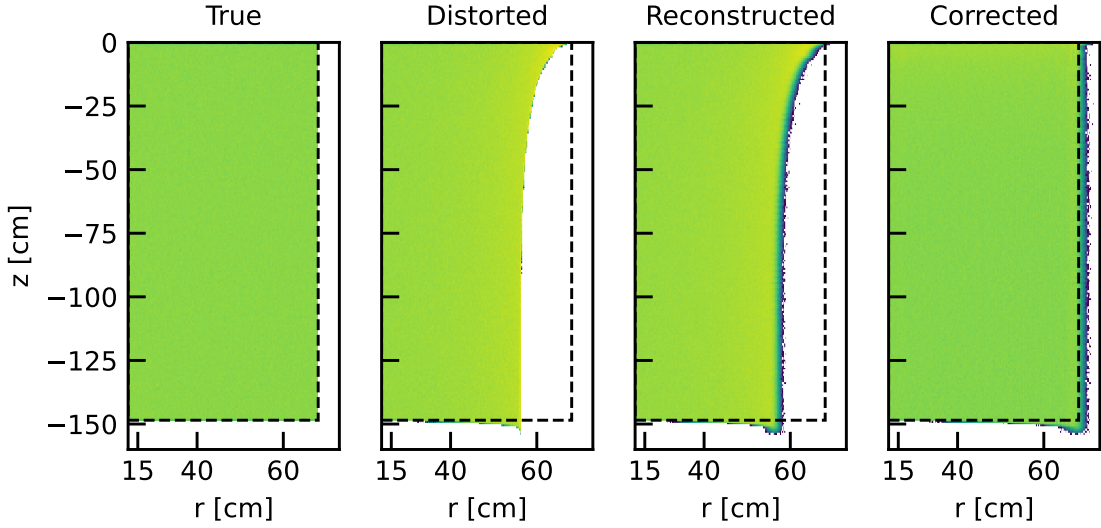


Figure 5.21 Simulated position distribution at different stages. From the left to the right: (1) original uniform event distribution reproducing the assumed ^{83m}Kr uniform distribution in the detector, (2) distorted events using the input from the field map, (3) distorted events including a radial reconstruction resolution and (4) corrected position distribution. The FDC map used for the final correction comes from applying the procedure described in Sec. 5.5.1 to the distribution simulated until (3).

on the fiducial mass is straightforward. In the following, we consider the fiducial volume used for the blind analysis of low-energy electronic recoil data from SR0 of XENONnT [114]. The definition of the shape and size of the fiducial volume is mainly the result of the minimization of space-dependent backgrounds, like the materials-induced ER and NR events and the *surface background*. The surface background consists of events from ^{222}Rn progeny happening close to the PTFE walls or the charge-insensitive volume, but reconstructed at smaller radii [166]. These events can lose a fraction of the liberated electrons, resulting in a lower S2/S1 ratio and thus representing an important background both for low energetic ER and WIMP searches. A data-driven approach based on a kernel-density-estimation method [250] was used both in XENON1T and XENONnT to model this background, characterized by a steep decrease for lower radii. Another input to define the fiducial volume is the precise knowledge of the electric field map. As reported in Fig. 5.7, a difference between the simulated and data-driven field map below 10 % is required to ensure the reliability of the field-dependent models used for the simulation of ER and NR ($cS1, cS2$) distributions. The different inputs led to the final fiducial volume shown as a solid black line in Fig. 5.22. Assuming a liquid xenon density of $\rho_{\text{LXe}} = 2.86 \text{ g/cm}^3$ at

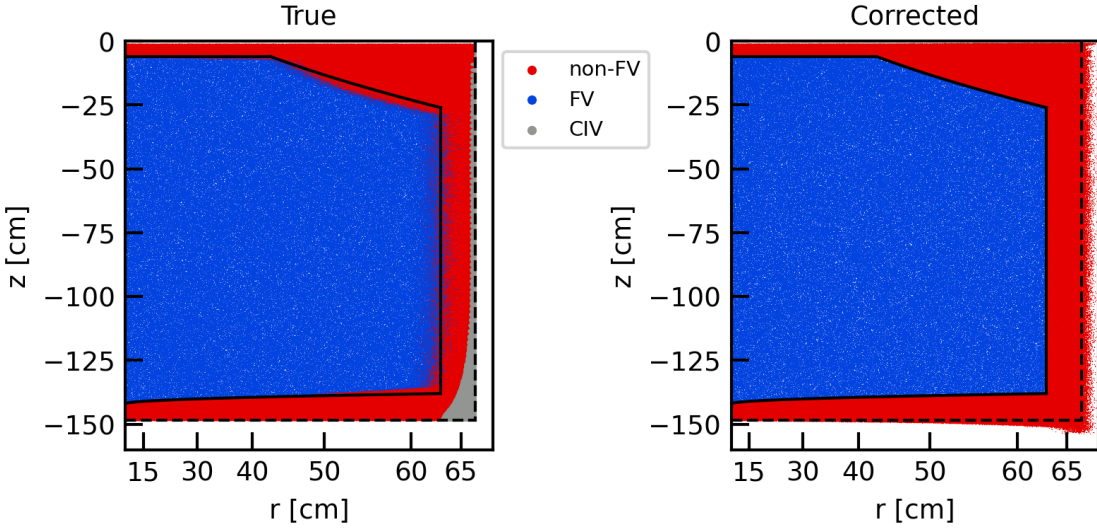


Figure 5.22 True position distribution of simulated ^{83m}Kr events (left) and corresponding corrected distribution (right). The events are marked in blue if they are selected by the definition of the fiducial volume (defined in the corrected space as in the right panel), red if they are not included and gray if they fall inside the CIV and are not reconstructed.

$T = -96^\circ\text{C}$ [251], the fiducial mass from the geometrical calculation is 4.55 t. Simulated events selected by the fiducial volume cuts are plotted in the true position space, along with the non-reconstructed events in gray. The selected fiducial volume is slightly smaller than its geometrical definition. The corresponding true mass is estimated by considering the ratio between the selected events and the number of simulated events, weighted for the total mass of the liquid xenon in the TPC. This ratio depends on the position reconstruction resolution of the considered population, as it is shown in Fig. 5.23 (blue line). For radial resolutions below 1 cm the ratio is stable around a value of about 95.7 %, corresponding to a real fiducial mass of 4.35 t. Above 1 cm, the ratio drops. Both for the low-energy ER and WIMP search, the expected S2 size is above 300 PE, therefore it is possible to assume the ratio to be independent on the signal size. The main source of uncertainty is the electric field map used to simulate the FDC effect. This uncertainty is estimated by comparing the results using the electric field map with charge-up of the PTFE walls (blue line in Fig. 5.23) with the map without charge-up (orange line). This is a conservative approach, as the results discussed in Sec. 5.2.1 reject the hypothesis of no charge-up by more than 2σ . From the difference between the two scaling factors, the ratio between the real fiducial mass and its geometrical value is estimated to be $(96 \pm 3)\%$. This results in a final fiducial mass of (4.37 ± 0.14) t used for the low-energy ER results of SR0 [114].

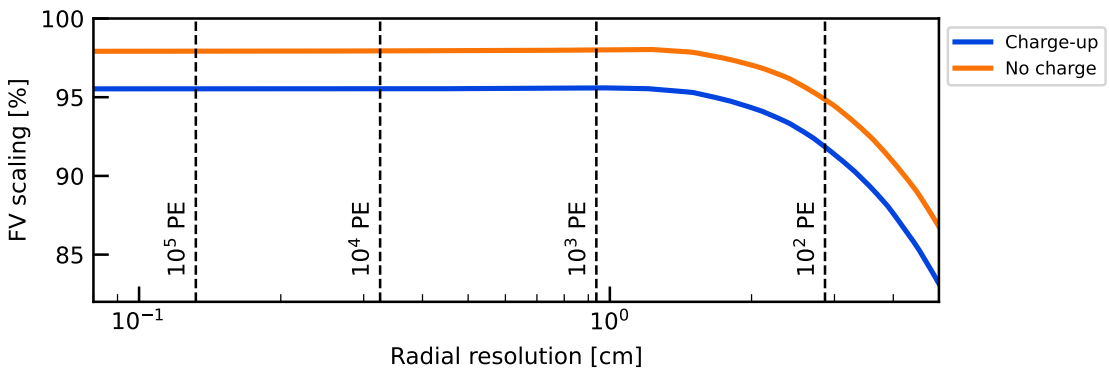


Figure 5.23 Ratio between the true fiducial volume and its geometrical estimation in the corrected space. This difference is due to the effect of the CIV and depends on the resolution of the position reconstruction algorithm. A smaller S2 area leads to a larger radial resolution and a larger impact of the CIV. This is shown both for the SR0 field map including wall charge-up (blue) and not including it (orange). The difference between the two maps is about 3 % and it is used as systematic uncertainty for the mass of the fiducial volume.

Chapter 6

Simulating the S2 region

After a particle interaction in the liquid xenon target, the electrons freed by the ionization process drift following the electric field as detailed in Chapter 4. As they reach the gate electrode, they are focused in a stronger field region and extracted in the gaseous phase, where they produce the proportional scintillation signal S2. The time profile and the intensity of this signal depends on the width of the gas gap, the gas pressure and the electric field strength, where the gas gap is defined as the volume between the liquid-gas interface and the anode's wire grid. These aspects are influenced by the position of the anode and gate electrodes, as well as the liquid level position, the main focus of Chapter 3. A careful modeling and testing of the deformation of the anode and gate electrodes is of utmost importance to understand and minimize the inhomogeneity of the gas gap, resulting in a space-dependent S2 signal. Assuming a given geometry of these electrodes, it is possible to simulate the time distribution of the electroluminescence photons using the detector simulation software Garfield++. This timing information is used to study the properties of the gas gap and as an input for the simulation of the S2 waveforms in the full-chain waveform simulator, introduced in Sec. 4.4.

This chapter focuses on the simulation of the region where the S2 signal is produced. Following a description of the electrodes design and machining in Sec. 6.1, the modeling of the deformation of the electrodes' wires under electrostatic force and their own weight is presented in Sec. 6.2. This model includes the electrostatic feedback effect from the change of the field as the wires sag. Its predictions are compared to measurements carried out using a laser system, resulting in a better agreement with respect to a simplified model not including any feedback. After the electrodes were tested at liquid xenon temperature ($\sim 170\text{ K}$), a large wire tension loss was observed. This led to the need to install perpendicular wires on the anode and gate in order to reduce their sagging. The cold

test and the impact of the perpendicular wires on the electrodes' deformation and electron drifting are described in Sec. 6.3. The electroluminescence process is then simulated using the simulation framework Garfield++. The software and its results are presented in Sec. 6.4, where a good agreement of the signal shape is observed between the single electrons reconstructed inside the TPC during the first science run SR0 and the simulations. This is of particular importance as the simulation does not take any data-driven input, but it relies on electron-atom cross sections and simulation-driven detector inputs. Finally, the Garfield++ output implementation within the full-chain waveform simulator is outlined in Sec. 6.5. This is used to compare the shape of measured single electron waveforms to the simulated ones for different gas gaps. An approximate sagging map is obtained in this way and compared to the sagging expectations from the model developed in Sec. 6.2.

6.1 | XENONnT electrodes

The relatively simple scalability of liquid xenon dual-phase TPCs made it possible to go from $\mathcal{O}(10\text{ kg})$ detectors [3, 252] to multi-tonne instruments like XENONnT or LZ [253] in about ten years. This size increase has posed several technical challenges, among which the design of the electrodes has assumed a central role in the last years. The strict requirements of optical transparency and mechanical stability that the electrodes need to satisfy are hard to combine. A high optical transparency is required to maximize the light collection efficiency and to ensure the detection of low energy signals, such as from WIMP scattering. This has to come with a high reliability against damages under mechanical and electrical stress, ensuring no light or charge emissions at fields higher than 50 kV/cm . Even small emissions of electrons or light from the electrodes' metallic surface would impact the detected signals, especially at low energies. In addition, the longer running time required for the large detectors means that the electrodes have to be able to withstand several cooling cycles without performance degradation. The strongest requirement for the electrodes is that their mechanical deformation under gravitational and electrostatic force is limited to a few millimeters (cathode and screens) or even at the sub-mm level, as in the case of anode and gate. This effect of *sagging* is of particular importance for the S2 signal production, as it can affect the electron path length in gaseous xenon and the electric field therein. While the sagging requirement can be easily met with the use of more massive electrode meshes, this would reduce the optical transparency, leading to a trade-off problem.

The electrodes deployed in the XENONnT TPC consist of individually fixed wire

grids. The wires are made of stainless steel type 316, characterized by a high molybdenum content which makes it especially resistant to corrosion and oxidation [254]. This is of particular importance as a correlation between the corrodibility and spurious electron emissions from cathodic surfaces was observed in [255]. The wires are installed by inserting them in individual through-holes around the electrode frame and using copper pins to fix them, as sketched in Fig. 6.1. Since the maximal wire deformation due to sagging is inversely proportional to the tension applied, the wires are stretched with a tension T before installation. As the tension applied is in the order of few newtons per wire, the frame is initially pre-stretched to prevent its deformation due to the total force above 200 N. The copper pins and the holes in the frame were designed to maximize the mechanical stability of the wire fixation while reducing the risk of damage for the wires due to sharp edges. The larger ductility of copper compared to steel allows the pin to deform when inserted in the hole with the wire, ensuring a highly efficient clamping. The surface electric fields around the pins were simulated using COMSOL Multiphysics® v5.4 [4], as they might represent a dangerous source of field enhancement. While a $\sim 30\%$ increase of the field is observed around the edges of the pins, the critical factor is the cut end of the wire inside the through-hole. The cut should be at least 1 mm inside the hole in order to avoid enhancements as high as 500 %. The risk is further reduced by encasing the electrode

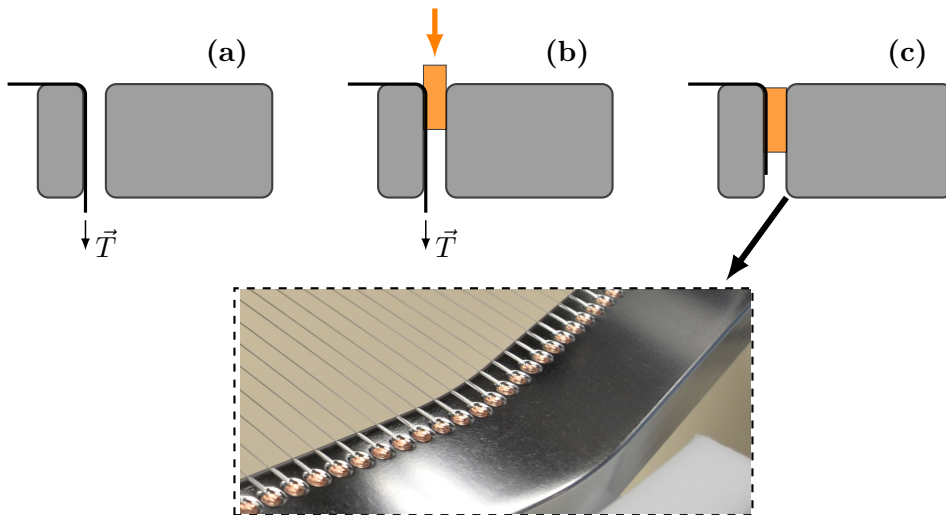


Figure 6.1 Sectional side view of the fixing procedure of the wires in the electrode frame. The wire is inserted inside the through-hole and stretched to the desired tension (a), then the copper pin is inserted (b). As the wire is clamped between the frame and the copper pin, it is released and cut (c). The picture in the inset is an example of the final assembly for the anode electrode.

	z_{warm} [mm]	z_{cold} [mm]	d_{wire} [μm]	p [mm]	Shape	V_{design} [kV]	Opt. trans. [%]
Top screen	35.5	35.1	216	5	24-pol.	-1.5	95.7
Anode	8	7.9	216	5	24-pol.	+6.5	95.7
Gate	0	0	216	5	24-pol.	-1.0	95.7
Cathode	-1510	-1486	304	7.5	circ.	-30.0	95.9
Bottom screen	-1566	-1541	216	7.5	circ.	-1.5	97.1

Table 6.1 Properties of the electrodes installed in the XENONnT TPC. The z -coordinate at room (warm) and liquid xenon (cold) temperature is given with respect to the gate position (0 by definition). Diameter and pitch of the wires are given, as well as the information on the shape of the frame (24-polygonal or circular), the design voltage and the optical transparency. The optical transparency is defined for incident light perpendicular to the electrode plane.

frames in a modular PTFE enclosure. This avoids any direct path between the electrode frames which could lead to discharges.

A total of five electrodes are installed in XENONnT: their properties are summarized in Tab. 6.1 and their position in the TPC is shown in Fig. 2.16. In the following the dimensions are given for room temperature, while the cold configuration is reported in the table. The bottom screen is placed 4 mm above the windows of the bottom array PMTs and protects the photosensors from high fields and potential sparks, as they are at the same voltage. The cathode is placed 56 mm above the bottom screen and plays a key role in setting the electric drift field together with the gate. As it must withstand voltages as low as -30 kV , this is the only electrode using wires of $304 \mu\text{m}$ diameter instead of $216 \mu\text{m}$ as used for the other electrodes. This reduces electron emission from the cathode surface due to the large electric field [256–258]. The cathode and bottom screen, together forming the “bottom stack”, feature a circular frame and a wire grid pitch of 7.5 mm. The “top stack” is formed by the gate, anode and top screen, featuring a 24-gon (icositetragon) frame shape and a wire grid pitch of 5 mm. The gate is positioned 1510 mm above the cathode and the bottom of its grid wires is used as the $z = 0$ for the coordinate system. It electrically separates the drift field region below and the extraction region above, characterized by a higher electric field in order to extract electrons into the gaseous xenon. This high field is established by the large potential difference between the gate and anode and the small nominal distance of 8 mm between the electrodes. Anode and gate wires are staggered to ensure that the electrons extracted in the gaseous xenon follow straight field lines to

the anode wire. This minimizes the time width of the S2 signal, while maximizing the energy and time resolution. As discussed in Sec. 6.3, the gate and anode feature two and four wires of 304 µm diameter installed perpendicularly across the wire grid. These were installed to reduce the average sagging and avoid possible problems from a few wires with an exceptionally low tension, such as a short-circuit or discharges between anode and gate. This was necessary as a result of a general loss in tension of the electrodes' wires following a cold test performed in liquid xenon, detailed in Sec. 6.3. Lastly, the top screen is placed 27.5 mm above the anode and it serves the same purpose as the bottom screen, but for the top PMT array.

6.2 | Wire sagging

The size of the proportional scintillation signal S2 directly depends on the length of the path in the gaseous xenon, as discussed in Sec. 2.1. The path depends on the gas gap length between the liquid-gas interface and the position of the anode wires. The liquid level is constantly monitored by the level meter system presented in Chapter 3. The level can be controlled by adjusting the xenon content of the inner vessel or varying the pressure inside the diving bell. The z position of the anode wires, however, can neither be monitored nor adjusted. Even ignoring the mechanical precision of the electrode machining and positioning, the sagging of the electrode wires due to the gravitational and electrostatic forces makes predictions complicated. Despite the precise available models, many variables such as temperature change or tension loss while handling the electrodes have an impact on the final result. The model proposed for the wire sagging is discussed in this section, with particular emphasis on the anode-gate system. The small distance between these electrodes means that even a sub-mm sagging can have a sizable impact on the electric field and the electrostatic force. As such force is the main cause of the sagging, this requires to consider a *feedback effect*.

6.2.1 | Feedback effect

The solution of the sagging (i.e., the maximal deflection) of a single wire is derived in Appendix B. In case the total force acting on the wire is much smaller than its tension, the maximal deflection of the wire w , typically referred to as the sagging of the wire, is

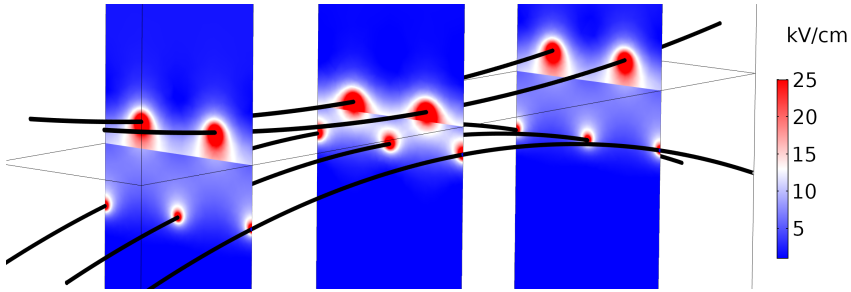


Figure 6.2 Three-dimensional COMSOL simulation of the sagging anode and gate wires used to determine the electrostatic force acting on them. The electric field intensity is shown and the liquid level is clearly visible as a sharp increase of the field. The XENONnT design field is used ($V_{\text{anode}} = 7.5 \text{ kV}$, $V_{\text{gate}} = -1 \text{ kV}$).

given by Eq. (B.12), reported here for clarity:

$$w = \frac{f L_0^2}{8} \left(\frac{1}{H} + \frac{1}{EA_0} \right). \quad (6.1)$$

In this equation f is the total force per unit length acting on the wire (e.g., gravitational and electrostatic), L_0 is the unstrained wire length, H is the horizontal component of its tension, E is Young's modulus and A_0 is the sectional area of the wire. This solution implies that the force f per unit length is constant along the entire wire, true in the case of the gravitational pull but considered an approximation for the electrostatic force. In addition, the electrostatic forces acting on the anode and gate of XENONnT have no analytical formulation, therefore they come from electrostatic simulations of approximations to the real geometries. The software COMSOL Multiphysics® is used to estimate the electrostatic force acting on the anode and gate wires for different sagging configurations. As the wires deform under the gravitational and electrostatic force, the electric field between the grids increases, leading to an increase in the electrostatic force itself. This is known as the feedback effect. It introduces an additional degree of complexity as the total force depends on the sagging of the wires. This relation can be mapped in the sagging space ($w_{\text{an}}, w_{\text{gt}}$) by producing three-dimensional simulations with catenary-shaped wires and different maximal sagging values. An example is shown in Fig. 6.2: the total length of the simulation does not reflect the actual length of the wires, but this was found to have a negligible impact on the force per unit length f_{es} . The results for the electrostatic force acting on anode and gate $f_{\text{es}} = f_{\text{es}}(w_{\text{an}}, w_{\text{gt}})$ are shown in Fig. 6.3. The electrostatic forces for a given combination of sagging values ($w_{\text{an}}, w_{\text{gt}}$) do not sum to zero as the system is not strictly two-body (anode and gate). Because of the different dielectric constants of the gaseous

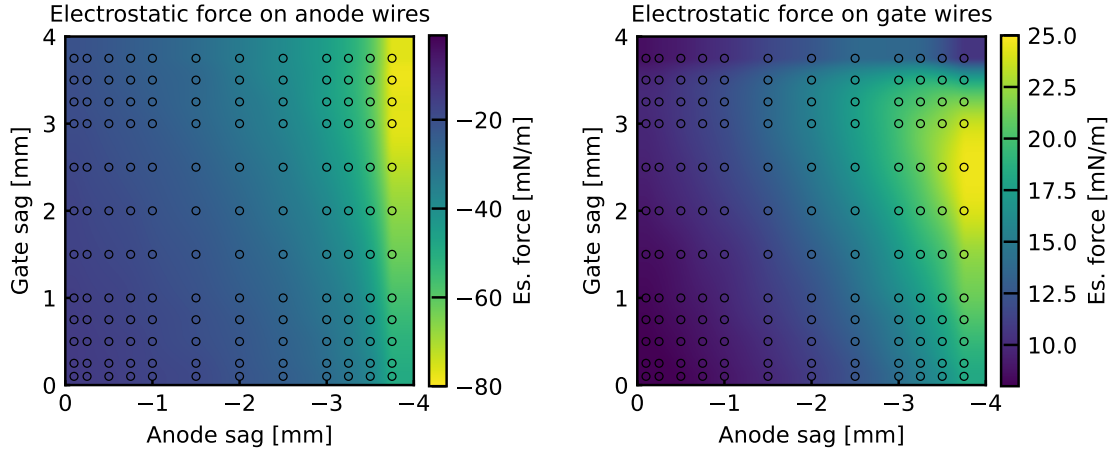


Figure 6.3 Interpolated electrostatic force on the anode (left) and gate (right) wires for different sagging combinations and XENONnT design field. The scatter points represent the 12×12 simulations produced for the interpolation.

and liquid phase, a polarization charge accumulates at the interface. An electrostatic force acts on this charge distribution and for this reason the interface takes part in the force balance. This leads to a negligible deformation of the liquid surface: from simulations and Gauss' law $\sigma_{\text{surf}} = \epsilon_0 |\varepsilon_{\text{GXe}} E_{\text{GXe}} - \varepsilon_{\text{LXe}} E_{\text{LXe}}| \sim 10 \text{ nC/m}^2$, from which considering the electrostatic pressure and the liquid xenon weight we can estimate a level increase of $h = \frac{\sigma |E_{\text{GXe}} - E_{\text{LXe}}|}{\rho_{\text{LXe}} g} \sim 3 \mu\text{m}$.

When producing the simulations for the electrostatic force, the anode and gate wires are considered to have all the same sagging along each grid, as shown in Fig. 6.2. This excludes effects of self-repulsion among the wires of the same electrode grid, as they cancel out when assuming the same vertical position for all wires. Including such effects would increase the dimensionality of the problem and it is therefore ignored at this stage.

When modeling the sagging, the wires cannot be treated individually. For example, when considering the deflection of an anode wire, the electrostatic force acting on it also depends on the gate sagging, as Fig. 6.3 shows. This means that a proper model including the feedback effect should always include at least one anode and one gate wire. The model developed here considers the measurements of tension and length from a single anode wire at a time and includes information coming from the two closest gate wires. This is due to the fact that these gate wires are equidistant from the anode wire by design and their impact on its deformation is equivalent, while the impact of farther gate wires is less

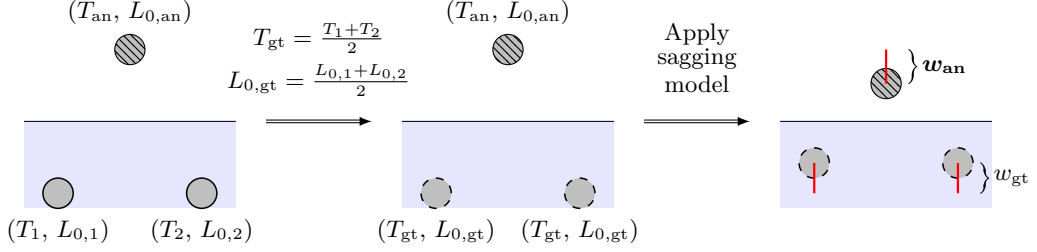


Figure 6.4 Sketch of the calculation of the maximal sagging w_{an} of an anode wire. The anode wire and the two closest gate wires are considered, each wire characterized by a tension T and unstrained length L_0 (left). Tension and length of the two gate wires are averaged leading to “effective” gate wires with identical properties (middle). Tension and unstrained length of the anode and the effective gate is fed to the model, which returns the sagging of anode w_{an} and the effective sagging of the gate w_{gt} (right). The latter is discarded, while the sagging of the anode is stored as solution.

important. Given an anode wire with tension T_{an} and unstrained length $L_{0,\text{an}}$, the two closest gate wires are defined by the tensions T_1 and T_2 , and unstrained lengths $L_{0,1}$ and $L_{0,2}$. As sketched in Fig. 6.4, this is treated as a system comprising an anode wire with the same characteristics and a gate wire with $(T_{\text{gt}}, L_{0,\text{gt}})$, the average of the properties of the two gate wires. In this case it is possible to simulate the configuration using the input coming from the COMSOL simulations, as the initial condition of the gate wires is identical and thus their sagging w_{gt} will be the same. Only the sagging value of the anode is saved as final solution of the model and the sagging of the gate is considered as an effective value, hence discarded. The same procedure is repeated for the gate wires, averaging over the two closest anode wires.

The maximal sagging w for a given wire is determined by the solution to the following conditions derived in Appendix B:

$$\begin{cases} \frac{fL_0}{2H} = \sinh \left(\frac{f\ell}{2H} - \frac{fL_0}{2EA_0} \right) & \leftarrow \quad \text{Eq. (B.13)} \\ w = \frac{fL_0^2}{8} \left(\frac{1}{H} + \frac{1}{EA_0} \right) & \leftarrow \quad \text{Eq. (6.1)} \\ f = f(w_{\text{an}}, w_{\text{gt}}) & \leftarrow \quad \text{Fig. 6.3} \end{cases}$$

where the tension on the wire is considered to be acting completely horizontally, hence $T = H$, and the three equations are repeated for anode and gate. This is a system of six equations which must be solved numerically as $f(w_{\text{an}}, w_{\text{gt}})$ has no analytic description.

This includes the results from the electrostatic simulations of Fig. 6.3, the wire weight and the buoyancy for the gate wires. The length of the unstrained wires L_0 is obtained using Eq. (6.1) from the tension measurement when the only force acting on them is their weight. The measurements are discussed in Sec. 6.2.2. This means that the variable to solve the system for are the total force per unit length f , the tension H and the maximal deflection w , both for anode and gate wire. Out of these six variables, only the maximal sagging for the wire under study is stored as solution and the other five solutions are discarded.

6.2.2 | Measurements and validation

The measurement of the wires' sagging and their tension was done using a setup developed at the University of Münster [259]. A red and a green laser are moved across the wires and the reflected light is measured by two sensors, each sensitive only to one of the two wavelengths. From the relative spatial distance of the two detection peaks, it is possible to determine the three-dimensional position of the wire with an accuracy of around $10\text{ }\mu\text{m}$. In addition, a nozzle flushing argon can excite vibrations in the wire and by measuring its frequency spectrum it is possible to determine its tension. The oscillation frequency ν_f of the first harmonic is related to the horizontal component of the wire tension H through the relation

$$\nu_f = \frac{1}{2L_0} \sqrt{\frac{H}{A_0 \rho}}, \quad (6.2)$$

with $\rho = 7990\text{ kg/m}^3$ being the density of stainless steel [254].

The model described in Sec. 6.2.1 was tested on the assembled gate electrode in a different configuration than in XENONnT (see Tab. 6.1). This configuration was chosen to reduce the number of electrodes involved in the tests, as the measurements were carried out outside the clean room. The model was tested considering the feedback effect coming only from the sagging of the gate electrode itself. The gate grid is positioned 5 mm above an aluminum slab connected to ground, as shown in Fig. 6.5. The sagging at the center of each wire is measured along the entire gate, both at ground and at 3 kV. The tension previously measured is then fed to the sagging models to compare the predicted values with the measured data. To exclude systematic effects coming from a tilt of the electrode, the sagging measurements of the gate at ground are subtracted from the 3 kV values. In this way also the gravitational sagging is cancelled out. Gravity is added back using Eq. (6.1) assuming only the gravitational force acting on the wire ($f_{\text{gr}} = \lambda g$). The results are shown in Fig. 6.6: the measurements (black dots) are compared to the model developed above

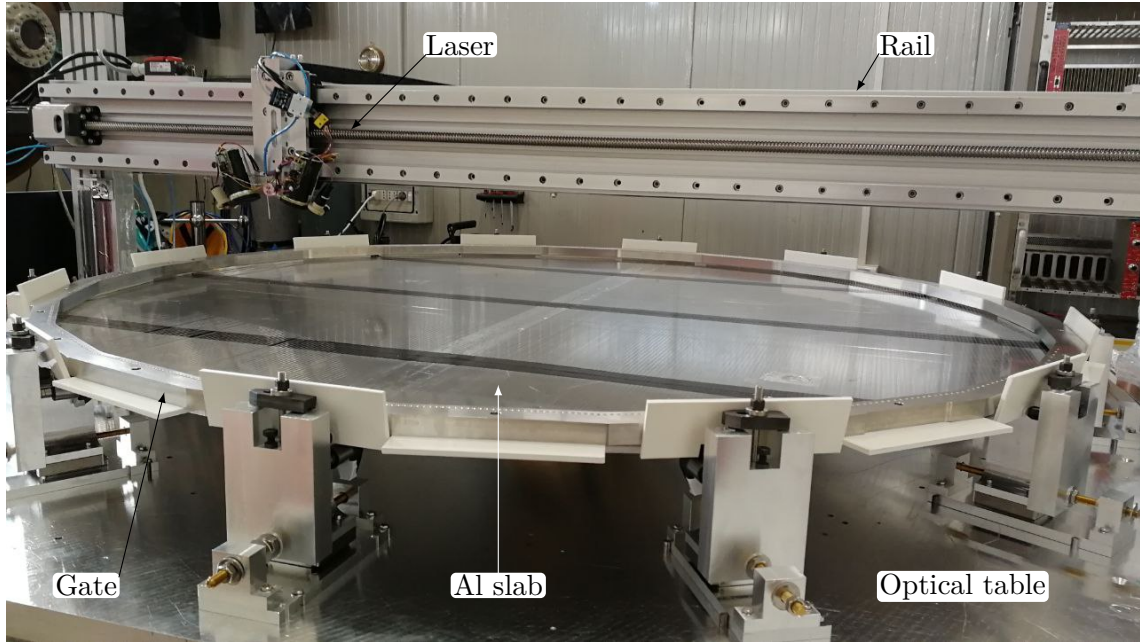


Figure 6.5 Setup to measure the sagging of the wires under electrostatic force. The aluminum slab 5 mm below the gate is grounded while the gate is either grounded or at 3 kV. The laser system is mounted on a rail positioned above the gate. The black tape on the aluminum plate avoids laser reflection.

(orange line) and to a “simplified” model (blue line). The simple model does not include the feedback effect, but uses the electrostatic force coming from COMSOL simulations without sagging. The Young’s module used for the calculation is (190 ± 10) GPa, where the uncertainty comes from the different values found in literature for SS316 [254, 260]. A 0.04 N resolution for the tension measurement as reported in [259] is used, together with a 0.1 mm uncertainty on the gate placement with respect to the aluminum slab.

When comparing the data to the model, an overall trend of larger sag on one side and a smaller on the other suggests a possible change in the gate tilt between the grounded and 3 kV measurements. The feedback effect improves the overall matching compared to the simplified model, in particular when considering the central longer wires. Considering the wires in the inner 30 cm range orthogonal to the wires’ direction as shown in Fig. 6.6, the reduced χ^2 goes from 11 for the model without feedback to 6.8. Nevertheless, the difference between the model with feedback and measured data is larger than 5σ , especially at the edges of the electrode. This means that the models should be used as useful approximation

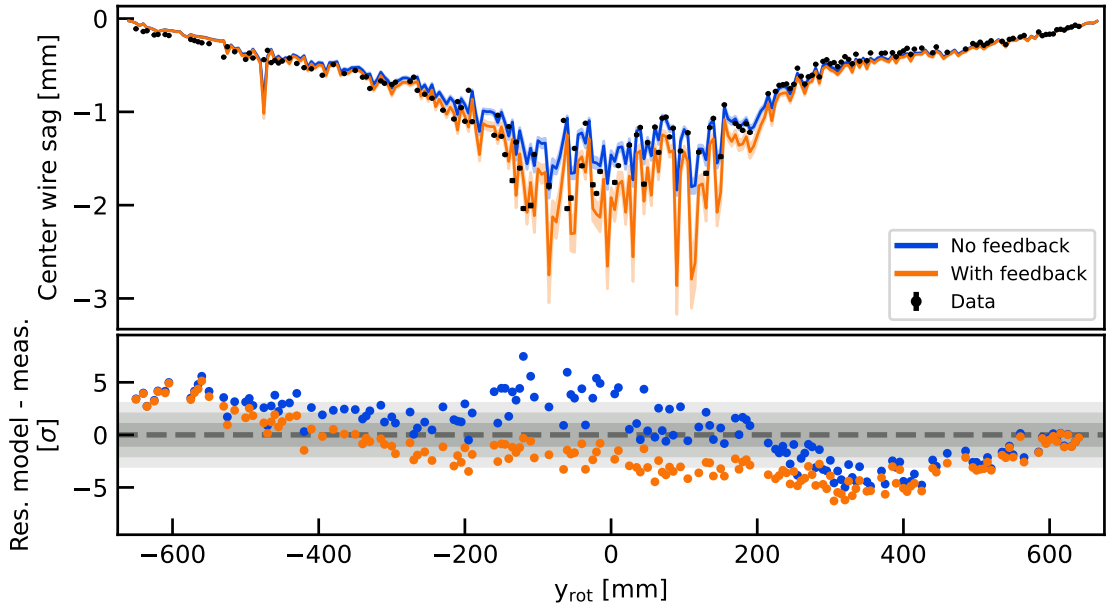


Figure 6.6 Measurement of the wire sagging at the center of the gate wires (black dots) compared to the simplified model (blue) and the model including feedback (orange). The difference between models and measurement in units of standard deviation σ in the bottom panel shows a better agreement for the model when the feedback effect is included, especially in the center of the electrode. The abscissa y_{rot} is the axis orthogonal to the electrode wires.

of the wires' deflection, but not for a precise estimation. It is also important to notice that the simplified model is biased towards smaller sagging than measured. This confirms the importance of including the feedback effect, especially for the XENONnT condition where this effect is expected to be more important because of the sagging of both electrodes, anode and gate.

6.3 | Perpendicular wires

After installing the wires on the electrodes' frames, a cold test was performed to assess the tension loss due to the thermal cycling down to the liquid xenon temperature of $T = -96^\circ\text{C}$ [116]. All five electrodes were assembled in top and bottom stacks and placed inside the cryostat vessels at a distance of about 10 cm between the stacks. In order to reduce the amount of xenon needed to completely submerge the bottom stack, the entire assembly was placed in the lower part of the cryostat. This limited the needed amount

of liquid xenon to only 2 t. The cooling procedure was controlled to ensure a maximum temperature difference between the frame and the wires below 10 °C, in order to avoid any thermal stress of the electrodes. After the cold test, the tension of the wires was measured for all the electrodes and an overall decrease was observed. In particular, the tension of the wires of the gate was on average $(34 \pm 11)\%$ lower, while for the anode it was $(25 \pm 10)\%$. Because of its continuous behaviour along the entire grid, the overall tension loss was attributed to a frame deformation during the cold test. The estimated maximal sagging of the anode and gate wire grids from the tension measurement is shown in Fig. 6.7, where the uncertainties are estimated in the same way as in Sec. 6.2.2. The tension values before the cold test were sufficient to keep the maximal sagging at design conditions, below or equal to 1 mm, even considering the feedback effect. The large tension loss increased the displacement up to three times for a few wires, reaching almost 3 mm sagging at the gate.

The new displacement values exceeded the 1 mm design limit, requiring a solution to limit the overall sagging. As an entire rewiring of the electrodes was not possible for logistical reasons, the solution adopted was to add *perpendicular wires* to the gate and anode grids. These are 304 μm diameter wires (the same as in the cathode) crossing the entire wire grid positioned such that they can counteract the electrostatic deformation. A total of two perpendicular wires were installed on the gate electrode and four on the anode,

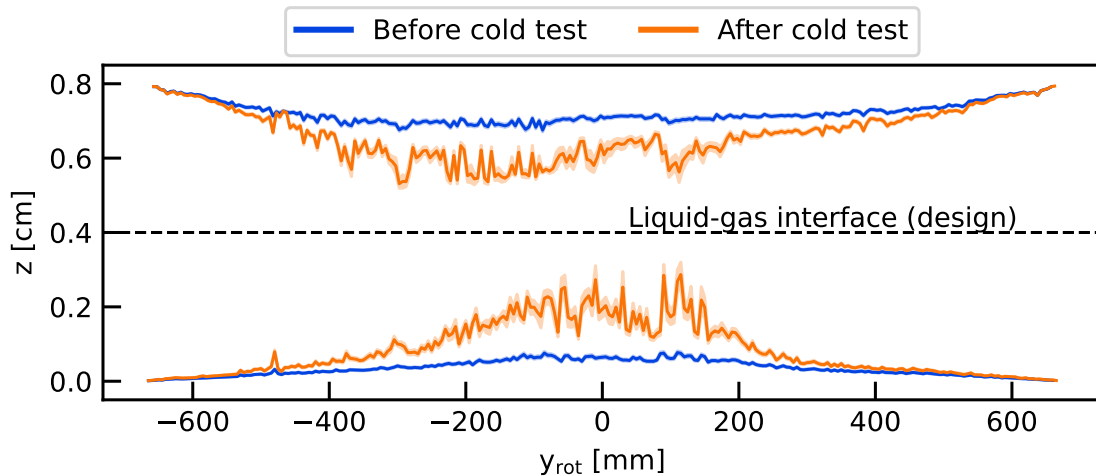


Figure 6.7 Displacement estimation of anode (top curves) and gate (bottom curves) wire grids assuming the tension before (blue) and after (orange) the cold test. The model includes the feedback effect.

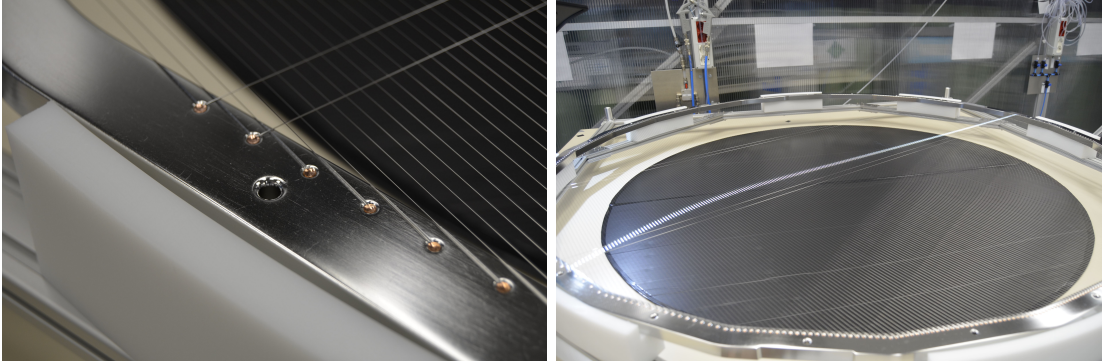


Figure 6.8 (left) Close-up picture of the fixing of the perpendicular wire. **(right)** Anode electrode after the perpendicular wire installation.

as the deflection of the latter has a large impact on the production of the S2 signal. They were fixed sharing the pins of the outermost and shortest grid wires, once this technique was tested using a mechanical sample of the anode frame. The fixation of the perpendicular wires is shown in Fig. 6.8. The larger cross-section of the perpendicular wires made it possible to apply a tension of 15–20 N, about an order of magnitude larger than the typical force acting on the grid wires. As the grid wires start to deform under the effect of the electric field, they are pushed against the perpendicular wires. Although these wires also feel both the electrostatic force and this push, their strong tension limits the maximal sagging. Along with reducing the average sagging, another advantage of the perpendicular wires is that they smooth out the overall deformation of the electrode grid, thereby limiting the maximum sag.

The impact of the perpendicular wires on the sagging of the electrodes was measured using the setup described in Sec. 6.2.2. The maximal sagging of the gate wire grid was measured before and after the installation of the perpendicular wires. This was done both with the gate at ground and with 3 kV applied. The results are shown in Fig. 6.9, where the values shown are the difference between the wires' displacement at 3 kV and 0 kV. The results without perpendicular wires (blue) show larger sagging compared to the results with (orange), confirming that the perpendicular wires limit large sagging while removing possible outliers. The installation of the perpendicular wires changes the conditions of the electrode wires, which are not anymore free to sag under the electrostatic and gravitational force. This requires a new modeling of the sagging, where the additional constraint of the newly added wires is included. In addition, as the perpendicular wires dampen the oscillation of the grid wires, after their installation it was not possible to measure the tension needed as input for the model, but it was still possible to measure their deflection.

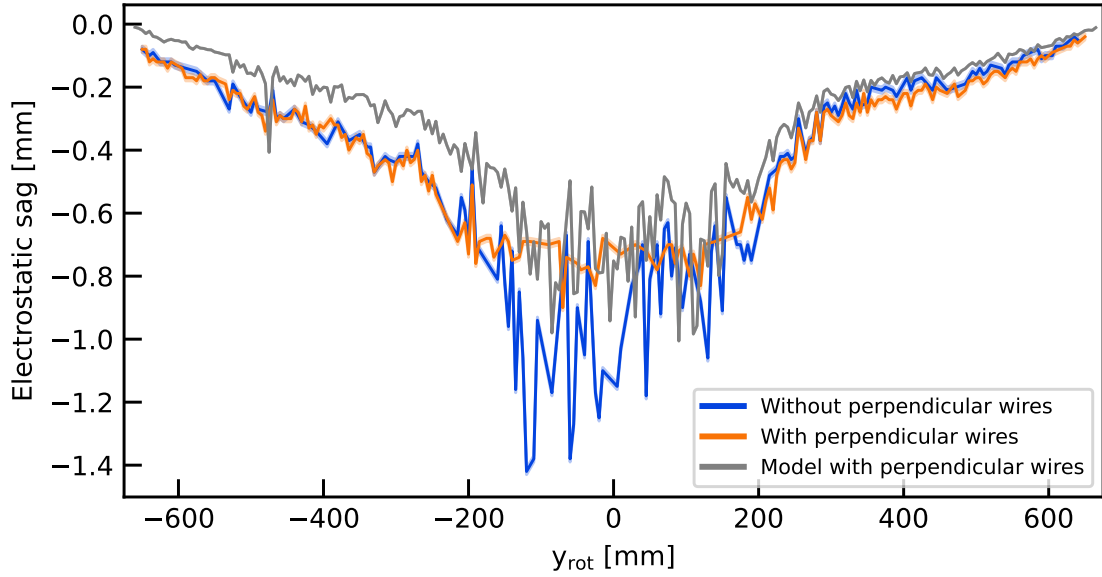


Figure 6.9 Measured electrostatic-only sagging at the center of the wires for the gate electrode before (blue) and after (orange) the perpendicular wires were installed. This quantity is given by the difference between the displacement of the gate at 3 kV and grounded. The data are compared to the feedback model (gray) where the effect of the perpendicular wires is included as a multiplicative constant of the electrodes' tension, in this case assumed to be 1.5.

In a first attempt to include the perpendicular wires in the model, the gate wires' tension is scaled by a constant factor k to match the model with the measurements. The factor $k = 1.5$ considered for the model and shown as gray line in Fig. 6.9 matches well the prediction with the measured sagging of the longest and most critical wires. A mismatch between the model and the measurements is observed for $y_{\text{rot}} < -150$ mm, due to a possible tilt of the gate electrode as discussed for Fig. 6.6. When including this factor for the tension of both anode and gate, the expected sagging returns to the acceptable value range, with a maximum sag of 1 mm.

6.3.1 | Electric field simulations for the perpendicular wires

The non-azimuthal nature of the perpendicular wires does not allow their implementation in a full scale two-dimensional axysymmetric TPC simulation as developed in Sec. 4.2. For this reason the impact of the perpendicular wires on the electric field is assessed via

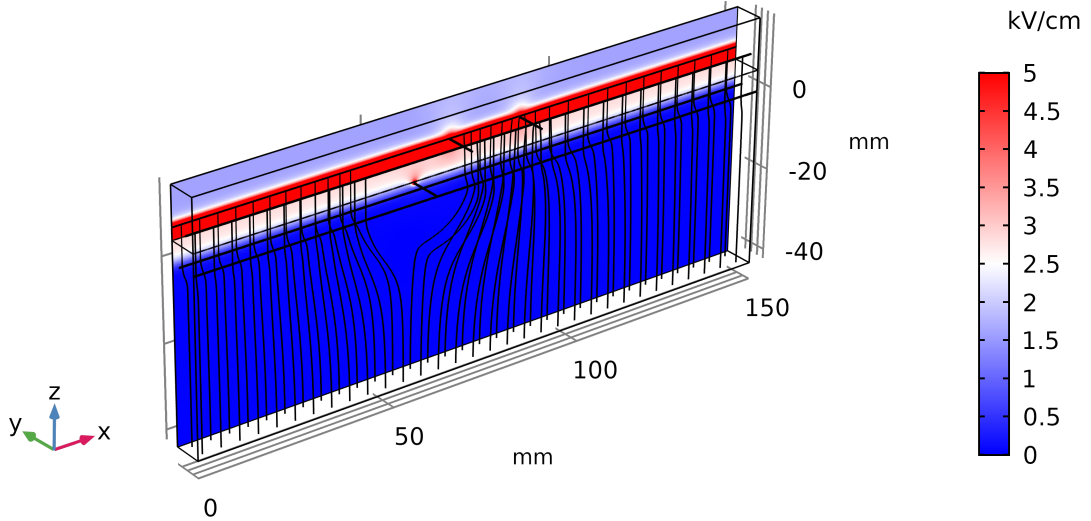


Figure 6.10 Three-dimensional electric field simulation of the region around the perpendicular wires using COMSOL Multiphysics® and field lines. The small y range is chosen to exploit the boundary condition symmetry while maximizing the x range given the finite available computing power.

local three-dimensional field simulations. The geometry is shown in Fig. 6.10, with the perpendicular wires along the y axis. The very narrow aspect ratio of the simulated volume is limited by the memory of the computer used to run the simulations. The boundary conditions are selected such that the field perpendicular to the lateral boundaries is null or negligible. For this reason the y range is limited to 1.5 wire pitches (7.5 mm), as in the xz -plane dividing the wire lengthways and between two wires the electric field has no y component. The condition is true for the x edges as its boundaries are far enough from the perpendicular wires not to feel their effect. This was cross-checked varying the x extent as much as allowed by the necessary resources and comparing the field behaviour at the edges. A final extension of 150 mm was selected, as its behaviour was identical to 200 mm. The bottom and top surface are set to the average voltage at the same height as coming from the 2D-axisymmetrical simulation. The main source of uncertainty is the z range of the simulation. The impact of these boundary conditions on the field between anode and gate is below 1% and thus it is considered negligible.

The three-dimensional simulation can be fed to PyCOMes [9] (see Sec. 4.2.3) in order to simulate the trajectory and behaviour of electrons in proximity to the perpendicular wires. The most striking feature of Fig. 6.10 is the splitting of the field lines below the

perpendicular wire of the gate, resulting in a lack of extracted electrons right above it. This corresponds to the effect observed in the (x, y) distribution of ^{83m}Kr events in Fig. 5.2. A total of 10^5 electrons were propagated starting at $z = -38$ mm (coordinate of Fig. 6.10) and uniformly distributed in (x, y) . The intersection of their trajectories at the liquid level is used as a proxy for the observed position reconstruction in the detector. The final distribution along x is plotted in Fig. 6.11 without any position resolution smearing (orange curve) and considering the more realistic 3 mm Gaussian radial resolution (brown). The simulated x is shifted in order to match the position of the perpendicular wires in the rotated coordinate system of the TPC, where the grids are parallel to the x_{rot} axis. The expectation is compared to the observed distribution of ^{83m}Kr events with a radial position lower than 40 cm (blue curve), where the distributions are normalized for the rates to match at $x_{\text{rot}} = 8$ cm. The data are shown for only half of the TPC, as for the same negative x_{rot} the structure repeats mirrored due to the other perpendicular wires. The main features of the data are captured by the simulations. The “valley”-like lack of reconstructed events around 13 cm is centered at the same position both in simulations and real data, but its width is underestimated. In the same way also the height of the bumps on the side of this feature is overestimated and the x_{rot} position of the double bump structure on the right is shifted. Although the source of this difference is not clear, a possible explanation is the

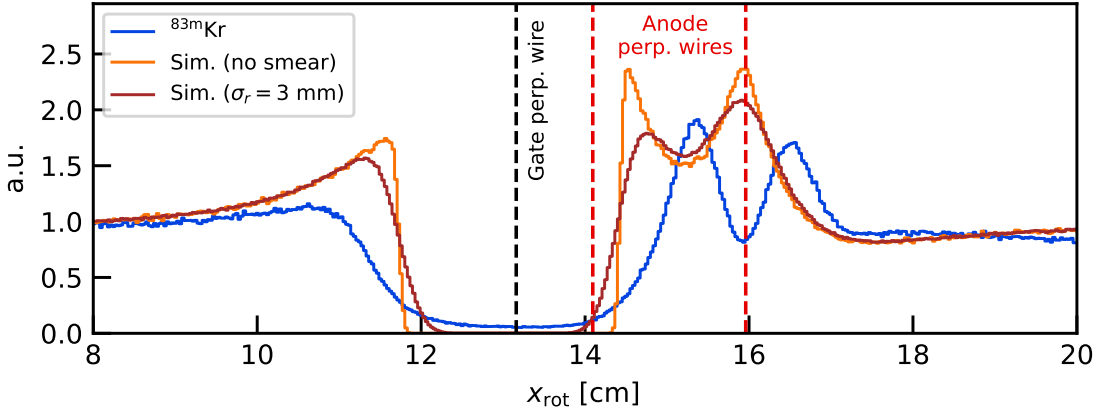


Figure 6.11 Position distribution of the ^{83m}Kr events along the rotated x -axis as reconstructed in calibration data (blue) and from the field simulations. Event distributions without (orange) and with (brown) a position reconstruction smearing of 3 mm are shown. While the main properties of the observed distribution are correctly predicted, their relative intensity and their position is not properly modeled. The y -values are scaled to match at $x_{\text{rot}} = 8$ cm.

training data set of the machine learning algorithms for the position reconstruction. The optical simulation used to generate and propagate VUV photons inside the detector use a uniform initial position distribution in the gas gap [10]. This is an imperfect model, as the electrons are focused by the gate wires in a small region right below the anode wires and the largest fraction of the S2 signal is produced around them, as detailed in Sec. 6.4.2 and shown in Fig. 6.15. This leads to a general underestimation of the “shadowing effect”, meaning the loss of optical photons due to the presence of the anode wire. This is a potential explanation of the stripe feature along the grid wires observed in Fig. 5.2. The magnitude of this effect can be estimated by the reasonable assumption that the electrons should be attracted by the anode perpendicular wire at higher x_{rot} , as the field simulations suggest. Assuming that the peak at around 16.5 cm corresponds to this wire, then the effect of the optical mismodeling of S2 is in the order of 5 mm, which is of the right scale to explain the observed overall mismatch.

The splitting of the field lines below the gate’s perpendicular wires affects not only the observed position distribution, but also the arrival time distribution of the electrons. Indeed, the splitting of the field lines at $z \simeq -20$ mm in Fig. 6.10 means that the electric field in this region significantly decreases. When an ionization cloud is in this region, the electrons closer to the perpendicular wires feel a lower electric field than the others. This translates into a non-uniform drift speed within the cloud, spreading the arrival time distribution of the electrons and hence the distribution of the S2 signal they produce in the gas. This is shown in Fig. 6.12. The simulated time distribution is not exactly that of the S2 signal, as it does not include the proportional scintillation photon production in gaseous xenon, the electron extraction time constant of about 140 ns [155] and the photon propagation time. Excluding the single electron shape, described in detail in Sec. 6.4, all these effects are at the 100 ns scale and can be neglected. Hence, the simulated distributions can be considered as proxies of the S2 signals and their interquartile ranges are good approximations of the S2 interquartile range, also known as *S2 width*.

The example used in Fig. 6.12 does not represent a real signal and is mostly pedagogical. Indeed, there is no data counterpart in XENONnT with zero spread in time at $z = -38$ mm and a transverse spread of 2.5 mm, as the values used in the simulation. However, a comparison with data is possible using the diffusion and drift speed obtained from data and combining them with the three-dimensional map of the perpendicular wires region obtained above. From $^{83\text{m}}\text{Kr}$ calibration data a drift speed of $v = (0.675 \pm 0.006)$ mm/ μs and a longitudinal diffusion coefficient of $D_L = (45.65 \pm 0.15)$ cm $^2/\text{s}$ are found. As the transverse diffusion coefficient cannot be inferred from the data, its average value along z is evaluated

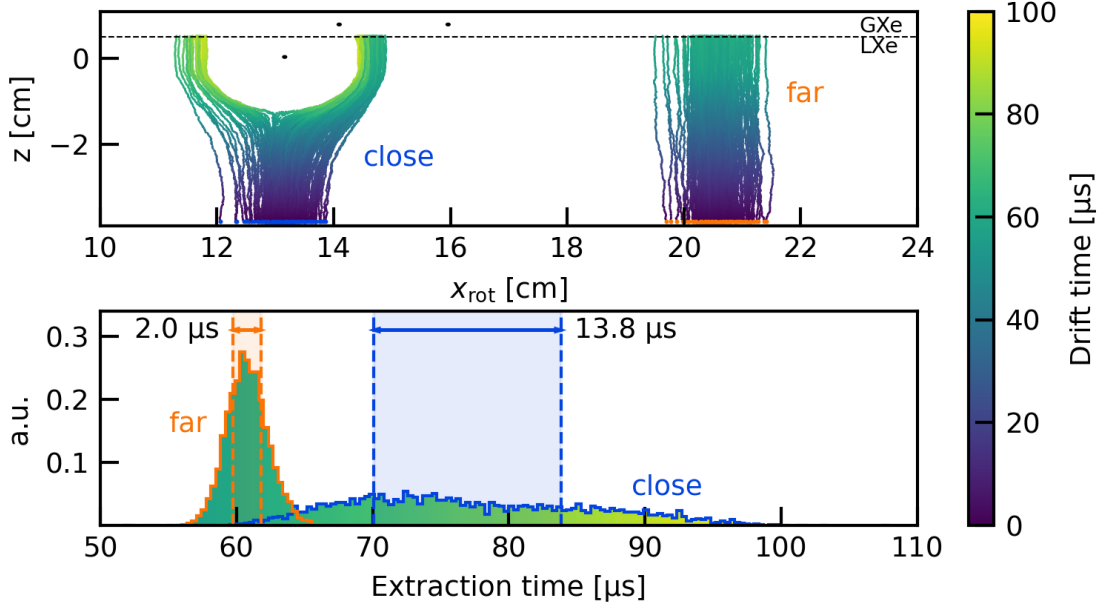


Figure 6.12 (top) Electron cloud propagation obtained from the three-dimensional simulation of the region around the perpendicular wires. The electrons starting below the gate’s perpendicular wire (“close”) are split by its effect, while the ones starting far from it (“far”) have linear trajectories. **(bottom)** Arrival time distribution at the liquid-gas interface for the electron clouds right below the gate perpendicular wire (blue contour) and far from it (orange contour). The electron cloud splitting increases the spread of the time distribution, as the time width values show.

from the corresponding electron transport property map discussed in Sec. 4.4. From these parameters, it is possible to determine the spatial and temporal spread of the electron cloud as a function of the interaction depth within the TPC. By uniformly sampling 10^5 initial z positions, the spread values are used to simulate times and positions at $z = -38$ mm (the z position from which the electrons are propagated in the 3D simulation) of the individual electrons making up the cloud, whose size is drawn from a Poisson distribution with a mean of 500. This is the average number of electrons liberated by the $^{83\text{m}}\text{Kr}$ interaction in liquid xenon, as predicted by NEST [133], ignoring the electron lifetime effect. The additional drift time from the last ~ 4 cm comes from sampling the drift time (x, y) map produced by uniformly propagating electrons in the three-dimensional simulation as done in Fig. 6.12. The simulated result along with the corresponding data is shown in Fig. 6.13,

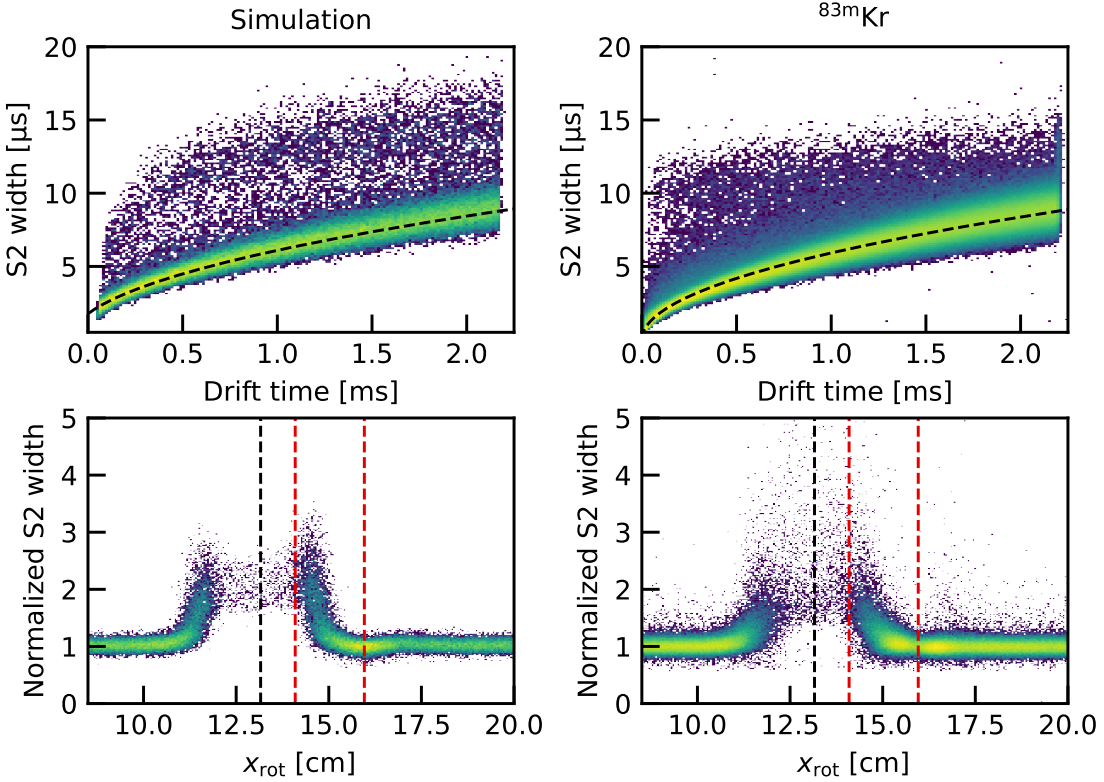


Figure 6.13 Comparison of the interquartile width of the time distributions from simulations (left panels) and the interquartile S2 width of ^{83m}Kr events reconstructed around the perpendicular wires (right panels). The drift speed and diffusion coefficient used in the simulations come from fits to real data. The simulated normalized width to the diffusion model of Eq. (6.3) as a function of x_{rot} (bottom left) matches well the observed distribution (bottom right). The position of the anode (gate) perpendicular wires are indicated with red (black) dashed lines. The color scale is logarithmic.

where the S2 width ω_{S2} vs. drift time t is fitted using the diffusion model

$$\omega_{\text{S2}} = \sqrt{\frac{2D_L t}{v^2} + \omega_{\text{SE}}^2}, \quad (6.3)$$

where the fit parameters are the longitudinal diffusion coefficient D_L and the width of the single electron signal ω_{SE} , defining the minimal width of the S2. The drift speed v is taken from independent measurements of the events close to the cathode. The comparison between simulation (left panels of Fig. 6.13) and measurement (right panels) returns a good agreement for the distribution of S2 width as a function both of drift time and x_{rot} .

This confirms the potential of using the electric field simulation to properly understand the observed signals. The most striking match is the proper reproduction of the feature around the gate's perpendicular wire in the S2 width vs. x_{rot} . The magnitude of the effect is well modeled, although the spread in width is slightly underestimated. This can be explained by the fact that the S2 width does not come from a full simulation of the S2 signal, but it is solely based on the arrival time distribution of the electrons. The normalized S2 width used for this comparison is the S2 width divided by the expected value coming from the fit to the diffusion model of Eq. (6.3) with the corresponding drift time.

6.4 | Electroluminescence simulation

The ionization electrons drift following the electric field lines in the active volume until they reach the liquid-gas interface between anode and gate. Here, the high extraction field in the liquid can extract them into the gaseous phase. The electron extraction efficiency $\varepsilon_{\text{extr}}$ is proportional to the extraction field and null for values below 2 kV/cm, while it saturates at almost 100 % above 5–6 kV/cm, as shown in Fig. 2.7. The extraction field during the first science run (SR0) of XENONnT was around 2.9 kV/cm, translating into an efficiency $\varepsilon_{\text{extr}} \simeq 53 \%$. This value was confirmed by comparing the expected number of ionization electrons from $^{83\text{m}}\text{Kr}$ interactions using NEST [133] to the ratio between the $^{83\text{m}}\text{Kr}$ S2 signal size and the single electron gain, which is the S2 signal intensity corresponding to a single electron. As the electrons are extracted into the gaseous xenon, they are accelerated by the strong electric field and produce proportional scintillation light, also known as electroluminescence and already discussed in Sec. 2.1. While the intensity of the signal can be modeled as a linear function of the electric field and the gas pressure, no information on the timing of the light emission is available through this simple model. This information can be derived from the cross sections of the different types of scattering between electron and xenon atoms, in particular for the collisions resulting in atomic excitations. This section focuses on the simulation of the time profile of the proportional scintillation signal for single electrons (SEs). These are key input for the simulations of S2 peaks and carry important information on the local gas gap length, being a useful tool to map the sagging of the electrodes.

6.4.1 | Garfield++ framework

As defined in its user guide, “Garfield++ is an object-oriented toolkit for the detailed simulation of particle detectors based on ionization measurement in gases or semiconductors” [261]. Garfield++ is the ROOT-based [262] C++ implementation of the original FORTRAN toolkit Garfield [6] and it combines several software packages developed to simulate different aspects of ionization-based detectors, such as electron transport. It also interfaces with many common software tools such as the particle propagator GEANT4 [231] and several finite and boundary element method solvers for the electric field, including COMSOL Multiphysics®. For simulating the proportional scintillation of electrons in gaseous xenon, the most useful features are the interface with COMSOL and the package *Magboltz* [263, 264]. This package was originally developed to solve the Boltzmann transport equation for electrons in different gas mixtures [265–267]. Its current version computes the electron transport properties for different gas mixtures using a semi-classical Monte Carlo simulation. It includes a database of the interaction cross section between electrons and more than 50 different atomic/molecular species for different types of collision, as shown in Fig. 6.14 for xenon atoms.

These cross sections are used to simulate electron propagation in a given gas mixture by estimating the collision rate $\tau^{-1}(\epsilon)$, with ϵ being the electron kinetic energy. The algorithm’s working principle is summarized in the following based on the detailed description given in [270]:

1. for an electron at position \vec{x} and kinetic energy ϵ , the duration of the free flight step

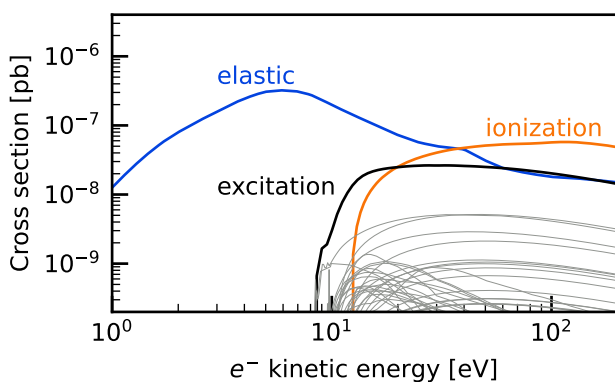


Figure 6.14 Cross section for different types of electron-Xe collisions used in *Magboltz* for the electron propagation properties in GXe [264]. The gray lines are the individual excitation channels, summing up to the black line. Data from LXCat database [268, 269].

is given by the total collision rate

$$\tau^{-1}(\epsilon) = \sum_j \sum_i \tau_{j,i}^{-1}(\epsilon) = \sum_j \sum_i N_j \sigma_{j,i}(\epsilon) v(\epsilon), \quad (6.4)$$

where i represents the number of available scattering processes, j the gas species with partial density N_j and $v = \sqrt{2\epsilon/m_e}$ is the electron velocity in the non-relativistic regime and m_e is the electron mass. In the xenon-only case the sum over the gas species j is reduced to a single component;

2. as the collision rate follows a Poisson distribution, the free flight duration Δt follows an exponential distribution and it can be sampled as $\Delta t(\epsilon) = -\tau(\epsilon) \ln(u)$ where u is a uniform random variable $u \in (0, 1]$;
3. the position and velocity of the electron is updated to new values assuming that the particle moves in vacuum between consecutive scatterings following the electric field \vec{E} sampled at the position \vec{x} for a time Δt . The scattering angle is defined by the type of collision;
4. repeat steps 1 to 3 until an endpoint is reached, such as an electrode.

The microscopic tracking described above was used to simulate the path of an electron extracted from the liquid-gas interface and the position of the excitations. The code imports the electric field output from COMSOL where the field maps are extracted from the two-dimensional simulations of Sec. 4.2. These consist of a close-up of the region around the anode and gate with a typical range of $[-0.5, 0.5]$ cm in r centered around the anode wire and $[-0.1, 1.0]$ cm in z with the gate position at 0 and the anode at about 0.8 cm. As the electric field in this region changes very rapidly, the electric field is mapped on a fine grid with a total of 2000×2500 points, i.e., the field is mapped in steps of $5 \mu\text{m}$ in r and $4.4 \mu\text{m}$ in z . The map is produced using the field far enough from $r = 0$ to avoid any axisymmetry-induced artifact and far from the electrodes' frames which could affect the field; typical values are $r \simeq 40$ cm. The initial z position of the electron is set at the liquid level and the radial position x_{rot} can be set to the desired value. The code tracks the primary electrons as well as secondaries produced via ionization, and returns the time and position of any collisional excitation, together with the total number of collisions and their type (e.g., elastic, inelastic or ionizing).

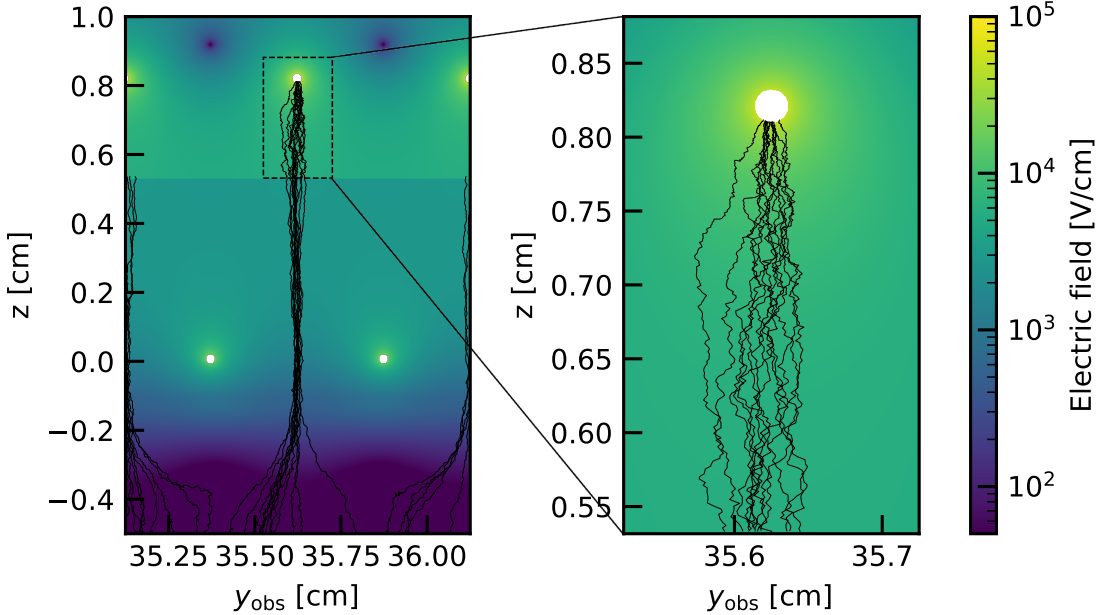


Figure 6.15 Electron propagation trajectories coming from the LXe bulk and focused by the gate in a small y_{obs} range along the liquid-gas interface. The trajectories within the liquid xenon are simulated using PyCOMes, the ones in gas are the interaction positions returned by Garfield⁺⁺.

6.4.2 | Single electron comparison

The Garfield⁺⁺ script detailed in the previous Section can be validated by comparing its output to single electron signals observed in XENONnT. The precise nature of these electrons is still under investigation [154, 271, 272], but photo-ionization induced by photo-electric effect after a large light signal and the capture and emission of drifting electron by impurities seem to be the primary causes of this background. As most SEs are expected to come from the liquid bulk, the focusing effect of the gate wires should be taken into account when selecting the initial position of the extracted electrons. The electrons drifting towards the liquid-gas interface are focused by the repulsive action of the gate and the attractive action of the anode. This results in the electrons being extracted only in a very narrow range of x_{rot} right under each anode wire, as is clear in Fig. 6.15. The focusing effect strongly reduces the time spread as the electrons follow straight field lines within the gaseous xenon.

The simulated time distribution and the detected one are not exactly the same, as

the simulation considers only the atomic excitation. A more direct comparison is possible by correcting the Garfield++ output for detector and photon emission/propagation effects: first, the de-excitation times are added to the initial simulated distribution of the atomic excitation times based on the singlet to triplet dimer state ratio. In gaseous xenon, around 15 % of the excited atomic states are singlet and they exponentially decay with a 5.88 ns lifetime [155]. The triplet states are characterized by a decay constant of 100 ns. An additional photon propagation time is added accounting for the fraction of photons detected by the top and bottom PMT arrays, characterized by different light propagation time distributions. These come from GEANT4 optical simulations, weighted for an average 70 % probability for each photon to be detected by the top array. Effects due to the transit time of the photoelectrons within the PMTs or the digitization of signals are not included. Together with the time information, Garfield++ returns information about the size of the electroluminescence signal. Also this quantity cannot be simply compared to the SE size, but it should be first corrected for detector effects, modeled using Monte Carlo simulations and discussed in [113]. A basic underlying assumption is that each excited atom leads to the production of a scintillation photon. This is justified by the fact that for xenon gas with a pressure larger than 100 mbar (the gas pressure of XENONnT is around 1.9 bar), the three-body collision of Xe^* producing excited dimers Xe_2^* is the dominant de-excitation process [123]. The total number of photons is corrected for the light collection efficiency (LCE), i.e., the probability for a photon to reach the photocathode of any PMT. It is $(23.2 \pm 0.8) \%$ for photons produced in the gas gap. Once a photon hits the photocathode of the PMT, it has a 30.7 % probability to produce a photoelectron at liquid xenon temperature [273]: this quantity is known as the quantum efficiency (QE). In 21 % of cases, two photoelectrons are emitted, increasing the observed signal size [274]. The last effect considered is the collection efficiency (CE), i.e., the probability for a photoelectron to be collected by the first dynode of the photomultiplier tube which is estimated to be 90 % [275]. The double photoelectron emission (DPE) probability is estimated looking at the single photoelectron spectrum. No detector resolution effect on the signal area is considered, such as the digitization of the signal. For this reason the simulated SE area is discrete and in units of detected photons, while in data the peak area is a continuous quantity.

The SE simulations are run using the SR0 configuration, with an extraction field of (2.91 ± 0.01) kV/cm and a liquid level of (5.1 ± 0.2) mm as measured by the short level meters. The simulations are compared to the single electrons extracted from data by selecting only S2-like peaks with an area smaller than 200 PE and an interquartile time range (“width”)

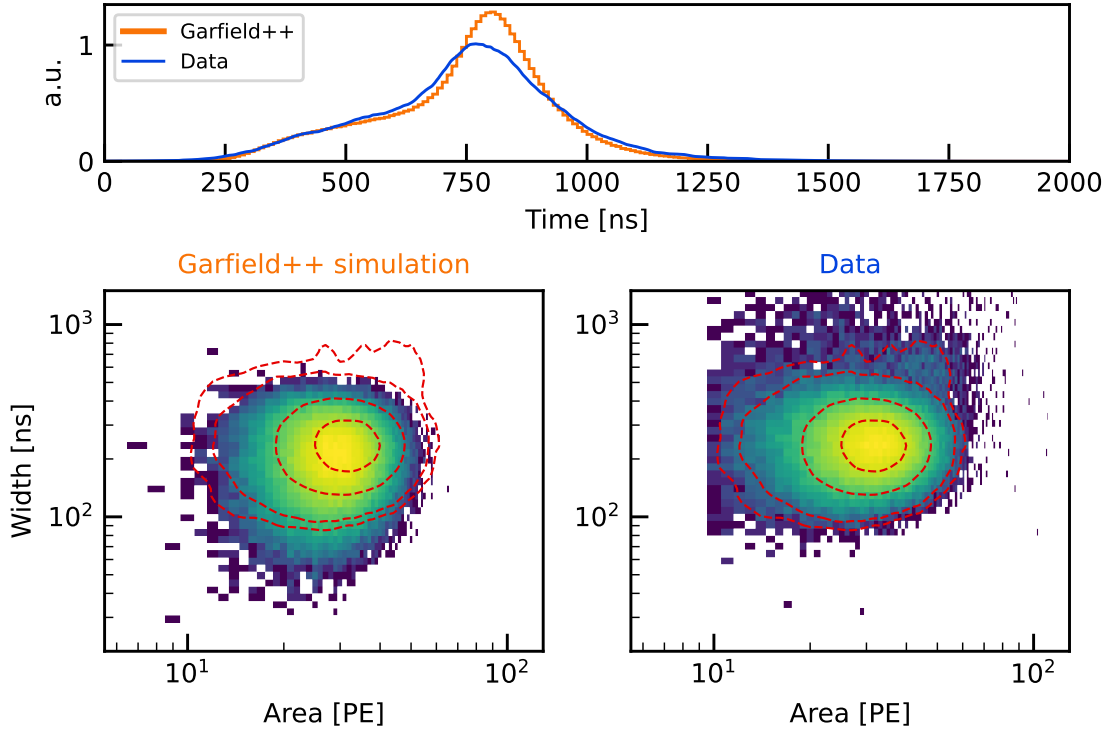


Figure 6.16 (top) “Waveform” from *Garfield++* (orange) compared to the SE waveform from data (blue). The two waveforms are centered around the weighted mean time and shifted by 750 ns. **(bottom)** Comparison between the area vs. width distribution from *Garfield++* simulations (left) and data (right). The contour lines indicate the profile distribution of the observed SE population. The color scale is logarithmic. The comparison shows an overall good agreement both for the time distribution and in the width vs. area space.

lower than 1500 ns. An additional isolation requirement is applied to exclude possible contamination coming from preceding large peak tails or PMT afterpulses⁽¹⁾. The isolation criterion rejects all peaks within 500 μ s of another peak. The SEs are selected from a radial position $r = 45$ cm and far from the perpendicular wires: in this way the impact of electrode sagging is minimized and the perpendicular wires effects can be neglected. The waveform shape is compared to the waveform from *Garfield++* in the top panel of Fig. 6.16, where both the peaks are centered around the weighted time average plus a 750 ns offset. No exact match is expected because of the omission of the effects coming from digitization as well as the impact of the sagging and the liquid level uncertainty. Still an overall good

⁽¹⁾An afterpulse (AP) is a signal recorded after a pulse due to the ionization of an atom inside the PMT. As the ionized atom follows the electric field from the first dynode to the photocathode, it can free a photoelectron once it reaches the latter.

agreement is reached between simulations and data, especially since the Garfield++ output solely depends on first principles and cross section calculations. Along with the distinct time profile, another key parameter space is area vs. time width (interquartile range of the waveform), particularly useful in the definition and selection of SEs. The comparison in the bottom panels of Fig. 6.16 shows that the simulation can reproduce the shape of the SE population. The simulation falls short to reproduce outliers at large time width, mainly focused around the perpendicular wires not included in this simulation, and at low widths, possibly due to neglecting digitization effects. A more complete comparison is possible through a full chain simulation where the final product is a waveform including PMT and digitization effects. In addition the matching should take into account the uncertainties coming from the level meter sensors and the unknown deformation of the anode and gate, possible by comparing different simulations where liquid level and electrode position are changed, as done in Sec. 6.5.

6.4.3 | Perpendicular wires

Garfield++ can be also used to simulate the region around the perpendicular wires. In this case the three-dimensional COMSOL simulation described in Sec. 6.3.1 is directly loaded into Garfield++ using the class `ComponentComsol` [261]. Because of the cm-scale resolution of the position reconstruction for SE-sized peaks, it is not possible to compare the properties of the SEs between simulations and data, as they present features well below the cm-scale that need to be resolved. Therefore ^{83m}Kr events are used, as the larger S2 size yields a 3 mm resolution. Since these events consist of many electrons, the longitudinal electron diffusion dominates the peak time spread and the distribution width has been modeled in Sec. 6.3.1, including the effect of the gate perpendicular wires. The presence of the additional wires strongly impacts the electric field within the gas gap, affecting both the extraction efficiency and the proportional scintillation. These two effects are considered separately and are combined later. The extraction efficiency is estimated evaluating the electric field right below the liquid-gas interface using measurements of $\varepsilon_{\text{extr}}$ (E_{extr}) from [228]. The results are reported in Fig. 6.17 (top panel): the larger field right below the anode perpendicular wires results in a 50 % relative increase of the extraction efficiency with respect to the rest of the TPC. The number of electroluminescence photons produced by a single extracted electron is simulated using Garfield++: the average intensity of the proportional signal from these photons as a function of the extraction position is shown in Fig. 6.17 (bottom panel). The presence of the anode perpendicular wires induces a

decrease of the proportional scintillation signal with respect to the region between the gate grid wires ($y_{\text{rot}} = 0.5 \text{ cm}$), where the ionization electrons are focused. This decrease is due to the fact that the electrons collected on these wires have a shorter path in gaseous xenon because of the $304 \mu\text{m}$ diameter of the perpendicular wires filling the gas gap, thus the electrons undergo less collisions. Fig. 6.18 clearly shows this effect in data as a drop of the SE gain along the perpendicular wires, extending across the entire TPC.

Following a similar procedure as described in Sec. 6.4.2 for the detector effects, it is possible to simulate the $^{83\text{m}}\text{Kr}$ S2 size. The simulation of the krypton ionization signal follows the procedure described in Sec. 6.3.1 with an average of 500 liberated electrons per interaction in liquid xenon. These electrons are propagated across the TPC and their position at the liquid-gas interface defines the average SE gain and $\varepsilon_{\text{extr}}$. The behaviour of the electrons within the electron cloud in the gas phase is assumed to be identical to that of individually extracted electrons. This assumption is confirmed by a dedicated simulation of the repulsion within the electron cloud, which showed that this effect is negligible when compared to the diffusion caused by the electrons' collisions with the xenon atoms in the gas. The results of the simulations of $^{83\text{m}}\text{Kr}$ events are shown in the top panel of Fig. 6.19. It is particularly interesting to notice that the size of the signal around

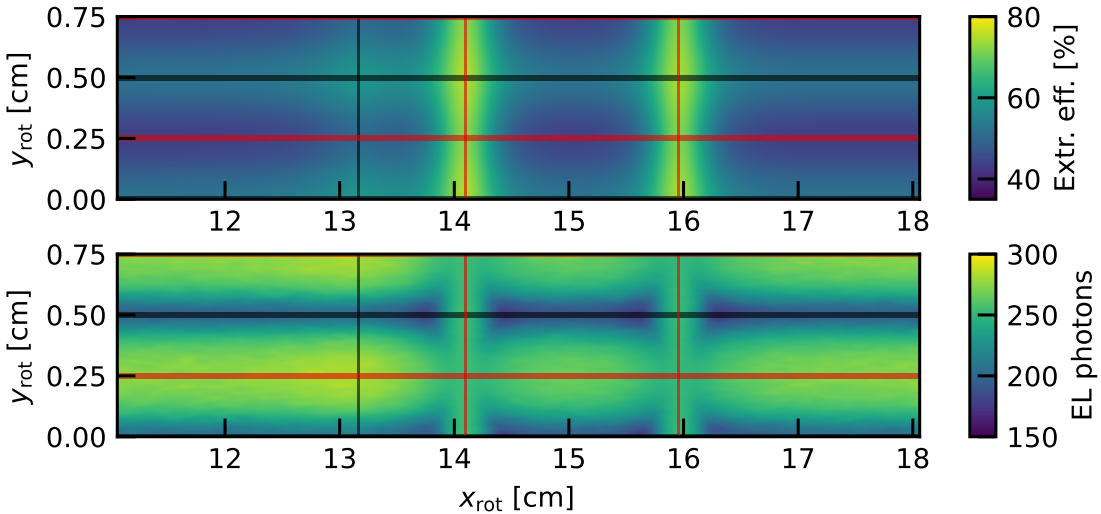


Figure 6.17 Extraction efficiency (top) and average number of electroluminescence photons (bottom) around the perpendicular wires for an electron at the given position ($x_{\text{rot}}, y_{\text{rot}}$) along the liquid-gas interface from simulations. The wires of the anode (gate) electrode are shown in red (black), parallel to x_{rot} . Perpendicular wires are along y_{rot} .

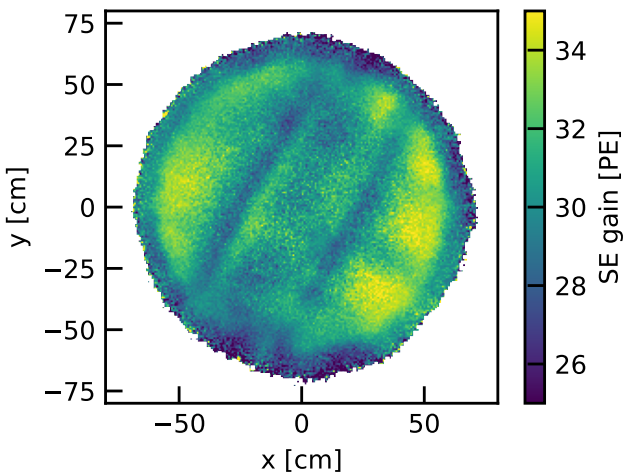


Figure 6.18 Measured single electron area (SE gain) in the (x, y) plane. The lower gain around the perpendicular wire is due to the smaller gas gap caused by the finite diameter of the perpendicular anode wires.

the anode perpendicular wire is slightly larger than farther away from it, in contrast with what observed for the SE gain in Fig. 6.18. This is due to the fact that while the SE area in this region is smaller, the extraction efficiency is higher. The simulated $^{83\text{m}}\text{Kr}$ S2 peaks are compared to the data shown in the bottom panel of Fig. 6.19: to minimize the effect of the sagging, only events at a radial position larger than 40 cm are selected. Apart for the different distribution along x_{rot} , already discussed in Sec. 6.3, the behaviour is well predicted by the simulation. Not only the average S2 size is well matched, but also the expected increase around the anode perpendicular wires is of the same magnitude as predicted by the simulations.

6.5 | Implementation in a full-chain waveform simulator

The results shown above are based on a simplified Monte Carlo method returning a proxy for the SE waveforms including detector and photon propagation effects as averaged quantities. This approach does not include digitization effects or signal production within the photomultiplier tubes themselves, leading to limitations such as the integer nature of the simulated SE gain.

A more precise simulation is possible by implementing the collisional excitation time distribution as an input for the waveform simulator *WFSim* [233], already discussed in Sec. 4.4. The output of the Garfield++ script is directly implemented in WFSim, as the additional effects coming from de-excitation and photon propagation are already included in the WFSim code. The information from Garfield++ about the intensity of

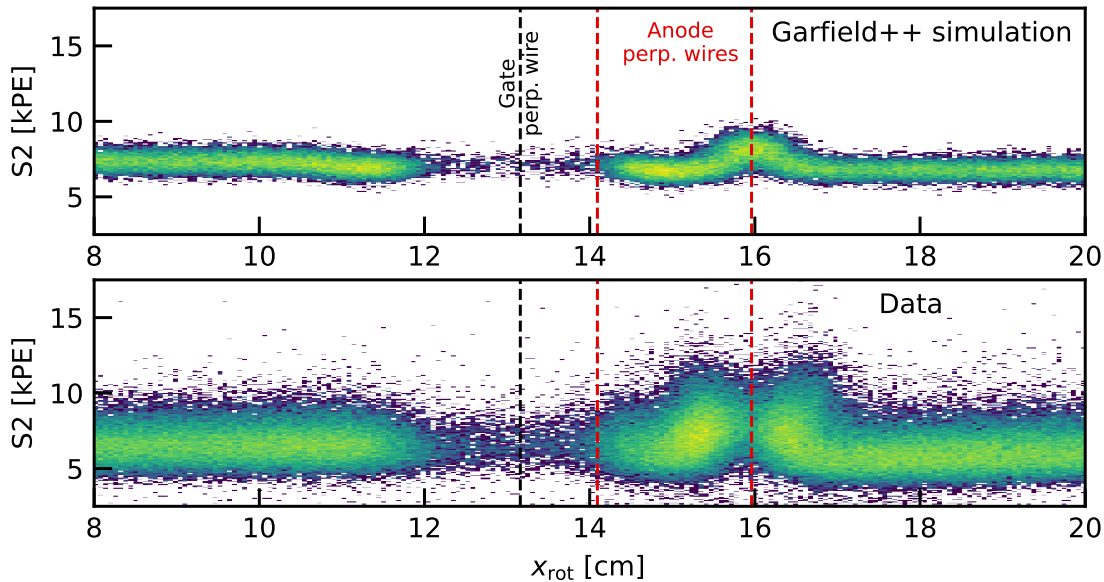


Figure 6.19 Simulated (top) and observed (bottom) area for the ^{83m}Kr calibration source. The larger area around the perpendicular wire of the anode at $x_{\text{rot}} \simeq 16\text{ cm}$ is due to the larger extraction efficiency. The color scale is logarithmic.

the electroluminescence signal is not used, as a data-driven approach was preferred. The excitation time distribution is implemented as a function of the liquid level and the x_{rot} position between two consecutive gate wires. The latter was implemented with the possibility to study the nature of the single electrons. Electrons coming from the liquid bulk would feel the focusing effect of the gate, while electrons trapped at the interface and later extracted could have some freedom to roam along the interface. The different extraction position affects the electron path in the gaseous xenon, leading to a narrower signal right below the anode wires and broader above the gate wires. The implemented time profile distributions are shown in Fig. 6.20 for two different liquid levels with the SR0 field configuration. A total of eight different liquid levels from 0.3 cm to 0.65 cm with 0.05 cm steps were simulated and implemented.

A fully detailed simulation of the waveforms makes it possible not only to compare the Garfield++ simulations with the observed SE signals, but also to extract information about the gas gap profile. For this purpose the time profile shown in Fig. 6.20 was restricted to the 0.5 mm right below the anode wire, where the electrons from the bulk are focused. The Garfield++ simulations were repeated keeping the gate wires fixed to the design position and varying the position of the anode, in order to simulate the sagging of the wires while

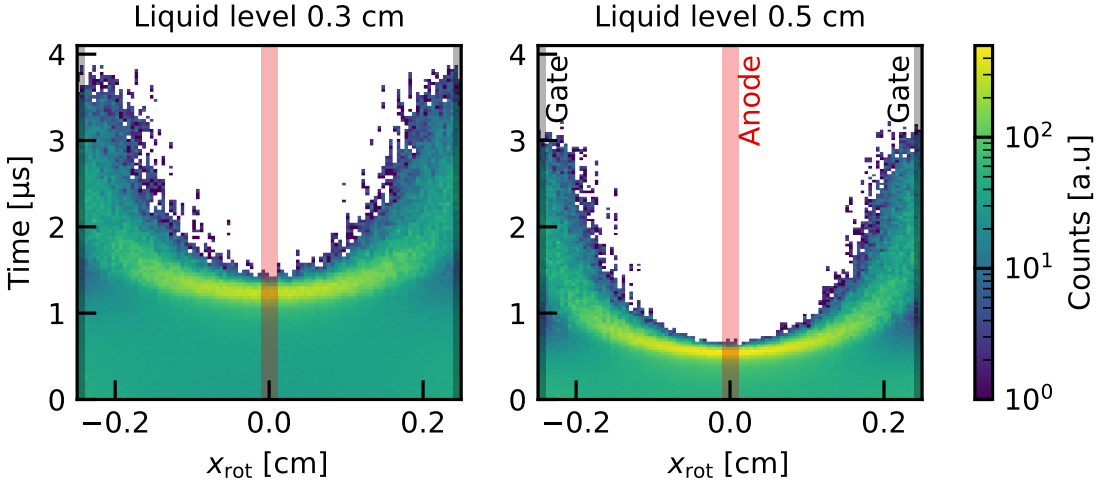


Figure 6.20 Time profile of the excitational collisions for a single electron as a function of the x_{rot} extraction position relative to the anode position. As the electron is extracted right below the anode, the field line it follows leads straight to the anode wire, while if it is extracted far away from it, the path is longer which translates into a larger time spread. This is shown for two different liquid levels. The color scale is logarithmic.

keeping the liquid level fixed to the measured (5.1 ± 0.2) mm. The sagging of the anode was varied with steps of 0.1 mm in the COMSOL simulation and the distribution of the collisional excitations for electrons coming from the bulk was simulated using Garfield++. These distributions were then used as an input for WFSim to produce templates of the SE waveform for different degrees of sagging. After binning the TPC in $5 \text{ cm} \times 5 \text{ cm}$ bins in (x, y) , the average SE waveform from each of these bins was compared to the templates and the value of the gas gap length corresponding to the best match was determined. The match was performed by minimizing the χ^2 of the waveform template and the average SE waveform allowing two degrees of freedom for normalization and time offset. The returned (x, y) gas gap length map coming from the matching of the SE waveform template can be compared to the expected sagging from the model of Sec. 6.2.1. This map is shown in the bottom right panel of Fig. 6.21 after the convolution with a Gaussian position reconstruction resolution of 3 cm, as expected for the SEs. The edges of the map show positive values of the sagging, whereas the anode is expected to sag towards negative values of z . This can be explained by a liquid level lower than the measured 0.51 cm above the gate, which would be interpreted as a positive sagging in this approach. In addition, the electrodes' frame can affect the shape of single electrons at larger radii. This suggests the need to be careful in the interpretation of the SE shape solely in terms of anode sagging.

The map obtained by matching the SE waveforms with the Garfield++ time profiles is compared to the expected sagging from the model described in Sec. 6.2.1. This is possible by estimating the electrostatic force from a three-dimensional COMSOL simulation with the SR0 configuration and including the effect of the perpendicular wires as a factor 1.5 for the wire tension, as described in Sec. 6.3. A full (x, y) map can be estimated by considering the catenary shape of Eq. (B.4) along x_{rot} for each individual wire and applying a 3 cm smearing. The result is shown in the bottom left panel of Fig. 6.21.

Although the overall match between the maps from the two approaches in the bottom panels of Fig. 6.21 has room for improvement, this does not consider the large uncertainties included in both models. The model of the anode wires deformation does not account for the spatial impact of the presence of the perpendicular wires, which would naturally affect the (x, y) distribution. Similarly, the Garfield++-driven map relies on the assumption that the spatial dependence of the SE waveform is solely due to the anode sagging. In particular, this model returns the size of the gas gap, converted into anode sagging by subtracting the liquid level position: this includes a large systematic uncertainty of 0.2 mm. The maximal deformation of the anode wires predicted by the two models is compared in the top panel of Fig. 6.21. The large uncertainty on the Garfield++-based model shows the strong impact that the liquid level measurement has on the estimation of the anode sagging. When considering the uncertainties, the two models show a better agreement. This is a promising result, as the two models come from independent approaches, input measurements and different physical considerations. The wire sagging model is solely based on the mechanical description of the deformation of the wires considering an electrostatic feedback effect, ignoring any data-driven input except the tension measurement. The Garfield++ model uses the predicted shape of the electroluminescence signal coming from first principles to match the observed SE and infer the length of the gas gap. The overall match between the two maps shows the potential of the two models and the Garfield++ framework, leading to a good confidence in our level of knowledge of the configuration of the S2 region of XENONnT.

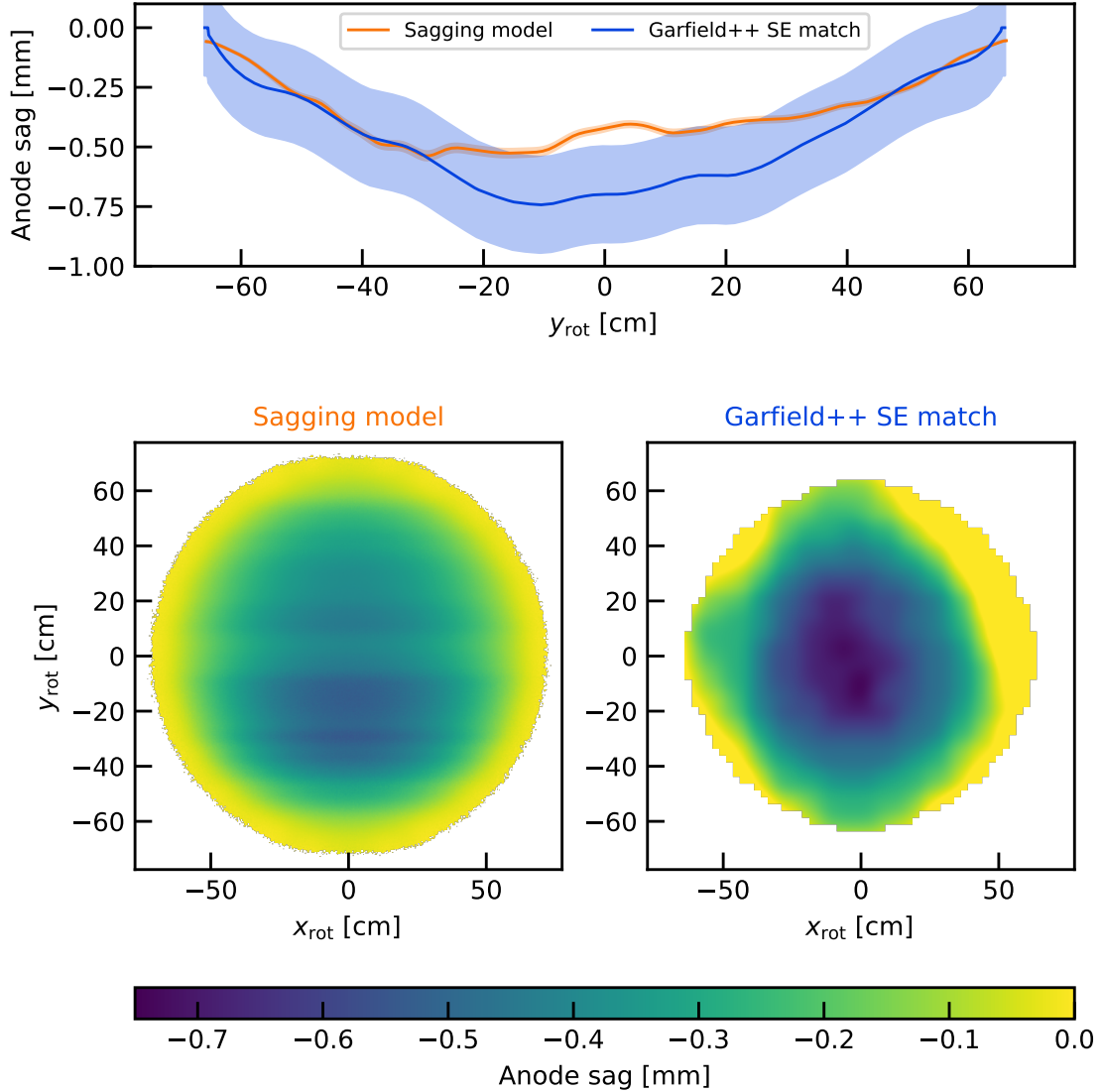


Figure 6.21 (top) Sagging in the middle of the grid wires as coming from the feedback model (orange) and the SE matching with the Garfield++ simulations (blue). The model uses a 50 % larger tension to account for the perpendicular wires. The main source of uncertainty for the SE matching is the 0.2 mm resolution of the SLMs. **(bottom)** Sagging (x,y) map as coming from the sagging model (left) and the Garfield++ matching (right). The two different approaches yield compatible results and a good agreement within uncertainties, confirming our understanding of the gas profile for the XENONnT TPC.

Summary and outlook

Almost a century after the observations by F. Zwicky [17], dark matter is still one of the most puzzling mysteries of modern physics, and a large number of experimental efforts aim for its detection. Dual-phase time projection chambers (TPCs) deploying a liquid xenon target have been leading the search for weakly interacting massive particle (WIMPs), one of the most promising candidates for particle dark matter. Liquid xenon is an ideal target material thanks to its radiopurity, high atomic number and large stopping power. The double-signal (scintillation S1, ionization S2) provided by the dual-phase TPC technology allows for a precise position and energy reconstruction, together with a discrimination power between background-like electronic recoils (ER) and WIMP-like nuclear recoils (NR). The XENON dark matter project at Laboratori Nazionali del Gran Sasso (LNGS) in central Italy is a pioneer for xenon-based dual-phase TPCs. In its several stages, XENON has been leading the hunt for WIMPs and its current phase, XENONnT, uses a 5.9 t active target with the lowest ER background ever achieved [114].

For a given energy deposition and interaction type the signal produced in a dual-phase TPC depends on the electric field in the active target. Hence, an inhomogeneous field translates into a non-uniform detector response, affecting the TPC performance and eventually leading to a worse sensitivity to WIMP interactions and other processes. For this reason, the optimization of the homogeneity of the electric drift field played a crucial role in the design of the XENONnT TPC and it is presented in Chapter 4. The homogeneity is ensured by a field cage comprising two nested arrays of copper electrodes enclosing the liquid xenon target which are electrically connected via two voltage dividers (“resistive chains”). The latter establish a linear potential drop along the field cage, with the applied voltages at its top and bottom representing degrees of freedom for the TPC design. The bottom end of the XENONnT field cage is connected to the cathode via a resistance of $7\text{ G}\Omega$, which is the optimal value at the design TPC voltage configuration including different possible variations. The top end is biased via an independent high voltage module, allowing for the tuning of the electric field even after sealing the detector.

Figures of merit considered for the optimization are the spread of the electric field strength inside the volume of the active target, indicating the homogeneity of the drift field, and the magnitude of the charge-insensitive volume (CIV). The CIV is the volume of liquid xenon from which liberated electrons are drifted by the field towards the lateral TPC walls, leading to signal loss. The electrostatic fields were simulated using the finite element method software COMSOL Multiphysics® [4], while the electron propagation was simulated using the custom tool PyCOMes [9]. The tools developed in this work were fundamental in the design of the field cage and resistive chain of the XENONnT TPC. They also played a crucial role after a short-circuit between cathode and bottom screen happened during the commissioning before SR0. This imposed a strongly reduced voltage at the cathode, reducing the electric drift field from the designed ~ 191 V/cm to 23 V/cm. The optimization of the bias voltage of the top end of the field cage allowed for the successful operation of the detector for WIMP searches.

Using $^{83\text{m}}\text{Kr}$ calibration data from the first science run (SR0) of XENONnT, the electric drift field inside the liquid xenon active target is studied and presented in Chapter 5. The comparison of the radial $^{83\text{m}}\text{Kr}$ distribution along the height of the TPC showed a disagreement between expectation and data. This could be explained and corrected by including a linear surface charge distribution along the PTFE walls ranging between (-0.1 ± 0.3) $\mu\text{C}/\text{m}^2$ at the bottom of the TPC and (-0.50 ± 0.05) $\mu\text{C}/\text{m}^2$ at the top. The corresponding electric field was compared to a data-driven drift field map. The maps differ of only $(3 \pm 2)\%$, showing an overall excellent agreement between data and simulation. The electric drift field simulation was used to correct the observed proportional scintillation S2 signals for the charge yield dependence on the electric field. In this way it was possible to explain the apparent source-dependence of the electron lifetime, which estimates the probability for a drifting electron to be lost to impurities in liquid xenon. The effect of the drift field on the estimation of the electron lifetime was studied also by changing the bias voltage of the top most field shaping ring of the field cage during a $^{83\text{m}}\text{Kr}$ calibration. The measured lifetime showed a clear dependence on the bias voltage V_{top} , which vanishes once the S2 signal is corrected using the electric field map. The inhomogeneity of the field affects also the path of the electrons in the active target, mainly resulting in an inward push of the reconstructed radius of the event positions. A data-driven map was developed to correct for this distortion effect, based on the assumption of uniformly distributed $^{83\text{m}}\text{Kr}$ events and no charge-insensitive volume. The impact of the presence of a $\mathcal{O}(100\text{ kg})$ CIV was included as a scaling factor for the fiducial volume. The scaling factor for SR0 was estimated to be $(96 \pm 3)\%$ resulting into a final fiducial volume of (4.35 ± 0.14) t, used for

the first science run results of XENONnT [114].

The experience obtained from the study of the electric field presented in this work is important for the development of the next generation of xenon-based dual-phase TPCs, such as the DARWIN observatory [276]. The simulation of the electric field was an important tool not only during the design phase of the TPC, but it was also crucial for the correct understanding of the signal response of the detector. Although particular effort should be invested in the realization of a three-dimensional simulation of the TPC, the good agreement between simulations and data demonstrated in this work shows that an axysymmetric two-dimensional geometry can be equally exploited. The faster two-dimensional simulations are particularly important during the design phase, when different geometries need to be simulated, requiring the production of a large number of simulations, available within hours for two-dimensional geometries, instead of days for three-dimensional implementations. Together with the proper simulation of the electric field, the flexibility in the biasing of the TPC field cage played a crucial role in the good outcome of XENONnT SR0, despite the sub-optimal configuration of the electrodes' voltages. A future dual-phase TPC deploying a field cage should allow for the independent bias of both its top and bottom ends, treating it as an independent electrode and not only as a passive element.

The intensity of the signal S2 depends not only on the electric field within the active target, but also on the path length of the extracted electrons in the gaseous xenon, together with the electric field in and the thermodynamic state of the gas. Hence, a precise monitoring of the liquid xenon level during operations is fundamental to understand any variation of the S2 signal formation, and for this reason a system of eight capacitive sensors (“level meters”) was developed. This system is described in Chapter 3. The liquid level position is continuously monitored during nominal TPC operation by a set of four short level meters with a resolution of a few tens of μm . Two long and two medium level meters are positioned along the entire $\sim 1.5\text{ m}$ height of the TPC and measure the level of the liquid during xenon recuperation and detector filling operations.

The secondary scintillation process induced by the electrons extracted into gaseous xenon is simulated and compared to data from SR0, as described in Chapter 6. The path of the extracted electrons through the gaseous xenon is simulated using the software Garfield++ which yields information about the time distribution of the scintillation photons. This information is used to simulate intensity and time profile of the S2 signals associated to single electrons (SEs) and the simulations are compared to SE signals observed in XENONnT. The comparison of the signal shape returns a good agreement, confirming

Summary and outlook

the proper understanding not only of the charge and light yield within the liquid xenon active volume, but also the electroluminescence mechanism in the gaseous phase. The comparison returns also important information on the size of the gas gap where the secondary proportional signal is produced, allowing for its precise mapping across the (x, y) plane of the TPC. This map is compared to the expected deformation of the wire grids of the anode and gate electrodes. This estimation is based on a model developed taking into account the feedback effect coming from the change of the electric field when the wires move due to the electrostatic force. The comparison between the two sagging maps yielded a good agreement, providing a cross-validation between the deformation model of the wire grids and the gas gap estimation from the SE signal shape.

Extra “perpendicular” wires were installed on the anode and gate electrodes in response to a large tension loss observed after the electrodes were tested at cryogenic liquid xenon temperature. The impact of these perpendicular wires on the drift paths of ionization electrons is simulated using COMSOL and the custom-developed PyCOMes. The comparison of the simulation with data returns an excellent agreement, explaining features in the position reconstruction distribution and time spread of the S2 signals around the perpendicular wires as an effect of the local electric field distortion. Similarly, the secondary scintillation of the extracted ionization electrons in the xenon gaseous phase near the perpendicular wires is simulated using the Garfield++ software. The simulations properly reproduce the observed smaller S2 size of the single electrons extracted close to the perpendicular wires, while confirming the larger size of the ^{83m}Kr S2 signals due to the larger extraction efficiency.

Although the impact of the perpendicular wires on the observed signals is well understood and properly simulated, their installation was the consequence of a large tension loss of the electrodes’ grid wires. Electrodes represent one of the most critical component of the dual-phase TPCs and particular care is taken for their design, production and testing. A model of the deformation of the wires under the electrostatic force was presented in this work, but a better understanding and simulations of the electrodes’ deformation are important for future detectors. Similarly, the realistic simulation of the proportional scintillation S2 is a valuable tool not only for the design of the electrodes, but also for the simulation of the expected signals. This should become a standard tool in the design and simulation of the next generation of xenon-based dual-phase TPCs.

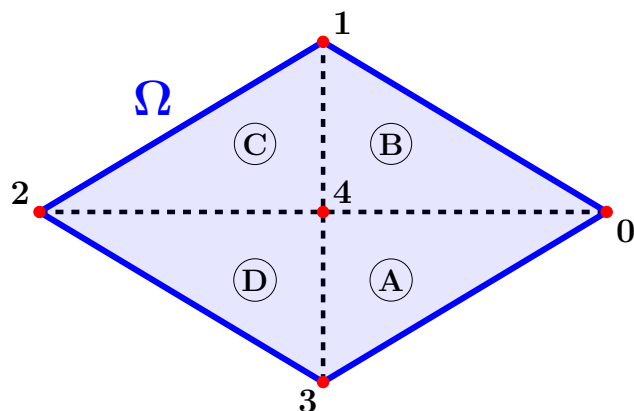
The results presented in this work played a crucial role in the successful design of the XENONnT TPC and the first science run of the experiment. The modeling of the

deformation of the wire grids under the effect of the electrostatic force led to the modification of the existing gate and anode electrodes. The expected deformation of the wires resulted in a hinder for the proper operation of the detector, leading to the decision to install a set of extra perpendicular wires. In addition, the innovative independent bias of the field cage made it possible to counteract the sub-optimal voltage configuration reached during the commissioning of the detector before SR0. The tools developed in this work allowed also for a deep understanding of the electric field within the active volume. After including a sub- $\mu\text{C}/\text{m}^2$ charge distribution on the wall of the detector, an excellent agreement of the electric field simulation with the data was reached under several aspects, such as the reconstructed position distribution of the events. The information of the electric drift field was not only included in the simulation of the signal production and the propagation of liberated ionization electrons in the active target, but it was also used to define the fiducial volume utilized for the first results of SR0.

Appendix A

Finite element method

The finite element method (FEM) is a technique to numerically solve a complex and continuous problem described by differential equations by reducing it into many simpler and smaller algebraic equations. It is based on the discretization of the space where the problem is defined into smaller *elements* making up the *mesh*. The points where the boundaries of two or more elements meet are called *nodes*. The FEM solution is precise at the nodes, while it is interpolated within the elements, returning a discrete approximated solution composed of a set of piecewise-continuous functions defined within each element. A precise description and treatment of the finite element method is given in [277]: in the following a simplified overview of the method is presented, considering the specific case of an electrostatic field calculation.



The first step is to discretize the problem space, a process known as meshing. This is typically done with simple shapes characterized by few nodes per element, such as triangles for the two-dimensional case or tetrahedra for the three-dimensions. Given the domain Ω shown above, the meshing is done by dividing it into four triangular elements (A to D)

for a total of five nodes (0 to 4). An arbitrary function is then selected to describe the behaviour of the potential within each element. Linear relations are typically preferred for simplicity:

$$V = a_1 + a_2 \cdot x + a_3 \cdot y. \quad (\text{A.1})$$

For a given element the potential function is constrained at the nodes, returning a unique solution for the coefficients \vec{a} :

$$\begin{pmatrix} v_i \\ v_j \\ v_k \end{pmatrix} = \begin{pmatrix} 1 & x_i & y_i \\ 1 & x_j & y_j \\ 1 & x_k & y_k \end{pmatrix} \begin{pmatrix} a_1 \\ a_2 \\ a_3 \end{pmatrix} \Rightarrow \vec{v} = \mathbb{X}\vec{a} \rightarrow \vec{a} = \mathbb{X}^{-1}\vec{v}. \quad (\text{A.2})$$

The choice of the indices should follow an anticlockwise order: for the element A a combination of (i, j, k) like $(3, 0, 4)$ is valid, while $(3, 4, 0)$ is not. Following the geometrical interpretation of the matrices, the determinant of \mathbb{X} is twice the area of the triangular anode A [278]. Therefore the inverse of the matrix can be written as

$$\mathbb{X}^{-1} = \frac{1}{2A} \begin{pmatrix} \alpha_i & \alpha_j & \alpha_k \\ \beta_i & \beta_j & \beta_k \\ \gamma_i & \gamma_j & \gamma_k \end{pmatrix} \quad (\text{A.3})$$

where the coefficients are:

$$\begin{aligned} \alpha_i &= x_j y_k - x_k y_j & \alpha_j &= x_k y_i - x_i y_k & \alpha_k &= x_i y_j - x_j y_i \\ \beta_i &= y_j - y_k & \beta_j &= y_k - y_i & \beta_k &= y_i - y_j \\ \gamma_i &= x_k - x_j & \gamma_j &= x_i - x_k & \gamma_k &= x_j - x_i. \end{aligned}$$

Having an explicit way to define the coefficients of the potential functions, the voltage can be rewritten as a function of the position and the voltages at the nodes:

$$V = \vec{a} \cdot \vec{x} = \mathbb{X}^{-1}\vec{v} \cdot \vec{x} = \overbrace{\mathbb{X}^{-1}\vec{x}}^{\vec{m}} \cdot \vec{v}. \quad (\text{A.4})$$

Based on the definition of the electric field, we obtain the gradient relationship:

$$\vec{E} = -\vec{\partial}V = - \begin{pmatrix} \partial_x \vec{m} \\ \partial_y \vec{m} \end{pmatrix} \vec{v} \equiv -\mathbb{M}\vec{v}, \quad \text{with } \mathbb{M} = \frac{1}{2A} \begin{pmatrix} \beta_i & \beta_j & \beta_k \\ \gamma_i & \gamma_j & \gamma_k \end{pmatrix} \quad (\text{A.5})$$

where the striking feature is that the electric field is constant, due to the decision to use a bilinear function to describe the potential inside each element. The physics input enters at this stage through the “stiffness matrix” \mathbb{K} . This is named after the original application of FEM to the displacement of solids, where this relationship is the matrix Hooke’s law $\vec{F} = \mathbb{K}\vec{X}$. For the electrostatic approach, this relationship is defined thanks to the *principle of minimum potential energy* by minimizing the electrostatic energy functional [279]:

$$\Pi_e = U_{\text{int}} + U_{\text{pot}}. \quad (\text{A.6})$$

The internal electrostatic energy stored by the electric field within a volume Ω with dielectric constant ε is proportional to the squared of the field intensity and can be written as a function of the nodal voltages:

$$U_{\text{int}} = \int_{\Omega} \frac{1}{2} \varepsilon E^2 d\Omega = \int_{\Omega} \frac{1}{2} \varepsilon (\mathbb{M}\vec{v})^T \mathbb{M} \vec{v} d\Omega = \frac{\varepsilon}{2} \vec{v}^T \left[\int_{\Omega} \mathbb{M}^T \mathbb{M} d\Omega \right] \vec{v}. \quad (\text{A.7})$$

The potential energy is given by the charge distribution ρ as

$$U_{\text{pot}} = - \int_{\Omega} \rho V d\Omega = - \int_{\Omega} \rho \vec{m} d\Omega \cdot \vec{v}. \quad (\text{A.8})$$

Minimizing the functional with respect to the nodal voltages, it is possible to define the stiffness matrix \mathbb{K} and the “force vector” \vec{f} , equivalent to the force due to the charge distribution:

$$\frac{\partial \Pi_e}{\partial \vec{v}} = \underbrace{\varepsilon \left[\int_{\Omega} \mathbb{M}^T \mathbb{M} d\Omega \right]}_{\mathbb{K}} \vec{v} - \underbrace{\int_{\Omega} \rho \vec{m} d\Omega}_{\vec{f}} = 0. \quad (\text{A.9})$$

The integrand in the stiffness matrix is constant, therefore this can be simplified as

$$\mathbb{K} = t A \mathbb{M}^T \mathbb{M} = \frac{\varepsilon t}{4A} \begin{pmatrix} \beta_i^2 + \gamma_i^2 & \beta_i \beta_j + \gamma_i \gamma_j & \beta_i \beta_k + \gamma_i \gamma_k \\ \beta_j^2 + \gamma_j^2 & \beta_j \beta_k + \gamma_j \gamma_k & \\ \beta_k^2 + \gamma_k^2 & & \end{pmatrix}, \quad (\text{A.10})$$

where A is the area of the element, t is the constant element thickness. The lower triangular elements are omitted as the matrix is symmetric. Assuming that the elements are small enough to consider the charge to be uniformly distributed within them, the charge-induced

potential energy is equally distributed between the three nodes:

$$\vec{f} = \frac{tA\rho}{3} \begin{pmatrix} 1 \\ 1 \\ 1 \end{pmatrix}. \quad (\text{A.11})$$

The solutions for each element are then combined into a single algebraic equations system by summing the forces acting on each node. As in a large mesh, most of the nodes do not belong to the same element, hence this leads to a sparse system of linear equations. Before solving the system, *boundary conditions* need to be applied in order to reduce the number of degrees of freedom. In FEM, the *Dirichlet conditions* are typically used and they consist in directly setting the nodal voltages, for example setting the voltages of some boundaries of the volume. Several resolution methods for large sparse system of linear equations have been developed and they can be divided into direct and iterative. In the direct case the returned solution is exact, but the computational requirement is larger. Iterative solutions are typically preferred for more complicated problems as they require less resources, but they return approximated solutions [280].

Considering the initial example, assuming a charge density of $\rho = 0$ and $\varepsilon = 1$, it is possible to use Eq. (A.9) and the definitions of its components for each of the four elements. The contribution from each elements to the five nodes is summed. Considering the stiffness of matrix $k_{ij}^{(N)} = t_N (\beta_i \beta_j + \gamma_i \gamma_j) / 4A_N$, with N being the index of the element, and i, j the indices of the considered nodes, the final system of linear algebraic equations is:

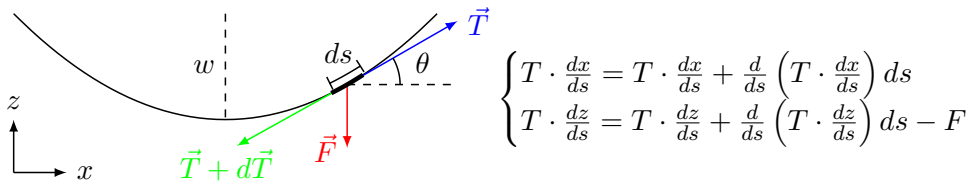
$$\begin{pmatrix} 0 \\ 0 \\ 0 \\ 0 \\ 0 \end{pmatrix} = \begin{pmatrix} k_{00}^{(A+B)} & k_{01}^{(B)} & 0 & k_{03}^{(A)} & k_{04}^{(A+B)} \\ & k_{11}^{(B+C)} & k_{12}^{(C)} & 0 & k_{14}^{(B+C)} \\ & & k_{22}^{(C+D)} & k_{23}^{(D)} & k_{24}^{(C+D)} \\ & & & k_{33}^{(D+A)} & k_{34}^{(D+A)} \\ & & & & k_{44}^{(A+B+C+D)} \end{pmatrix} \begin{pmatrix} v_0 \\ v_1 \\ v_2 \\ v_3 \\ v_4 \end{pmatrix},$$

where $k_{ij}^{(N+M)} = k_{ij}^{(N)} + k_{ij}^{(M)}$. As node 4 belongs to all the four elements, a contribution comes from all of them, while node 1-3 and 2-0 do not belong to any common element, therefore the entries corresponding to their interaction are zero. Eventually, the boundary conditions are set and the linear equation system is solved for the remaining degrees of freedom of the nodal voltages.

Appendix B

Sagging model

The model for the sagging of a real wire under a known tension is developed based on [281]. A wire is a solid body characterized by its extension L_0 along a single direction and defined by its mass m , with linear density $\lambda = m/L_0$. Once a wire is fixed only at the ends, its gravitational force arranges it to a configuration which balances the tension forces acting on each of its elements. Initially we consider an ideal and unextendable wire with Young modulus $E \rightarrow +\infty$. The Young modulus is defined as $E = \sigma/(\Delta L/L_0)$, where $\sigma = F/A$ is the *stress* (force per unit area) acting on the body and $\Delta L/L_0$ is the *strain* (relative deformation), valid only in the elastic regime. Considering the gravitational force acting on each infinitesimal wire element of length $ds = \sqrt{dx^2 + dz^2}$, the equilibrium condition for each element in the x - and z -coordinates is:



As $ds \neq 0$, the x axis condition requires $\frac{d}{ds} \left(T \cdot \frac{dx}{ds} \right) ds = dT_x = 0$, meaning that the x component of the tension along the wire is constant. It is possible to define this component as $T \cdot \frac{dx}{ds} = T \cos \theta = H$, with H being the horizontal component of the tension at the edge of the wire. Plugging this information in the z component equilibrium condition, the following relation is obtained:

$$\frac{d}{ds} \left(T \cdot \frac{dz}{ds} \right) ds = \frac{d}{ds} \left(T \cdot \frac{dx}{ds} \cdot \frac{dz}{dx} \right) ds = \frac{d}{ds} \left(H \cdot \frac{dz}{dx} \right) ds = F_{\text{gr}} = f_{\text{gr}} \cdot ds \quad (\text{B.1})$$

where the weight per unit length $f_{\text{gr}} = \lambda g$ ($g = 9.81 \text{ m}^2/\text{s}$) is written out. Removing the dependencies from ds in Eq. (B.1) using its definition, a differential equation for the shape function $z(x)$ is obtained:

$$\frac{dx}{ds} \frac{d}{dx} \left(H \cdot \frac{dz}{dx} \right) ds = \lambda g \cdot ds \quad \rightarrow \quad H \cdot \frac{d^2 z}{dx^2} = \lambda g \sqrt{1 + \left(\frac{dz}{dx} \right)^2}. \quad (\text{B.2})$$

Defining the variable $\eta = \frac{dz}{dx}$, Eq. (B.2) becomes

$$\dot{\eta} = \frac{\lambda g}{H} \sqrt{1 + \eta^2}, \quad (\text{B.3})$$

which can be solved by separation of variables, leading to a *catenary* shape

$$z(x) = \frac{H}{\lambda g} \cosh\left(\frac{\lambda g}{H}x\right) + \kappa, \quad (\text{B.4})$$

where κ is an offset set to $\kappa = -\frac{H}{\lambda g}$ to satisfy the boundary condition $z(0) = 0$, as $x = 0$ is the minimum of the function. As in most of the use cases x is such that $H \gg \lambda g x^{(1)}$, it is possible to rewrite the function as a Taylor expansion:

$$z(x) = \frac{H}{\lambda g} + \frac{\lambda g}{2H} x^2 - \frac{H}{\lambda g} + O(x^4) \quad \rightarrow \quad z(x) \simeq \frac{\lambda g}{2H} x^2. \quad (\text{B.5})$$

In presence of an electrostatic force f_{es} per unit length, which is assumed to be uniform along the entire wire, it is vector summed to the gravitational force to yield a total linear force $f = f_{\text{gr}} + f_{\text{es}}$. The maximal sagging w for a wire of length L_0 is given by Eq. (B.5) for $x = L_0/2$, i.e., at the center of the wire:

$$w = \frac{f L_0^2}{8H}. \quad (\text{B.6})$$

This relation shows that for the same applied force, the maximal sagging of the wire scales with the square of the length L_0 and linearly decreases with the (horizontal) tension H applied. For this reason this problem is of particular importance for TPCs with a large diameter.

If the assumption of an ideal wire is abandoned, it is important to include in the equilibrium conditions also the elastic contributions due to the wire extension. An additional variable p is included to represent the position along the extended wire, taking the place of

⁽¹⁾For a typical XENONnT anode wire $H = 3 \text{ N}$ and $\lambda g = 2 \times 10^{-3} \text{ N/m}$ with a wire length of few meters.

s , the position along the unstretched wire. By definition of the Young modulus:

$$E = \frac{F/A_0}{\Delta L/L_0} = \frac{T/A}{(dp - ds)/ds} \rightarrow \frac{dp}{ds} = \frac{T(s)}{EA_0} + 1, \quad (\text{B.7})$$

where $A_0 = \pi r_0^2$ is the secitonal area of the wire. As shown above, the x component of the tension is constant while the z component can be rewritten as:

$$\frac{d}{dp} \left(T \cdot \frac{dz}{dp} \right) dp = f ds \rightarrow T \cdot \frac{dz}{dp} = fs + \text{const.} \quad (\text{B.8})$$

Including the vertical reaction V at the support and considering the coordinate system with the weight direction along negative z , the equilibrium condition is

$$\begin{cases} T \cdot \frac{dx}{dp} = H \\ T \cdot \frac{dz}{dp} = V - fs. \end{cases} \quad (\text{B.9})$$

Including the geometric constraint $\left(\frac{dx}{dp}\right)^2 + \left(\frac{dz}{dp}\right)^2 = 1$, this returns

$$T(s) = \sqrt{H^2 + (V - fs)^2}. \quad (\text{B.10})$$

Combining the information from Equations (B.7), (B.9) and (B.10), we obtain a differential equation for $z(s)$ with the solution [281]:

$$z(s) = \frac{fL_0 s}{EA_0} \left(\frac{1}{2} - \frac{s}{2L_0} \right) + \frac{H}{f} \left[\sqrt{1 + \left(\frac{fL_0}{2H} \right)^2} - \sqrt{1 + \left(f \frac{L_0 - 2s}{2H} \right)^2} \right], \quad (\text{B.11})$$

where the vertical reaction $V = fL_0/2$ is due to the equal share of the linear force acting on the wire by both the edges. The maximum sagging is obtained by setting $s = L_0/2$ and considering $fL_0/H \ll 1$:

$$w = \frac{fL_0^2}{8} \left(\frac{1}{H} + \frac{1}{EA_0} \right). \quad (\text{B.12})$$

The horizontal tension component H must satisfy the following relation between the length of the unstretched wire L_0 and the distance between the two fixed edges ℓ , i.e., $x(s = L_0) = \ell$:

$$\sinh \left(\frac{f\ell}{2H} - \frac{fL_0}{2EA_0} \right) = \frac{fL_0}{2H} \quad (\text{B.13})$$

and this relation is typically used to determine the unstretched wire length starting from the gravitational sagging only.

Bibliography

- [1] PLANCK collaboration, *Planck 2018 results. VI. Cosmological parameters*, *Astron. Astrophys.* **641** (2020) A6 [[1807.06209](#)].
- [2] M. Schumann, *Direct Detection of WIMP Dark Matter: Concepts and Status*, *J. Phys. G* **46** (2019) 103003 [[1903.03026](#)].
- [3] E. Aprile, J. Angle, F. Arneodo, L. Baudis, A. Bernstein, A. Bolozdynya et al., *Design and performance of the XENON10 dark matter experiment*, *Astropart. Phys.* **34** (2011) 679 [[1001.2834](#)].
- [4] COMSOL AB, Stockholm, Sweden, “COMSOL Multiphysics®”
<http://www.comsol.com>.
- [5] XENON collaboration, *XENON1T Dark Matter Data Analysis: Signal Reconstruction, Calibration and Event Selection*, *Phys. Rev. D* **100** (2019) 052014 [[1906.04717](#)].
- [6] R. Veenhof, *Garfield* - simulation of gaseous detectors, website (2022).
- [7] D. Ramírez García, D. Baur, J. Grigat, B.A. Hofmann, S. Lindemann, D. Masson et al., *GeMSE: a low-background facility for gamma-spectrometry at moderate rock overburden*, *JINST* **17** (2022) P04005 [[2202.06540](#)].
- [8] C.W. Geis, *The XENON1T water Cherenkov muon veto system and commissioning of the XENON1T Dark Matter experiment*, Ph.D. thesis, Johannes Gutenberg Universität Mainz, Mainz, 2018.
- [9] F. Toschi, *PyCOMes* - load and handle electric field data from electrostatic simulations in COMSOL, GitHub repository (2022).

Bibliography

- [10] D.R. García, *Simulating the XENONnT Dark Matter Experiment: Backgrounds and WIMP Sensitivity*, Ph.D. thesis, Albert-Ludwigs-Universität Freiburg, Freiburg, 2022.
- [11] H. Poincaré, *The Milky Way and the Theory of Gases*, *Popular Astronomy* **14** (1906) 475.
- [12] G. Bertone and D. Hooper, *History of dark matter*, *Rev. Mod. Phys.* **90** (2018) 045002 [[1605.04909](#)].
- [13] W. Kelvin, *Baltimore lectures on molecular dynamics and the wave theory of light*, C.J. Clay and Sons (1904).
- [14] J.H. Oort, *The force exerted by the stellar system in the direction perpendicular to the galactic plane and some related problems*, *Bull. Astron. Inst. Netherlands* **6** (1932) 249.
- [15] J.H. Jeans, *The motions of stars in a Kapteyn-Universe*, *Mon. Not. R. Astron. Soc.* **82** (1922) 122.
- [16] E. Hubble and M.L. Humason, *The Velocity-Distance Relation among Extra-Galactic Nebulae*, *Astrophys. J.* **74** (1931) 43.
- [17] F. Zwicky, *Die Rotverschiebung von extragalaktischen Nebeln*, *Helv. Phys. Acta* **6** (1933) 110.
- [18] F. Zwicky, *On the masses of nebulae and of clusters of nebulae*, *Astrophys. J.* **86** (1937) 217.
- [19] V.C. Rubin and W.K. Ford, Jr., *Rotation of the Andromeda Nebula from a Spectroscopic Survey of Emission Regions*, *Astrophys. J.* **159** (1970) 379.
- [20] F. Lelli, S.S. McGaugh and J.M. Schombert, *SPARC: Mass Models for 175 Disk Galaxies with Spitzer Photometry and Accurate Rotation Curves*, *Astron. J.* **152** (2016) 157 [[1606.09251](#)].
- [21] M.W. Werner et al., *The Spitzer Space Telescope mission*, *Astrophys. J. Suppl.* **154** (2004) 1 [[astro-ph/0406223](#)].
- [22] P. Li, F. Lelli, S. McGaugh and J. Schombert, *A comprehensive catalog of dark matter halo models for SPARC galaxies*, *Astrophys. J. Suppl.* **247** (2020) 31 [[2001.10538](#)].

- [23] J.F. Navarro, C.S. Frenk and S.D.M. White, *The Structure of cold dark matter halos*, *Astrophys. J.* **462** (1996) 563 [[astro-ph/9508025](#)].
- [24] J.J. Adams et al., *Dwarf galaxy dark matter density profiles inferred from stellar and gas kinematics*, *Astrophys. J.* **789** (2014) 63 [[1405.4854](#)].
- [25] S.-H. Oh et al., *High-resolution mass models of dwarf galaxies from little things*, *The Astronomical Journal* **149** (2015) 180 [[1502.01281](#)].
- [26] J.I. Read et al., *Understanding the shape and diversity of dwarf galaxy rotation curves in Λ CDM*, *Mon. Not. R. Astron. Soc.* **462** (2016) 3628 [[1601.05821](#)].
- [27] J.I. Read, O. Agertz and M.L.M. Collins, *Dark matter cores all the way down*, *Mon. Not. R. Astron. Soc.* **459** (2016) 2573 [[1508.04143](#)].
- [28] A.D. Cintio et al., *A mass-dependent density profile for dark matter haloes including the influence of galaxy formation*, *Mon. Not. R. Astron. Soc.* **441** (2014) 2986 [[1404.5959](#)].
- [29] D. Clowe, A. Gonzalez and M. Markevitch, *Weak lensing mass reconstruction of the interacting cluster 1E0657-558: Direct evidence for the existence of dark matter*, *Astrophys. J.* **604** (2004) 596 [[astro-ph/0312273](#)].
- [30] M. Bradac, S.W. Allen, T. Treu, H. Ebeling, R. Massey, R.G. Morris et al., *Revealing the properties of dark matter in the merging cluster MACSJ0025.4-1222*, *Astrophys. J.* **687** (2008) 959 [[0806.2320](#)].
- [31] M.C. Weisskopf, H.D. Tananbaum, L.P. van Speybroeck and S.L. O'Dell, *Chandra X-ray observatory (CXO): overview*, *Proc. SPIE Int. Soc. Opt. Eng.* **4012** (2000) 2 [[astro-ph/0004127](#)].
- [32] R. Massey, T. Kitching and J. Richard, *The dark matter of gravitational lensing*, *Rept. Prog. Phys.* **73** (2010) 086901 [[1001.1739](#)].
- [33] K. Umetsu, *Cluster-galaxy weak lensing*, *Astron. Astrophys. Rev.* **28** (2020) 7 [[2007.00506](#)].
- [34] A.A. Penzias and R.W. Wilson, *A measurement of excess antenna temperature at 4080-Mc/s*, *Astrophys. J.* **142** (1965) 419.

Bibliography

- [35] R.A. Sunyaev, *The thermal history of the universe and the spectrum of relic radiation*, in *Confrontation of Cosmological Theories with Observational Data*, M.S. Longair, ed., vol. 63, pp. 167–173, Jan., 1974, [10.1007/978-94-010-2220-0_14](https://doi.org/10.1007/978-94-010-2220-0_14).
- [36] D.J. Fixsen, *The Temperature of the Cosmic Microwave Background*, *Astrophys. J.* **707** (2009) 916 [[0911.1955](#)].
- [37] PLANCK collaboration, *Planck 2018 results. X. Constraints on inflation*, *Astron. Astrophys.* **641** (2020) A10 [[1807.06211](#)].
- [38] R.K. Sachs and A.M. Wolfe, *Perturbations of a Cosmological Model and Angular Variations of the Microwave Background*, *Astrophys. J.* **147** (1967) 73.
- [39] B.D. Fields, *The primordial lithium problem*, *Ann. Rev. Nucl. Part. Sci.* **61** (2011) 47 [[1203.3551](#)].
- [40] A. Udalski, M. Szymanski, J. Kaluzny, M. Kubiak and M. Mateo, *The Optical Gravitational Lensing Experiment*, *Acta Astronomica* **42** (1992) 253.
- [41] MACHO collaboration, *MACHO Collaboration search for baryonic dark matter via gravitational microlensing*, in *PASCOS / HOPKINS 1995 (Joint Meeting of the International Symposium on Particles, Strings and Cosmology and the 19th Johns Hopkins Workshop on Current Problems in Particle Theory)*, pp. 467–484, 3, 1995 [[astro-ph/9506016](#)].
- [42] EROS-2 collaboration, *Limits on the Macho Content of the Galactic Halo from the EROS-2 Survey of the Magellanic Clouds*, *Astron. Astrophys.* **469** (2007) 387 [[astro-ph/0607207](#)].
- [43] J. Lesgourgues and S. Pastor, *Neutrino mass from Cosmology*, *Adv. High Energy Phys.* **2012** (2012) 608515 [[1212.6154](#)].
- [44] B. Follin, L. Knox, M. Millea and Z. Pan, *First Detection of the Acoustic Oscillation Phase Shift Expected from the Cosmic Neutrino Background*, *Phys. Rev. Lett.* **115** (2015) 091301 [[1503.07863](#)].
- [45] M.C. Gonzalez-Garcia and M. Maltoni, *Phenomenology with Massive Neutrinos*, *Phys. Rept.* **460** (2008) 1 [[0704.1800](#)].
- [46] SUPER-KAMIOKANDE collaboration, *Evidence for oscillation of atmospheric neutrinos*, *Phys. Rev. Lett.* **81** (1998) 1562 [[hep-ex/9807003](#)].

- [47] Y.B. Zel'dovich, *Fragmentation of a homogeneous medium under the action of gravitation*, *Astrophysics* **6** (1970) 164.
- [48] S.D.M. White, C.S. Frenk and M. Davis, *Clustering in a neutrino-dominated universe*, *Astrophys. J. Lett.* **274** (1983) L1.
- [49] N.A. Maksimova, L.H. Garrison, D.J. Eisenstein, B. Hadzhiyska, S. Bose and T.P. Satterthwaite, *AbacusSummit: a massive set of high-accuracy, high-resolution N-body simulations*, *Mon. Not. R. Astron. Soc.* **508** (2021) 4017 [[2110.11398](#)].
- [50] I. Aitchison, *Supersymmetry in Particle Physics: An Elementary Introduction*, Cambridge University Press (2007), [10.1017/CBO9780511619250](#).
- [51] S.P. Martin, *A Supersymmetry primer*, *Adv. Ser. Direct. High Energy Phys.* **18** (1998) 1 [[hep-ph/9709356](#)].
- [52] D. Perkins, *Particle Astrophysics, Second Edition*, Oxford Master Series in Physics, OUP Oxford (2008).
- [53] G. Steigman and M.S. Turner, *Cosmological Constraints on the Properties of Weakly Interacting Massive Particles*, *Nucl. Phys. B* **253** (1985) 375.
- [54] R.D. Peccei and H.R. Quinn, *CP Conservation in the Presence of Instantons*, *Phys. Rev. Lett.* **38** (1977) 1440.
- [55] S. Weinberg, *A New Light Boson?*, *Phys. Rev. Lett.* **40** (1978) 223.
- [56] L. Di Luzio, M. Giannotti, E. Nardi and L. Visinelli, *The landscape of QCD axion models*, *Phys. Rept.* **870** (2020) 1 [[2003.01100](#)].
- [57] J.L. Feng, *Dark Matter Candidates from Particle Physics and Methods of Detection*, *Ann. Rev. Astron. Astrophys.* **48** (2010) 495 [[1003.0904](#)].
- [58] M. Milgrom, *A Modification of the Newtonian dynamics as a possible alternative to the hidden mass hypothesis*, *Astrophys. J.* **270** (1983) 365.
- [59] M. Milgrom, *A modification of the Newtonian dynamics: implications for galaxy systems*, *Astrophys. J.* **270** (1983) 384.
- [60] J.D. Bekenstein, *Relativistic gravitation theory for the modified newtonian dynamics paradigm*, *Phys. Rev. D* **70** (2004) 083509 [[astro-ph/0403694](#)].

Bibliography

- [61] LIGO SCIENTIFIC, VIRGO collaboration, *GW170817: observation of gravitational waves from a binary neutron star inspiral*, *Phys. Rev. Lett.* **119** (2017) 161101 [[1710.05832](#)].
- [62] LIGO SCIENTIFIC, VIRGO, FERMI GBM, INTEGRAL collaboration, *Gravitational waves and gamma-rays from a binary neutron star merger: GW170817 and GRB 170817a*, *The Astrophysical Journal* **848** (2017) L13 [[1710.05834](#)].
- [63] S. Boran, S. Desai, E.O. Kahya and R.P. Woodard, *GW170817 Falsifies Dark Matter Emulators*, *Phys. Rev. D* **97** (2018) 041501 [[1710.06168](#)].
- [64] J.-J. Wei, X.-L. Fan, B.-B. Zhang, X.-F. Wu, H. Gao, P. Mészáros et al., *Multimessenger tests of the weak equivalence principle from GW170817 and its electromagnetic counterparts*, *JCAP* **11** (2017) 035 [[1710.05860](#)].
- [65] H. Wang et al., *The GW170817/GRB 170817A/AT 2017gfo Association: Some Implications for Physics and Astrophysics*, *Astrophys. J. Lett.* **851** (2017) L18 [[1710.05805](#)].
- [66] I.M. Shoemaker and K. Murase, *Constraints from the time lag between gravitational waves and gamma rays: Implications of GW170817 and GRB 170817A*, *Phys. Rev. D* **97** (2018) 083013 [[1710.06427](#)].
- [67] O. Buchmueller, C. Doglioni and L.T. Wang, *Search for dark matter at colliders*, *Nature Phys.* **13** (2017) 217 [[1912.12739](#)].
- [68] ICECUBE collaboration, *Search for annihilating dark matter in the Sun with 3 years of IceCube data*, *Eur. Phys. J. C* **77** (2017) 146 [[1612.05949](#)].
- [69] SUPER-KAMIOKANDE collaboration, *Search for neutrinos from annihilation of captured low-mass dark matter particles in the Sun by Super-Kamiokande*, *Phys. Rev. Lett.* **114** (2015) 141301 [[1503.04858](#)].
- [70] ANTARES collaboration, *Limits on Dark Matter Annihilation in the Sun using the ANTARES Neutrino Telescope*, *Phys. Lett. B* **759** (2016) 69 [[1603.02228](#)].
- [71] ICECUBE collaboration, *Search for Neutrinos from Dark Matter Self-Annihilations in the center of the Milky Way with 3 years of IceCube/DeepCore*, *Eur. Phys. J. C* **77** (2017) 627 [[1705.08103](#)].

- [72] SUPER-KAMIOKANDE collaboration, *Indirect search for dark matter from the Galactic Center and halo with the Super-Kamiokande detector*, *Phys. Rev. D* **102** (2020) 072002 [[2005.05109](#)].
- [73] ANTARES collaboration, *Search for dark matter towards the Galactic Centre with 11 years of ANTARES data*, *Phys. Lett. B* **805** (2020) 135439 [[1912.05296](#)].
- [74] FERMI-LAT collaboration, *Searching for Dark Matter Annihilation from Milky Way Dwarf Spheroidal Galaxies with Six Years of Fermi Large Area Telescope Data*, *Phys. Rev. Lett.* **115** (2015) 231301 [[1503.02641](#)].
- [75] H.E.S.S. collaboration, *Search for dark matter annihilations towards the inner Galactic halo from 10 years of observations with H.E.S.S.*, *Phys. Rev. Lett.* **117** (2016) 111301 [[1607.08142](#)].
- [76] PAMELA collaboration, *Cosmic-Ray Positron Energy Spectrum Measured by PAMELA*, *Phys. Rev. Lett.* **111** (2013) 081102 [[1308.0133](#)].
- [77] AMS collaboration, *Towards Understanding the Origin of Cosmic-Ray Positrons*, *Phys. Rev. Lett.* **122** (2019) 041102.
- [78] C.-H. Chen, C.-W. Chiang and T. Nomura, *Dark matter for excess of AMS-02 positrons and antiprotons*, *Phys. Lett. B* **747** (2015) 495 [[1504.07848](#)].
- [79] D. Hooper, I. Cholis, T. Linden and K. Fang, *HAWC Observations Strongly Favor Pulsar Interpretations of the Cosmic-Ray Positron Excess*, *Phys. Rev. D* **96** (2017) 103013 [[1702.08436](#)].
- [80] J.D. Lewin and P.F. Smith, *Review of mathematics, numerical factors, and corrections for dark matter experiments based on elastic nuclear recoil*, *Astropart. Phys.* **6** (1996) 87.
- [81] J.I. Read, *The Local Dark Matter Density*, *J. Phys. G* **41** (2014) 063101 [[1404.1938](#)].
- [82] M.C. Smith et al., *The RAVE Survey: Constraining the Local Galactic Escape Speed*, *Mon. Not. Roy. Astron. Soc.* **379** (2007) 755 [[astro-ph/0611671](#)].
- [83] R.H. Helm, *Inelastic and Elastic Scattering of 187-Mev Electrons from Selected Even-Even Nuclei*, *Phys. Rev.* **104** (1956) 1466.

Bibliography

- [84] S.A. Hertel, A. Biekert, J. Lin, V. Velan and D.N. McKinsey, *Direct detection of sub-GeV dark matter using a superfluid ^4He target*, *Phys. Rev. D* **100** (2019) 092007 [[1810.06283](#)].
- [85] B. von Krosigk et al., *DELight: a Direct search Experiment for Light dark matter with superfluid helium*, in *14th International Workshop on the Identification of Dark Matter 2022*, 9, 2022 [[2209.10950](#)].
- [86] S. Zhang et al., *Transition edge sensor-based detector: from X-ray to γ -ray*, *Nucl. Sci. Tech.* **33** (2022) 84 [[2204.00010](#)].
- [87] CDMS collaboration, *Exclusion limits on the WIMP-nucleon cross section from the first run of the Cryogenic Dark Matter Search in the Soudan Underground Laboratory*, *Phys. Rev. D* **72** (2005) 052009 [[astro-ph/0507190](#)].
- [88] CDMS collaboration, *Silicon Detector Dark Matter Results from the Final Exposure of CDMS II*, *Phys. Rev. Lett.* **111** (2013) 251301 [[1304.4279](#)].
- [89] CRESST collaboration, *First results from the CRESST-III low-mass dark matter program*, *Phys. Rev. D* **100** (2019) 102002 [[1904.00498](#)].
- [90] DAMA collaboration, *The DAMA/LIBRA apparatus*, *Nucl. Instrum. Meth. A* **592** (2008) 297 [[0804.2738](#)].
- [91] DAMA collaboration, *First model independent results from DAMA/LIBRA-phase2*, *Nucl. Phys. Atom. Energy* **19** (2018) 307 [[1805.10486](#)].
- [92] XENON collaboration, *Search for Electronic Recoil Event Rate Modulation with 4 Years of XENON100 Data*, *Phys. Rev. Lett.* **118** (2017) 101101 [[1701.00769](#)].
- [93] LUX collaboration, *Search for annual and diurnal rate modulations in the LUX experiment*, *Phys. Rev. D* **98** (2018) 062005 [[1807.07113](#)].
- [94] XMASS collaboration, *Direct dark matter search by annual modulation in XMASS-I*, *Phys. Lett. B* **759** (2016) 272 [[1511.04807](#)].
- [95] J.L. Feng, J. Kumar, D. Marfatia and D. Sanford, *Isospin-Violating Dark Matter*, *Phys. Lett. B* **703** (2011) 124 [[1102.4331](#)].
- [96] COSINE-100 collaboration, *Strong constraints from COSINE-100 on the DAMA dark matter results using the same sodium iodide target*, *Sci. Adv.* **7** (2021) abk2699 [[2104.03537](#)].

- [97] J. Amare et al., *Annual Modulation Results from Three Years Exposure of ANAIS-112*, *Phys. Rev. D* **103** (2021) 102005 [[2103.01175](#)].
- [98] DAMIC collaboration, *Direct Dark Matter Search using CCDs*, *J. Phys. Conf. Ser.* **203** (2010) 012033 [[0911.2668](#)].
- [99] DAMIC collaboration, *Results on low-mass weakly interacting massive particles from a 11 kg-day target exposure of DAMIC at SNOLAB*, *Phys. Rev. Lett.* **125** (2020) 241803 [[2007.15622](#)].
- [100] XENON collaboration, *Search for Light Dark Matter Interactions Enhanced by the Migdal Effect or Bremsstrahlung in XENON1T*, *Phys. Rev. Lett.* **123** (2019) 241803 [[1907.12771](#)].
- [101] DARKSIDE-50 collaboration, *Search for low-mass dark matter WIMPs with 12 ton-day exposure of DarkSide-50*, [\[2207.11966\]\(#\)](#).
- [102] XENON collaboration, *Search for coherent elastic scattering of solar 8B neutrinos in the XENON1T dark matter experiment*, *Phys. Rev. Lett.* **126** (2021) 091301 [[2012.02846](#)].
- [103] PANDAX-4T collaboration, *Dark Matter Search Results from the PandaX-4T Commissioning Run*, *Phys. Rev. Lett.* **127** (2021) 261802 [[2107.13438](#)].
- [104] XENON collaboration, *Dark matter search results from a one ton-year exposure of XENON1T*, *Phys. Rev. Lett.* **121** (2018) 111302 [[1805.12562](#)].
- [105] XENON collaboration, *XENON100 Dark Matter Results from a Combination of 477 Live Days*, *Phys. Rev. D* **94** (2016) 122001 [[1609.06154](#)].
- [106] LZ collaboration, *First Dark Matter Search Results from the LUX-ZEPLIN (LZ) Experiment*, [\[2207.03764\]\(#\)](#).
- [107] C. Savage, G. Gelmini, P. Gondolo and K. Freese, *Compatibility of DAMA/LIBRA dark matter detection with other searches*, *JCAP* **04** (2009) 010 [[0808.3607](#)].
- [108] XENON collaboration, *First Results from the XENON10 Dark Matter Experiment at the Gran Sasso National Laboratory*, *Phys. Rev. Lett.* **100** (2008) 021303 [[0706.0039](#)].
- [109] PANDAX-4T collaboration, *Dark matter search results from the PandaX-4T commissioning run*, *Phys. Rev. Lett.* **127** (2021) 261802 [[2107.13438](#)].

Bibliography

- [110] M. Ibe, W. Nakano, Y. Shoji and K. Suzuki, *Migdal Effect in Dark Matter Direct Detection Experiments*, *JHEP* **03** (2018) 194 [[1707.07258](#)].
- [111] H.M. Araújo et al., *The MIGDAL experiment: Measuring a rare atomic process to aid the search for dark matter*, [2207.08284](#).
- [112] T. Marrodán Undagoitia and L. Rauch, *Dark matter direct-detection experiments*, *J. Phys. G* **43** (2016) 013001 [[1509.08767](#)].
- [113] XENON collaboration, *Projected WIMP sensitivity of the XENONnT dark matter experiment*, *JCAP* **11** (2020) 031 [[2007.08796](#)].
- [114] XENON collaboration, *Search for New Physics in Electronic Recoil Data from XENONnT*, *Phys. Rev. Lett.* **129** (2022) 161805 [[2207.11330](#)].
- [115] E. Aprile and T. Doke, *Liquid xenon detectors for particle physics and astrophysics*, *Rev. Mod. Phys.* **82** (2010) 2053.
- [116] D. Akimov, A. Bolozdynya, A. Buzulutskov and V. Chepel, *Two-phase emission detectors*, World Scientific Publishing Co. Pte Ltd, Singapore (July, 2021), [10.1142/12126](#).
- [117] R. Platzman, *Total ionization in gases by high-energy particles: An appraisal of our understanding*, *The International Journal of Applied Radiation and Isotopes* **10** (1961) 116.
- [118] V. Nikolaev and I. Dmitriev, *On the equilibrium charge distribution in heavy element ion beams*, *Phys. Lett. A* **28** (1968) 277.
- [119] J. Lindhard, M. Scharff and H.E. Schiøett, *Range concepts and heavy ion ranges (Notes on atomic collisions, II)*, *Mat. Fys. Medd. Dan. Vid.. Selsk.* **33** (1963) [<http://gymarkiv.sdu.dk/MFM/kdvs/mfm%2030-39/mfm-33-14.pdf>].
- [120] A. Mangiarotti, M.I. Lopes, M.L. Benabderahmane, V. Chepel, A. Lindote, J. Pinto da Cunha et al., *A Survey of energy loss calculations for heavy ions between 1-keV and 100-keV*, *Nucl. Instrum. Meth. A* **580** (2007) 114 [[physics/0610286](#)].
- [121] T. Doke, A. Hitachi, J. Kikuchi, K. Masuda, H. Okada and E. Shibamura, *Absolute Scintillation Yields in Liquid Argon and Xenon for Various Particles*, *Jap. J. Appl. Phys.* **41** (2002) 1538.

- [122] P. Sorensen and C.E. Dahl, *Nuclear recoil energy scale in liquid xenon with application to the direct detection of dark matter*, *Phys. Rev. D* **83** (2011) 063501 [[1101.6080](#)].
- [123] P.K. Leichner, K.F. Palmer, J.D. Cook and M. Thieneman, *Two- and three-body collision coefficients for Xe(3P_1) and Xe(3P_2) atoms and radiative lifetime of the Xe₂(1_u) molecule*, *Phys. Rev. A* **13** (1976) 1787.
- [124] A.J.P.L. Policarpo, *Light production and gaseous detectors*, *Phys. Scr.* **23** (1981) 539.
- [125] A. Buzulutskov, A. Bondar and A. Grebenuk, *Infrared scintillation yield in gaseous and liquid argon*, *EPL* **94** (2011) 52001 [[1102.1825](#)].
- [126] K. Fujii, Y. Endo, Y. Torigoe, S. Nakamura, T. Haruyama, K. Kasami et al., *High-accuracy measurement of the emission spectrum of liquid xenon in the vacuum ultraviolet region*, *Nucl. Instrum. Meth. A* **795** (2015) 293.
- [127] A. Hitachi, T. Takahashi, N. Funayama, K. Masuda, J. Kikuchi and T. Doke, *Effect of ionization density on the time dependence of luminescence from liquid argon and xenon*, *Phys. Rev. B* **27** (1983) 5279.
- [128] E. Hogenbirk, J. Aalbers, P.A. Breur, M.P. Decowski, K. van Teutem and A.P. Colijn, *Precision measurements of the scintillation pulse shape for low-energy recoils in liquid xenon*, *JINST* **13** (2018) P05016 [[1803.07935](#)].
- [129] U. Sowada, J.M. Warman and M.P. de Haas, *Hot-electron thermalization in solid and liquid argon, krypton, and xenon*, *Phys. Rev. B* **25** (1982) 3434.
- [130] A. Mozumder, *Free-ion yield and electron-ion recombination rate in liquid xenon*, *Chem. Phys. Lett.* **245** (1995) 359.
- [131] J. Thomas and D.A. Imel, *Recombination of electron-ion pairs in liquid argon and liquid xenon*, *Phys. Rev. A* **36** (1987) 614.
- [132] E. Hogenbirk et al., *Field dependence of electronic recoil signals in a dual-phase liquid xenon time projection chamber*, *JINST* **13** (2018) P10031 [[1807.07121](#)].
- [133] M. Szydagis et al., *NEST: a comprehensive model for scintillation yield in liquid xenon*, *JINST* **6** (2011) P10002.
- [134] M. Szydagis et al., *NEST - Noble Element Simulation Technique* [v2.3.6], Zenodo (2022).

Bibliography

- [135] C.E. Dahl, *The physics of background discrimination in liquid xenon, and first results from Xenon10 in the hunt for WIMP dark matter*, Ph.D. thesis, Princeton U., 2009.
- [136] EXO-200 collaboration, *Measurement of the scintillation and ionization response of liquid xenon at MeV energies in the EXO-200 experiment*, *Phys. Rev. C* **101** (2020) 065501 [[1908.04128](#)].
- [137] L. Baudis, P. Sanchez-Lucas and K. Thieme, *A measurement of the mean electronic excitation energy of liquid xenon*, *Eur. Phys. J. C* **81** (2021) 1060 [[2109.07151](#)].
- [138] A. Hitachi, T. Doke and A. Mozumder, *Luminescence quenching in liquid argon under charged-particle impact: Relative scintillation yield at different linear energy transfers*, *Phys. Rev. B* **46** (1992) 11463.
- [139] O. Njoya et al., *Measurements of electron transport in liquid and gas Xenon using a laser-driven photocathode*, *Nucl. Instrum. Meth. A* **972** (2020) 163965 [[1911.11580](#)].
- [140] E. Gushchin, A. Kruglov and I. Obodovskii, *Electron dynamics in condensed argon and xenon*, *Sov. Phys. JETP* **55** (1982) .
- [141] EXO-200 collaboration, *Measurement of the drift velocity and transverse diffusion of electrons in liquid xenon with the EXO-200 detector*, *Phys. Rev. C* **95** (2017) 025502 [[1609.04467](#)].
- [142] F. Jörg et al., *Characterization of alpha and beta interactions in liquid xenon*, *Eur. Phys. J. C* **82** (2022) 361 [[2109.13735](#)].
- [143] L. Baudis, Y. Biondi, C. Capelli, M. Galloway, S. Kazama, A. Kish et al., *A Dual-phase Xenon TPC for Scintillation and Ionisation Yield Measurements in Liquid Xenon*, *Eur. Phys. J. C* **78** (2018) 351 [[1712.08607](#)].
- [144] S.S. Huang and G.R. Freeman, *Electron mobilities in gaseous, critical, and liquid xenon: Density, electric field, and temperature effects: Quasilocalization*, *J. Chem. Phys.* **68** (1978) 1355.
- [145] L.S. Miller, S. Howe and W.E. Spear, *Charge transport in solid and liquid Ar, Kr, and Xe*, *Phys. Rev.* **166** (1968) 871.
- [146] Y. Sakai, *Quasifree electron transport under electric field in nonpolar simple-structured condensed matters*, *J. Phys. D* **40** (2007) R441 .

- [147] G. Boyle, R. McEachran, D. Cocks, M. Brunger, S. Buckman, S. Dujko et al., *Ab initio electron scattering cross-sections and transport in liquid xenon*, *J. Phys. D* **49** (2016) 355201 [[1603.04157](#)].
- [148] A. Herzenberg, *Attachment of slow electrons to oxygen molecules*, *J. Chem. Phys.* **51** (1969) 4942 [[10.1063/1.1671887](#)].
- [149] A.A. Radzig and B.M. Smirnov, *Reference data on atoms, molecules, and ions*, vol. 31, Springer Science & Business Media (2012), [10.1007/978-3-642-82048-9](#).
- [150] G. Bakale, U. Sowada and W.F. Schmidt, *Effect of an electric field on electron attachment to sulfur hexafluoride, nitrous oxide, and molecular oxygen in liquid argon and xenon*, *The Journal of Physical Chemistry* **80** (1976) 2556 [[10.1021/j100564a006](#)].
- [151] J.D. Jackson, *Classical electrodynamics*; 2nd ed., Wiley, New York, NY (1975).
- [152] A. Bondar, A. Buzulutskov, A. Grebenuk, D. Pavlyuchenko and Y. Tikhonov, *Electron emission properties of two-phase argon and argon-nitrogen avalanche detectors*, *JINST* **09** (2009) 09013 [[0908.2915](#)].
- [153] E.M. Gushchin et al., *Electron emission from condensed noble gases*, *Sov. Phys. JETP* **49** (1979) 856.
- [154] XENON collaboration, *Observation and applications of single-electron charge signals in the XENON100 experiment*, *J. Phys. G* **41** (2014) 035201 [[1311.1088](#)].
- [155] J. Mock et al., *Modeling pulse characteristics in xenon with NEST*, *JINST* **9** (2014) T04002 [[1310.1117](#)].
- [156] NEXT COLLABORATION collaboration, *Neutral bremsstrahlung emission in xenon unveiled*, *Phys. Rev. X* **12** (2022) 021005 [[2202.02614](#)].
- [157] C. Oliveira, P. Correia, A. Ferreira, S. Biagi, R. Veenhof and J. Veloso, *Simulation of gaseous Ar and Xe electroluminescence in the near infra-red range*, *Nucl. Instrum. Meth. A* **722** (2013) 1.
- [158] P. Lindblom and O. Solin, *Atomic near-infrared noble gas scintillations I: Optical spectra*, *Nucl. Instrum. Meth. A* **268** (1988) 204.
- [159] C. Monteiro, L. Fernandes, J. Lopes, L. Coelho, J. Veloso, J. dos Santos et al., *Secondary scintillation yield in pure xenon*, *JINST* **2** (2007) P05001 [[0702142](#)].

Bibliography

- [160] C.A.B. Oliveira et al., *A simulation toolkit for electroluminescence assessment in rare event experiments*, *Phys. Lett. B* **703** (2011) 217 [[1103.6237](#)].
- [161] C. Silva et al., *Reflectance of polytetrafluoroethylene for xenon scintillation light*, *J. Appl. Phys.* **107** (2010) 064902 [[0910.1056](#)].
- [162] XENON collaboration, *Energy resolution and linearity of XENON1T in the MeV energy range*, *Eur. Phys. J. C* **80** (2020) 785 [[2003.03825](#)].
- [163] XENON collaboration, *Results from a Calibration of XENON100 Using a Source of Dissolved Radon-220*, *Phys. Rev. D* **95** (2017) 072008 [[1611.03585](#)].
- [164] XENON100 collaboration, *Response of the XENON100 Dark Matter Detector to Nuclear Recoils*, *Phys. Rev. D* **88** (2013) 012006 [[1304.1427](#)].
- [165] R.F. Lang, J. Pienaar, E. Hogenbirk, D. Masson, R. Nolte, A. Zimbal et al., *Characterization of a deuterium–deuterium plasma fusion neutron generator*, *Nucl. Instrum. Meth. A* **879** (2018) 31 [[1705.04741](#)].
- [166] XENON collaboration, *XENON1T dark matter data analysis: Signal and background models and statistical inference*, *Phys. Rev. D* **99** (2019) 112009 [[1902.11297](#)].
- [167] LUX collaboration, *Discrimination of electronic recoils from nuclear recoils in two-phase xenon time projection chambers*, *Phys. Rev. D* **102** (2020) 112002 [[2004.06304](#)].
- [168] LUX collaboration, *The Large Underground Xenon (LUX) Experiment*, *Nucl. Instrum. Meth. A* **704** (2013) 111 [[1211.3788](#)].
- [169] XENON collaboration, *The XENON1T dark matter experiment*, *Eur. Phys. J. C* **77** (2017) 881 [[1708.07051](#)].
- [170] M. Laubenstein and I. Lawson, *Low background radiation detection techniques and mitigation of radioactive backgrounds*, *Front. Phys.* **8** (2020) .
- [171] LZ collaboration, *The LUX-ZEPLIN (LZ) radioactivity and cleanliness control programs*, *Eur. Phys. J. C* **80** (2020) 1044 [[2006.02506](#)].
- [172] XENON collaboration, *Material radiopurity control in the XENONnT experiment*, *Eur. Phys. J. C* **82** (2022) 599 [[2112.05629](#)].

- [173] XENON collaboration, *Excess electronic recoil events in XENON1T*, *Phys. Rev. D* **102** (2020) 072004 [[2006.09721](#)].
- [174] D.R. Lide, *CRC Handbook of Chemistry and Physics, 85th Edition*, CRC Press, 85 ed. (2004).
- [175] S. Rosendahl, E. Brown, I. Cristescu, A. Fieguth, C. Huhmann, M. Murra et al., *A cryogenic distillation column for the XENON1T experiment*, *J. Phys. Conf. Ser.* **564** (2014) 012006.
- [176] XENON collaboration, *Removing krypton from xenon by cryogenic distillation to the ppq level*, *Eur. Phys. J. C* **77** (2017) 275 [[1612.04284](#)].
- [177] XENON collaboration, *Observation of two-neutrino double electron capture in ^{124}Xe with XENON1T*, *Nature* **568** (2019) 532 [[1904.11002](#)].
- [178] XENON collaboration, *Double-Weak Decays of ^{124}Xe and ^{136}Xe in the XENON1T and XENONnT Experiments*, *Phys. Rev. C* **106** (2022) 024328 [[2205.04158](#)].
- [179] M. von Sivers, B.A. Hofmann, r. Rosén and M. Schumann, *The GeMSE facility for low-background γ -ray spectrometry*, *JINST* **11** (2016) P12017 [[1606.03983](#)].
- [180] L. Baudis, A. Ferella, A. Askin, J. Angle, E. Aprile, T. Bruch et al., *Gator: a low-background counting facility at the gran sasso underground laboratory*, *JINST* **6** (2011) P08010 [[1103.2125](#)].
- [181] G. Heusser, M. Laubenstein and H. Neder, *Low-level germanium gamma-ray spectrometry at the $\mu\text{Bq}/\text{kg}$ level and future developments towards higher sensitivity*, in *Radionuclides in the Environment*, P. Povinec and J. Sanchez-Cabeza, eds., vol. 8 of *Radioactivity in the Environment*, pp. 495–510, Elsevier (2006), [10.1016/S1569-4860\(05\)08039-3](#).
- [182] CAEN, *DT5781 - Dual/Quad Digital Multi Channel Analyzer - Desktop*, 2014.
- [183] CAEN, *MC² Analyzer - Graphical software tool for digitizers running DPP-PHA firmware*, 2017.
- [184] XENON collaboration, *The XENON100 dark matter experiment*, *Astropart. Phys.* **35** (2012) 573 [[1107.2155](#)].

Bibliography

- [185] XENON collaboration, *Lowering the radioactivity of the photomultiplier tubes for the XENON1T dark matter experiment*, *Eur. Phys. J. C* **75** (2015) 546 [[1503.07698](#)].
- [186] T. Haruyama, K. Kasami, H. Nishiguchi, S. Mihara, T. Mori, W. Otani et al., *LN₂-free operation of the MEG liquid xenon calorimeter by using a high-power pulse tube cryocooler.*, *AIP Conf. Proc.* **823** (2006) 1695.
- [187] A. Dobi, D.S. Leonard, C. Hall, L. Kaufman, T. Langford, S. Slutsky et al., *Study of a zirconium getter for purification of xenon gas*, *Nucl. Instrum. Meth. A* **620** (2010) 594 [[1002.2791](#)].
- [188] Hamamatsu, *Large photocathode area photomultiplier tubes*, 2019.
- [189] XENON1T collaboration, *Conceptual design and simulation of a water Cherenkov muon veto for the XENON1T experiment*, *JINST* **9** (2014) P11006 [[1406.2374](#)].
- [190] XENON collaboration, *First Dark Matter Search Results from the XENON1T Experiment*, *Phys. Rev. Lett.* **119** (2017) 181301 [[1705.06655](#)].
- [191] LUX collaboration, *Results from a search for dark matter in the complete LUX exposure*, *Phys. Rev. Lett.* **118** (2017) 021303 [[1608.07648](#)].
- [192] PANDAX-II collaboration, *Dark Matter Results From 54-Ton-Day Exposure of PandaX-II Experiment*, *Phys. Rev. Lett.* **119** (2017) 181302 [[1708.06917](#)].
- [193] XENON collaboration, *Light Dark Matter Search with Ionization Signals in XENON1T*, *Phys. Rev. Lett.* **123** (2019) 251801 [[1907.11485](#)].
- [194] L.L. Lucas and M.P. Unterweger, *Comprehensive review and critical evaluation of the half-life of tritium*, *J. Res. Natl. Inst. Stand. Technol.* **105** (2000) 541 [<https://nvlpubs.nist.gov/nistpubs/jres/105/4/j54luc2.pdf>].
- [195] SAES, *St 707 - pills & pieces*, 2012.
- [196] G. Plante, E. Aprile, J. Howlett and Y. Zhang, *Liquid-phase purification for multi-tonne xenon detectors*, *Eur. Phys. J. C* **82** (2022) 860 [[2205.07336](#)].
- [197] ICARUS collaboration, *Design, construction and tests of the ICARUS T600 detector*, *Nucl. Instrum. Meth. A* **527** (2004) 329.

- [198] M. Murra, D. Schulte, C. Huhmann and C. Weinheimer, *Design, construction and commissioning of a high-flow radon removal system for XENONnT*, [2205.11492](#).
- [199] A. Mancuso, *Neutron Veto of XENONnT: final construction design of the system and extensive study and calibration of the PMTs*, M.Sc. thesis, Università di Bologna, Bologna, 2020.
- [200] P. Mazzoldi, M. Nigro and C. Voci, *Fisica 2: elettromagnetismo e onde*, EdiSES, Napoli, 2 ed. (2008).
- [201] NIST, *CODATA value* - vacuum electric permittivity, website (2018).
- [202] J. Marcoux, *Dielectric constants and indices of refraction of Xe, Kr, and Ar*, *Canadian Journal of Physics* **48** (1970) 244.
- [203] R.L. Amey and R.H. Cole, *Dielectric constants of liquefied noble gases and methane*, *Chem. Phys.* **40** (1964) 146.
- [204] R. Sawada et al., *Capacitive level meter for liquid rare gases*, *Cryogenics* **43** (2003) 449.
- [205] XENON collaboration, *Material radioassay and selection for the XENON1T dark matter experiment*, *Eur. Phys. J. C* **77** (2017) 890 [[1705.01828](#)].
- [206] G. Heusser, M. Laubenstein and H. Neder, *Low-level germanium gamma-ray spectrometry at the $\mu\text{Bq}/\text{kg}$ level and future developments towards higher sensitivity*, in *Radionuclides in the Environment*, vol. 8, pp. 495–510, Elsevier (2006), [10.1016/S1569-4860\(05\)08039-3](#).
- [207] M. Laubenstein, *Screening of materials with high purity germanium detectors at the Laboratori Nazionali del Gran Sasso*, *Int. J. Mod. Phys. A* **32** (2017) 1743002.
- [208] Smartec, *Datasheet Universal Transducer Interface*, 2016.
- [209] Pasternack, *RF Cables Techincal Datasheet RG196A/U REV1.3*, 2017.
- [210] Microchip, *PIC16F87XA - Pin Enhanced Flash Microcontrollers*, 2013.
- [211] B. Smith, P. Gardner and E. Parker, *Surface tension and energy of liquid xenon*, *Chem. Phys.* **47** (1967) .
- [212] L.G.S. J and C. G, *Determination of the kinematic viscosity by the liquid rise in a capillary tube*, *Rev. Bras. Ensino Fis.* **35** (2013) 3310.

Bibliography

- [213] M. Yamashita et al., *Scintillation response of liquid Xe surrounded by PTFE reflector for gamma rays*, *Nucl. Instrum. Meth. A* **535** (2004) 692.
- [214] M.J. Carson et al., *Neutron background in large scale xenon detectors for dark matter searches*, *Astropart. Phys.* **21** (2004) 667 [[hep-ex/0404042](#)].
- [215] L. Althüser et al., *VUV transmission of PTFE for xenon-based particle detectors*, *JINST* **15** (2020) P12021 [[2006.05827](#)].
- [216] M. Ángel Vargas, *Data analysis in the XENON1T Dark Matter Experiment*, Ph.D. thesis, Westfälische Wilhelms-Universität Münster, Münster, 2019.
- [217] F. Paschen, *Über die zum Funkenübergang in Luft, Wasserstoff und Kohlensäure bei verschiedenen Drucken erforderliche Potentialdifferenz*, *Annalen der Physik* **273** (1889) 69
[<https://onlinelibrary.wiley.com/doi/pdf/10.1002/andp.18892730505>].
- [218] OHMITE, *HVF Series - High Voltage Flip Chip Film*, 2017.
- [219] Chauvin Arnoux, *C.A. 6526*, 2021.
- [220] S. COMSOL AB, Stockholm, *AC/DC Module User's Guide*. COMSOL.
- [221] R.K. Kirby, *Thermal expansion of polytetrafluoroethylene (Teflon) from -190° to 300°C* , *J. Res. Nat. Bur. Stand.* **57** (1956) 91.
- [222] P. Kurowski, *Finite Element Analysis for Design Engineers*, Electronic publications, SAE International (2017).
- [223] P. Belli, R. Bernabei, S. d'Angelo, L. Andreanelli, F. Bronzini, A. Buccheri et al., *Liquid-xenon detectors and their applications*, *Nucl. Instrum. Meth. A* **299** (1990) 191.
- [224] P. Ehrlich, L.E. Amborski and R.L. Burton, *Dielectric properties of Teflon from room temperature to 314°C and from frequencies of 10^2 to 10^5 c/s* , in *1953 Conference on Electrical Insulation*, pp. 28–30, 1953, [10.1109/EIC.1953.7508671](#).
- [225] S.K. Lam, A. Pitrou and S. Seibert, *Numba: a LLVM-based python JIT compiler*, in *Proceedings of the Second Workshop on the LLVM Compiler Infrastructure in HPC*, LLVM '15, (New York, NY, USA), Association for Computing Machinery, 2015, [10.1145/2833157.2833162](#).

- [226] C.R. Harris et al., *Array programming with NumPy*, *Nature* **585** (2020) 357.
- [227] LUX collaboration, *Discrimination of electronic recoils from nuclear recoils in two-phase xenon time projection chambers*, *Phys. Rev. D* **102** (2020) 112002 [2004.06304].
- [228] J. Xu et al., *Electron extraction efficiency study for dual-phase xenon dark matter experiments*, *Phys. Rev. D* **99** (2019) 103024 [1904.02885].
- [229] CAEN, *CAEN A1580H* - 8/16 Channel 8 kV/20 μ A Common Floating Return Boards, website (2022).
- [230] B. Rebel et al., *High voltage in noble liquids for high energy physics*, *JINST* **9** (2014) T08004 [1403.3613].
- [231] GEANT4 collaboration, *GEANT4—a simulation toolkit*, *Nucl. Instrum. Meth. A* **506** (2003) 250.
- [232] XENON collaboration, *epix* - Electron and Photon Instructions generator for XENON [v0.3.2], GitHub repository (2022).
- [233] XENON, *WFSim* - The XENON waveform simulator [v1.0.0], GitHub repository (2022).
- [234] XENON collaboration, *straxen* - Streaming analysis for XENON(nT) [v1.7.2], GitHub repository (2022).
- [235] AxFoundation, *strax* - Streaming analysis for xenon experiments [v1.2.3], GitHub repository (2022).
- [236] J. Xu, S. Pereverzev, B. Lenardo, J. Kingston, D. Naim, A. Bernstein et al., *Electron extraction efficiency study for dual-phase xenon dark matter experiments*, *Phys. Rev. D* **99** (2019) 103024 [1904.02885].
- [237] LUX collaboration, *^{83m}Kr calibration of the 2013 LUX dark matter search*, *Phys. Rev. D* **96** (2017) 112009 [1708.02566].
- [238] A. Chan, H. Crawley, D. Edsall, A. Firestone, M. Gorbics, L. Gorn et al., *Performance of the HPC calorimeter in DELPHI*, *IEEE Trans. Nucl. Sci.* **42** (1995) 491 [<https://cds.cern.ch/record/276655/files/ppe-95-004.pdf>].

Bibliography

- [239] LUX collaboration, *3D Modeling of Electric Fields in the LUX Detector*, *JINST* **12** (2017) P11022 [[1709.00095](#)].
- [240] M. Wigard, *Modeling electric fields inside the XENON1T TPC and comparison to data*, M.Sc. thesis, Westfälische Wilhelms-Universität Münster, Münster, 2018.
- [241] R. Kressmann, G. Sessler and P. Gunther, *Space-charge electrets*, *IEEE Trans. Dielectr. Electr. Insul.* **3** (1996) 607.
- [242] B. Efron and R.J. Tibshirani, *An Introduction to the Bootstrap*, no. 57 in Monographs on Statistics and Applied Probability, Chapman & Hall/CRC, Boca Raton, Florida, USA (1993), [10.1201/9780429246593](#).
- [243] D. Masson, *Novel Ideas and Techniques for Large Dark Matter Detectors*, Ph.D. thesis, Purdue U., 2018.
- [244] L. Baudis et al., *Response of liquid xenon to Compton electrons down to 1.5 keV*, *Phys. Rev. D* **87** (2013) 115015 [[1303.6891](#)].
- [245] E.M. Boulton et al., *Calibration of a two-phase xenon time projection chamber with a ^{37}Ar source*, *JINST* **12** (2017) P08004 [[1705.08958](#)].
- [246] S. Liang et al., *Domain-informed neural networks for interaction localization within astroparticle experiments*, *Front. Artif. Intell.* **5** (2022) 832909 [[2112.07995](#)].
- [247] A. Weiser and S.E. Zarantonello, *A note on piecewise linear and multilinear table interpolation in many dimensions*, *Math. Comput.* **50** (1988) 189.
- [248] D. Shepard, *A two-dimensional interpolation function for irregularly-spaced data*, in *Proceedings of the 1968 23rd ACM National Conference*, ACM '68, (New York, NY, USA), p. 517–524, Association for Computing Machinery, 1968, [10.1145/800186.810616](#).
- [249] R. Hammann, *Investigation of a Charge Insensitive Volume in XENONnT, Analysis of Goodness-of-Fit Techniques, and Feasibility Studies for an Automated Krypton Assay System*, M.Sc. thesis, Max-Planck-Institut für Kernphysik, Heidelberg, 2022.
- [250] F. Pedregosa et al., *Scikit-learn: Machine learning in Python*, *JMLR* **12** (2011) 2825 [[1201.0490](#)].
- [251] F. Theeuwes and R.J. Bearman, *The p , v , t behavior of dense fluids v. the vapor pressure and saturated liquid density of xenon*, *J. Chem. Thermodyn.* **2** (1970) 507.

- [252] D.Y. Akimov et al., *The ZEPLIN-III dark matter detector: instrument design, manufacture and commissioning*, *Astropart. Phys.* **27** (2007) 46 [[astro-ph/0605500](#)].
- [253] LZ collaboration, *The LUX-ZEPLIN (LZ) experiment*, *Nucl. Instrum. Meth. A* **953** (2020) 163047 [[1910.09124](#)].
- [254] Metalspiping, *SS316/SS316L* - physical and chemical properties, website (2022).
- [255] A. Tomás et al., *Study and mitigation of spurious electron emission from cathodic wires in noble liquid time projection chambers*, *Astropart. Phys.* **103** (2018) 49 [[1801.07231](#)].
- [256] R.H. Fowler and L.W. Nordheim, *Electron emission in intense electric fields*, *Proc. R. Soc. A* **119** (1928) 173.
- [257] B.M. Cox and W.T. Williams, *Field-emission sites on unpolished stainless steel*, *J. Phys. D* **10** (1977) L5.
- [258] D.W. Williams and W.T. Williams, *Preebreakdown and breakdown characteristics of stainless steel electrodes in vacuum*, *J. Phys. D* **7** (1974) 1173.
- [259] M. Prall et al., *A contact-less 2-dimensional laser sensor for 3-dimensional wire position and tension measurements*, *IEEE Trans. Nucl. Sci.* **57** (2010) 787.
- [260] R.K. Blandford, D.K. Morton, S.D. Snow and T.E. Rahl, *Tensile Stress-Strain Results for 304L and 316L Stainless Steel Plate at Temperature*, in *ASME 2007 PVP*, vol. 6 of *Pressure Vessels and Piping Conference*, pp. 617–628, 2007, [10.1115/PVP2007-26096](#).
- [261] H. Schindler, *Garfield++ User Guide*. CERN, 2022.
- [262] R. Brun et al., *ROOT* - analyzing petabytes of data, scientifically [v6.18/02], Zenodo (2019).
- [263] S.F. Biagi, *Monte Carlo simulation of electron drift and diffusion in counting gases under the influence of electric and magnetic fields*, *Nucl. Instrum. Meth. A* **421** (1999) 234.
- [264] R. Veenhof, *Magboltz* - transport of electrons in gas mixtures, website (2022).
- [265] K. Kumar, *The physics of swarms and some basic questions of kinetic theory*, *Phys. Rep.* **112** (1984) 319.

Bibliography

- [266] S. Biagi, *A multiterm boltzmann analysis of drift velocity, diffusion, gain and magnetic-field effects in argon-methane-water-vapour mixtures*, *Nucl. Instrum. Meth. A* **283** (1989) 716.
- [267] S. Biagi, *Accurate solution of the boltzmann transport equation*, *Nucl. Instrum. Meth. A* **273** (1988) 533.
- [268] S.F. Biagi, *Biagi database*, 2014.
- [269] L.C. Pitchford et al., *LXCat : an open-access, web-based platform for data needed for modeling low temperature plasmas*, *Plasma Process. Polym.* **14** (2017) 1600098.
- [270] H. Schindler, *Microscopic Simulation of Particle Detectors*, Ph.D. thesis, Vienna, Tech. U., Atominst., 2012.
- [271] A. Kopec et al., *Correlated single- and few-electron backgrounds milliseconds after interactions in dual-phase liquid xenon time projection chambers*, *JINST* **16** (2021) P07014 [[2103.05077](#)].
- [272] LUX collaboration, *Investigation of background electron emission in the LUX detector*, *Phys. Rev. D* **102** (2020) 092004 [[2004.07791](#)].
- [273] V.C. Antochi et al., *Improved quality tests of R11410-21 photomultiplier tubes for the XENONnT experiment*, *JINST* **16** (2021) P08033 [[2104.15051](#)].
- [274] B. López Paredes, H.M. Araújo, F. Froborg, N. Marangou, I. Olcina, T.J. Sumner et al., *Response of photomultiplier tubes to xenon scintillation light*, *Astropart. Phys.* **102** (2018) 56 [[1801.01597](#)].
- [275] Hamamatsu Photonics K.K., *Photomultiplier Tubes: Basics and Applications*, 2017.
- [276] DARWIN collaboration, *DARWIN: towards the ultimate dark matter detector*, *JCAP* **11** (2016) 017 [[1606.07001](#)].
- [277] D. Logan, *A First Course in the Finite Element Method*, Cengage Learning (2016).
- [278] S. Colley and S. Leon, *Math 311 Linear Algebra and Vector Calculus*, Pearson College Division (2013).
- [279] L. Anand and S. Govindjee, *Principles of minimum potential energy and complementary energy*, in *Continuum Mechanics of Solids*, Oxford University Press (2020), [10.1093/oso/9780198864721.003.0012](#).

- [280] Y. Saad, *Iterative Methods for Sparse Linear Systems*, Other Titles in Applied Mathematics, SIAM, second ed. (2003), [10.1137/1.9780898718003](https://doi.org/10.1137/1.9780898718003).
- [281] H.M. Irvine, *Cable structures*, MIT Press Cambridge, Mass (1981).

Acknowledgments

This journey called “PhD” has not always been the easiest, but it was filled with satisfaction and really helped me growing not only as a physicist, but as a person. This was only possible thanks to the great people I met along this journey: I would like to end this thesis work by thanking them.

First of all I would like to thank Prof. Marc Schumann for the opportunity to join his group and for “pushing” me to leave my comfort zone and to test myself, even when I was too stubborn to understand how important it was. Thank you Prof. Horst Fischer, because whenever I needed help or a suggestion, I found your door open and wise words (and sometimes cables!). A special “Danke” goes to Dr. Sebastian Lindemann for the many discussions and his great support and help during these years. Either during a trip to GeMSE or at 2 a.m. in the clean room mounting the field cage, it has been a pleasure to share these moments with you.

The people of the Freiburg Astroparticle group made the 6th floor a special place. I want to thank Dr. Daniel Coderre and Dr. Darryl Masson for the many beers after work, and Dr. Adam Brown for the beers we never really managed to have together. Thanks to my old office-mate Diego and the many Vietnamese baguette we had together. Thanks also to my old/new office-mate Alexey: one journey ends, the other begins, but the travel buddy remains. My gratitude goes to all my fellow PhD colleagues during these years for the continuous help and the precious memories we built together. In particular I want to thank Daniel B. and Julia M. for our trip to LNGS, you really made those 30 hours in the truck worth it!

Being part of the XENON collaboration has been (and is still) an incredible experience and I am really grateful for this collaboration. I would like to especially mention Masatoshi, Jingqiang, Micha, Francesco, Carla, Petr, Junji, Jacques and Luca for the help, discussions, and experiences we shared. Special thanks to the Bologna group with whom my journey in XENON started. Thank you Prof.ssa Sartorelli for introducing me to the XENON project

Acknowledgments

since my bachelor work and thanks to Pietro, Marco S. and Marco G. for the help and patience you had with a young Francesco. Speaking of the past, I want to express my gratitude also for the future and the adventure I am starting right now. Thank you Dr. Belina von Krosigk and the entire KIT Dark Matter group for welcoming me, I am very excited to see what the future holds.

The PhD years are a part of a much longer journey and I have been blessed with incredible people as travel companions. I want to thank my closest friends: Pre, Lella, Pedro, Carli and Bizzo. Thank you for making me always feel as if those days of high schools when we had nothing to worry about never ended. In particular, Bizzo, thank you for being the best friend I could hope for and for always being there. And together with the old friend, I am grateful for the new ones that I found in Freiburg. Thank you Charlotte for being an incredible person, I consider myself really lucky that our paths crossed here in Freiburg. An “obrigado” also to the Brazilian community of Freiburg, who made an Italian guy living in Germany feel more than welcome.

Ovviamente non posso non ringraziare la mia famiglia, a cui questo lavoro di tesi è dedicato. Grazie ai miei genitori, Paolo e Renza, per essermi sempre accanto e avermi supportato (e sopportato) più di quanto voi possiate immaginare, anche quando questo ha portato a non essere più nello stesso paese. Grazie ai miei fratelli, Federica e Alberto, per tutti questi anni di liti, urla, abbracci e risate e perché alla fine so di poter sempre contare su di voi. Grazie alla Lena, perché non è sempre necessario essere parenti per essere una famiglia.

I would like to end this thesis thanking the person who gave a completely different meaning to Freiburg. Thank you Max for these amazing years and the many more to come.